

## Durham E-Theses

---

### *Theoretical studies of one-dimensional and two-dimensional photonic structures*

Andrew Alan Reeves

#### How to cite:

---

Reeves, Andrew Alan (2004) Theoretical studies of one-dimensional and two-dimensional photonic structures. Doctoral thesis, Durham University.

#### Use policy

---

The full-text may be used and/or reproduced, and given to third parties in any format or medium, without prior permission or charge, for personal research or study, educational, or not-for-profit purposes provided that:

- a full bibliographic reference is made to the original source
- a <https://etheses.durham.ac.uk/id/eprint/3019/> is made to the metadata record in Durham E-Theses
- the full-text is not changed in any way

The full-text must not be sold in any format or medium without the formal permission of the copyright holders.

Please consult the [full Durham E-Theses policy](#) for further details.

University of Durham



**Theoretical Studies of One-Dimensional  
and Two-Dimensional Photonic  
Structures**

**Andrew Alan Reeves**

Department of Physics

**A copyright of this thesis rests with the author. No quotation from it should be published without his prior written consent and information derived from it should be acknowledged.**

A thesis submitted for  
the degree of Doctor of Philosophy



2004

- 6 DEC 2004

# Abstract

This thesis is concerned with the theoretical study of one-dimensional and two-dimensional photonic structures. Plane-wave calculation methods have been employed to model one-dimensional waveguides and two-dimensional photonic crystals. The one-dimensional structures considered are slab waveguide interferometer devices. A transfer matrix method is described which has been implemented in a biosensor technique known as dual polarisation interferometry. The method presented is used for the characterisation of thin biological films. A similar slab waveguide device is described for the wavelength locking of diode lasers and a novel athermal solution to the problem is proposed.

The study of two-dimensional photonic crystals employed a standard bandstructure method and also proposed new approaches to complex photonic bandstructures which are not believed to be available elsewhere. An interface matching calculation is described which employs complex photonic bandstructures and is believed to be the first use of the method described for photonic structures. The theoretical methods are applied to consider the superprism effect in square and hexagonal lattice photonic crystals. Optimum superprism structures are arrived at for both lattices. Reflection results from the optimum hexagonal structure are also considered, combined with coupling efficiency to the superprism mode.

As a result of the work on photonic crystals new theoretical approaches have been described and implemented to assist with their establishment as calculation tools for two-dimensional photonic crystal structures.

Work presented in this thesis has contributed to the following publications:

- G H Cross, A A Reeves, S Brand, J F Popplewell, L L Peel, M J Swann, N J Freeman, "A new quantitative optical biosensor for protein characterisation", *Biosens. Bioelectron.* **19**, 383 (2003)
- G H Cross, A Reeves, S Brand, M J Swann, L L Peel, N J Freeman and J R Lu, "The metrics of surface absorbed small molecules on the Youngs fringe dual-slab waveguide interferometer", *J. Phys. D:Appl. Phys.* **37**, 74 (2004)
- N J Freeman, L L Peel, M J Swann, G H Cross, A Reeves, S Brand and J R Lu, "Real time, high resolution studies of protein absorbtion at the solid-liquid interface using dual polarization interferometry", *J. Phys.: Condens. Matter* **16**, S2493 (2004)

In addition work from Chapter 3 entitled "Diode Laser Tracking" has contributed to the following patent:

- A A Reeves and G H Cross "Design of an integrated multi-layer slab waveguide as an athermal wavelength sensitive interferometer", British Patent Filed by Farfield Sensors Ltd. (2003)

# **Declaration**

The work presented in this thesis was carried out in the Condensed Matter Theory Group in the Department of Physics, University of Durham, between October 2000 and April 2004. The work has not been submitted for any other degree in the University of Durham or elsewhere, and unless stated otherwise, is the original work of the author.

# **Copyright**

The copyright of this thesis rests with the author. No quotation from it should be published without his prior written consent and information derived from it should be acknowledged.

# Acknowledgements

I am indebted to my supervisor Dr. Stuart Brand for his depth of knowledge, assistance and patience throughout my studies. I would also like to thank Prof. M. Burt for his notes on complex bandstructures. A major influence in the direction this work took came from Dr. Graham Cross and Farfield Sensors Ltd. I am grateful to Graham for both the discussions regarding the interesting applications for this work and also for his eternal optimism. The financial support provided by EPSRC and Farfield Sensors Ltd. was also greatly appreciated.

Outside of work, my time in Durham has been made enjoyable by many people especially Michaela and also the members of the CMT group. In addition, welcome distractions from work have also been provided by the many friends which I have found in DUSKC. Finally, I would like to acknowledge the constant love and support of my family which will always be remembered.

# Contents

<b>1</b>	<b>Introduction</b>	<b>1</b>
1.1	Photonics . . . . .	1
1.1.1	Advantages of Light . . . . .	2
1.2	One-dimensional Photonic Structures . . . . .	3
1.2.1	Waveguide Interferometry . . . . .	3
1.3	Two-dimensional Photonic Structures . . . . .	4
1.3.1	Concept of Photonic Crystals . . . . .	4
1.3.2	Early Experimental Structures . . . . .	6
1.3.3	Two dimensional Structures . . . . .	8
1.3.4	Superprisms . . . . .	8
1.4	Description of the work . . . . .	9
<b>2</b>	<b>Dual Polarisation Interferometry</b>	<b>10</b>
2.1	Introduction . . . . .	10
2.2	Protein Analysis . . . . .	11
2.3	Biosensors . . . . .	12
2.3.1	Surface Plasmon Resonance . . . . .	12
2.3.2	Resonant Mirror Sensors . . . . .	13
2.3.3	Dual Polarisation Interferometry . . . . .	13
2.4	Principle of Interferometry . . . . .	14
2.5	Waveguide Interferometry . . . . .	16
2.5.1	Total Internal Reflection . . . . .	16
2.5.2	Operating Principles . . . . .	17
2.5.3	Phase Detection . . . . .	19

2.6	Plane-wave Approach . . . . .	20
2.6.1	Optogeometrical Parameters . . . . .	21
2.6.2	Guided Modes . . . . .	21
2.6.3	Maxwell's Equations . . . . .	22
2.6.4	TM . . . . .	25
2.6.5	TE . . . . .	27
2.6.6	Matrix methods . . . . .	28
2.6.7	Guided Modes . . . . .	32
2.7	sense . . . . .	33
2.8	Chip Design . . . . .	34
2.9	Manufacturing Tolerances . . . . .	38
2.9.1	Chip Structure . . . . .	38
2.9.2	Approach . . . . .	39
2.9.3	Results . . . . .	39
2.9.4	Discussion . . . . .	47
2.10	Verification of technique . . . . .	48
2.10.1	Instrument Details . . . . .	48
2.10.2	Biotin/streptavidin . . . . .	49
2.10.3	BS <sup>3</sup> /anti-HSA . . . . .	51
2.10.4	Discussion . . . . .	51
2.11	Conclusions and Future Work . . . . .	51
<b>3</b>	<b>Diode Laser Tracking</b>	<b>53</b>
3.1	Introduction . . . . .	53
3.2	Telecommunications Background . . . . .	54
3.2.1	Dense Wavelength Division Multiplexing . . . . .	54
3.2.2	Diode Lasers . . . . .	56
3.2.3	Double Hetrostructures . . . . .	56
3.2.4	Distributed Feedback Lasers . . . . .	58
3.2.5	Stability . . . . .	59
3.2.6	Stabilisation Systems . . . . .	59
3.3	Integrated Wavelength Interferometry . . . . .	60

3.4	Design Concept . . . . .	61
3.5	Theoretical Method . . . . .	62
3.5.1	Linear Thermal Expansion . . . . .	62
3.5.2	Refractive Index Dispersion Relations . . . . .	63
3.5.3	Modes . . . . .	64
3.6	Structure Response . . . . .	65
3.6.1	Advantages . . . . .	67
3.7	Conclusions and Future work . . . . .	72
<b>4</b>	<b>Photonic Crystal Theory</b>	<b>73</b>
4.1	Introduction . . . . .	73
4.1.1	Analogy with Semiconductors . . . . .	73
4.1.2	Physical Origin of Bandstructures . . . . .	74
4.2	Computational Approaches . . . . .	74
4.2.1	Scalar Wave Approximation . . . . .	75
4.2.2	Frequency Domain Approach . . . . .	75
4.2.3	Time Domain Approach . . . . .	76
4.2.4	Transfer Matrix Approach . . . . .	76
4.3	Plane-wave Methods . . . . .	77
4.3.1	Coordinate System . . . . .	77
4.4	Maxwell's Equations . . . . .	78
4.4.1	Electrical Properties . . . . .	79
4.4.2	Magnetic Properties . . . . .	80
4.4.3	Maxwell's Equations for Photonic Crystals . . . . .	80
4.5	Plane-wave Expansion . . . . .	81
4.5.1	Permittivity . . . . .	82
4.6	Standard Bandstructure Method . . . . .	83
4.6.1	TE Modes . . . . .	83
4.6.2	Brillouin Zone . . . . .	84
4.6.3	Eigenvalue Equation . . . . .	85
4.6.4	Scaling Law . . . . .	86
4.6.5	Matrix Methods . . . . .	87

4.6.6	TM modes . . . . .	89
4.7	Out of Plane Propagation . . . . .	92
4.8	Permittivity . . . . .	93
4.8.1	Circular Rods . . . . .	93
4.8.2	Coated rods . . . . .	96
4.9	Complex Bandstructure . . . . .	97
4.9.1	Complex Wavevector . . . . .	99
4.10	Electronic Structure Analogy . . . . .	99
4.10.1	TE Mode . . . . .	99
4.10.2	Directional Bandstructures . . . . .	101
4.10.3	TM mode . . . . .	103
4.11	Dual Field Approach . . . . .	103
4.11.1	Eigenvalue Equation . . . . .	104
4.11.2	TM Mode . . . . .	105
4.11.3	TE Polarisation . . . . .	109
4.11.4	Directional Bandstructure . . . . .	112
4.12	Refraction Law . . . . .	113
4.12.1	Uniform Media . . . . .	113
4.12.2	Superprisms . . . . .	116
4.13	Summary . . . . .	118
<b>5</b>	<b>Square Lattice Calculations</b>	<b>119</b>
5.1	Introduction . . . . .	119
5.2	Square Lattice . . . . .	120
5.2.1	Brillouin Zone . . . . .	122
5.3	Convergence . . . . .	123
5.4	Bandstructures . . . . .	125
5.4.1	Standard Bandstructures . . . . .	125
5.4.2	Field Profiles . . . . .	130
5.5	Refraction Properties . . . . .	135
5.5.1	Multiple Solutions . . . . .	136
5.6	Bandstructure Anisotropy . . . . .	139

5.6.1	Results . . . . .	143
5.7	Refraction Properties . . . . .	151
5.7.1	Angle Sensitivity . . . . .	151
5.7.2	Wavelength Sensitivity . . . . .	151
5.8	Conclusions . . . . .	153
<b>6</b>	<b>Hexagonal Lattice Calculations</b>	<b>154</b>
6.1	Introduction . . . . .	154
6.2	The Hexagonal Lattice . . . . .	155
6.2.1	Primitive Lattice Vectors . . . . .	157
6.2.2	Reciprocal Lattice Vectors . . . . .	157
6.2.3	Brillouin Zone . . . . .	158
6.3	Results . . . . .	159
6.3.1	Convergence . . . . .	159
6.4	Bandstructures . . . . .	161
6.4.1	Field Profiles . . . . .	161
6.4.2	Complete Band Gap . . . . .	162
6.5	Refraction Properties . . . . .	166
6.5.1	Bandstructure Anisotropy . . . . .	166
6.5.2	Gradient Method . . . . .	166
6.6	Optimisation Results . . . . .	168
6.7	Dispersion Characteristics . . . . .	172
6.7.1	Angular Deviation . . . . .	172
6.7.2	Frequency Deviation . . . . .	172
6.8	Conclusions . . . . .	174
<b>7</b>	<b>Interface Matching</b>	<b>175</b>
7.1	Introduction . . . . .	175
7.2	Complex Bandstructures . . . . .	176
7.2.1	Bloch States . . . . .	176
7.2.2	Bandstructure Plots . . . . .	177
7.2.3	Complex Bandstructure Convergence . . . . .	179

---

7.3	Interface Matching . . . . .	179
7.3.1	TE polarisation . . . . .	181
7.3.2	TM Polarisation . . . . .	191
7.4	Fresnel Equations . . . . .	197
7.5	Results . . . . .	199
7.5.1	Uniform Materials . . . . .	199
7.5.2	Photonic Crystals . . . . .	201
7.5.3	Optimisation . . . . .	202
7.5.4	Matching . . . . .	207
7.6	Conclusions . . . . .	208
<b>8</b>	<b>Conclusions and Suggestions for Future Work</b>	<b>210</b>
8.0.1	Conclusions . . . . .	210
8.0.2	Suggestions for Future Work . . . . .	212
	<b>Appendix A</b>	<b>214</b>
	<b>Appendix B</b>	<b>215</b>
	<b>References</b>	<b>220</b>

# List of Figures

1.1	Schematic of a slab waveguide interferometer. . . . .	4
1.2	A one-dimensional photonic crystal forming a dielectric stack, or multi-layer film. . . . .	6
1.3	Yablonovite. The complex fabrication method utilising three different drilling angles for each hole is shown. . . . .	7
2.1	Experimental arrangement for biosensors based on surface plasmon resonance (SPR) . . . . .	12
2.2	Experimental arrangement for biosensors based on resonant mirror (RM) sensing. . . . .	14
2.3	Schematic representation of the original Michelson-Morley interferometer experiment. . . . .	15
2.4	Total internal reflection demonstrating the confinement of light to a waveguide a) simple ray model b) wave model. . . . .	17
2.5	Vertically integrated dual-slab waveguide structure. . . . .	18
2.6	Arrangement used for the detection of phase changes in the output of the dual-slab waveguide interferometer. . . . .	20
2.7	Interface matching notation for first interface. . . . .	29
2.8	Interface matching notation for a general interface. . . . .	30
2.9	Unique thickness and refractive index solutions identified by dual polarisation curve. . . . .	35
2.10	Electric field profiles for the two modes present in a dual-slab waveguide interferometer. . . . .	37
2.11	Four layer chip structure used for the base waveguide interferometer structure. . . . .	37

2.12	Effect of Layer four manufacturing tolerances on a low refractive index film for (a) thickness (b) refractive index (c) combined. . . . .	40
2.13	Effect of variation in layer four tolerance effects on different deposited layer thicknesses (a) thickness (b) refractive index. . . . .	43
2.14	Effect of Layer four manufacturing tolerances on a low refractive index film for (a) thickness (b) refractive index (c) combined. . . . .	44
2.15	Results for a worst case structure (a) resolved layer thickness (b) resolved layer refractive index. . . . .	46
2.16	(a) Schematic of dual polarisation interferometry experimental arrangement. (b) Photo of the apparatus. . . . .	50
3.1	Double hetrostructure diode semiconductor laser arrangement. . . . .	57
3.2	(a) Distributed feedback laser arrangement. (b) Bragg reflector laser arrangement. . . . .	58
3.3	Proposed waveguide interferometer arrangement for diode laser wavelength tracking. . . . .	60
3.4	Proposed athermal structure for waveguide interferometry. . . . .	62
3.5	Single guided mode region for a symmetric three layer upper guide. . . . .	65
3.6	Plot of the change in the difference between the upper and lower guided mode propagation constants due to a 1 K temperature increase. . . . .	66
3.7	Plot of the change in the difference between the upper and lower guided mode propagation constants due to a 1 nm wavelength increase. . . . .	66
3.8	Signal response (a) and thermal noise (b) for a range of dual uniform guide structures. . . . .	68
3.9	Signal to noise ratio for a dual uniform waveguide interferometer (a) and for an athermal design (b). . . . .	69
3.10	(a) Electric field profiles for proposed athermal waveguide interferometer. (b) Diffraction pattern variation due to a 1 nm wavelength change. . . . .	71
4.1	Coordinate system for two-dimensional photonic crystals. . . . .	78
4.2	The electric and magnetic field directions for the transverse magnetic (TE) polarisation. . . . .	84

4.3	The electric and magnetic field directions for a single plane-wave of a transverse magnetic (TM) polarisation. . . . .	89
4.4	An arbitrary shaped unit cell containing a circular dielectric rod of a differing refractive index to the uniform background dielectric. . . . .	94
4.5	An arbitrarily shaped unit cell containing a circular dielectric rod with a coating of a differing refractive index set in a homogenous background dielectric. . . . .	96
4.6	Complex bandstructure example. . . . .	98
4.7	Conservation of phase at the interface between two uniform materials. . . . .	114
4.8	Refraction at an interface between two uniform materials with equi-frequency lines indicated. . . . .	115
4.9	Refraction law for photonic crystals. . . . .	117
5.1	Two-dimensional square lattice type with lattice constant $a$ and rods of radius $pa$ indicated. . . . .	121
5.2	The square lattice in reciprocal space with Brillouin Zone indicated. . . . .	121
5.3	Convergence for (a) TE modes (b) TM modes (c) differing positions (d) differing rod radii. . . . .	124
5.4	TE square lattice bandstructures for alumina rods in air with rod radii of (a) $r \approx 0$ , (b) $r = 0.1a$ , (c) $r = 0.2a$ , (d) $r = 0.3a$ , (e) $r = 0.4a$ , (f) $r = 0.5a$ . . . . .	126
5.5	TM square lattice bandstructures for alumina rods in air with rod radii of (a) $r \approx 0$ , (b) $r = 0.1a$ , (c) $r = 0.2a$ , (d) $r = 0.3a$ , (e) $r = 0.4a$ , (f) $r = 0.5a$ . . . . .	127
5.6	Electric field profiles for the first (a) and second (b) bands of the TM polarisation at the $M$ point. . . . .	131
5.7	TM electric field profiles for the first two bands at the high symmetry Brillouin Zone points. . . . .	133
5.8	TE magnetic field profiles for the first two bands at the high symmetry Brillouin Zone points. . . . .	134
5.9	Equi-frequency curves (TE modes) for square lattice of alumina rods $r = 0.2a$ at frequencies (a) $\omega = 0.3c/a$ and (b) $\omega = 0.4c/a$ . . . . .	137
5.10	Frequencies which exhibit single refraction angles for the TM polarisation and a square lattice structure consisting of dielectric rods in air. . . . .	140

5.11	An example bandstructure (a) with dispersion surfaces plotted for three different frequencies (b) $\omega = 0.4c/a$ , (c) $\omega = 0.58c/a$ and (d) $\omega = 0.69c/a$ . . . . .	142
5.12	The anisotropy ratio plotted as a function of frequency for $r = 0.1a$ , $n = 2$ and a TE polarisation. . . . .	144
5.13	TE anisotropy ratios for rod radii of $0.1a$ (a), $0.2a$ (b), $0.3a$ (c), $0.4a$ (d) and $0.5a$ (d). . . . .	146
5.14	TE anisotropy ratios for the rod radii with the highest peak values. The ratios have been plotted as a function of frequency for (a) $n = 3$ , (c) $n = 4$ , (e) $n = 5$ and (g) $n = 6$ . The peak value dispersion surfaces are shown (b) $n = 3$ , (d) $n = 4$ , (f) $n = 5$ and (h) $n = 6$ . . . . .	147
5.15	TM anisotropy ratios for the rod radii with the highest peak values. The ratios have been plotted as a function of frequency (a) $n = 2$ , (c) $n = 3$ and (e) $n = 4$ . The peak value dispersion surfaces are shown (b) $n = 2$ , (d) $n = 3$ and (f) $n = 4$ . . . . .	149
5.16	TM anisotropy ratios for the rod radii with the highest peak values. The ratios have been plotted as a function of frequency (a) $n = 5$ and (c) $n = 6$ . The peak value dispersion surfaces are shown (b) $n = 5$ and (d) $n = 6$ . . . . .	150
5.17	Dispersion surface for an optimum structure (a). The refraction properties are also shown for changes in angle of incidence (b). In (c) the dispersion surface for the optimum structure is shown with the black line indicating the original frequency, the green a 1% frequency increase and the red a 1% frequency decrease. The refraction properties are also shown (d). Note there is no 1% decrease line in (d) due to the existence of multiple refraction angles for a given angle of incidence. . . . .	152
6.1	The hexagonal lattice type with a lattice constant and rod diameter indicated. . . . .	155
6.2	The two-dimensional hexagonal lattice with Wigner-Seitz unit cell indicated. . . . .	156
6.3	Hexagonal lattice in reciprocal space with Brillouin Zone indicated. . . . .	156
6.4	Convergence for the hexagonal lattice for (a) TE modes (b) TM modes (c) Brillouin Zone position (d) rod radii. . . . .	160
6.5	Bandstructures for a structure consisting of 27% air ( $n=1$ ), 16% oxide ( $n=1.5$ ) and 57% semiconductor ( $n=3.42$ ). . . . .	161

6.6	TE magnetic field profiles for the first and second bands at the high symmetry points. . . . .	163
6.7	TM electric field profiles for the first and second bands at the high symmetry points. . . . .	164
6.8	Width of complete band-gaps for a variety of refractive indices and rod radii.	165
6.9	The TE (a) and TM (b) bandstructure for the optimum absolute band-gap structure . . . . .	165
6.10	A bandstructure is shown (a) with three frequencies ( $\omega = 0.15c/a$ , $\omega = 0.26c/a$ and $\omega = 0.35c/a$ ) indicated and the dispersion surfaces plotted at these points. . . . .	167
6.11	An example of a positive gradient in the $\Gamma - M$ direction. Dispersion surface is for $n = 2$ , $r = 0.4a$ and $\omega = 0.65c/a$ . . . . .	169
6.12	Sharpest dispersion surfaces identified. (a) TE $n = 3$ , $r = 0.4a$ , $\omega = 0.58c/a$ (b) TM $n = 2$ , $r = 0.4a$ , $\omega = 0.65c/a$ (c) TE $n = 2$ , $r = 0.3a$ , $\omega = 0.78$ (d) TM $n = 2$ , $r = 0.1a$ $\omega = 0.34c/a$ . . . . .	171
6.13	Dispersion surfaces and refraction properties for the optimum structure. . .	173
7.1	Example of a complex bandstructure. . . . .	178
7.2	Convergence tests for imaginary solutions. The lowest magnitude imaginary solution is considered at a mid frequency. . . . .	180
7.3	Arrangement for interface matching. . . . .	181
7.4	Allowed solutions on the air side of the interface. . . . .	184
7.5	Reflection at an interface between two materials of uniform refractive index.	198
7.6	Fresnel Equations plotted for the TM (a) and TE (b) polarisations, together with results generated by the interface matching calculations. . . . .	200
7.7	Outline of interface matching calculation. . . . .	203
7.8	Optimum dispersion surfaces for the TE and TM polarisations in the directions $\Gamma - K$ and $\Gamma - M$ . (a) TE $n = 5$ , $\omega = 0.9c/a$ , $r = 0.4a$ . (b) TM $n = 3$ , $\omega = 0.68c/a$ , $r = 0.1a$ . (c) TE $n = 5$ , $\omega = 0.81c/a$ , $r = 0.1a$ . (d) TM $n = 3$ , $\omega = 0.93$ , $r = 0.1a$ . . . . .	206
7.9	Reflection from the optimum single angle of refraction structure. . . . .	207

---

A-1	Frequencies which exhibit single refraction angles for the TE polarisation and a square lattice structure consisting of dielectric rods in air. . . . .	214
A-2	Square lattice in reciprocal space. . . . .	216
A-3	Hexagonal lattice in reciprocal space. . . . .	217
A-4	Hexagonal lattice with an interface. . . . .	218

# List of Tables

2.1	Optogeometrical parameters for the base waveguide chip structure. . . . .	36
2.2	Variations in the optogeometrical parameters of the chip structure which are permitted by the manufacturing tolerances. . . . .	38
2.3	Lower layer tolerance effects on the resolved thickness of a 100 nm ( $n = 1.45$ ) deposited layer. . . . .	47
3.1	ITU standards for single fibre bandwidths. . . . .	55
3.2	Values of relevant Si and SiO <sub>2</sub> coefficients. . . . .	64
3.3	Optimised waveguide structure. . . . .	67
5.1	Electric field factors for TM and TE modes at the high symmetry X and M points. . . . .	135
5.2	Rod radii, refractive index contrast and frequency used for the anisotropy optimisation study. . . . .	143
5.3	Highest anisotropy ratios for each refractive index value (TE polarisation). . . . .	148
5.4	Highest anisotropy ratios for each refractive index value (TM polarisation). . . . .	150
6.1	The fraction of the electric field energy found in the holes for TE and TM modes at the high symmetry X and M points (hexagonal lattice). . . . .	162
6.2	Extreme inverse gradient values for the $\Gamma - M$ direction. . . . .	170
6.3	Extreme gradient values for the $\Gamma - K$ direction. . . . .	170
7.1	Extreme values in the $\Gamma - K$ direction. . . . .	205
7.2	Extreme values in the $\Gamma - M$ direction. . . . .	205

# Chapter 1

## Introduction

### 1.1 Photonics

The modern world is part of a technological age. It is almost entirely reliant on electrical devices to provide the now fundamental services which enable our society to function on a daily basis. The continual need of man for advancement has demanded that electrical devices operate at increasingly rapid speeds in order to keep pace with the ever expanding number of applications for them. Increasing the speed of electrical devices normally means a reduction in the size of the individual features. This realisation led, in 1965, to Moore's law [1] which still holds today [2]. The law describes how the number of transistors per unit area of an integrated circuit roughly doubles every two years.

The semiconductor industry has managed to keep pace with the demand for smaller components through the continual refinement of its electrical circuit manufacturing techniques. The miniaturisation of components may currently be achieved to impressively small scales. However, the decrease in dimensions of an electrical device leads to an increase in the resistance experienced by the moving electrons. This creates increased power dissipation problems. A further restriction on the operational speed of conventional electrical circuits is the physical speed at which an electron can be made to move through a semiconductor. The use of classical electrical circuits also places some fundamental limits on the reductions in size possible. Currently these limitations have no solutions [3].

Whilst research into extracting enhanced performance from electrical devices will continue within the semiconductor fraternity [4] the time is also ripe to thoroughly examine al-

ternatives. One possibility is to consider devices which use light to perform their operations. The advantages offered by light over electrons has already been exploited by the telecommunications industry. Optical fibre technology [5] has revolutionised the industry by enabling greatly increased data and voice traffic across large distances. The study of optical fibres and other technologies that either generate or harness light and other forms of radiant energy, whose quantum unit is the photon, is usually referred to as 'photonics'.

One particular type of photonic structure may be formed by modulating the refractive index of a structure in one or more dimensions. The first structures considered in this thesis possess a refractive index which varies in just one dimension. These structures may be referred to as one-dimensional photonic structures. A different type of photonic structure may be formed by periodically modulating the refractive index in two dimensions. Structures which possess a periodic refractive index modulation are often referred to as photonic crystals. In this work two-dimensional photonic crystals are studied for their novel refraction properties. This chapter provides an overview of the one-dimensional and two-dimensional photonic structures studied and also a description of the work presented in the subsequent chapters.

### 1.1.1 Advantages of Light

Whilst research into optical devices is by no means still in its infancy there is an enormous, and currently only partially tapped, potential in the use of light to convey information. Light transmitted by the propagation of photons has two distinct advantages over electrons: Firstly, photons in close proximity are free from the strong interactions experienced by electrons which are in near proximity [6]; secondly, the speeds at which photons can propagate in dielectric materials is much greater than those achievable by electrons in conventional wires or circuits [7]. The potential advantages of photons over electrons has led to attempts to create photonic devices with similar functionality to certain electronic devices. The field of photonics, however, is far more diverse than simply recreating the functionality of electronic devices. Photons interact with the optical properties of materials and subsequently may provide information on these properties. The first waveguide interferometer application described in this work utilises photon-material interactions to produce a novel sensing technique.

## 1.2 One-dimensional Photonic Structures

### 1.2.1 Waveguide Interferometry

An optical waveguide may be defined as a dielectric structure which transports energy as electromagnetic radiation at wavelengths in the infrared or visible regions [8]. The term dielectric is used to refer to any material which may support an electric field. This is equivalent to the definition of a dielectric as any material which has very low electrical conductivity. Dielectric waveguides are extremely familiar in the form of optical fibres [8]. Such systems, in the simplest case, are composed of two nearly transparent dielectric regions, a core and a cladding region. Optical fibres have had a tremendous influence in telecommunications networks due to their ability to transport information over large distances with relatively low losses when compared to electrical systems.

Waveguides are designed with a low refractive index cladding region and a high refractive index core region. This produces high to low refractive index interfaces and may lead to the phenomenon known as total internal reflection at the interfaces [8]. When total internal reflection occurs the majority of the light incident at an interface is reflected back into the core region. This permits light to be confined to the core and enables it to be channelled in a desired direction. For effective total internal reflection to occur there is a need for interfaces which are planar on the scale of the wavelength of the incident light.

In the expression 'total internal reflection' the word 'reflection' implies a simple change in direction of the incident light at the interface. 'Reflection' does not provide a full account of the physics at the interface; the wave nature of light needs to be considered for an accurate representation of the system. Light may be described through the use of electromagnetic fields. The adoption of such an approach may be used to show that whilst the majority of the field is confined to the high refractive index material, a proportion of the field intensity will always exist beyond the confining region. The electromagnetic fields decay spatially away from the confining region and are normally referred to as 'evanescent fields'. The presence of field intensity beyond the confining region produces interactions between the evanescent field and the surrounding non-confining regions. These interactions may be exploited to probe the optical properties of the materials outside of the confining region. This is known as 'waveguide sensing' [9, 10].



**Figure 1.1:** Schematic of a slab waveguide interferometer. High refractive index (turquoise) and low refractive index (grey) regions are combined to create two different optical paths. The arrangement may be used as an interferometer to allow differences between the two optical paths to be investigated.

The waveguide sensing method described in this thesis makes use of a sensing structure composed of vertically integrated two-dimensional layers, as shown in Fig. 1.1. The structure may be referred to as a planar or slab waveguide [11]. Fig 1.1 shows two electromagnetic field confinement layers. They have been combined in the configuration shown to produce an interferometer type arrangement. Interferometers are devices which use interference patterns to make accurate measurements [12]. The device shown in Fig. 1.1 initially couples light from the source into the two different confining regions. The light is then allowed to propagate along the length of the slab waveguides before being recombined to form an interference pattern at the detector. Differences between the two optical paths may be inferred through analysis of the resultant interference pattern. The study of such waveguide interferometers forms the foundation of the first two photonic devices studied in this work.

## 1.3 Two-dimensional Photonic Structures

### 1.3.1 Concept of Photonic Crystals

The two-dimensional photonic structures considered in this thesis are part of a new breed of materials known as photonic crystals [13]. Photonic crystals are structures with a periodicity in their refractive index, or dielectric constant. The periodicity is designed to influence the electromagnetic fields which may exist within the materials. The original concept of photonic crystals was born out of an appealing analogy between the optical properties of periodic dielectric structures and the electrical properties of semiconductors. The original photonic crystal papers [14, 15] noted the success of semiconductors before considering the

possibility of producing photonic crystals. At the most simplistic level semiconductors [7] are materials where the atoms or molecules are arranged in a spatially periodic manner in order to produce a crystal lattice. Electrons propagating within the lattice see the crystal as a periodic potential and the conduction properties of the crystal are dictated by the geometry of the potential. The mechanism which brings about these properties may be thought of as Bragg-like diffraction. This produces a semiconductor structure in which electrons are forbidden to propagate within certain ranges of energy for given directions. The electrons are effectively restricted to a set of allowed energy bands. One of the fundamental concepts in semiconductor theory is that of the 'forbidden gap'. This is a forbidden range of electron energies which exists for all directions. A forbidden gap normally occurs between the valence and conduction bands in a semiconductor and allows for a high degree of control over the conduction properties of the material. The utility of semiconductor devices is unquestionable; the control which they provide over the propagation of electrons has produced an endless array of applications. If photonic crystals can achieve anything close to the level of penetration into our daily lives which semiconductors have achieved then they will represent a major technology for the future.

The periodic dielectric structures [13] of photonic crystals were a sensible extension of an existing optical arrangement that was already well established in the field of optics. Dielectric stacks, or multi-layer films were established for several key applications well before the term 'photonic crystal' was born. These structures consist of alternating high refractive index and low refractive index layers, for example see Fig. 1.2. The dielectric stack arrangement could now be referred to as a one-dimensional photonic crystal. The structure is designed to form a forbidden frequency in the electromagnetic dispersion relation for light propagating perpendicular to the structure. For an infinite structure there is a single frequency at which the structure acts as a perfect mirror, reflecting all the incident light. The arrangement is used, for example, in Fabry-Perot resonators [16], Bragg reflectors and also distributed feedback lasers [17].

The photonic crystal proposal by Yablonovitch [14] extended the one-dimensional periodicity of a dielectric stack arrangement to three dimensions. The three-dimensional periodicity was predicted to create a forbidden band-gap in the electromagnetic dispersion relation, irrespective of propagation direction, in essence forming a 'complete photonic band-

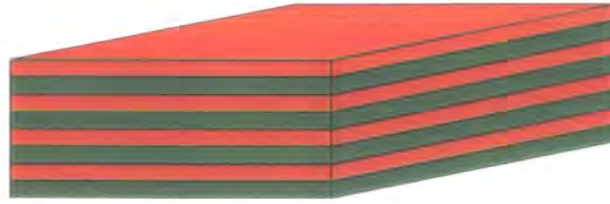


**Figure 1.2:** Two materials with different refractive indices (red and green) may be used to form a dielectric stack, or multi-layer film. The periodicity of the layers restricts the propagation of electromagnetic waves perpendicular to their surface. The device could also be referred to as a one-dimensional photonic crystal.

gap' structure. The utility of such an arrangement was originally discussed in relation to the inhibition of spontaneous emission in semiconductor lasers and other quantum electronic devices. For these devices substantial efficiency enhancements were anticipated through the use of photonic band-gaps. It was also realised that the absence of electromagnetic modes over a range of frequencies could be used to alter the basic properties of many atomic, molecular and excitonic systems [18, 19]. Early studies of photonic crystals used a theory based approach or employed microwave analogies as the technology capable of producing suitable structures on the optical scale was not available. More recently technologies capable of fabricating such structures have been developed.

### 1.3.2 Early Experimental Structures

The Bragg-like diffraction [7] off the periodic structure of photonic crystals was predicted to produce an allowed band situation similar to that seen for semiconductors. The semiconductor electronic valence and conduction band are replaced by photonic bands commonly labelled the 'dielectric' and 'air' bands. The two photonic bands are separated by a forbidden range of energies or frequencies known as the band-gap. The labels of 'air' and 'dielectric' bands stem from a consideration of the electromagnetic field confinement in one-dimensional photonic crystals. In such structures the lowest band has the majority of the electric field intensity confined within the high dielectric constant layers and the second band contains the majority of the intensity confined to the low dielectric constant material, which is often air.

Early work focused on producing a complete photonic band-gap structure with a for-

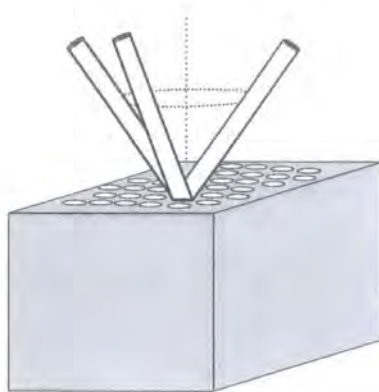


**Figure 1.3:** Yablonovite. The complex fabrication method utilising three different drilling angles for each hole is shown.

bidden range of frequencies in all directions for any polarisation of light, a situation normally referred to as an ‘absolute band-gap’. The first photonic crystal structure fabricated [20, 21] was a three-dimensional face-centered-cubic structure formed from a set of packed spheres. The spheres were made of  $\text{Al}_2\text{O}_3$  with a refractive index of slightly over 3 and had diameters of the order of 6 mm. When a structure of spherical air holes in a  $\text{Al}_2\text{O}_3$  background was fabricated the arrangement appeared to produce an absolute photonic band-gap, even if a somewhat narrow one, in the millimeter regime. However, this was later shown not to be the case [22]. The first true absolute photonic band-gap structure was produced in 1991 [23], again in the mm regime by using chemical-beam-assisted etching to drill holes into a dielectric wafer. The complexity of the three drill directions required to form such a structure, named Yablonovite after its proposer, may be seen from the schematic diagram shown in Fig. 1.3. To operate with a particular wavelength of electromagnetic radiation a photonic crystal structure is required to possess periodicity of the same order as the wavelength. The natural period of the atomic arrangement within a semiconductor corresponds to the length scale required for influencing the propagation of electrons. Periodicity on the length scales necessary for the most useful photonic crystals needs to be fabricated artificially. The usual operating wavelength of the optoelectronics community is in the infra-red regime, somewhere in the region of  $1.5 \mu\text{m}$ . This means that the basic size of a photonic crystal unit cell needs to be of the order of a micron, which is 1000 times larger than that of atomic crystals; however, it is still of a small enough order to represent a very significant fabrication challenge.

In the last 15 years several novel approaches have been adopted in the attempt to pro-

duce a three-dimensional absolute photonic band-gap structure which could operate at infrared wavelengths. Until around 2000 such a suitable structure had proved elusive and photonic band-gap structures were really limited to other wavelength regimes [24]. However, since then fabrication methods have been designed which permit such structures to be built. The current work on synthesizing such structures falls into three main camps: those using colloidal self-assembly techniques to produce opal or reverse opal structures [25–27]; those using layer by layer techniques [28–33]; and those using pore drilling techniques [34, 35]. It is worth noting that holographic approaches are also being pursued and have been shown to produce viable three-dimensional structures [36, 37].

### 1.3.3 Two dimensional Structures

Photonic band-gaps are not unique to three-dimensional structures [39–41]. For many opto-electronic applications two-dimensional structures which possess similar optical properties to their three-dimensional counterparts also offer great potential [42]. Two-dimensional structure fabrication methods benefit from the existence of well developed integrated circuit manufacturing techniques [43]. Whilst the  $1.5 \mu\text{m}$  scale is still a challenging regime for fabrication, it is more readily achievable in two dimensions than in three. The first two-dimensional structure [44], similar to the first three-dimensional structure, was also produced and tested in the millimeter regime. The first two-dimensional structure consisted of alumina rods which were arranged to form a periodic square lattice in an air background. The structure possessed a photonic band-gap for one polarisation only. The square lattice experiments were soon followed by experiments based on a hexagonal, or triangular lattice [45]. This lattice type was shown to be capable of producing an absolute photonic band-gap and in recent years structures have been produced which operate at near-infrared wavelengths [46].

### 1.3.4 Superprisms

‘Superprisms’ are one of the potentially useful applications for both two and three dimensional photonic crystal structures [47–53]. Superprisms derive their name from the conventional optical devices known as prisms. Prisms are commonly used to refract light or separate light of similar wavelengths from a multi-wavelength beam. Glass prisms are often demonstrated separating white light into rainbow patterns through the wavelength de-

pendence of their angular deviation. Certain photonic crystal systems are referred to as superprisms as they demonstrate similar wavelength separation but with greater differences in angular deviation than is achievable by conventional uniform media. Superprisms have also been shown to possess an angle of refraction which is highly dependent on the incident angle. The high sensitivity to the incident angle and wavelength has led to the proposal of potential superprism based devices for use in a variety of beam-steering and wavelength separation applications.

## 1.4 Description of the work

This thesis is concerned with theoretical calculations on both one-dimensional waveguide interferometers and two-dimensional photonic crystals. Chapters 2 and 3 present theoretical studies using waveguide interferometry arrangements. The former is concerned with a new biosensor technique known as ‘Dual Polarisation Interferometry’ and the latter with a proposed athermal wavelength tracker for diode lasers. The following four chapters are concerned with two-dimensional photonic crystals. Chapter 4 describes the theoretical methods which are employed for studying such structures. The methods are applied in the following two chapters to describe the basic properties of firstly the square and then the hexagonal lattices. The chapters also include original work on the optimisation of bandstructure anisotropy and the effect this has on the refraction properties of the structures. The final results chapter is Chapter 7 which describes a method for calculating reflection coefficients at air-photonic crystal interfaces. Results are given from the application of this new method. Chapter 8 summaries the main results presented in the previous chapters and also draws conclusions on the utility of the photonic structures previously discussed.

# Chapter 2

## Dual Polarisation Interferometry

### 2.1 Introduction

Dual Polarisation Interferometry (DPI) is a technique pioneered by Farfield Sensors Ltd. for the detection and investigation of the properties of thin films [54]. The technique uses multi-layered waveguides in an interferometry type arrangement to allow for the quantitative resolution of the optogeometrical parameters of unknown layers deposited onto a well defined waveguide structure [8]. The structure may be considered as a one-dimensional photonic device and theoretically modelled using a plane-wave transfer matrix type approach [55]. This chapter presents the theoretical work which was undertaken to produce a model allowing both the refractive index and thickness of deposited layers to be calculated from the information available from the waveguide interferometer arrangement.

Waveguide interferometers possess a high sensitivity to small optogeometrical variations which is fundamental to their ability to assist in the characterisation of thin films. However, the high level of sensitivity may also cause such a device to be susceptible to variations in the optogeometrical parameters of the individual layers which form the base waveguide structure. Variations of this nature will be unavoidably introduced into the structure by the fabrication process. An actual base structure will have layer optogeometrical properties which are only defined to within certain manufacturing tolerances. A theoretical study was undertaken to establish the influence of these manufacturing tolerances on the detection ability of a dual polarisation interferometer device. Results from the study are included in this chapter with a discussion of their implications.

The theoretical model presented is based on a set of assumptions, the validity of which cannot be ensured without the comparison of experimental results produced by dual polarisation interferometry with those produced by alternative methods. Dr. Graham Cross *et al.* [56] have provided results of this nature, using the theoretical model presented in this chapter. A discussion of their experimental results has been included to allow experimental verification of the dual polarisation interferometry technique to be given.

## 2.2 Protein Analysis

The ability to investigate the optical and physical properties of thin films has applications across a wide range of scientific fields. The dual polarisation interferometry technique has been developed specifically for the characterisation of thin biological films. The technique provides information that is believed to be of utility for the examination of the real-time bonding behaviour of proteins under differing conditions.

A protein [57] is defined as any of a group of complex organic macromolecules that contain carbon, hydrogen, oxygen, nitrogen, and usually sulphur. All living cells are built from proteins including many substances such as enzymes, hormones, and antibodies, which are necessary for the proper functioning of an organism. Proteins are formed from one or more chains of a group of organic compounds known as amino acids. There are 20 different amino acids which combine in a variety of different configurations to form all the proteins present in the human body. Understanding the behaviour of these proteins in a range of differing environments is an essential element in the search for cures and vaccines for many diseases. Biosensor devices which are highly sensitive to protein changes are currently a vital research field. Seemingly small changes in proteins are often the key to the potential causes of life changing diseases and disorders. Existing techniques which offer real-time sensitivity to protein bonding events tend to provide only a qualitative indication of the changes occurring, rather than definite quantitative data. The current techniques lack the ability to provide the type of unambiguous optogeometrical information that dual polarisation interferometry offers for the real-time investigation of biomolecular interactions.

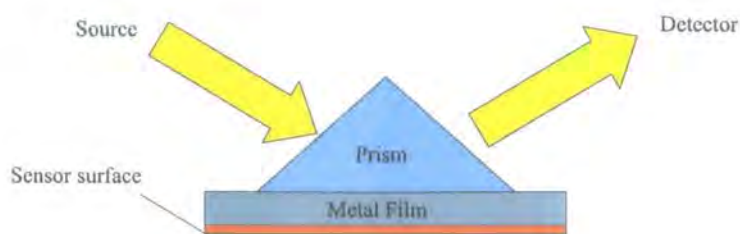


**Figure 2.1:** Surface plasmon resonance (SPR) uses a prism to couple light to a thin metal film. Variations in the reflected intensity are monitored to allow for the detection of protein bonding events at the sensing surface.

## 2.3 Biosensors

The field of biosensing is extremely diverse. It contains numerous devices which have been developed using a variety of different physical and chemical techniques. The field is also one which is expanding rapidly. Before 1985 there were just 213 scientific publications on biosensors. However, by mid 1996 there were over 6000 publications [58]. An overview of the biosensor field is available in the review article by Collings *et al.* [58]. The two dominant techniques used in untagged protein studies are surface plasmon resonance (SPR) [59], especially the BIAcore system [60], and resonant mirror sensing [61]. Both techniques are commonly deployed for the detection of protein interactions and represent the closest alternatives to dual polarisation interferometry. This section provides a brief description of these techniques to allow the advantages of a dual polarisation interferometry approach to be seen.

### 2.3.1 Surface Plasmon Resonance

Surface plasmon resonance (SPR) was first reported in 1959 [62]. It is a phenomenon that may occur when light is reflected off a thin metal film. Plasmons are delocalised electron excitations located within the thin metal film and may be excited by electromagnetic radiation. The resonant frequency of these plasmons is dominated by a property of the material bonded to the back of the film which is often referred to as ‘mass concentration’. This property makes the arrangement suitable for use in a sensor device [59, 63]. Mass concentration is a combined refractive index and thickness parameter with the two individual quantities in-

separable from each other by the exclusive use of information available from the technique. Fig. 2.1 shows a schematic of the experimental arrangement. Polarised light is directed on to the metal film using a prism which also couples the reflected intensity back from the film. A charge-coupled device (CCD) is used to detect changes in the intensity of the reflected light producing a 'sensogram' measuring intensity variations in 'response units'. From these changes it is possible to detect real-time protein bonding events which occur at the material bonded to the back of the thin metallic film [64]. Commercial surface plasmon devices are available [60] and further details of the technique can be found in review articles [65] [66].

### 2.3.2 Resonant Mirror Sensors

Resonant mirror sensors combine the highly sensitive surface plasmon resonance technique, summarised in the previous section, with waveguiding principles to create a device with the ability to sense events in the near vicinity of the sensing surface, as well as directly at the surface [67]. This is achieved by coupling light from the prism into a high refractive index resonant layer surrounded by two low refractive index layers, to create a waveguide. The arrangement is shown in Fig. 2.2. The evanescent field of the waveguide (see Section 2.5.1) means that the resonant frequency of the plasmons is influenced by the mass concentration up to a distance of the order of 100 nm from the sensing surface. Sensing events are measured in a method similar to the SPR technique; light is coupled back from the waveguide through the prism for detection by a CCD. The articles by Edwards *et al.* [68], Goddard *et al.* [69] and the review article by Yeung *et al.* [70] provide further details of the technique and its uses.

### 2.3.3 Dual Polarisation Interferometry

The two aforementioned techniques are highly sensitive to protein interactions but are limited by the ambiguity of the information available by solely monitoring the intensity of the reflected light. The mass concentration parameter measured by these techniques combines two key physical parameters: layer thickness and layer refractive index. Methods for the separation of the two physical quantities are available but are heavily assumption based, making their reliability questionable. Dual polarisation interferometry allows unambiguous determination of refractive indices and thicknesses from the information available from the

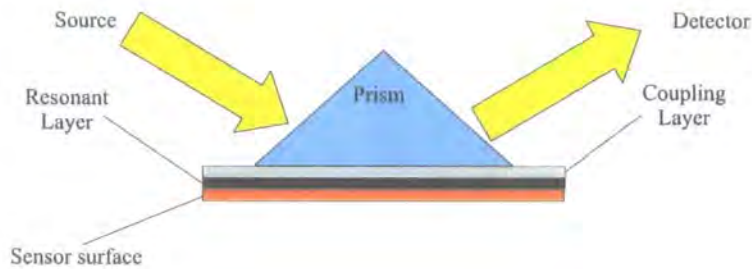


**Figure 2.2:** Resonant mirror sensing couples light into a high refractive index resonant layer between two low refractive index layers to produce a waveguide arrangement. The evanescent field extends beyond the sensing surface, providing a device sensitive to changes up to approximately 100 nm from the sensing surface.

waveguide instrument. The following sections describe the technique in detail.

## 2.4 Principle of Interferometry

Fundamentally interferometry involves the direction of electromagnetic waves along two differing optical paths and the interference of the emergent waves. The interference pattern may then be used to infer differences between the two optical paths [5]. Probably the most famous use of this well established scientific technique was the 1887 ether experiment by Albert Michelson and Edward Morley [71]. A schematic diagram of the Michelson-Morely arrangement (Fig. 2.3) demonstrates the principle of interferometry clearly. Light from a single source is separated by a beam splitter and it propagates along two different paths; the light is then recombined to form an interference pattern at the detector, which allows the difference between the two optical paths to be detected. The appearance of a modern waveguide interferometer sensor differs greatly from the Michelson-Morely experiment, but the operating principles remain the same.

Interferometers utilise the electromagnetic wave nature of light for the detection of changes of the same order of magnitude as the wavelength of the incident light. It is essential to the technique that any initial difference in phase between the light traversing the two optical paths is precisely known. A single coherent source of light, for example a laser, is normally used as the source for both paths. This ensures that the initial frequency ( $\omega$ ) and phase of the light for both optical paths are identical. Light from such a source may be

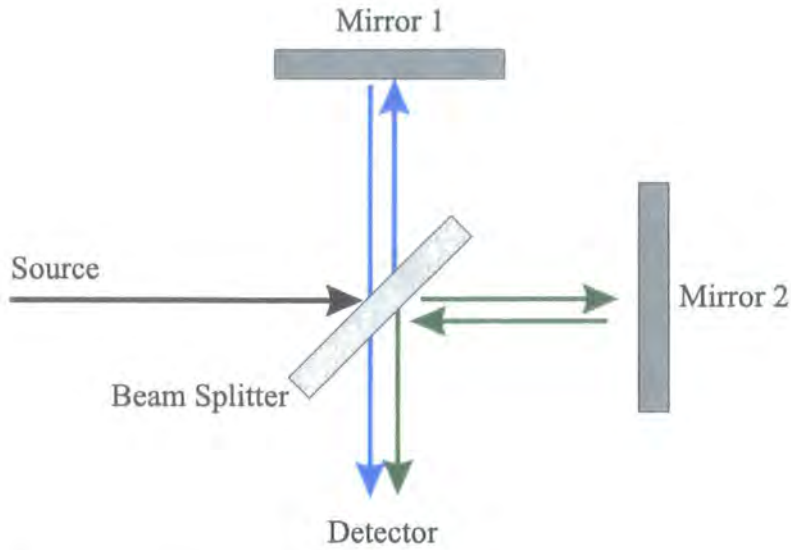


**Figure 2.3:** Schematic representation of the original Michelson-Morley interferometer. The device illustrates the principle of interferometry: Light from a single source is split along two optical paths (blue and green arrows), then recombined at the detector. The resultant signal can be used to infer a difference between the two optical paths.

represented as a plane-wave [72]. A plane-wave is simply a wave of the form:

$$\mathbf{E}(\mathbf{r}, t) = \mathbf{E}_0 e^{i(\mathbf{k} \cdot \mathbf{r} - \omega t)} \quad (2.1)$$

Mathematically the direction of propagation of a plane-wave in a uniform material is represented by a wavevector  $\mathbf{k}$ , and  $\mathbf{E}_0$  is a constant giving the magnitude, phase and polarisation direction. If a position,  $\mathbf{r}$ , is considered then equation (2.2) defines the plane-wave travelling perpendicular to a plane with points  $\mathbf{r}_0$ .

$$(\mathbf{r} - \mathbf{r}_0) \cdot \mathbf{k} = 0 \quad (2.2)$$

If the phase of the plane-wave is separated from  $\mathbf{E}_0$  then the wave may be written in terms of a phase term,  $e^{i\phi}$ , and a new constant term,  $\mathbf{E}'_0$ :

$$\mathbf{E}(\mathbf{r}, t) = \mathbf{E}'_0 e^{i(\mathbf{k} \cdot \mathbf{r} - \omega t)} e^{i\phi} \quad (2.3)$$

Initially light from a coherent source will have a single phase,  $\phi$ . The interferometer divides the plane-wave into two independent waves, the function of the beam splitter in Fig. 2.3. Differences between the two optical paths traversed by the plane-waves will manifest themselves as a phase difference,  $\Delta\phi$ , between the two plane-waves at the output point of the interferometer. Variations in the relative phase difference between the two paths will alter the interference pattern created at the detector. In the example of the ether experiment, motion in one direction relative to an immovable ether would effectively change the optical path length in that direction compared to the other, thus introducing a phase difference. Interference pattern analysis is discussed for waveguide interferometry in Section 2.5.3.

## 2.5 Waveguide Interferometry

### 2.5.1 Total Internal Reflection

Waveguide devices operate through the principle of total internal reflection which allows light to be confined to a high refractive index guiding material surrounded by a low refractive index cladding material [8]. Total internal reflection is the process in which electromagnetic radiation incident at an interface between an initial, high refractive index ( $n_1$ ) medium, and an adjacent, lower refractive index ( $n_2$ ) medium, is reflected. The effect is shown using a simple ray model for light in Fig. 2.4a. Provided that the rays incident at each high-low refractive index interface are above a certain minimum, or critical, angle then the incident light is reflected at the interface. The critical angle [8] is given by:

$$\theta_c = \sin^{-1} \left( \frac{n_2}{n_1} \right) \quad (2.4)$$

The simple ray model is not sufficient to fully describe the physics present in waveguides. Light travels as electromagnetic waves and is not simply reflected at high-low refractive index interfaces; a proportion of the incident electromagnetic field intensity extends beyond the interface into the cladding region. The electromagnetic radiation inside the cladding region is usually referred to as the evanescent field. Fig. 2.4b shows an electric field intensity schematic for a simple confined field. The electric field intensity possesses a peak within the high refractive index region and the evanescent field extends to the cladding regions. The

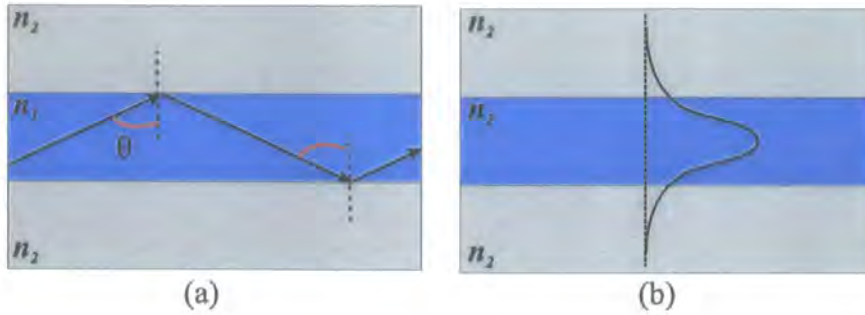


**Figure 2.4:** Total internal reflection allows the confinement of light to a waveguide. The effect can be considered using a simple ray model (a) and using a wave model (b). The wave model shows the electric field profile and it may be seen that the evanescent field of the confined mode extends beyond the guiding region (turquoise) into the cladding regions (grey).

rapidity of the decay of the field outside of the high refractive index region is determined by the refractive index contrast between the two regions and the angle  $\theta$ ; higher refractive index contrasts create more rapidly decaying profiles [11]. The arrangement may act as a sensor provided that at least one of the low refractive index regions is sufficiently thin to allow for a significant intensity of the evanescent field to exist outside of the structure [10, 73–78]. Studies exist which discuss evanescent waveguide sensing and optimise the evanescent field to maximise its sensitivity to a particular material under investigation [9, 79].

### 2.5.2 Operating Principles

The propagating waves supported by waveguides are limited to a discrete number of allowed wavevectors. These are referred to as the allowed, or guided, modes of the given structure. The method of waveguide interferometry described here effectively uses two two-dimensional slab waveguides to provide the two differing optical paths required for interferometry. Fig 2.5 shows a schematic of the arrangement. The upper high refractive index layer does not have an upper cladding layer; there is a low refractive index fluid region above the guiding layer, which provides the confinement. The evanescent field of a guided mode propagating in the upper high refractive index layer will extend into the fluid region. Provided that both high refractive index layers are of sufficiently low thickness the total structure will support just two guided modes, one with a field intensity peak in the upper high refractive index region, referred to as the upper guide, and the other with a peak in the lower high

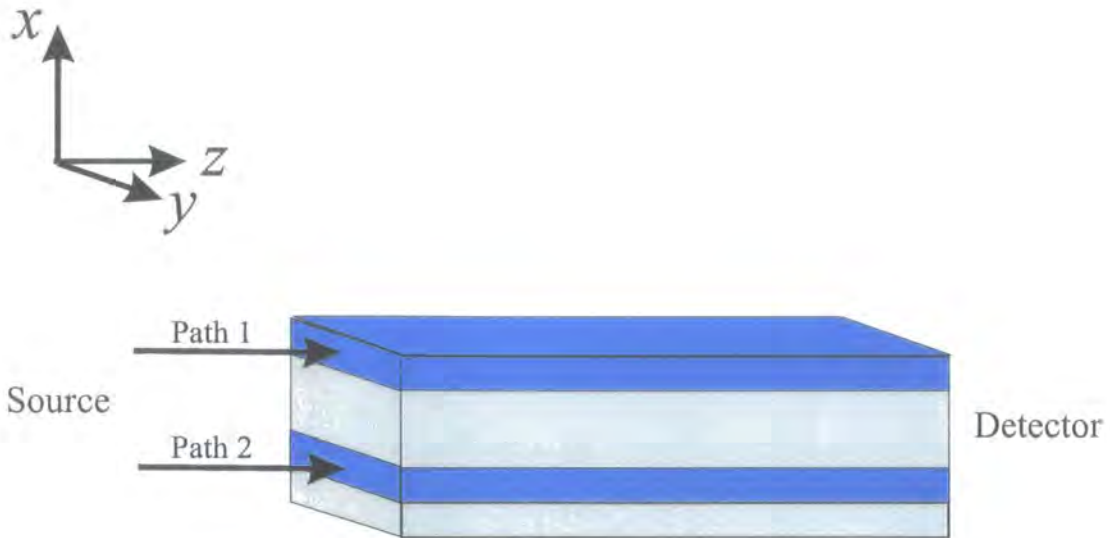


**Figure 2.5:** Vertically integrated dual-slab waveguide structure. Changes above the upper layer will alter the phase difference between light that has propagated the along length of the two guide layers (turquoise).

refractive index region: the lower guide.

The device operates as a sensor by allowing light from a single coherent laser source to propagate along the two optical paths, the lower and upper guides, simultaneously. The allowed wavevector for each guided mode is dependent on the entire waveguide structure, together with the regions above and below the structure. However, provided that the lower guide is at a sufficient distance from the upper region, the evanescent field from the lower guide will have decayed to a negligible amplitude at the upper guide. The region above the structure will then have a negligible effect on the lower guide mode. The prescribed situation may be ensured by creating a structure design with a thick, low refractive index region between the two guides. The proximity of the upper guide to the region above the structure produces a second, upper guide mode, which is highly dependent on this region. If both the upper and lower guide modes are simultaneously excited then they will propagate along the length of the structure to the output end. At the output end the high level of dependence of the upper mode on the region above the structure will create a phase difference between the two modes. In this manner the structure may be used as a sensor to detect small changes in the sensing region above the structure. Previous work has used this sensitivity to detect changes in gases, which were allowed to flow over such a waveguide interferometer

structure [80].

### 2.5.3 Phase Detection

After both guided modes have propagated the length of the structure the necessary phase difference information may be extracted from the interferometer by positioning a photosensitive detector at some distance,  $L$ , from the output edge of the structure. If  $L$  is large in comparison to the separation of the upper and lower guides then the detected pattern will be a far-field interference pattern [5]. The large distance  $L$  makes the output from the waveguide structure effectively two line sources. This creates a similar situation to the classic Young's Fringe experiment, shown schematically in Fig. 2.6. The intensity of the interference pattern at any point,  $P$ , in the detection plane is proportional to the square of the sum of the contributions from the two sets of cylindrical-waves corresponding to the upper and lower guide modes. The contribution from each of the two line sources depends on both the amplitude of the wave at point  $P$  and also the phase of the wave at this point. The phase of the wave due to the upper guide mode at  $P$  may be denoted by,  $\phi_1^P$ , and that of the lower guide mode by,  $\phi_2^P$ . Maxima will exist in the interference pattern when the light from both sources is in-phase. The condition for this occurrence is:

$$\phi_1^P - \phi_2^P = \frac{2\pi d \sin \theta}{\lambda} = 2\pi n \quad , \quad (2.5)$$

$d$  is the source separation,  $n$  is an integer or zero and  $\theta$  is the angle defined as in Fig. 2.6. As  $L \gg d$ , the small angle trigonometry approximations may be used and equation (2.5) rewritten in terms of the vertical position,  $x$ , of the maxima at the detector:

$$\frac{\phi_1^P - \phi_2^P}{2\pi} = \frac{dx}{\lambda L} = n \quad . \quad (2.6)$$

If an additional phase difference,  $\Delta\phi$ , is introduced between the two-plane waves, due to a sensing event, then the vertical position of the maxima will shift by a distance  $\Delta x$ , given by [81]:

$$\Delta x = \frac{\lambda L}{2\pi d} \Delta\phi = \frac{x \Delta\phi}{2\pi} \quad (2.7)$$

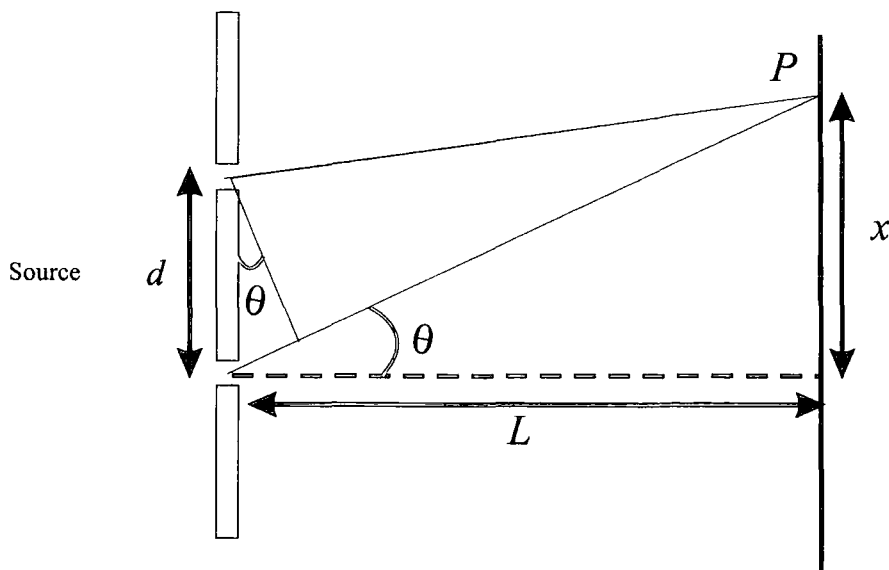


**Figure 2.6:** The output interface of the waveguide structure is similar to Young's double slit experiment shown here. Two line sources create cylindrical wavefronts which interfere to produce an interference pattern at a distance  $L$  from the two sources.

The use of the far-field interference pattern to examine phase information for a sensor device has been previously investigated [82, 83], and it was concluded that the approach provided both a compact and low cost solution to the phase detection problem.

## 2.6 Plane-wave Approach

This section describes the plane-wave transfer matrix method implemented for the calculation of allowed waveguide modes within one-dimensional multi-layered structures. A transfer matrix is a matrix that allows the plane-wave amplitudes at one position to be calculated from those at some other, initial position. The transfer matrix method described here achieves this through matching the relevant electromagnetic field amplitudes at individual layer interfaces throughout the structure. The method allows the wavevectors of the guided modes to be found, and also the electric and magnetic field profiles across the multi-layer structure. The structure under consideration is referred to as one-dimensional due to refractive index variation occurring in one direction only, although the structure is assumed to be infinite in all three dimensions.

### 2.6.1 Optogeometrical Parameters

The basic physical properties of the individual dielectric layers which form the waveguide structure are the refractive index and thickness of the layer. In the model described here the thickness of the individual layers will be assumed to be uniform, hence the layers give rise to planar interfaces with each other. It is possible that the layer thickness will alter due to the thermal expansion of the structure layers. However, such effects will be negligible in the structures under consideration, due to the tight thermal control which will be enforced on the experimental structures.

The refractive indices of the individual layers used in the model also require some consideration. For a non-conducting dielectric material the refractive index of a material may be described as the ratio of the speed of light in a vacuum ( $c$ ) to the magnitude of the phase velocity ( $v_{ph}$ ) of the light in the particular dielectric of interest [11]:

$$n = \frac{c}{v_{ph}} \quad (2.8)$$

However, individual materials may not be isotropic and homogenous and may exhibit birefringence: a different refractive indices in different directions. In addition the refractive index may depend on frequency or a variety of other thermal, non-linear and absorption related properties [11]. The existence of such effects would make it inappropriate to attribute a single refractive index value to an individual layer. Here the assumption is made that such effects are absent from the dielectrics that form the waveguide structure and also those that form any deposited layer. A single fixed refractive index value is attributed to each of the individual layers that form the structure.

### 2.6.2 Guided Modes

The wavevectors of modes which propagate through a waveguide are limited to discrete values. If an unsupported mode is coupled into a waveguide then the electromagnetic field amplitudes are rapidly attenuated; the electromagnetic radiation escapes to the cladding layers or layers surround the cladding layers. Guided modes possess peaks in the relevant field profiles within the high refractive index guiding layers. Either side of the structure the

profiles show a decay in field intensity with distance from the structure. If a wavevector which does not represent a guided mode of the structure is used in the transfer matrix calculation then, once calculated, the relevant field profile would display fields that increase with distance from the structure. In practice, the total electromagnetic field intensity is limited by the incident intensity. Hence, an increasing field profile in the unbounded region outside of the structure indicates that all of the incident intensity would be lost to the surrounding regions rather than propagating the length of the waveguide.

### 2.6.3 Maxwell's Equations

Maxwell's equations offer a convenient form for the macroscopic laws of electromagnetism. They were originally formulated, by Maxwell in 1865 [84], as a set of 20 equations with 20 unknowns, before Heaviside and Gibbs reformulated Maxwell's equations into 4 vector equations in 1884. These four equations describe the behaviour of both the electric and magnetic fields in media and provide a basis for studying the interactions between light and materials. They may be found in any standard physics textbook, for example [85] or [86], and bring together all the laws on classical electricity and magnetism into one complete theory. Maxwell's equations are given in their most general form by equations (2.9) to (2.12), where standard SI units have been used. In these equations the following notation has been used:  $\mathbf{B}$  is the magnetic induction field or magnetic flux density (in units of tesla, T);  $\mathbf{H}$  is the magnetic field strength (in units of A/m);  $\mathbf{E}$  is the electric field (in units of V/m);  $\mathbf{D}$  is the electric displacement (in units of C/m<sup>2</sup>);  $\mu$  is the permeability (in units of W/mA);  $\epsilon$  is the permittivity (in units of F/m);  $\rho$  the free charge density (in units of C/m<sup>3</sup>) and  $\mathbf{J}$  the free electric current density (in units of A/m<sup>2</sup>).

$$\nabla \cdot \mathbf{D} = \rho \quad (2.9)$$

$$\nabla \cdot \mathbf{H} = 0 \quad (2.10)$$

$$\nabla \times \mathbf{E} = \frac{\partial \mathbf{B}}{\partial t} \quad (2.11)$$

$$\nabla \times \mathbf{H} = \mathbf{J} + \frac{\partial \mathbf{D}}{\partial t} \quad (2.12)$$

The first of Maxwell's Equations can be interpreted as implying that the electric flux through any surface is equal to the enclosed charge. The second is equivalent to the nonexistence of magnetic monopoles, hence the magnetic flux through any surface must be zero. The third and fourth of Maxwell's Equations correspond to Faraday's Law of Induction and Ampere's Law (with a displacement current) respectively.

The concept of plane-waves was described in Section 2.4. Mathematically a plane-wave can be expressed by the form:

$$\mathbf{E} = \mathbf{E}'_0 e^{i(\mathbf{k} \cdot \mathbf{r} - \omega t + \phi)} \quad (2.13)$$

The direction of propagation is specified by the wavevector,  $\mathbf{k}$ , and in general  $\mathbf{E}'_0$  is a constant complex vector giving the polarisation of the wave. In a planar waveguide of the type being discussed here the electromagnetic wave can exist in two different polarisations, commonly referred to as the transverse electric, TE, and transverse magnetic, TM, modes. The modes are defined with the aid of Fig. 2.5. The TE mode is defined as having a planar ( $y$ ) component for the electric field and the TM mode is defined as having a magnetic field with a component in the  $y$  direction only. The solution of Maxwell's Equations in less than three dimensions allows the two modes to be considered separately without the loss of information. The coordinate system which has been adopted has the  $z$  coordinate directed along the structure length and the  $x$  coordinate directed perpendicular to the layer interfaces. The standard right handed coordinate system is completed by defining the  $y$  axis as existing in a direction in the plane of the layers. This allows the wavevector  $\mathbf{k}$  to be written in terms of the components  $k_x$ ,  $k_y$  and  $k_z$ , hence:

$$\mathbf{E} = \mathbf{E}'_0 e^{i(k_x x + k_y y + k_z z - \omega t + \phi)} \quad (2.14)$$

Wave propagation in the  $z$  direction requires that the  $e^{i(k_z z - \omega t)}$  part of the exponential term in equation (2.14) is equivalent for all of the individual layers, for a given  $z$  and

*t.* Physically this is equivalent to the light having a fixed frequency and also wavevector component in the  $z$  direction. Were the  $z$  component of the wavevector not constant then the unphysical situation would exist with different portions of the wave travelling with different group velocities along the waveguide.

Calculation of the curl of both sides of Maxwell's fourth equation allows the cross product term in the equation to be replaced through the use of the standard vector identity:  $\nabla \times \nabla \times \mathbf{A} = \nabla(\nabla \cdot \mathbf{A}) - \nabla^2 \mathbf{A}$ , where  $\mathbf{A}$  is any vector [87]. For non-magnetic media  $\mathbf{H} = \mathbf{B}/\mu_0$  and the curl of equation (2.12) gives:

$$\nabla \times \nabla \times \mathbf{B} = \mu_0 \nabla \times \mathbf{J} + \mu_0 \epsilon \frac{\partial \nabla \times \mathbf{E}}{\partial t} \quad (2.15)$$

A single homogeneous material may be considered and the electrical conductivity,  $\sigma$  ( $\sigma = 1/\rho$ ), may be assumed to be invariant with position. The use of the vector identity, together with the substitution  $\mathbf{J} = \sigma \mathbf{E}$ , then gives:

$$\nabla(\nabla \cdot \mathbf{B}) - \nabla^2 \mathbf{B} = \mu_0 \sigma (\nabla \times \mathbf{E}) + \mu_0 \epsilon \frac{\partial (\nabla \times \mathbf{E})}{\partial t} \quad (2.16)$$

Comparison of the first term on the left-hand side with equation (2.10) allows the term to be set to zero. The two  $\nabla \times \mathbf{E}$  terms on the right-hand side can also be simplified through the use of equation (2.11). The result is the following electromagnetic wave equation:

$$\nabla^2 \mathbf{B} = \mu_0 \sigma \frac{\partial \mathbf{B}}{\partial t} + \mu_0 \epsilon \frac{\partial^2 \mathbf{B}}{\partial t^2} \quad (2.17)$$

In general, plane-wave forms for the electric and magnetic fields will have a time dependence that is proportional to  $e^{-i\omega t}$  and spatial dependence proportional to  $e^{i(k_x x + k_y y + k_z z)}$ . The choice of a time dependence proportional to  $e^{i\omega t}$  would also be equally valid. If the spatial and temporal components have different signs then the wave is forward travelling and if they are of the same sign then the propagation direction is reversed. If the differential terms in equation (2.18) are evaluated, then the following condition may be produced:

$$\mathbf{k}^2 = k_x^2 + k_y^2 + k_z^2 = -i\mu_0 \sigma \omega + \omega^2 \mu_0 \epsilon \quad (2.18)$$

The condition is generally applicable for either polarisation. Any plane-wave solution of Maxwell's equations must have the property dictated by equation (2.18). It may be simplified for the dielectric systems under consideration by employing the assumption that the waveguide layers are non-conducting, hence  $\sigma = 0$ . Additionally the appearance of the expression may be simplified by use of  $c^2 = 1/\mu_0\epsilon_0$ , together with the notation,  $\epsilon = \epsilon_{rel}\epsilon_0$ . As  $k_y = 0$  for the two-dimensional structures under consideration:

$$k_x^2 = \omega^2 \mu_0 \epsilon - k_z^2 = \frac{\omega^2}{c^2} \epsilon_{rel} - k_z^2 \quad . \quad (2.19)$$

The value of  $k_z$  for a particular guided mode,  $m$ , is often referred to as the propagation constant of the mode and given the notation,  $\beta_m$ . The quantity is fixed throughout the structure by the angle of incidence of the original light ray on the waveguide structure. If the angle of incidence at the core-cladding interface is  $\theta_m$ , then:

$$\beta_m = k_z = n_{eff} k_0 = n_i \sin \theta_m k_0 \quad . \quad (2.20)$$

$k_0$  is the magnitude of the free-space wavevector and  $n_i$  is the actual core material refractive index. The propagation constants for guided modes may be found by scanning through valid  $k_z$  values until a solution is found which propagates within the structure and decays outside of the structure. Another common method for referring to guided modes is by their effective refractive indices,  $n_{eff}$ . Equation (2.20) gives the relationship between effective refractive index and propagation constant.

#### 2.6.4 TM Transfer Matrix

The use of a transfer matrix method greatly assists with the calculation of the guided mode propagation constants; it conveniently enables the effect of a complete structure to be treated as a single matrix, irrespective of the number of individual layers present. The matrix must contain the field components that when matched at layer interfaces will provide field continuity across the structure. For this reason the field components tangential to the plane of the layer interfaces are required. The TM mode is defined with,  $H_x = H_z = 0$  and accordingly  $E_y = 0$ . The first step in the transfer matrix method is the separation of the

electric,  $\mathbf{E}$ , and magnetic,  $\mathbf{H}$ , fields into two plane-wave sets, one in the  $+x$  direction and the other in the  $-x$  direction. These are given by equations (2.21) to (2.23). The electric field has two components  $E_x$  and  $E_z$ . However, only the component tangential to the layer interfaces,  $E_z$ , is required for the transfer matrix; both are shown for completeness.

$$H_x(x, z, t) = (A'e^{-ik_x x} + B'e^{ik_x x}) e^{i(k_z z - \omega t)} \quad (2.21)$$

$$E_z(x, z, t) = (A''e^{-ik_x x} + B''e^{ik_x x}) e^{i(k_z z - \omega t)} \quad (2.22)$$

$$H_y(x, z, t) = (Ae^{-ik_x x} + Be^{ik_x x}) e^{i(k_z z - \omega t)} \quad (2.23)$$

The number of amplitude coefficients,  $A$ s and  $B$ s, may be reduced through the use of Maxwell's fourth equation (equation 2.12) to relate the electric field to the magnetic field. The equation rearranges to give:

$$\nabla \times \mathbf{B} = \mu_0 \mathbf{J} + \mu_0 \epsilon \frac{\partial \mathbf{E}}{\partial t} \quad (2.24)$$

For the dielectric materials under consideration the free current density is taken to be zero ( $\mathbf{J} = 0$ ). Hence, use of the plane-wave field forms gives (for  $e^{-ik_x x}$  terms):

$$-ik_x B_y = -ik_x \mu_0 H_y = -i\omega \mu_0 \epsilon E_z \quad (2.25)$$

The coefficients  $A''$  and  $B''$ , for the  $z$  component of the electric field, may now be expressed in terms of the magnetic field coefficients,  $A$  and  $B$ . Hence,

$$E_z(x, z, t) = \frac{k_x}{\omega \epsilon} (Ae^{-ik_x x} - Be^{ik_x x}) e^{i(k_z z - \omega t)} \quad (2.26)$$

This allows both the fields required for matching to be conveniently combined in a single matrix. The frequency and  $k_z$  dependence of the fields will be the same across all layers. Thus, the matrix needs to only contain  $H_y(x)$  and  $E_z(x)$ :

$$\begin{pmatrix} H_y(x) \\ E_z(x) \end{pmatrix} = \begin{pmatrix} e^{-ik_x x} & e^{ik_x x} \\ \frac{k_x}{\epsilon \omega} e^{-ik_x x} & \frac{-k_x}{\epsilon \omega} e^{ik_x x} \end{pmatrix} \begin{pmatrix} A \\ B \end{pmatrix} \quad (2.27)$$

The matrix relates the coefficients in one layer to those in the next. Section 2.6.6 describes the extension of the field amplitude matching method to an arbitrary number of layers.

### 2.6.5 TE Mode Analysis

The TE mode is defined with,  $E_x = E_z = 0$  and  $H_y = 0$ . The remaining components may be written in a plane-wave form. The terms in the  $+x$  and  $-x$  directions can be separated from each other by adopting a similar approach to that utilised for the TM polarisation. This allows the electric and magnetic field components to be written as:

$$E_y(x, z, t) = (Ae^{-ik_x x} + Be^{ik_x x})e^{i(k_z z - \omega t)} \quad (2.28)$$

$$E_x(x, z, t) = (A'e^{-ik_x x} + B'e^{ik_x x})e^{i(k_z z - \omega t)} \quad (2.29)$$

$$H_z(x, z, t) = (A''e^{-ik_x x} + B''e^{ik_x x})e^{i(k_z z - \omega t)} \quad (2.30)$$

In this instance, a rearrangement of Maxwell's third equation (equation (2.11)) allows the number of amplitude coefficients to be reduced. If the assumption is made that the permittivity,  $\epsilon$ , is independent of time, and recalling that the material is non-magnetic ( $\mathbf{H} = \mathbf{B}/\mu_0$ ), allows equation (2.11) to be written in the form:

$$\mathbf{H} = \frac{\mathbf{B}}{\mu_0} = \frac{-i}{\mu_0 \omega} \nabla \times \mathbf{E} \quad (2.31)$$

The field components tangential to the layer interfaces are the  $y$  component of the electric field and the  $z$  component of the magnetic field. The substitution of the plane-wave forms for the electric field into equation (2.31) gives:

$$\mathbf{H} = \begin{pmatrix} \frac{-i}{\mu_0 \omega} (-ik_z A e^{-ik_x x} - ik_z B e^{ik_x x}) \\ 0 \\ \frac{-i}{\mu_0 \omega} (-ik_x A e^{-ik_x x} + ik_x B e^{ik_x x}) \end{pmatrix} e^{i(k_z z - \omega t)} \quad (2.32)$$

This may be rearranged to provide the magnetic field amplitude coefficients in the  $z$  direction in terms of the electric field coefficients:

$$H_z(x, z, t) = \frac{-k_x}{\mu_0 \omega} (Ae^{-ik_x x} - Be^{ik_x x}) e^{i(k_z z - \omega t)} \quad . \quad (2.33)$$

The frequency and  $k_z$  components will be identical across all layers, hence, the final electric and magnetic field matrix may be written as:

$$\begin{pmatrix} E_y(x) \\ H_z(x) \end{pmatrix} = \begin{pmatrix} e^{-ik_x x} & e^{ik_x x} \\ \frac{-k_x}{\mu_0 \omega} e^{-ik_x x} & \frac{k_x}{\mu_0 \omega} e^{ik_x x} \end{pmatrix} \begin{pmatrix} A \\ B \end{pmatrix} \quad (2.34)$$

### 2.6.6 Field Continuity

This section describes the method used to ensure that the necessary electromagnetic field components are continuous at the individual layer interfaces. The similarity between equations (2.27) and (2.34) makes it convenient to adopt the same notation for both modes. Both equations may be written in the form:

$$\mathbf{b}_f = \mathbf{M} \mathbf{b}_i \quad . \quad (2.35)$$

The field component amplitudes a distance  $x$  from the initial field amplitudes  $\mathbf{b}_i$  are contained in the matrix  $\mathbf{b}_f$ . The initial amplitudes are given by:

$$\mathbf{b}_i = \begin{pmatrix} A \\ B \end{pmatrix} \quad . \quad (2.36)$$

In the TM instance the matrix  $\mathbf{M}$  is given by:

$$\mathbf{M} = \begin{pmatrix} e^{-ik_x x} & e^{ik_x x} \\ \frac{k_x}{\epsilon \omega} e^{-ik_x x} & \frac{-k_x}{\epsilon \omega} e^{ik_x x} \end{pmatrix} \quad , \quad (2.37)$$

and in the TE case by:

$$\mathbf{M} = \begin{pmatrix} e^{-ik_x x} & e^{ik_x x} \\ \frac{-k_x}{\mu_0 \omega} e^{-ik_x x} & \frac{k_x}{\mu_0 \omega} e^{ik_x x} \end{pmatrix} \quad . \quad (2.38)$$

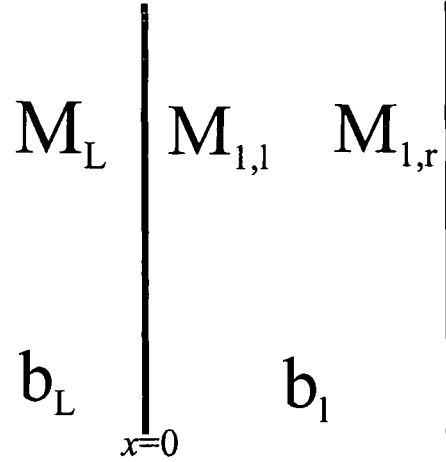


**Figure 2.7:** Interface matching notation at the first interface. The matrices on each side of each interface are labelled  $M$  and the field amplitude column vectors are labelled  $b$ .

For a mode to propagate through a multi-layer waveguide the tangential components of both the electric and magnetic fields must match at each planar interface. To achieve this the structure is broken down into a series of piece-wise sublayers and the matching condition is applied at each layer interface through the use of transfer matrices. A reflection coefficient,  $R$ , may be defined at the first interface ( $x = 0$ ) to represent the proportion of the initial electric field amplitude which is reflected at the first interface. For the TM mode the situation may be described by:

$$\begin{pmatrix} H_y(x=0) \\ E_z(x=0) \end{pmatrix} = \begin{pmatrix} 1 & 1 \\ -k'_L & k'_L \end{pmatrix} \begin{pmatrix} R \\ 1 \end{pmatrix} = \begin{pmatrix} 1 & 1 \\ -k'_L & k'_L \end{pmatrix} \begin{pmatrix} b_1^H \\ b_1^E \end{pmatrix} \quad (2.39)$$

The notation  $k' = \frac{-k_x}{\epsilon\omega}$  has been introduced to simplify the appearance of the matrix. The expression for  $k'$  evaluated to the left of  $x = 0$  may then simply be denoted  $k'_L$ . The upper and lower components of the field amplitude matrix,  $b_1$ , have been labelled  $b_1^H$  and  $b_1^E$  respectively. Further simplification has also been achieved by setting the incident amplitude for the magnetic field to unity.

If the TE mode is considered and the notation:  $k' = \frac{k_x}{\mu_0\omega}$  used; then, with an incident electric field amplitude of unity:

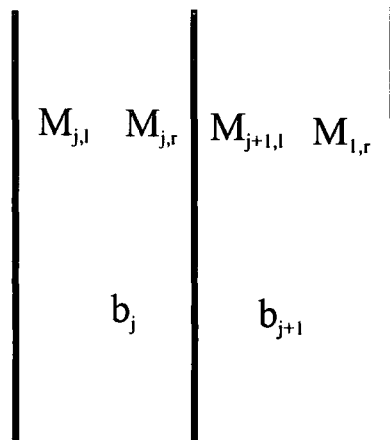


**Figure 2.8:** A general interface between the  $j$ th and  $j + 1$ th layers. The matrices at each side of each interface are labelled  $M$  and the field amplitude column vectors are labelled  $b$ .

$$\begin{pmatrix} E_y(x) \\ H_z(x) \end{pmatrix} = \begin{pmatrix} 1 & 1 \\ -k'_L & k'_L \end{pmatrix} \begin{pmatrix} R \\ 1 \end{pmatrix} = \begin{pmatrix} 1 & 1 \\ -k'_L & k'_L \end{pmatrix} \begin{pmatrix} b_1^E \\ b_1^H \end{pmatrix} \quad . \quad (2.40)$$

Note the differing positions of the  $b_1$  components,  $b_1^H$  and  $b_1^E$ . This is due to the electric field term appearing as the top component on the left-hand side of the equation.

The left-hand side of the structure is considered as a semi-infinite layer, with a layer matrix given by the matrix  $M_L$ . The field amplitudes at the interface between the semi-infinite layer and the first layer of the structure ( $x = 0$ ) are given by  $b_L$ . The situation is shown schematically in Fig. 2.7. The matching condition for both polarisations at the first interface using the new notation is,

$$M_L b_L = M_{1,l} b_1 \quad . \quad (2.41)$$

$M_{1,l}$  is the matrix for the first layer evaluated at the left hand-side of the layer and  $b_1$  contains the field amplitudes for the layer. The condition may be generalised to all interfaces in the manner shown in Fig 2.8. The general matching condition at all interfaces, using the TM mode as an example, is

$$\begin{pmatrix} e^{-ik_j x} & e^{ik_j x} \\ -k'_j e^{-ik_j x} & k'_j e^{-ik_j x} \end{pmatrix} \begin{pmatrix} b_j^H \\ b_j^E \end{pmatrix} = \begin{pmatrix} e^{-ik_{j+1} x} & e^{ik_{j+1} x} \\ -k'_{j+1} e^{-ik_{j+1} x} & k'_{j+1} e^{-ik_{j+1} x} \end{pmatrix} \begin{pmatrix} b_{j+1}^H \\ b_{j+1}^E \end{pmatrix} \quad (2.42)$$

The same expression could equally apply for the TE mode if the **E** and **H** terms were exchanged. Generalising this expression to a condition applicable for both modes at a general interface between the  $j$ th and  $(j + 1)$ th layers gives:

$$\mathbf{M}_{j,r} \mathbf{b}_j = \mathbf{M}_{j+1,l} \mathbf{b}_{j+1} \quad (2.43)$$

If  $\mathbf{A}^{-1}$  is defined as the inverse of any matrix **A**, then equation (2.43) may be written in a manner which relates the field amplitudes for the next adjacent layer,  $(j + 1)$ , to those of the current layer,  $j$ :

$$\mathbf{b}_{j+1} = \mathbf{M}_{j+1,l}^{-1} \mathbf{M}_{j,r} \mathbf{b}_j \quad (2.44)$$

The combined matrix  $\mathbf{M}_{j+1,l}^{-1} \mathbf{M}_{j,r}$  is usually referred to as a transfer matrix as it relates the field amplitudes from one layer to the next. Between the first and second layers the matching condition is:

$$\mathbf{M}_{1,r} \mathbf{b}_1 = \mathbf{M}_{2,l} \mathbf{b}_2 \quad (2.45)$$

and this may be written using equation (2.44) in the form:

$$(\mathbf{M}_{1,r} \mathbf{M}_{1,l}^{-1}) \mathbf{M}_L \mathbf{b}_L = \mathbf{M}_{2,l} \mathbf{b}_2 \quad (2.46)$$

The process will continue in an identical manner for the entire  $N$  layer structure until the final  $(N + 1)$  semi-infinite right-hand side layer is reached. At this point the following matching condition is needed:

$$\mathbf{M}_{N,r} \mathbf{b}_N = \mathbf{M}_R \mathbf{b}_R \quad (2.47)$$

The notation  $\mathbf{M}_R$  has been used to represent the matrix on the right hand-side of the structure and the field amplitude coefficients for this layer are given by  $\mathbf{b}_R$ . Rearrangement of equation (2.47) yields:

$$\mathbf{b}_R = \mathbf{M}_R^{-1} \mathbf{M}_{N,r} \mathbf{b}_N \quad (2.48)$$

For the complete structure the final field component amplitude coefficients,  $\mathbf{b}_R$  will be related to the initial field component amplitude coefficients,  $\mathbf{b}_L$ , in the following manner:

$$\mathbf{b}_R = \mathbf{M}_R^{-1} (\mathbf{M}_{N,r} \mathbf{M}_{N,l}^{-1}) \dots (\mathbf{M}_{1,r} \mathbf{M}_{1,l}^{-1}) \mathbf{M}_L \mathbf{b}_L \quad (2.49)$$

$$= \mathbf{M} \mathbf{b}_L = \begin{pmatrix} M_{11} & M_{12} \\ M_{21} & M_{22} \end{pmatrix} \mathbf{b}_L \quad (2.50)$$

The interface matching method can also be used to calculate the field amplitude coefficients for each individual layer rather than just for the final right hand-side layer. Equation (2.49) may be used but only terms up to the layer of interest included. The amplitude coefficients, combined with the appropriate matrix for the individual layers, allows field profiles to be plotted for each individual layer. In this manner field amplitudes or intensities at any point across the entire structure can be plotted and guided modes identified. If the only requirement is for the value of the guided mode propagation constant then it is both unnecessary and computationally inefficient to plot field profiles across whole structures. The following section describes an efficient method for the calculation of guided mode propagation constants without the necessity of plotting field profiles.

### 2.6.7 Guided Modes

The right-hand side electric or magnetic field coefficients may be calculated from the initial left-hand side field coefficients using equation (2.50). For a guided mode to exist in the structure the electric and magnetic fields must decay outside of the structure. This means

that the value of  $k_x$  for the mode must be imaginary outside of the structure. A real value would lead to a non-decaying mode, due to the  $e^{ik_x x}$  dependence of the plane-wave field forms, given by equations (2.21) to (2.23) and (2.28) to (2.30). With a positive imaginary  $k_x$  the plane-wave form adopted for the fields contains two exponential terms, one increasing, the other decreasing with  $x$ . In order for the total field to be decaying with distance from the structure any exponentially increasing term must be absent; an exponentially increasing term would become increasingly dominant as the magnitude of  $x$  increases. If an exponentially increasing term is forbidden then the top coefficient of  $\mathbf{b}_R$  must be zero. In terms of the final matrix the requirement is for matrix element  $M_{11}$  to be equal to zero in equation (2.50).

The method employed here for the calculation of guided modes examined the  $M_{11}$  coefficient in equation (2.50). The value of the coefficient was calculated for the range of possible  $k_z$  values, with their corresponding  $k_x$  values. A decaying field was entered on the left-hand side by the use of a zero value for the top component in  $\mathbf{b}_L$ . Zero points were identified when the sign of matrix component  $M_{11}$  differed between two consecutive  $k_z$  values in the allowed range. Each zero point indicated a decaying field on the right-hand side of the structure. The efficiency of locating guided modes was significantly improved through the use of an initial scan with relatively wide  $k_z$  spacings. The initial scan allowed the approximate location of each guided mode propagation constant to be found without the need for a computationally intensive fine  $k_z$  scan across a wide  $k_z$  range. The required level of precision for the propagation constants was achieved by conducting repeated scans within the increasingly narrowed  $k_z$  solution range. Once the width of the  $k_z$  spacings was below some acceptable threshold value, the propagation constant was arrived at to the required level of accuracy.

## 2.7 Dual Polarisation Sensing

The theoretical model described in the previous section allows the propagation constants of guided modes to be calculated for well defined structures. The transfer matrix method is also of use for calculating the optogeometrical parameters of an additional layer placed above the well defined structure. Provided that both the structure and the propagation constant of the mode are known then a trial and error approach may be adopted to char-

acterising a deposited layer. A variety of possible deposited layer parameters may be tried until they produce a guided mode with the required propagation constant. For either the TE or TM polarisations it is possible to find a refractive index at any reasonable thickness that will produce a guided mode with the required propagation constant. It is therefore possible to produce a curve of potential thickness and refractive index values suitable for each polarisation. The basis of dual polarisation interferometry is that it allows the curves for both polarisations to be plotted simultaneously as shown in Fig. 2.9a. The crossing point indicates the position at which a unique thickness and refractive index combination can be obtained. The results will then be consistent for both polarisations.

Two polarisation curve plotting is both computationally expensive and also unnecessary for the location of a crossing point. A Monte Carlo type approach was adopted that allowed for the more efficient and rapid location of crossing points. If Fig 2.9b is examined it may be seen that to the left of the crossing point the TM mode curve is above the TE, and after crossing the situation is obviously reversed. The solution algorithm implemented made use of a repeated narrowing of the thickness range that a unique solution could exist in. A random thickness value was selected, within the allowed range, and the TE and TM refractive index solutions found for this thickness. The solutions were then compared to those at the range limits to determine whether the unique solution was at a higher or lower thickness. This allowed the limits to be repeatedly redefined until they differed by an amount equal to the required sensitivity of the final solution.

## 2.8 Chip Design

The Young's fringe method described in Section 2.5.3 allows phase differences to be calculated between the upper and lower guides provided that the structure supports only two allowed modes; one with an intensity peak in the upper guide and the other with a peak in the lower guide. The waveguide structure used in dual wavelength interferometry is a chip produced by Plasma Enhanced Chemical Vapour Deposition (PECVD) [88,89]. The method produces silicon oxo-nitride layers deposited on a silicon substrate to form the required multi-layer slab waveguide structure detailed by Table 2.1. The corresponding electric field profiles for the two TE modes of this structure are shown in Fig. 2.10.

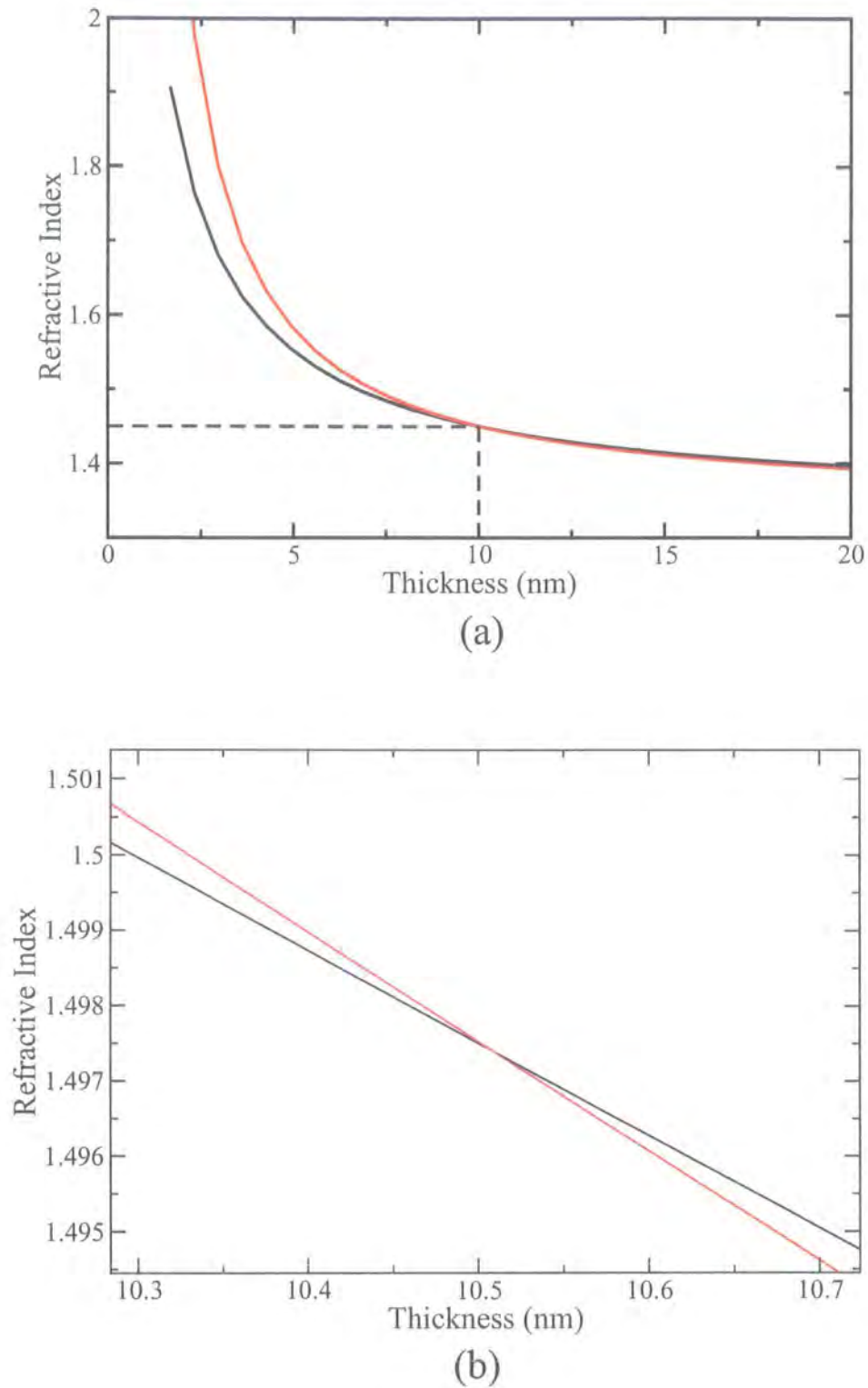


**Figure 2.9:** TE and TM solution curves, showing allowed deposited layer configurations for a specific fixed propagation constant (a). The TE curve is shown in black and the TM curve in red. The lower graph (b) is a magnified section allowing the crossing point to be seen more clearly.

Layer	Thickness ( $\mu m$ )	Refractive Index
Lower		1.485
1	2.0	1.485
2	1.0	1.520
3	3.0	1.470
4	1.0	1.520
Upper		1.333

**Table 2.1:** Optogeometrical parameters for the base waveguide chip structure.

Phase changes detected by the interferometer method correspond to changes in the phase difference between the upper and lower modes due to a sensing event. If  $\Delta\beta$  is the difference in propagation constants for the two modes present in the waveguide structure at an initial time,  $i$ , and final time,  $f$ , then the phase change measured,  $\Delta\phi$ , is given by:

$$\begin{aligned}\Delta\phi &= L (\Delta\beta^f - \Delta\beta^i) \\ &= L (\beta_1^i - \beta_2^i) - L (\beta_1^f - \beta_2^f) \quad ,\end{aligned}\quad (2.51)$$

where  $L$  is the active chip length. Fig. 2.10 demonstrates that the electric field intensity for the lower guide mode has decayed to a negligible value at the upper chip surface, the sensing surface. This means that the propagation constant for the lower mode does not change between the initial and final situations ( $\beta_1^f = \beta_1^i$ ). Hence, the phase change difference detected by the interferometer will effectively be solely dependent on the phase change of the upper guide mode:

$$\Delta\phi = L (\beta_2^f - \beta_2^i) \quad (2.52)$$

The TM modes are of similar appearance.

Since the initial propagation constant can be calculated for the defined chip structure the detected phase change can be used to calculate the propagation constant of the upper guide mode after a sensing event. The propagation constants for both polarisations can then be used to find the unique thickness and refractive index solution for the additional layer deposited between the initial and final propagation constants.

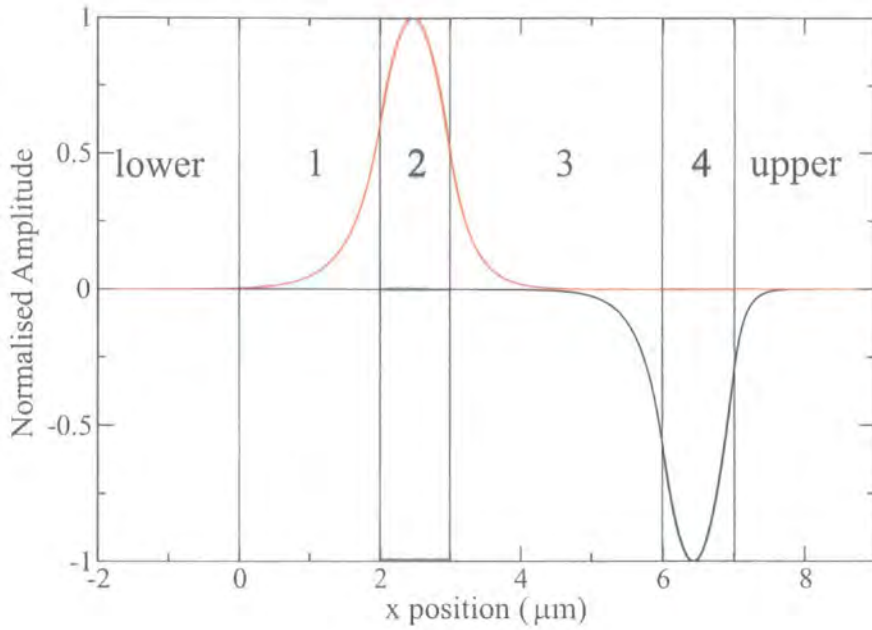


**Figure 2.10:** Electric field profiles for the two TE modes in the structure described by Table 2.10. The red curve indicates the lower guide mode and the black curve the upper guide mode.

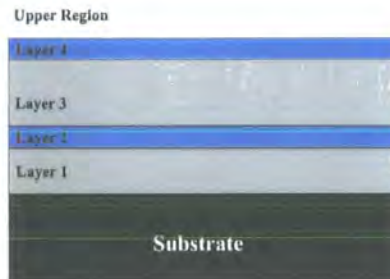


**Figure 2.11:** The 4 layer chip formed by PECVD with a fluid region above the structure; occupied in this instance by water.

Layer	Thickness ( $\mu\text{m}$ )	Refractive Index
1	$\pm 0.100$	$\pm 0.005$
2	$\pm 0.050$	$\pm 0.005$
3	$\pm 0.100$	$\pm 0.002$
4	$\pm 0.025$	$\pm 0.002$

**Table 2.2:** Variations in the optogeometrical parameters of the chip structure which are permitted by the manufacturing tolerances.

## 2.9 Manufacturing Tolerances

In the discussion thus far the only uncertainties in the calculation have lain with the optogeometrical parameters of the deposited layer. The layers forming the basic waveguide structure itself have been assumed to possess well defined optogeometrical parameters. Fluctuations inherent in the fabrication process of any real structure will lead to individual layer thicknesses and refractive indices that contain some degree of uncertainty. The usual way to quantify this uncertainty is for a manufacturer to quote the layer optogeometrical parameters as accurate to within some tolerance. The highly sensitive nature of the waveguide interferometer arrangement to the refractive index and thickness of a deposited layer make it conceivable that variations in the base structure, due to manufacturing tolerances, will significantly reduce the effectiveness of the device for characterising thin films. The base structure is used in both calculating the absolute propagation constant of the upper guide mode, prior to the resolution of the deposited film; and for calculating the optogeometrical parameters of the deposited layer. This section presents the results of a theoretical study which was undertaken to investigate the effect of manufacturing tolerances on the ability of the device to resolve the properties of thin films. Discussion of the results is included with suggestions to alleviate the effect of manufacturing tolerances.

### 2.9.1 Chip Structure

The intended, or ideal, base waveguide structure was defined in Table 2.1. It consisted of 4 silicon-oxi-nitride layers with different refractive indices and thicknesses. The microelectronics fabrication technique of PECVD [88, 89] provides a base waveguide structure defined to within quoted manufacturing tolerances. These are given in Table 2.2.

## 2.9.2 Approach

A two stage approach was adopted for investigating the effect of manufacturing tolerances on the the ability of the dual polarisation technique to resolve deposited layers using only the estimate of the base structure provided by the ideal structure. The transfer matrix method, implemented in Section 2.6, allows the propagation constants of guided modes to be calculated for any well defined one-dimensional structure. The first stage of the method made use of this feature; the theoretical phase changes were calculated for a particular well defined deposited layer on a structure that differed from the ideal structure. The second stage of the method calculated the refractive index and thickness of the deposited layer using the idealised structure, combined with the theoretical phase changes calculated in the first stage. By this method discrepancies between actual deposited layers and resolved deposited layers, due to the use of an estimate of the base structure, were investigated.

Deposited layers within the thickness range of 1 to 100 nm, and refractive indices within the range of 1.34 to 1.45 were investigated. When dual polarisation interferometry is used for characterising thin biological films the deposited layers are expected to possess a refractive index of the order of 1.4 or above, and thicknesses of below 20 nm. Hence, the chosen optogeometrical range for investigation was expected to adequately cover such layers.

Fig. 2.10 indicates that the largest proportion of the upper, sensing mode field intensity is contained within the upper guide, layer 4. Correspondingly the manufacturing tolerances for this particular layer were anticipated to be the most influential on the ability of the dual polarisation interferometry technique to resolve deposited layers accurately. For this reason layer 4 was singled out for for individual consideration, in the first instance, prior to the consideration of the overall structure.

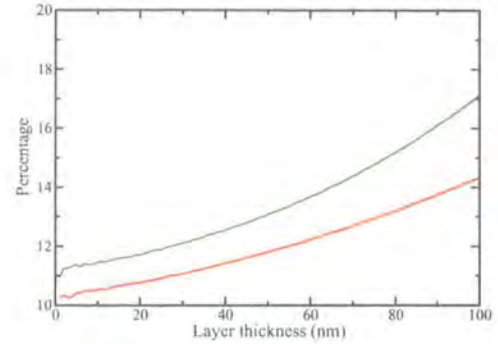
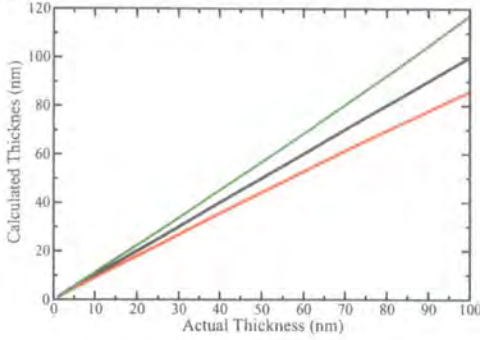
## 2.9.3 Results

### Layer 4 Tolerances

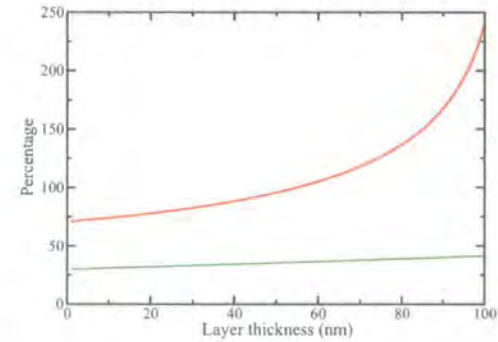
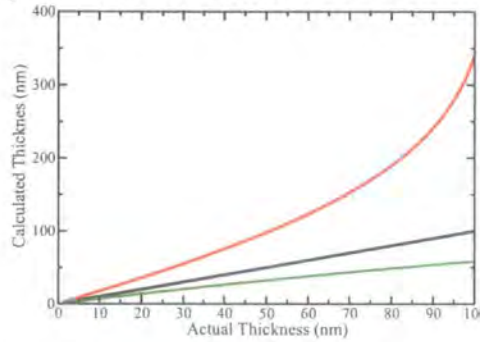
#### Low Refractive Index Film

The type of deposited layer anticipated to be the most sensitive to the manufacturing tolerances was a layer with a refractive index slightly above that of the fluid region. A high

a) Thickness



b) Refractive Index



c) Combined

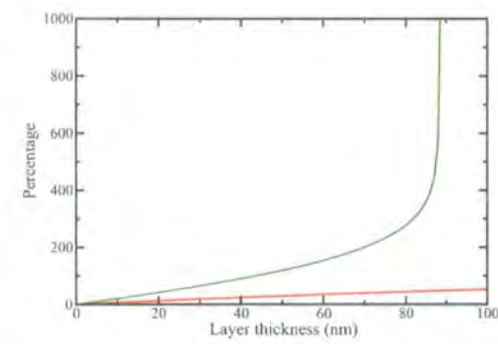
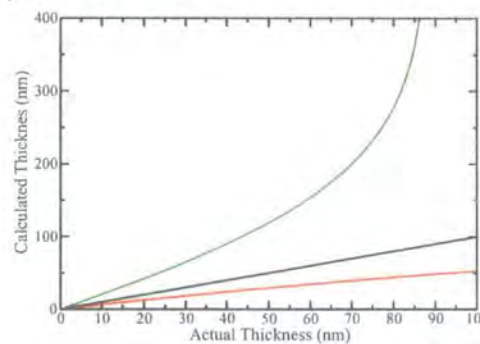


**Figure 2.12:** Effect of layer 4 manufacturing tolerances on a low refractive index ( $n = 1.34$ ) film with a variety of thicknesses (actual). The graphs show the resolved (calculated) thicknesses with red lines indicating the upper limit, green lines the lower limit and black lines the original structure. The left-hand column shows actual values and the right-hand column percentage discrepancies. The top figures (a) are for the thickness tolerance, the middle (b) for the refractive index tolerance and the lower (c) for a combined refractive index and thickness tolerance.

sensitivity for low refractive index layers was anticipated due to the relatively large width of a low refractive index layer required to significantly alter the effective refractive index of the upper guide mode. The results presented in this section are for deposited layers with a refractive index of 1.34 and a variety of thicknesses.

The first set of results, Fig 2.12a, show the variation in the thickness of the resolved layer in response to variations in the thickness of the upper guide layer. The thickness of the deposited layer was found to be reasonably resilient to these upper guide thickness variations. The low thickness deposited layers (below 20 nm) varied by less than 12% from their actual value and the thickest (100 nm) films varied by less than 18%. The results show that an overestimate of the upper guide thickness results in a thicker resolved layer to compensate for this. The overestimate increases the proportion of the field profile in the high index region and increasing the thickness of the deposited layer reduces the field intensity in the high refractive index region to cancel the effect on the propagation constant. For the same reason, the underestimated upper guide thickness caused an underestimate of the deposited layer thickness.

Refractive index variation in the upper guide, shown in Fig. 2.12b, was found to be the most significant factor affecting the accuracy of the resolved layer thickness value. The resolution of even low thickness films had an error of 75% and the thickest films had a discrepancy in the region of 250%. This has possible implications if improved fabrication methods are available in the future. An improved fabrication process might allow the manufacturing tolerances to be tightened. The results given here indicate that the most critical tolerance is the refractive index tolerance, and accordingly a reduction in the uncertainty of the refractive index would have the greatest influence on the accuracy of the technique at resolving deposited layers. In physical terms, an upper guide at the lower tolerance limit would reduce the resolved thickness of the deposited layer. The lower limit would mean an overestimate of the refractive index of the upper guide was made. This would require more material with an index above that of the background fluid in order to raise the average refractive index of the upper guide mode.

The combination of both the thickness and refractive index tolerances are shown in Fig 2.12c. The maximum thickness limit and the minimum refractive index limit, and vice-versa, have been paired to create a 'worst case' scenario for the layer 4 tolerance effects.

The figure demonstrates that the accuracy of the device has been greatly reduced by the manufacturing tolerances, particularly for the thicker deposited layers; where resolved layer thicknesses differed from their ideal values by the order of 1000%. The utility of the device was already brought into question, even without the tolerances of the remaining three layers being considered. The high sensitivity of the thicker films to the tolerances is due to the rapidity of the decay of the evanescent field. The rapid decay reduces the influence that material a significant distance from the sensing surface has on the propagation constant of the upper guided mode.

It is of interest to further investigate the effects that tighter manufacturing tolerances might have on these results. Figure 2.13 shows 1 nm, 50 nm and 100 nm deposited layers resolved for a variety of thicknesses and refractive indices of the upper guide. The variation in resolved layer thickness due to upper guide thickness shows only slight curvature, indicating that discrepancies in resolved thicknesses are approximately proportional to fluctuations in the upper guide thickness. However, the upper guide refractive index graph shows noticeably more curvature. This highlights the problem that the thickness of resolved layers is highly dependent on the refractive index of the upper guide. The shape of the curve shows severe discrepancies occurring between the resolved layer and the actual layer due to the upper guide thickness being above that estimated. The 1 nm curve shows an irregular appearance which is attributable to the convergence of the resolving algorithm. The algorithm resolves thicknesses to 0.01 nm which produces the noticeable percentage variations from a smooth curve for very thin films.

### High Refractive Index Film

Films of a high refractive index ( $n = 1.45$ ) were expected to show greater resilience to the upper guide manufacturing tolerances. Small variations in the width of a high refractive index layer will have a greater influence on the effective refractive index of the upper guide mode. Structures within the upper guide thickness tolerance limits led to a deviation of the resolved layer thickness of less than 7% from the actual value (Fig 2.14a). The refractive index variations, shown in Fig 2.14b, were also much lower than for a low refractive index deposited layer; the largest deviations seen differed from the ideal values by less than 5%. The combined effect of both upper guide manufacturing tolerances, shown in Fig 2.15c, was seen to introduce an error of at most 12% in resolved thickness value. Such resilience to

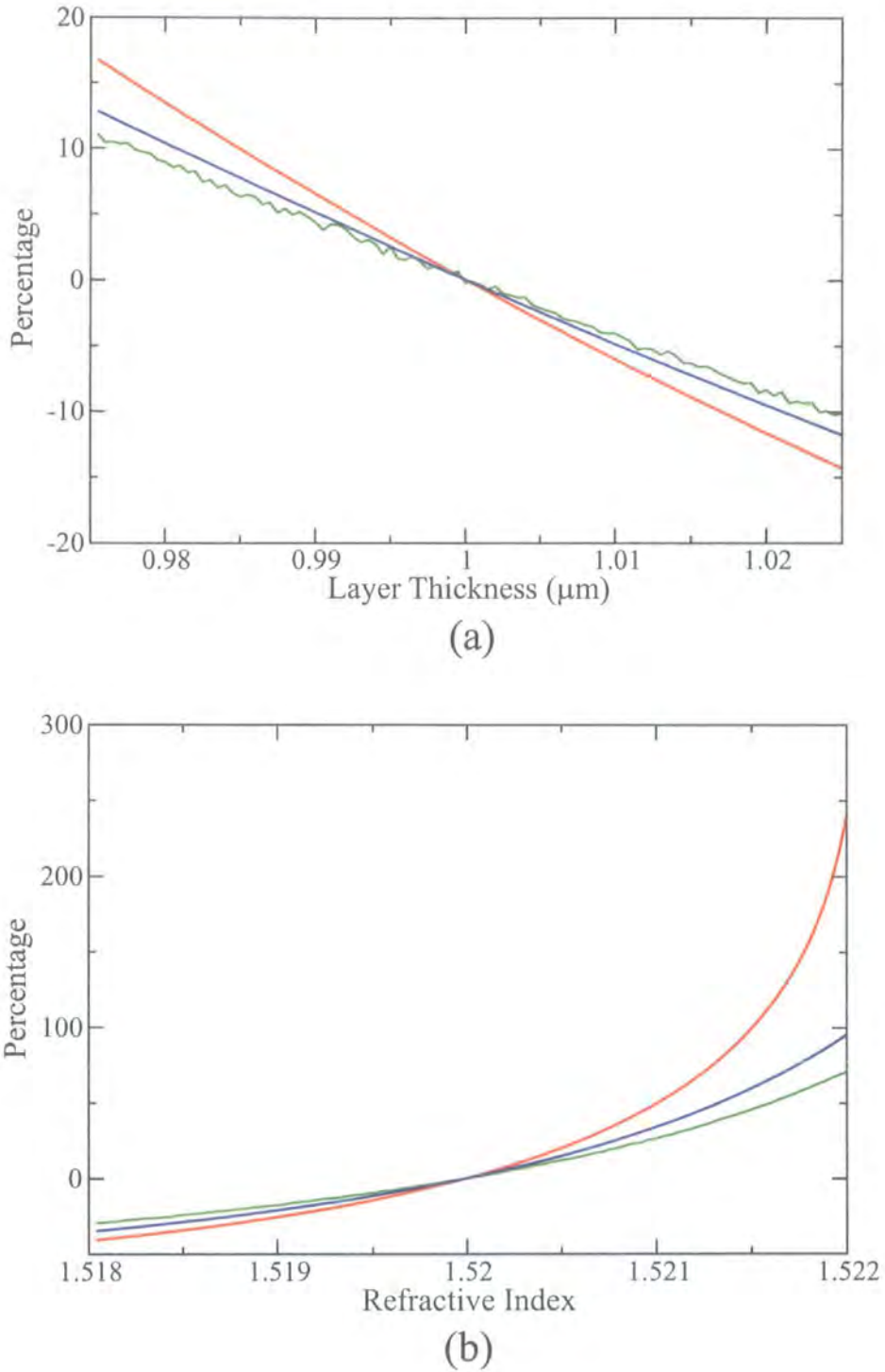


**Figure 2.13:** The effect of a variation in layer 4 thickness (a) and refractive index (b) on 1 nm (green), 50 nm (blue) and 100 nm (red) deposited layers with a refractive index of 1.34.

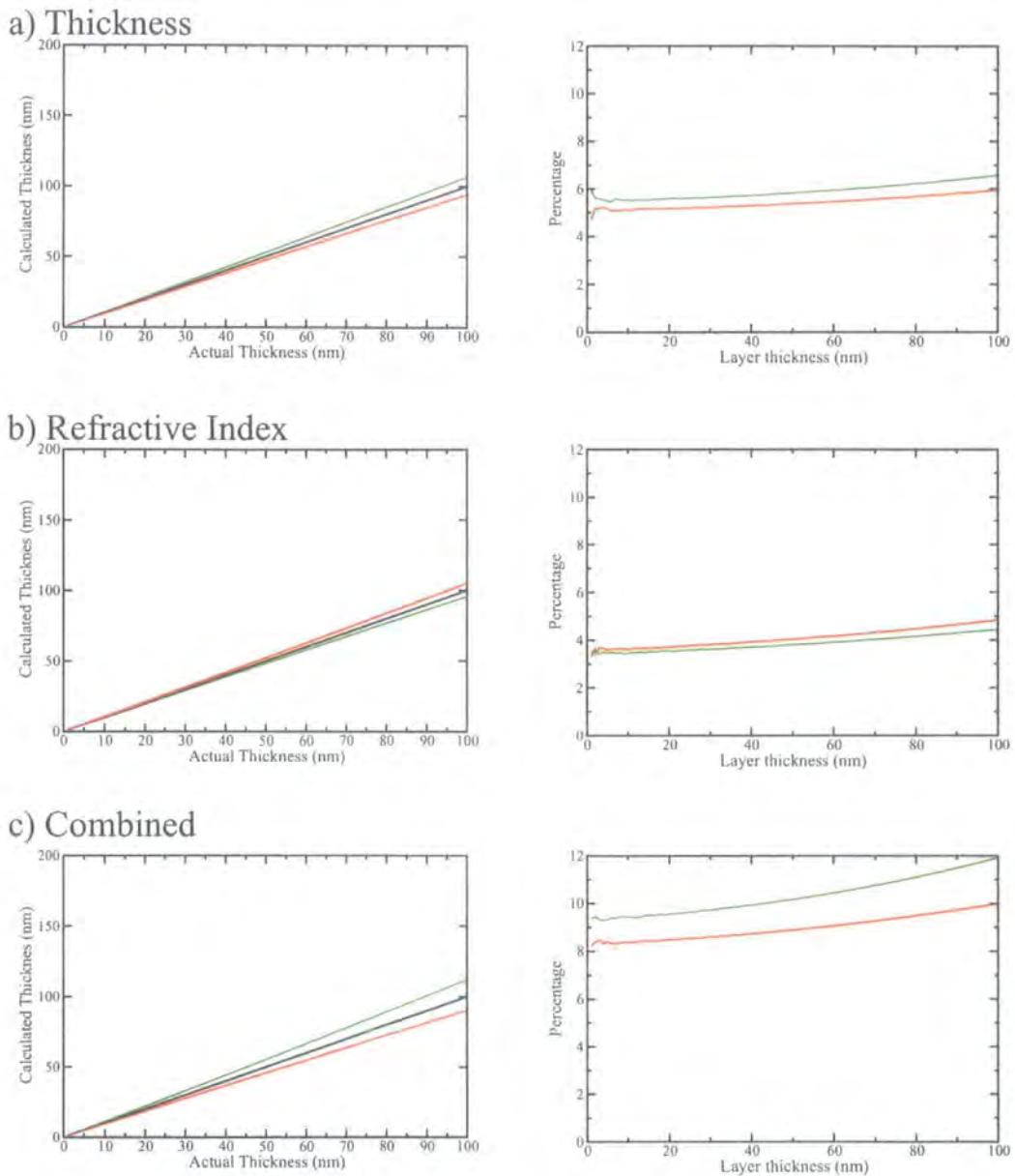


**Figure 2.14:** The effect of layer 4 manufacturing tolerances on a high refractive index ( $n = 1.45$ ) film of a variety of thicknesses. The upper tolerance limits are indicated by red lines and lower limits by green lines. The black lines are for the original structure. The left-hand column shows actual values and the right-hand column percentage discrepancies. The top figures (a) are for the thickness tolerance, the middle (b) for the refractive index tolerance and the lower (c) for a combined refractive index and thickness tolerance.

the manufacturing tolerances for high index films is particularly relevant for protein analysis with typical refractive indices anticipated to be closer to the high refractive index film situation than the low refractive index one.

### Total Structure

In addition to the layer 4 tolerances, the other base waveguide structure layers may also influence the accuracy of the resolution of deposited layers. Table 2.3 shows the effect of the manufacturing tolerance limits of layers 2 and 3 on a 100 nm film of  $n = 1.45$ . The influence of the lower layer manufacturing tolerances was anticipated to be much less significant than the upper guide tolerances. This was born out by the results, Layer 3 was seen to exert some influence on the resolved layer but layers below Layer 3 were calculated to have a negligible effect on the resolved layer thickness.

Combining the tolerances of layers 3 and 4 allowed a 'worst case' structure to be found. This was used to investigate the discrepancies in resolved refractive indices and thicknesses due to the total effect of the combined manufacturing tolerances. Fig. 2.15a shows that the discrepancies for the resolved thickness are highly refractive index dependent. The higher refractive index deposited films showed a much greater resilience than the very low refractive index films did to the overall manufacturing tolerances. If a 50% limit was place on the acceptable thickness error then films with a refractive index of greater than 1.37 could be resolved for any thickness up to the 100 nm limit.

### Refractive Index Resolution

The variations in resolved refractive index are surprisingly resilient to manufacturing tolerances, in percentage terms. The results shown in Fig. 2.15b are for the worst case structure. The greatest variation seen was for the thinnest films and even then it was only of the order of 0.4%, or 0.06 in actual terms. The convergence limit of 0.01nm creates some noise on the 1 nm film curve. The limit could simply have been reduced to produce a smoother curve. However, it was felt it was important to use the same level of convergence in the study as the final algorithm used.

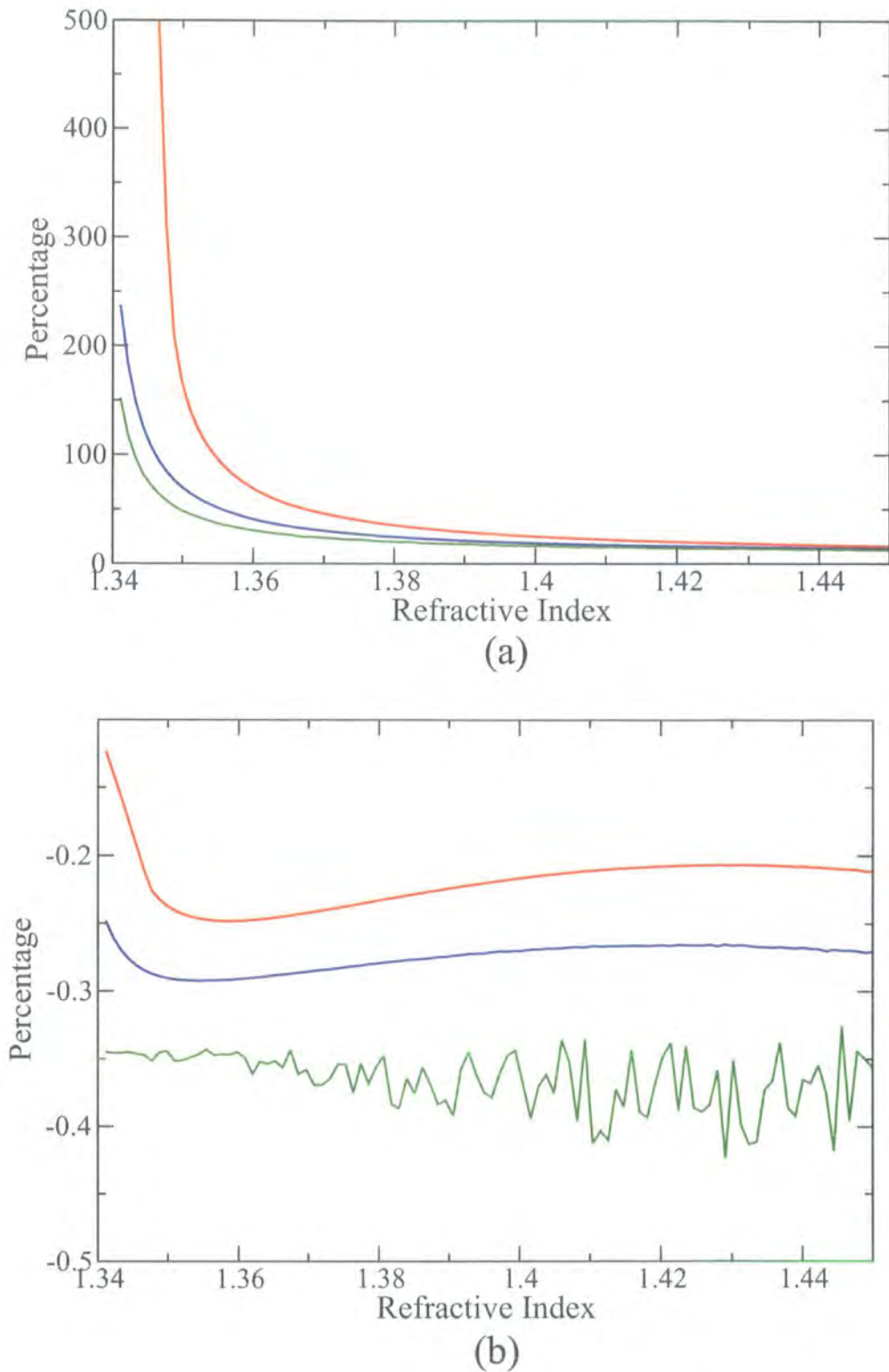


**Figure 2.15:** Results for a worst case structure with a 1 nm (green), 50 nm (blue) and 100 nm (red) deposited layer and a varying refractive index. The top graph (a) shows thickness deviations and the bottom graph (b) refractive index deviations from the ideal value.

Combined Layer 3 and Layer 4

Layer 3 Refractive Index	Layer 3 Thickness	Resolved Thickness (nm)
max	min	115.9
max	max	107.9
min	max	107.9
min	min	115.9

Combined Layer 2 and Layer 3 and Layer 4

Layer 2 Refractive Index	Layer 2 Thickness	Resolved Thickness (nm)
max	min	115.9
max	max	115.9
min	max	115.9
min	min	115.9

**Table 2.3:** Lower layer tolerance effects on the resolved thickness of a 100 nm ( $n = 1.45$ ) deposited layer.

### 2.9.4 Discussion

The study showed that the effect of the manufacturing tolerances on a biological film with a refractive index greater than 1.4 could be resolved with an error of less than 25% on the thickness value and 0.4% on the refractive index value. However, this is not acceptable given the high level of accuracy anticipated for the dual interferometry technique.

Whilst manufacturing tolerances are unavoidable, it is possible to reduce the effect of these tolerances on the calculation of the refractive index and thickness of a deposited layer. The transfer matrix method implemented for resolving the thickness and refractive index of an unknown layer uses two pieces of information, the TE and TM mode proportion constants, to fix the two optogeometrical parameters of the unknown layer. A similar approach can be used to calibrate the top guide by running the device without a deposited layer but with two known refractive index semi-infinite layers. The change from one known refractive index fluid to another above the device provides enough information to define the optogeometrical parameters of the upper guide. In this manner a form of calibration of the base chip structure can be achieved. Consequently, the dependence on chip manufacturing tolerances can be

alleviated to a great extent.

## 2.10 Verification of technique

The transfer matrix theory, based on Maxwell's equations, utilises assumptions that differ from the actual protein detection situation. Protein molecules will be of differing shapes and be deposited in a manner that may not provide a uniform isotropic coverage and planar interfaces. The validity of the relatively simple theoretical method can only be justified through the comparison of dual polarisation interferometry experimental results with those obtained by alternative methods for similar, or preferably identical systems. This section compares experimental results analysed using the dual polarisation interferometry technique with those available in the literature for similar systems. The findings are taken from reference [56] for two protein systems: the absorption of NHS-LC-Biotin and streptavidin molecules and that of anti-human serum albumin (anti-HSA).

Streptavidin [90] is a protein isolated from the bacterium *streptomyces avidinii* which is often used to detect biotin in tissue due to their high affinity to each other. Studies have been conducted on the streptavidin/biotin system as it is felt if the interactions responsible for this tight binding could be understood it might lead to an understanding of similar systems.

Anti-human serum albumin is an antibody. Antibodies are normally produced in immune systems and seek out harmful cells, viruses and other organisms before bonding onto them. It will readily bond to bis(sulphosuccinimydyl) suberate, BS<sup>3</sup> molecules.

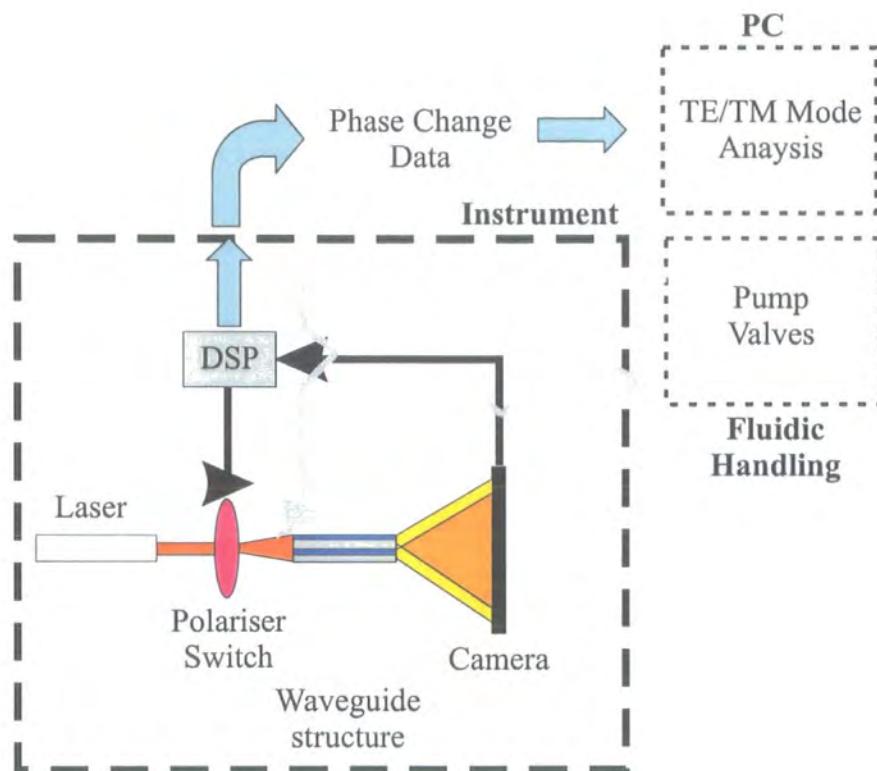
### 2.10.1 Instrument Details

The dual polarisation interferometry results were taken using an instrument known as the *Analight Bio200*, shown in Fig. 2.16. The device uses a sensor chip with a 4 layer structure as shown in Fig. 2.5 to create the two optical paths. The chip is clamped in a temperature controlled housing allowing the temperature to be set with less than 1mK variations. The chip clamping system is also designed to provide the fluidic interface to the sensor surface allowing different fluids to be passed over the chip surface. The actual dimensions of the chip are of the order of 5 mm by 20 mm. Light was provided by a helium neon laser (632 nm) which was coupled to the chip through the use of a Powell lens.

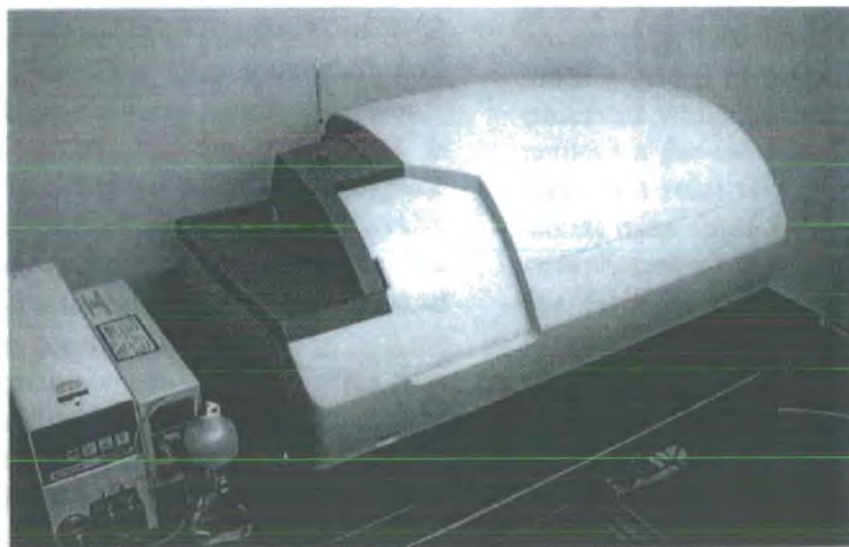
The two polarisations were selected by a ferroelectric liquid crystal half-wave plate that oscillated at 50 Hz, controlled by a digital signal processing (DSP) chip. After traversing the chip length the emergent light forms an interference pattern that was detected by a 1024x1024 element imaging device, located 6 mm from the output face of the chip. Information from the photo-detector was sent to the DSP to allow the relative phase position to be calculated every 20 ms. The relative phase changes could then be supplied to a personal computer where the transfer matrix method was used to resolve the refractive index and thickness of additional layers above the chip structure.

### 2.10.2 Biotin/streptavidin

Before data was taken the upper guide layer was calibrated using the method described in section (2.9.4) as a method for alleviating the manufacturing tolerance effects. The fluid system was then used to pass a buffer solution over the chip to give a stable starting point for the experiment. Into this buffer solution 2 mg/ml of sulpho-NHS-LC-biotin was added and flow continued to allow bonding with the aminated sensing surface to occur. The molecule is known to be 2.24 nm in length but is only expected to show a surface increase of around 0.5 nm due to the flexible manner in which the molecule bonds [56]. The phase change results using dual polarisation interferometry gave a resolved thickness of 0.46nm which was considered acceptable. The test part of the experiment was then to pass streptavidin at 40  $\mu\text{g/ml}$  over the sulpho-NHS-biotin layer and examine the results after washing with buffer solution. Streptavidin is a highly rigid molecule allowing for comparison with results obtained by alternative techniques. The results from dual polarisation interferometry produced an average layer thickness of 6.1 nm. This is comparable with literature values [91, 92] for solved structures placing the typical short axis of a avidin at 5.6 nm and an alternative optical technique placing thickness increases in the region of 4.2-5.8 nm. Neutron data also exists [93] which places a streptavidin layer thickness at  $4.4 \text{ nm} \pm 0.2 \text{ nm}$  and x-ray crystallography data gives it as 4.8nm [91, 92], slightly below the value seen for DPI. Cross *et al.* offered the following two possible explanations for the slightly high thicknesses seen using dual polarisation interferometry. Firstly, it is known that an additional water layer [94, 95] may form between the biotin and streptavidin layers, and secondly the layers will contain some flexibility giving disorder compared to the rigid highly immobilised structures used for



(a)



(b)

**Figure 2.16:** Top (a) schematic of the experimental arrangement. Bottom (b) a photograph of the physical embodiment of the apparatus.

x-ray and neutron experiments.

### 2.10.3 BS<sup>3</sup>/anti-HSA

This experiment laid a BS<sup>3</sup> layer on the aminated chip surface which was calculated to be 0.4 nm thick, compared to literature values which give BS<sup>3</sup> a 1.14 nm spacer [96]. This led Cross *et al.* to believe the layer lacked the regular order necessary to give molecules extended perpendicular to the surface. When anti-HSA was introduced it gave a layer thickness of 5.0 nm which is low compared to literature values of 6 nm [97]. However, they also used the resolved refractive index to calculate that their layer had an average density of 0.366 g/cm, implying that only half the sensor area was covered by the anti-HSA. This brings into question the homogeneity assumption made in section 2.6.1 for this particular system. However, the value is still reasonable compared to literature values, especially considering the flexible nature of the molecules which may have meant that the bound antibody was disorientated.

### 2.10.4 Discussion

The dual polarisation interferometry technique provided results that generally appeared consistent with those of other techniques. Particularly good agreement was seen for the streptavidin experiment due to the relatively rigid nature of the protein. Dual polarisation interferometry was seen to be a complementary technique to x-ray and neutron methods. The other methods may provide molecular structures with high precision but this is without the laboratory based *in vivo* benefits that dual polarisation interferometry can provide.

## 2.11 Conclusions and Future Work

A new biosensor technique has been presented which assists with the characterisation of thin biological films. The technique is based on the use of a waveguide interferometer with both TE and TM incident light polarisations to produce a single refractive index and thickness value for a deposited film. The resolution of the phase change data produced by the interferometer into refractive index and thickness values for a deposited film is based on the theoretical methods presented here. The theoretical methods are reliant on a well

defined base waveguide structure. Variations in the base structure due to manufacturing tolerances were shown to severely effect the accuracy of the method. A calibration method was suggested that would allow for the alleviation of such effects. Additionally, experimental work was discussed that compared the results of dual polarisation interferometry with results from other methods.

Whilst the technique described is still in its infancy; promise has been shown for the dual polarisation approach to become a well established biosensor technique. The work presented here shows that the relatively simple theoretical methods outlined in this chapter allow the accurate characterisation of thin films. There is scope for future work to consider more complex theoretical techniques, perhaps for resolving birefringent layers. More complex techniques would require more information to be known about a deposited layer, perhaps through the use of dual wavelengths in addition to dual polarisations.

# Chapter 3

## Diode Laser Tracking

### 3.1 Introduction

The previous chapter considered one-dimensional photonic structures and their use in a novel biosensor application. The application used a dual slab waveguide interferometer arrangement to examine modifications to the overall waveguide structure. In this chapter a similar slab waveguide interferometer arrangement is investigated for a telecommunications application.

In addition to a sensitivity to the guiding structure, the waveguide interferometer arrangement also possesses a high sensitivity to the wavelength of the incident light. Consequently the arrangement may provide a means for detecting fluctuations in the incident wavelength. The ability to track incident wavelength deviation from some initial value has a potential application in the telecommunications industry. Optical telecommunication networks are reliant on the output of semiconductor laser diodes to transmit the light carrying information over the networks. In such a situation fluctuations in the output wavelength of the transmitters is undesirable due to the detrimental effect it may have on the faithful transmission of voice or data traffic. The quantitative tracking of wavelength fluctuations in the output of the diode lasers could form one of the fundamental elements in a feedback system. Specific information on the wavelength fluctuations would allow corrections to be applied to the laser to compensate for any variations. Thus, the output wavelength of the laser could effectively be locked to its original intended value.

In this chapter a theoretical investigation is undertaken to determine the sensitivity of the slab waveguide interferometry approach to incident wavelength fluctuations. If corrections are to be properly applied to the laser then other effects which may cause similar responses in the interferometer need to be considered; responses due to wavelength variations need to be distinguishable from those due to other effects. As an example, ambient temperature fluctuations will cause variations in the optogeometrical properties of the waveguide structure, which may create interferometer responses indistinguishable from wavelength effects. If an interferometer design is to possess a high wavelength sensitivity then the effect of optogeometrical variations in the waveguide structure must either be absent, or at least minimised to avoid overwhelming the wavelength effects.

The possibility of an optimised athermal waveguide structure is considered in this chapter. Athermal structure design represents an approach for limiting the effect which ambient temperature fluctuations may have on the wavelength sensitivity of the arrangement. The potential advantages of such an athermal approach over the basic dual slab waveguide approach [56] are discussed. The work presented forms part of the research currently being undertaken towards the realisation of the Picolock wavelength monitoring system under development by Farfield Photonics Ltd.

## **3.2 Telecommunications Background**

### **3.2.1 Dense Wavelength Division Multiplexing**

During the last 15 years a technology known as Dense Wavelength Division Multiplexing (DWDM) has been making an increasingly significant contribution to optical telecommunications networks [98, 99]. Optical networks use a technique known as Pulse Code Modulation (PCM) [100] to enable the use of light to send digital information along low loss optical fibres. The capacity of an optical fibre to carry information is referred to as the bandwidth of the fibre and is measured in terms of the number of bits of information which can be sent along the fibre in a specific unit of time. The International Telecommunications Union (ITU) has produced a set of industry-wide standards which define the bandwidths for standard single wavelength optical fibre systems; these are shown in Table 3.1.

Single wavelength systems use the technique of time division multiplexing (TDM) to

SONET	SDH	Bandwidth (Mb/s)	Channels
OC-1		51.84	672
OC-3	STM-1	155.52	2,016
OC-12	STM-4	622.08	8,064
OC-48	STM-16	2,488.32	32,256
OC-192	STM-64	9,953.28	129,024

**Table 3.1:** ITU standards for single fibre bandwidths [100]. The Synchronous Optical Network (SONET) and Synchronous Digital Hierarchy (SDH) codes for the varying standards are also shown.

enable different information signals, or channels, to be simultaneously transmitted. Current communication systems tend to operate at the STM-16 level with a bandwidth of 2.5 Gb/s, supplying of the order of 32,000 simultaneous voice channels. The fundamental principle of DWDM techniques is the combination of different wavelengths of light, each carrying different information signals, within the same optical fibre. In this manner several virtual fibres may be created within the single physical fibre. The technique allows for greatly increased data rates within the fibre, thus reducing the number of fibres necessary to carry an equivalent quantity of traffic. This is highly attractive for telecommunications network operators as it offers significant cost savings over conventional approaches for equivalent quantities of traffic. Equally importantly, it also provides the flexibility and scalability to increase network capacity without the laying of additional fibre. DWDM is expected to grow into a central technology for optical networks in the near future.

The ITU have an agreed set of wavelength transmission bands which give the operating frequencies to which specific optical systems should conform. The wavelength band in the most widespread use in current communications networks is the C-band, which encompasses the wavelength region from 1525 to 1562 nm. The C-band is 37 nm wide, which means that currently developed wavelength division systems, which utilise wavelengths differentiated by 1.6 nm (200 GHz) or 0.8 nm (100 GHz), may transmit 23 or 46 different simultaneous wavelength channels. Future demand for additional bandwidth capacity in the optical networks is likely to bring the wavelength divisions closer together, to 0.4 nm (50 GHz) or lower. The increase in available bandwidth from the use of DWDM techniques is extremely significant. For example, a 0.4 nm system would be capable of transmitting 92 different wavelengths simultaneously in a single fibre, producing bandwidths of the order of

200 Gb/s.

To operate without the mixing of separate information signals, known as cross-talk, DWDM systems are highly reliant on the wavelength stability of the semiconductor diode lasers which are used to transmit the signals. Semiconductor diode lasers are essentially the only practical laser for optical communications networks as they uniquely provide small size, low cost devices which are capable of being modulated at the gigahertz speeds necessary for PCM [101].

### 3.2.2 Diode Lasers

The physics of semiconductor diode lasers [101–105] is an extension of the standard  $p$ - $n$  junction theory. When  $p$  and  $n$  type semiconductors are brought together a  $p$ - $n$  junction is created and the diffusion of electrons and holes occurs to create a charge build up. The  $p$ -side becomes negatively charged and the  $n$  side positively charged, thus discouraging any further motion of the free carriers. The recombination of the free electrons and holes occurs around the junction interface thereby creating a depletion region. In the depletion region bending of the valence and conduction bands occurs to allow the fermi level to remain constant. For lasing to occur population inversion is required and the number of electrons in the lower part of the conduction band must be greater than the number in the upper part of the valence band. This situation may be created by using strongly doped  $p$ -type and  $n$ -type materials and applying a strong enough bias that the number of holes on the  $p$ -side is large and the number of electrons on the  $n$ -side is also high. The depletion region would then have a lack of electrons in the valence band and a surplus in the conduction band, producing the required population inversion. To achieve this type of arrangement with a single  $p$ - $n$  junction a large threshold current would usually be required. The threshold current may be greatly reduced through the use of the double hetrostructure design present in most modern diode lasers.

### 3.2.3 Double Hetrostructures

The double hetrostructure arrangement, shown in Fig 3.1, allows population inversion in the depletion region to be produced at a much lower threshold current than is possible with a simple  $p$ - $n$  junction. Three materials are used to form the double hetrostructure arrangement, with the middle layer forming the depletion region. The middle material possesses a

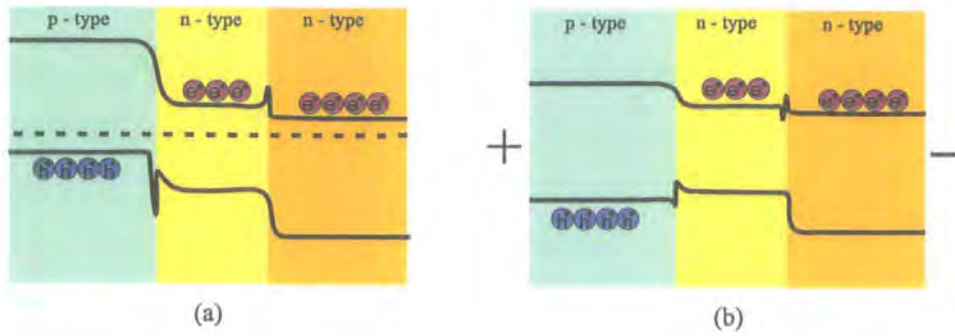


**Figure 3.1:** A double heterostructure semiconductor laser consisting of three different materials. The structure is shown unbiased (a) and with a forward bias (b). The solid black lines indicate the conduction and valence bands and the dashed line, in (a), the fermi level.

reduced band-gap compared to the outer two materials, allowing it to be filled with electrons and holes with relative ease. This arrangement facilitates population inversion at a greatly reduced threshold current. Additionally, the use of a low band-gap material, between the two high band-gap materials, narrows the depletion region to the width of the layer by limiting diffusion. This increases the free carrier density in the depletion region, again assisting with population inversion. A further benefit of the three layer design is that the refractive index of the central region may be greater than that of the layers on either side. This assists with the confinement of light to the active region of the laser arrangement, thus increasing gain. It is worth noting that spikes occur in the conduction and valence bands due to the alignment of the fermi level across the double heterostructure. The spikes act to slightly increase the energy requirement for carrier motion. However, under a forward bias the carriers will have sufficient energy to tunnel through the spikes and enter the central layer [106].

In optical communications networks the most commonly utilised alloy system for the active layer of a double heterostructure is InGaAsP. This is due to the alloy system providing a band-gap with wavelengths which may be adjusted to fall within the absorption minimum of optical fibres. The exact emission wavelength is dependent on the band-gap of the active region. It is the recombination of electrons and holes in this region which produces the laser output. In addition to the alloy system the band-gap will also be influenced by external factors such as the operating temperature and any applied electric field.

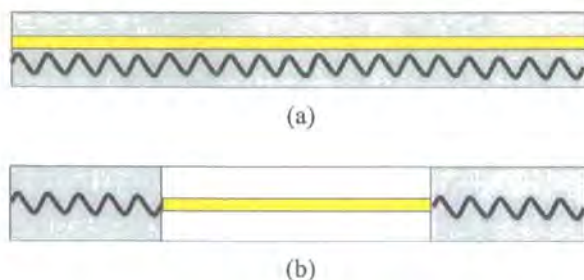


**Figure 3.2:** A schematic showing (a) the distributed feedback (DFB) laser arrangement normally used in DWDM systems and (b) the end reflector type approach, used in a distributed Bragg reflector (DBR) configuration.

### 3.2.4 Distributed Feedback Lasers

The type of lasers most frequently used for DWDM application are known as distributed feedback (DFB) lasers. Confinement to the laser cavity occurs through the periodic refractive index modulation distributed throughout the cavity length, as shown in Fig 3.2a. The periodicity acts to diffract waves propagating in the cavity, confining only those of a particular wavelength to the active region. Traditional laser designs use reflectors placed at both ends of the laser cavity, shown in Fig 3.2b, to produce confinement. The DFB laser arrangement is intended to provide gain for a single wavelength only. However, the temperature dependence of the refractive index contrast is responsible for a temperature dependence in the gain wavelength.

Optical networks generally make use of DFB lasers designed to operate at a single wavelength. The use of multiple wavelengths by DWDM networks requires multiple laser diodes at very specific wavelengths. Such laser arrangements were heavily researched in the 1980s but only became viable in the 1990s when InP based optoelectronic integrated circuits were developed [100, 107]. If a 50 GHz line spacing is enforced, the fixed laser solution requires a 180 laser array per fibre, due to the requirement that each of the 90 main lasers has a backup in case of failure. Each individual laser is required to maintain its output within the narrow wavelength channel spacings required for DWDM.

### 3.2.5 Stability

Single wavelength DFB lasers are tuned to their operating wavelength at the factory and are required to maintain the wavelength over the expected lifetime of the system, which is about 30 years [108]. There are a number of possible causes for the wavelength of a diode laser to deviate from its intended wavelength. These include thermal effects, changes in the driving current and also, on a longer timescale, the possibility of ageing effects.

Initial reports suggested that factory tuning would be sufficient for wavelength stability and no appreciable degradation in wavelength would occur over time [109]. However, diode laser devices are highly stressed in terms of the optical field strengths and current densities that exist in the structures. It was later recognised that ageing effects were significant and lead to a gradual degradation in their operating characteristics [110]. Whilst the majority of the individual processes responsible for this degradation with time have been identified and removed from the system, the possibility still remains for the output wavelength of a laser to vary with ageing.

Given the possibility of wavelength deviation from the intended value there is a need for some external means of tracking the output wavelength of diode lasers. The tracking of wavelength fluctuations, irrespective of their origin, would permit electrical or thermal feedback to be supplied to the laser to stabilise its operating wavelength.

### 3.2.6 Stabilisation Systems

The wavelength locking of DFB lasers is deemed to be a key issue in DWDM networks and currently forms an active area of research. The research has generated a variety of different methods which potentially offer improvements in the wavelength stability of diode lasers. These include devices based on fibre Bragg gratings [194], arrayed waveguide gratings (AWGs) [112], ring resonators and the most popular, Fabry-perot etalons [113, 114]. Despite the seemingly adequate range of approaches currently available, the spectrum of devices may not represent the most convenient or cost effective solution possible. A waveguide interferometry approach would allow for the integration of the feedback device at wafer level when the diode laser is fabricated. The advantages of this would be both a reduction in the manufacturing costs and an ability to perform wafer level component testing. Wafer level component testing is preferential to package level testing as it allows for increased yield of

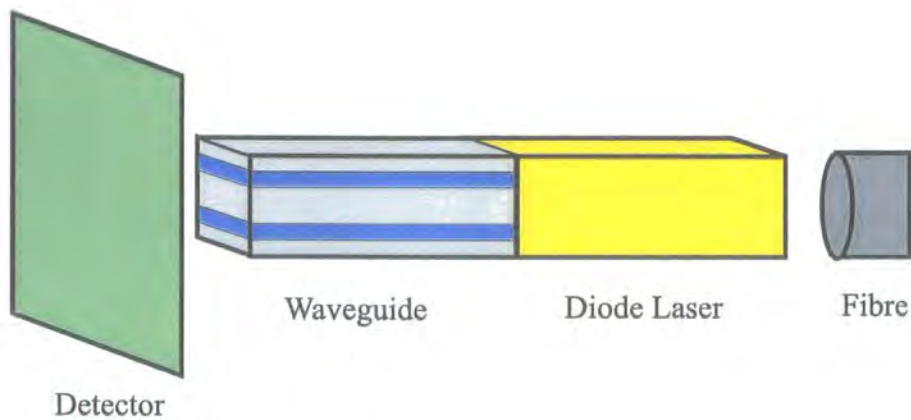


**Figure 3.3:** Proposed waveguide interferometer arrangement. Light is simultaneously coupled from the diode laser to the fibre and the interferometer. A detector is used to examine phase changes, attributable to wavelength fluctuations, allowing corrections to be applied to the laser.

the final packaged product.

### 3.3 Integrated Wavelength Interferometry

The use of waveguide interferometry for the application of tracking the output wavelength of diode lasers was proposed in 2002 by Cross *et al.* [56]. The waveguide interferometer arrangement utilised by Cross *et al.* made use of a dual slab waveguide structure, similar to that described in Chapter 2. They presented promising experimental results for tracking wavelength fluctuations in a 635 nm source laser. The demonstrated threshold for the detection of wavelength fluctuations in the laser output was 6.1 pm, well below the 0.4 nm wavelength channel spacing required for DWDM systems. Their work demonstrated the viability of the waveguide interferometry technique for the application of diode laser wavelength tracking. However, the simple two uniform guiding layer system required tight temperature control, to the 10 mK level, to permit the stated wavelength sensitivity threshold above thermal effects.

The proposed arrangement for the integration of the waveguide interferometer and the diode laser, is shown in Fig. 3.3. The arrangement makes use of the knowledge that the laser produces light propagating in both the forward and backward directions. The forward

direction is coupled to the fibre for the transmission of PCM signals and the backward directed light is available for the waveguide interferometer. A CCD is positioned behind the output end of the waveguide structure to allow for the detection of phase changes via the interference pattern method (described in Chapter 2). The arrangement allows for wafer level integration of the waveguide structure and the laser structure.

### 3.4 Design Concept

Here the viability of an athermal interferometer design is investigated to alleviate the reliance on tight temperature controls imposed by the dual uniform guide approach. Athermal waveguide structures have been proposed in the literature for different applications. The proposals have tended to rely on the combination of different classes of materials [115, 116]. Suitable combinations may have opposing thermal optogeometrical properties allowing for the cancellation of the thermal effects. The athermal nature of such waveguides is achieved through the design of structures with temperature independent values of the individual mode propagation constants. Such an approach is unnecessary for waveguide interferometry, as it is only the relative phase difference between the two propagating modes which is detected. The design concept utilised here permits changes in the propagation constants of both interferometer modes to occur, provided that both propagation constants change by an identical amount.

The athermal structures considered here are assumed to be fabricated by the silicon-on-oxide fabrication method. The silicon-on-oxide method limits the materials available to form a structure to just silicon and silicon dioxide. The choice of fabrication method was due to its proposal [117] in the literature for the production of wafer scale waveguides in integrated optoelectronic devices. For simplicity the number of layers forming the guiding structure was limited to 7.

The athermal design differs from the previously proposed dual waveguide interferometer design by the inclusion of an additional low index layer within the upper guide, shown in Fig 3.4. The fabrication of such an arrangement has been reported in the literature using silicon-on-oxide techniques [118]. The additional layer allows for some degree of control over the propagation constant of the upper mode. Temperature variations will, in general,

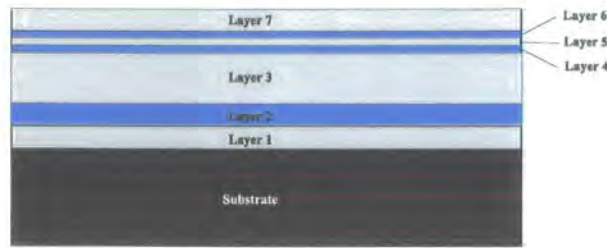


**Figure 3.4:** The athermal structure is similar to the dual-slab waveguide structure. However, the upper guide has a thin low refractive index material (grey) in the centre of the high refractive index (turquoise) guide.

alter the guided mode propagation constants for the upper and lower guided modes by a different amount. Control of the upper guide (layers 4-6) propagation constant allows for thermal changes to the upper guided mode propagation constant to be matched to those of the lower guided mode. Purely thermal effects will then be undetectable in the phase changes calculated from the interference pattern.

## 3.5 Theoretical Method

The guided mode propagation constants for a well defined structure may be calculated through the transfer matrix method described in Chapter 2. In general the individual layers, which combine to form the overall waveguide interferometer structure, will possess refractive index and thickness values which are temperature-dependent. In this section the effect of ambient temperature fluctuations on the refractive index and thickness of individual layers is examined.

### 3.5.1 Linear Thermal Expansion

Temperature may be defined as a measure of the average internal kinetic energy of the atoms or molecules that form a crystal lattice. Anharmonic terms in the potential energy give a crystal an average lattice point displacement which varies with temperature. This causes the crystal to expand with increasing temperature. Thermal expansion of a dimension  $L$ , caused by a temperature change from  $T$  to  $T + \delta T$ , is usually described by the use of a linear thermal expansion coefficient,  $\alpha$ , such that:

$$L(T + \delta T) = L(T) + \alpha \delta T L(T) \quad . \quad (3.1)$$

Values for the linear thermal expansion coefficient for specific materials are available in the literature. The value of the coefficients for silicon and silicon dioxide are given in Table 3.2 [119].

### 3.5.2 Refractive Index Dispersion Relations

The variation of the refractive index of a material with temperature, at constant pressure, is called the thermo-optic coefficient and denoted  $dn/dT$ . The effect in glasses is attributable to the thermal variation of electronic polarisability and the thermal expansion of the material. Polarisability is related to the ease of distortion of the molecular electron clouds to an applied electric field. An expression yielding the thermo-optic coefficient was derived by Johnston [120] based on the phenomenological calculations of Tsay *et al.* [121]. The equation derived by Johnston may be written as:

$$2n \frac{dn}{dT} = K^2 \left( -3\alpha R + \frac{2}{\lambda_g} \frac{d\lambda_g}{dT} R^2 \right) \quad . \quad (3.2)$$

The expression is dependent on the linear thermal expansion coefficient,  $\alpha$ , the wavelength of the energy gap  $\lambda_g$  and a material dependent constant,  $K$ . It is also dependent on the wavelength of interest,  $\lambda$ , which contributes in the form of a normalised dispersive wavelength,  $R$ , where,

$$R = \frac{\lambda^2}{\lambda^2 - \lambda_g^2} \quad . \quad (3.3)$$

The thermo-optic coefficient expression may be simplified to provide an expression for use with data interpolation:

$$2n \left( \frac{dn}{dT} \right) = GR + HR^2 \quad . \quad (3.4)$$

Values for the two constants,  $G$  and  $H$ , may be calculated from the best fit with experimental

Material	n	G ( $\times 10^{-6}/K$ )	H ( $\times 10^{-6}/K$ )	$\lambda_g$ ( $\mu m$ )	$\alpha$ ( $\times 10^{-6}/K$ )
Si	3.45	-86.1087	1159.2000	0.4196	2.62
SiO <sub>2</sub>	1.44	-1.9969	25.5833	0.106	0.62

**Table 3.2:** Values of the relevant Si and SiO<sub>2</sub> coefficients [119, 122].

values. The values used here are taken from the literature [122] and are given in Table 3.2. When considered in the centre of the C band (1543.5 nm) equation (3.4) gives a value for  $dn/dT$  of silicon as  $1.824 \times 10^{-3} K^{-1}$  and, similarly, the value for silicon dioxide as  $8.271 \times 10^{-6} K^{-1}$ .

### 3.5.3 Modes

The operation of the dual slab waveguide interferometer, discussed in Chapter 2, imposed the stipulation that the overall dual slab waveguide structure supported just two guided modes. This requires that the upper and lower guides both support just one symmetric mode each. Consequently, both individual guiding layer thicknesses must be kept below the two mode cut-off thickness. The cut-off thickness ( $t_{co}$ ), above which an anti-symmetric mode would also be present, is given by [8]:

$$t_{co} = \frac{\lambda}{2(n_1^2 - n_2^2)} \quad (3.5)$$

In this expression  $n_2$  is the refractive index of the cladding layers and  $n_1$  is the refractive index of the core guiding layer.

In the athermal structure design the lower guide, layer 2, is uniform and equation (3.5) gives the cut-off thickness. The upper guide, layers 4-6, has the appearance of two coupled symmetrical waveguides. It is widely stated that two symmetrical waveguides have no second mode cut-off thickness, due to coupled systems always containing at least one symmetric and one anti-symmetric mode. This is, however, an over generalization of the situation for very low guide separations. Calculations showed that the 3 layer upper guide could effectively operate as a single uniform guide, with a single guided mode, provided that the central low index layer was of sufficiently low thickness. Fig. 3.5 shows the second mode cut-off frequencies calculated for a range of possible thicknesses of the low index and

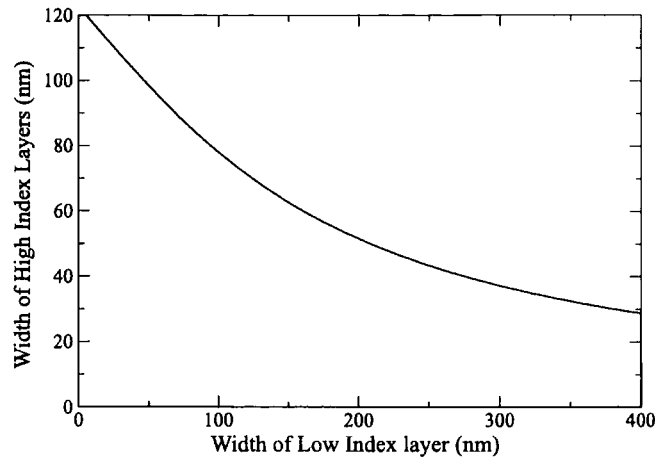


**Figure 3.5:** Single guided mode region for a three layer upper guide. The guide consists of a low refractive index central layer sandwiched between two high refractive index layers of equal thickness.

high index regions which form the three layer upper guide. The large spatial separation of the upper and lower guides, together with the high refractive index contrast of the fabrication materials, allows the two guides to be considered as separate systems for such propagation mode constant calculations.

### 3.6 Structure Response

For the range of possible three layer symmetric upper guide configurations shown in Fig 3.5 it is possible to find a thickness of the lower guide which produces an athermal structure. The required lower guide thickness can be found by plotting the change in the difference between the upper and lower guided mode propagation constants due to a 1 K temperature change. The results of such a calculation are shown in Fig 3.6 for an arbitrary upper guide configuration. It can be seen that at a particular lower guide thickness value the thermal response of the structure is extinguished. This implies that the upper and lower guided mode propagation constants have changed by an equal amount.

The application of such an approach across the whole of the available two parameter space defined by Fig 3.5 allows multiple athermal structures to be found. All of the structures will be resilient to thermal effects and by examining the signal response of the structures an optimum athermal structure may be found. The signal responses were compared by calcu-

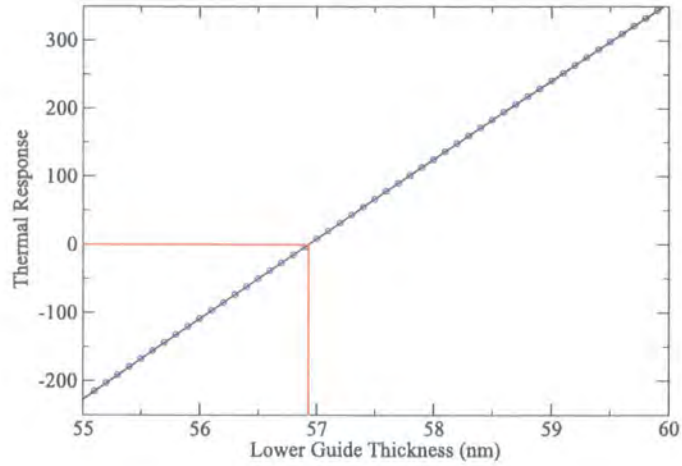


**Figure 3.6:** An example plot of the change in the difference between the upper and lower guided mode propagation constants due to a 1 K temperature increase. The upper guide structure is fixed and the lower guide thickness is given by the  $x$  coordinate.

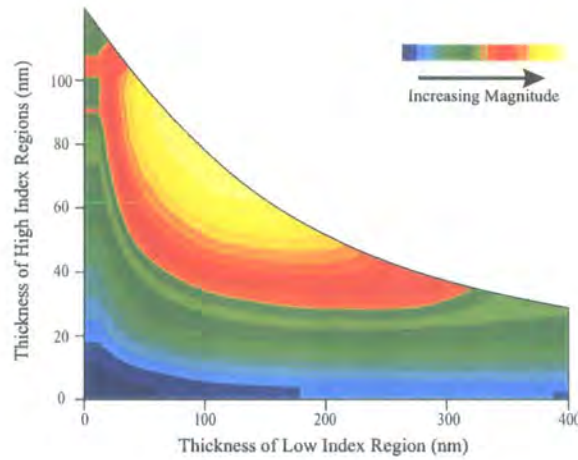


**Figure 3.7:** Plot of the change in the difference between the upper and lower guided mode propagation constants due to a 1 nm wavelength increase. The upper guide configuration is given by the two axes. The lower guide thickness is the required value for an athermal structure when combined with the specified upper guide configuration.

Layer	Material	Refractive index	Thickness (nm)
Lower	SiO <sub>2</sub>	1.44	∞
1	Si	3.45	94.4
2	SiO <sub>2</sub>	1.44	400
3	Si	3.45	80
4	SiO <sub>2</sub>	1.44	90
5	Si	3.45	80
Upper	SiO <sub>2</sub>	1.44	∞

**Table 3.3:** Optimised waveguide structure.

lating the difference in the propagation constants of the two guided modes before and after a 1 nm wavelength increase at the mid-point of the C-band. The results are shown in Fig. 3.7 as a contour plot. The change in difference between the two guided modes will be referred to as the signal response of the structure. Signal responses of between 1 and 187 m<sup>-1</sup> were calculated. The highest signal response was seen for the structure detailed in Table 3.3.

### 3.6.1 Advantages

Whilst of clear academic interest, the athermal approach needs to show performance advantages over the simple dual slab waveguide structure design in order to justify its increased fabrication complexity in practice. Phase changes detected by the interferometer arrangement are due to changes in the difference between the two guided mode propagation constants,  $\Delta(\Delta\beta_1 - \Delta\beta_2)$ . Whilst detected phase changes may be due to wavelength fluctuations, referred to as the signal response, similar changes may be seen due to temperature fluctuations. The temperature fluctuations limit the ability of the arrangement to detect distinguishable wavelength fluctuations. Consequently phase changes due to thermal fluctuations will be referred to as the thermal noise of the structure.

The athermal structure designs were calculated to possess a lower signal response than was achievable with the additional design freedom available from a dual uniform guide approach. Fig 3.8a shows a contour plot of the signal response of the dual uniform guide approach for a range of possible upper and lower guide thicknesses. Comparison of this with Fig 3.8b allows it to be seen that structures with the highest sensitivity to wavelength fluctuations also possess the highest sensitive to thermal fluctuations. For a device to be able to distinguish between wavelength fluctuations and thermal fluctuations it is the signal to noise

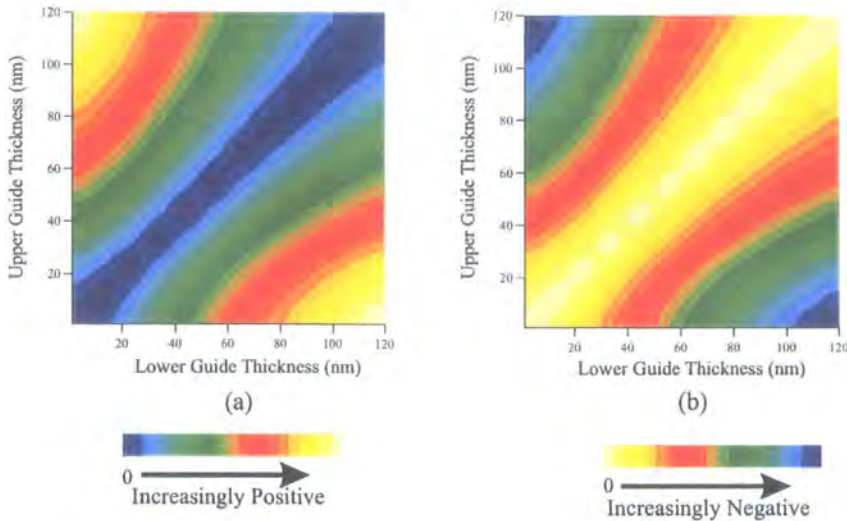


**Figure 3.8:** Signal response (a) and thermal noise (b) for a range of dual uniform guide structures. Note the signal responses are positive for a 1 nm increase and negative for a 1 K increase.

ratio which is crucial. Provided that the signal response is above the minimum detectable level then the limiting factor on wavelength sensitivity is the signal to noise ratio. Responses detected by the interferometer can only be assured to represent genuine wavelength fluctuations if they are above those achievable by thermal fluctuations. Thus a sensitivity threshold exists, above which wavelength fluctuations may be distinguished from ambient temperature fluctuations and corrections applied to the laser.

The overall signal to noise ratio for the complete range of dual uniform guide structures varies between 0.37 and 0.45, for a 1 nm wavelength fluctuation and a 1 K thermal fluctuation. For temperature control to the 1 K level the device could, at best, lock wavelengths to within 2.2 nm. This is well above the wavelength channel separation required for DWDM applications, making the device unsuitable for the intended application. Recall, that the experimental results from Cross *et al.* [56] made use of 10 mK temperature control. If a similar regime was imposed on a silicon/silicon dioxide dual uniform guide structure then the reduction in the noise level would produce a signal to noise ratio of approximately 45, which allows for a wavelength sensitivity threshold of around 2.2 pm.

Performance of the optimised athermal structure at the exact athermal point must be limited by a factor other than thermal noise. In this instance the limiting factor would be the 3 mrad experimental detection threshold achievable for detectable phase changes [123].

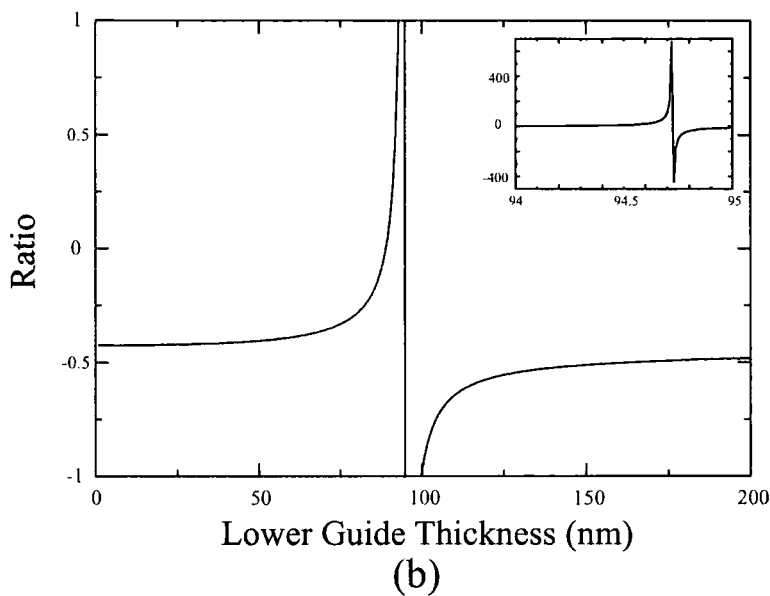
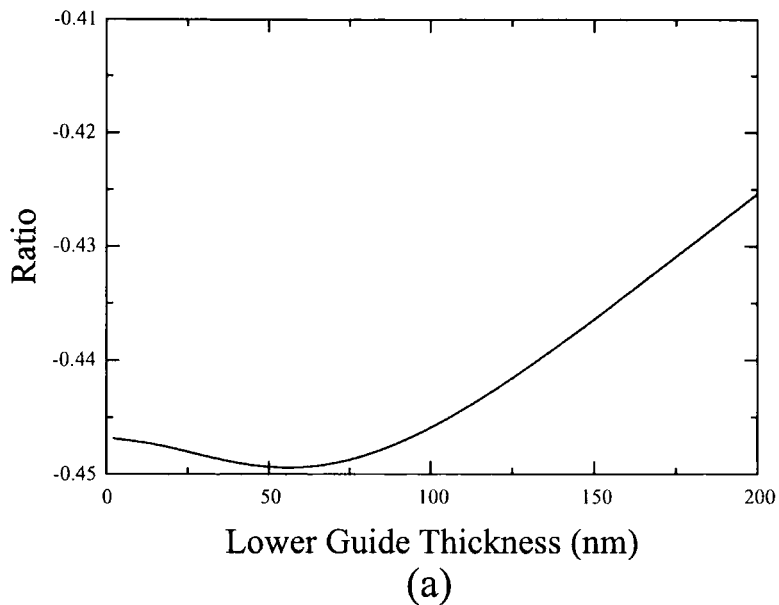


**Figure 3.9:** Signal to noise ratio for a dual uniform waveguide interferometer (a) and for an athermal design (b).

With a signal response of approximately  $200 \text{ m}^{-1}/\text{nm}$  a 10 mm chip would have a sensitivity threshold of around 0.15 pm. Unfortunately, an exact athermal structure is unlikely to be achievable experimentally due to the requirement of a fabrication precision at the atomic level. However, if 1 K temperature control was exercised and the exact athermal point was missed by the order of 1 nm then the athermal structure would produce results similar to a tightly temperature controlled dual uniform waveguide structure. Fig 3.9b shows that the athermal structure retains a small advantage over the dual uniform waveguide design for a range of lower guide thicknesses around the athermal point.

The recommendation for future devices would be a compromise between an athermal structure and, say, 100 mK temperature control which is easily achievable at package level. This would allow structures with a lower guide proximity to the athermal point of around 10 nm to have a wavelength sensitivity threshold of approximately 5 pm.

A plot of the electric field profile for both the modes present in the idealized athermal structure is shown in Fig 3.10a. The effect of the low refractive index material in the upper guide may be seen as a slight reduction in the field amplitude. Fig 3.10b shows the diffraction pattern calculated by assuming that the output edge of the structure consisted of a range of circular wave producing point sources. The amplitude of the point sources is being taken from the electric field profile for the two modes. Maxima in the interference pattern can be seen to move with wavelength variation. The field pattern is unsymmetrical due to the different field profiles for the two guided modes. Such maxima movement would allow for a calibration of maxima position against wavelength drift to produce the necessary data for laser correction.

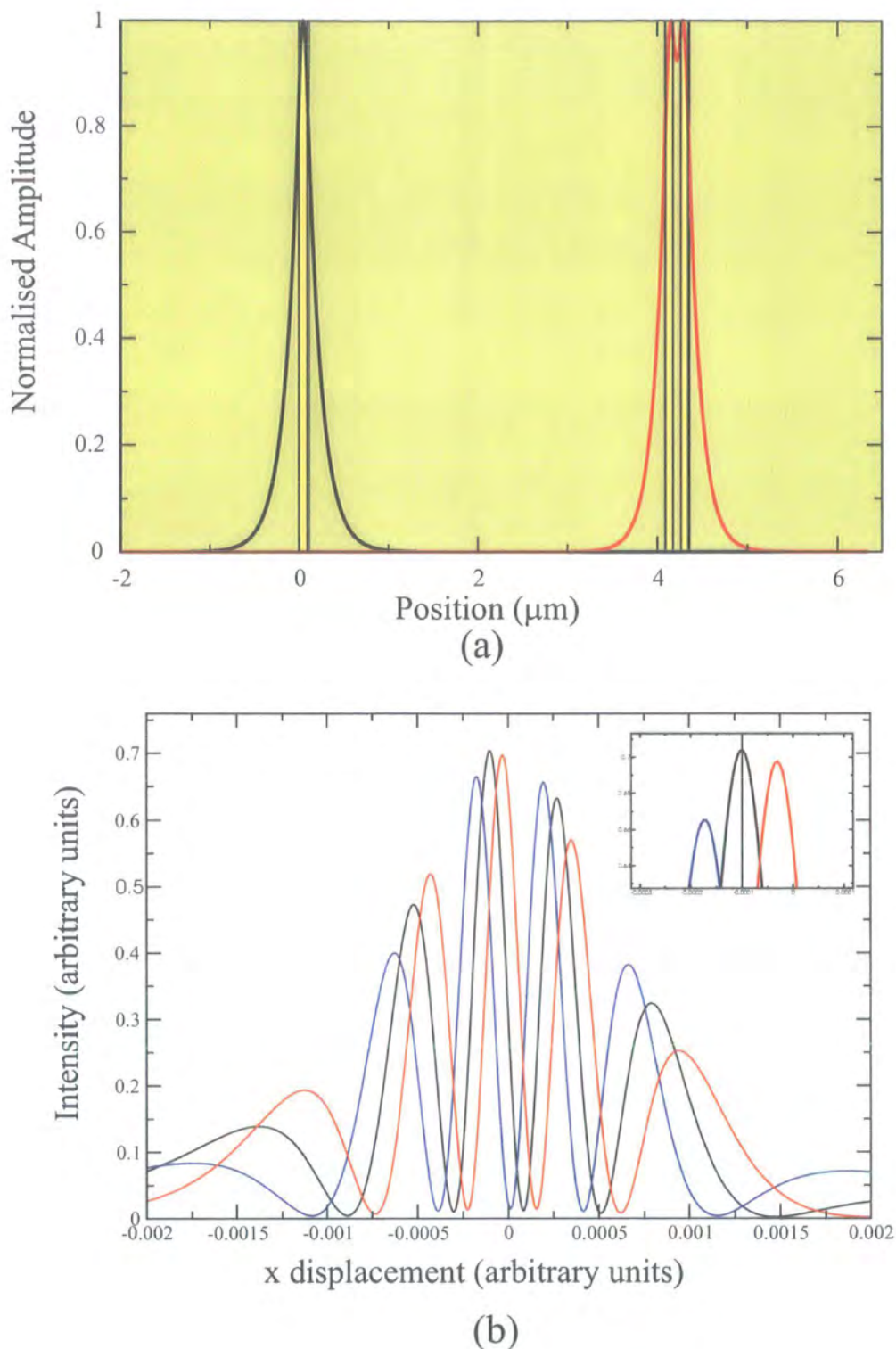


**Figure 3.10:** The normalized electric field profiles (a) for the two guided modes present in the optimised athermal guide. The different colours indicate the two different refractive indices. A far-field diffraction pattern is also shown in (b) for a 1 nm wavelength increase (red) and a 1 nm wavelength decrease (blue). Maxima movement may be seen with the wavelength change providing a means for calibration of maxima position against wavelength.

### 3.7 Conclusions and Future work

An athermal waveguide interferometer has been proposed for tracking fluctuations in the output wavelength of diode lasers. The athermal approach was investigated as a method of alleviating the tight temperature control required by a standard dual uniform slab waveguide approach. A silicon and silicon dioxide structure designed using the standard approach was calculated to need 10 mK temperature control to achieve a 5 pm sensitivity to incident wavelength fluctuations. The athermal approach proposed here was predicted to achieve similar performance with just 100 mK temperature control, together with the requirement that the lower guide thickness was within 10 nm of the athermal point.

Future work on wavelength locking by similar methods to those considered here should also consider the need for inter-vendor compatibility in ITU networks. Such a requirement would make it necessary for the calibration of all wavelength lockers in a network against known standards. There is the possibility that this could be undertaken at the factory, when the DFB laser is assigned its frequency. However, the exact implementation of such an approach requires investigation. The effect of variations in refractive index and thickness, introduced by manufacturing tolerances, also needs consideration. Methods for alleviating these through calibration may be feasible.

In conclusion, the athermal approach has demonstrated the scope to provide the necessary sensitivity to wavelength fluctuations required for providing feedback to diode lasers at a level comparable or superior to existing technologies. The realisation of a commercially viable device requires further research to assess its potential.

# Chapter 4

## Photonic Crystal Theory

### 4.1 Introduction

#### 4.1.1 Analogy with Semiconductors

The theoretical techniques employed for the study of photonic crystals [13,124] exist in close analogy with those applied to the theoretical study of semiconductors. It is indisputable that our current depth of understanding of semiconductor properties would not have been achieved without the assistance of well developed theoretical techniques. Theoretical studies are both essential to assist with the understanding of the underlying physics responsible for structure properties and they also provide the useful ability to study the properties of proposed structures without the need for expensive structure fabrication. The strength of theory has been particularly evident in the field of photonic crystals where, until recently, the field was dominated by theorists, as experimentalists struggled to realise the structures proposed by their theoretical colleagues.

The standard bandstructure calculation techniques constitute key theoretical tools for studying semiconductors. Whilst bandstructure techniques were originally developed to aid with the understanding of the electrical properties of semiconductors, similar techniques are equally valuable in understanding the optical properties of photonic crystals. The periodic dielectric contrast of photonic crystals acts in a manner analogous to the periodic potentials of semiconductor structures. The periodicity of these two properties produces bands of allowed and forbidden electron or photon energies within the appropriate structures. For

semiconductors, the accurate calculation of these energies is achieved through the solution of the quantum mechanical Schrödinger equation (see for example [125] or [6]). For photonic crystals it is Maxwell's equations [86] which represent the governing physics and describe the optical properties of such structures. The graphical representation of allowed solutions in specific directions within a structure is termed a 'bandstructure'. The interpretation of bandstructures may provide useful information on both the transmission and refraction properties of photonic crystal structures.

### 4.1.2 Physical Origin of Bandstructures

The allowed solutions which may be displayed as bandstructures are the result of scattering events occurring within the photonic crystal structures. The structures contain multiple interfaces between materials of different refractive indices which create multiple reflections of the incident light. In photonic crystals the pattern of the refractive index contrast is engineered to be spatially periodic, making the diffraction Bragg-like [126] in nature. This produces the required regions of allowed and forbidden frequencies similar to those that exist for electron energies in semiconductors. Accurate theoretical calculations of these allowed frequencies is essential when studying the properties of photonic crystals. In this chapter a standard method for performing calculations of this nature is presented. Additionally, a variation on the standard bandstructure calculation method known as a 'complex photonic bandstructure' method is introduced. The complex bandstructure method facilitates the production of equi-frequency, or dispersion, surfaces [127] which are also presented in this chapter. The type of structures considered here are all two-dimensional photonic crystal structures.

## 4.2 Computational Approaches

The development of the theoretical techniques currently associated with photonic crystals began soon after the realisation that periodic dielectric contrasts could permit the same degree of restriction over the propagation of photons that periodic potentials can provide for electrons. Yablonovitch [14] and John [15] introduced the idea of using photonic crystals to control optical properties to the physics community in 1987. Since then a variety of theoretic-

cal techniques have been, and are continuing to be, developed for the eigen-decomposition of electromagnetic systems. The different methods provide a range of sophisticated approaches for modelling and predicting the behaviour of dielectric systems. Each of the individual approaches are suited to different types of systems or different types of problems [128, 129].

The theoretical techniques employed for the study of photonic crystals fall into four main broad styles of approach. The merits of the individual approaches are introduced in this section. A broad outline of each general approach has been provided, but within each approach there exists a wide range of variations in the actual implementation. Detailed discussion of all the variations is impossible, but references have been included to some of the more common implementations.

### 4.2.1 Scalar Wave Approximation

Early theoretical studies attempted to reformulate the Korringa, Kohn and Rostoker (KKR) method [6] of electronic structure calculation for photonic crystals. The method was modified for the calculation of photonic bandstructures through the use of a scalar wave approximation [130–132]. Later work [133–135] showed that such an approach could produce qualitatively incorrect results. The scalar wave approximation neglected the vector nature of electromagnetic fields. This led to the absence of important symmetry information from the method and consequently the calculations were found to be inadequate. Light propagates as electromagnetic waves and possesses a vector nature which requires full consideration for an accurate understanding of the physical phenomena witnessed in photonic crystals.

### 4.2.2 Frequency Domain Approach

The first approach to be developed utilising the full vector nature of electromagnetic waves expanded the electromagnetic fields into definite frequency states to form a complete basis set [133–136]. The complete set was then truncated to create a linear eigenvalue problem solvable by standard matrix methods. Such approaches are referred to as frequency domain methods and are akin to the nearly free electron model for semiconductors. The photonic crystal method is superior in its accuracy to the nearly free electron method, due to the absence of the electron-electron interactions which exist for electronic systems. When dealing with photonic crystals a larger number of states is usually included, enabling a more

accurate representation of the electromagnetic fields to be achieved. There are a large number of variations of frequency domain photonic crystal calculation methods in the literature [129, 130, 133, 137–147]. The main drawback of the method is that the computational time scales as the cube of the number of states included in the electromagnetic field expansions [137]. This can make the method impractical for complex systems, although to some extent this can be alleviated through the use of a smoothed effective dielectric tensor [148] or effective medium theory [149].

### 4.2.3 Time Domain Approach

The second approach utilising the full vector nature of electromagnetic waves was developed in analogy with the tight binding models for semiconductors and is referred to as the time domain approach. The method utilises the direct simulation of Maxwell's Equations over a discrete grid by finite difference time domain (FDTD) algorithms. These methods compute Fourier transforms of the time-varying response of the system and then analyse the spectrum peaks to locate the eigenvalues. Full descriptions of variations of these time domain methods exist in the literature [150–155]. The methods allow for the production of computational algorithms where the computational time scales linearly with the number of real space points. The high level of efficiency of these methods make them the most appropriate choice when performing calculations based on complex systems.

### 4.2.4 Transfer Matrix Approach

The fourth type of approach is referred to as the transfer matrix method [17, 156–162]. The method is not an eigen-decomposition technique but is of great utility for calculating the transmission through photonic crystal structures. The method computes a transfer matrix which relates the relevant electromagnetic field amplitudes at either end of a unit cell at a constant frequency. The derivation of an individual transfer matrix may be achieved by the application of finite difference, analytical or other methods. The resulting matrix is repeatedly applied to calculate the transmission through structures in a stepwise manner. The photonic crystal method makes use of a similar methodology to that applied in the previous two chapters for the study of multi-layer waveguides.

### 4.3 Plane-wave Methods

The comparative merits of the different theoretical techniques available are dependent on the type of problem being attempted: frequency-domain methods are often used for simple systems due to their computational efficiency and their relative simplicity of implementation; time-domain methods are more efficient for complex structures or the consideration of time dependent problems; whilst transfer matrix methods are appropriate to frequency dependent dielectrics and situations where the structures are divisible into simple components.

The choice of method used here is a frequency domain approach utilising a plane-wave expansion form for the electric and magnetic fields. The method is presented in detail in the following sections therefore only the justification for the method is given here. The main advantages of the plane-wave method are that it forms a stable and reliable algorithm for the calculation of allowed photonic crystal frequencies, and its simplicity and transparency with regard to the underlying physics make it an intuitive method.

The appropriateness of the plane-wave method for this study was also due to its analogy with an electronic structure method which has been extended to the production of complex bandstructure [163]. For the simple systems under consideration the disadvantages of the plane-wave method were not significant enough to outweigh the advantages. The three main disadvantages of standard plane-wave methods are: convergence problems for complex structures; a difficulty dealing with frequency dependent dielectric constants; and the lack of reflection coefficients. These were not anticipated to present significant disadvantages for this study as problems in convergence of the method were not expected due to the simple form of the structures under consideration. The dielectric constants to be dealt with could be assumed to be independent of frequency and the complex plane-wave bandstructure calculation would enable the calculation of the reflection coefficients.

#### 4.3.1 Coordinate System

A consistent cartesian coordinate system is utilised for all the calculations presented in this chapter and throughout the remainder of the thesis. The coordinate system is defined in relation to the two-dimensional photonic crystals for study by the manner demonstrated in Fig. 4.1. The  $x$  axis is defined as the direction parallel to the direction in which there

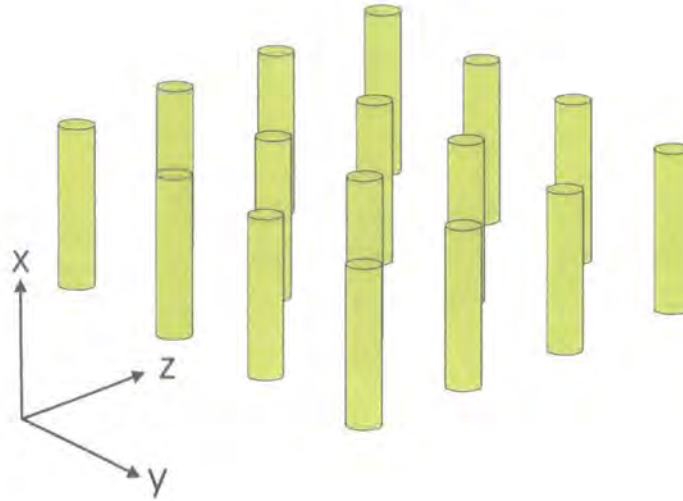


**Figure 4.1:** The coordinate system is defined with the  $x$  axis parallel to the direction of the dielectric rods and the  $y$  and  $z$  directions in the plane of the two-dimensional dielectric constant modulation.

is no variation in dielectric constant, and consequently the  $y$  and  $z$  axis are defined in the plane of the two-dimensional dielectric constant modulation to form a standard right-handed coordinate system. Vectors residing in the  $y$ - $z$  plane may be referred to as existing in an in-plane direction. To aid with notation simplification it is convenient to define a two component in-plane position vector,  $\rho$ , as:

$$\rho = \rho(y, z) \quad . \quad (4.1)$$

## 4.4 Maxwell's Equations

The behaviour of photons in media can be described in full vector form by Maxwell's macroscopic equations of electromagnetism [86]. Maxwell's equations were introduced in Section 2.6.3, where they were given in their most general form by equations (2.9) to (2.12). The generally applicable equations may be applied to specific systems through the use of assumptions based on the type of media under consideration. The system-dependent functions in the equations are the permittivity,  $\epsilon$ , the free charge density,  $\rho$ , and the conductivity,  $\sigma$ . An understanding of how these terms are related to the materials of interest allows equations (2.9) to (2.12) to be written in a form of greater utility for the photonic crystals of interest.

### 4.4.1 Electrical Properties

In general the permittivity involves vector and tensor terms to relate the electric displacement field to the macroscopic electric field. If the permittivity is assumed to be time invariant then the relationship is of the form [13]:

$$\mathbf{D} = \sum_j \epsilon_j \mathbf{E}_j + \sum_{jk} X_{jk} \mathbf{E}_j \mathbf{E}_k + O(\mathbf{E}^3) \quad . \quad (4.2)$$

The field strengths dealt with in this work are assumed to be of low magnitude and consequently a linear regime is applicable. Furthermore, the media being dealt with are both macroscopic and isotropic within each individual region within the structure. The permittivity may also be assumed to be a local function only; non-locality generally results from atomic scale processes that are below the scale of the processes of interest for photonic crystals. This allows the dielectric constant to be taken as scalar and a function of only frequency and position:

$$\mathbf{D}(\mathbf{r}, \omega) = \epsilon(\mathbf{r}, \omega) \mathbf{E}(\mathbf{r}, \omega) \quad . \quad (4.3)$$

The assumption may also be made that a single frequency is appropriate to the system under investigation. The permittivity of each individual material may therefore be assigned a constant value appropriate to the specific frequency of interest. This enables additional simplification through the lifting of any frequency dependence complications. For metallic materials the dielectric constant will be strongly dependent on frequency. For most insulators though any frequency dependence is negligible across selected ranges of frequencies, for example the optical frequency range of interest. It should be noted that this may not be applicable for other frequency regimes, for example the microwave or infra-red regions may possess frequency dependences.

The final assumption regarding the dielectric properties of the materials under consideration is that they are low loss dielectrics. The dielectric constant will then be a purely real quantity with no imaginary component. The final system specific form for the dielectric constant is dependent on position only. It may be separated into a relative permittivity term,  $\epsilon_r$ , and a permittivity of free space term,  $\epsilon_0$ , such that:

$$\mathbf{D}(\mathbf{r}) = \epsilon(\mathbf{r})\mathbf{E}(\mathbf{r}) = \epsilon_0\epsilon_r(\mathbf{r})\mathbf{E}(\mathbf{r}) \quad . \quad (4.4)$$

The photonic crystal structures under consideration will be composed of non-conducting media. This means that both the electric current density,  $\mathbf{J}$ , and the free charge density,  $\rho$ , are zero. Hence,

$$\rho = 0 \quad (4.5)$$

$$\mathbf{J} = 0 \quad . \quad (4.6)$$

#### 4.4.2 Magnetic Properties

Knowledge of the magnetic properties of the dielectric materials being considered allows for similar simplification of the permeability term,  $\mu$ . The term relates the magnetic flux density,  $\mathbf{B}$ , to the magnetic field strength,  $\mathbf{H}$ . Permeability may be described as the degree of magnetisation of a material in response to an applied magnetic field. In a linear regime it may be written that:

$$\mathbf{B}(\mathbf{r}) = \mu_r\mu_0\mathbf{H}(\mathbf{r}) \quad . \quad (4.7)$$

In this expression the permeability term has been separated into a relative permeability term,  $\mu_r$ , and a permeability of free space term,  $\mu_0$ . The relative permeability for all of the materials under consideration will be taken as unity. This is equivalent to the assumption that all the materials are non-magnetic. In this situation the permeability of each individual material is simply that of free space,  $\mu = \mu_0$  and it may be written that  $\mathbf{H} = \mathbf{B}/\mu_0$ .

#### 4.4.3 Maxwell's Equations for Photonic Crystals

The assumptions concerning both the electrical and magnetic nature of the media being considered allows the general form of Maxwell's equations to be written in a simplified form. Equations (4.8) to (4.11) show the revised form of Maxwell's equations specific to the photonic crystals under consideration.

$$\nabla \cdot \mathbf{H} = 0 \quad (4.8)$$

$$\nabla \cdot \mathbf{D} = 0 \quad (4.9)$$

$$\nabla \times \mathbf{E} + \frac{\partial \mathbf{B}}{\partial t} = 0 \quad (4.10)$$

$$\nabla \times \mathbf{H} - \epsilon \frac{\partial \mathbf{E}}{\partial t} = 0 \quad (4.11)$$

The solutions of these equations will be electromagnetic waves propagating with specific frequencies in specific directions. A wavevector, usually referred to as the 'photon wavevector', may be used to describe the propagation direction of a specific solution. In general the photon wavevector,  $\mathbf{K}$ , at a particular frequency, may possess  $x$ ,  $y$  and  $z$  components. For two dimensional structures it is appropriate to define a two-dimensional in-plane photon wavevector,  $\mathbf{k}$ :

$$\mathbf{k}_\omega = \mathbf{k}_\omega(y, z) \quad . \quad (4.12)$$

## 4.5 Plane-wave Expansion

In general, the electric and magnetic field solutions of Maxwell's equations will be functions of both position and time. The linearity of Maxwell's equations allows the time dependence to be factored from the field representations. It may be written as a separate term involving time and frequency. In the previous section the permittivity was assumed to be appropriate for a single specific frequency of interest. The use of a single frequency approach for the solution of Maxwell's equations assists with simplification of the calculation. Using such an approach means that the electromagnetic fields are represented as single frequency functions, normally referred to as harmonic modes. The electromagnetic fields present within a photonic crystal may contain multiple frequencies and it is important to note that the physical fields are not restricted in any manner by adopting this representation for the fields. Any required solution may be assembled as a Fourier series through the use

of the appropriate set of single frequency harmonic modes. Here the field solutions will be restricted to solutions which vary harmonically with time. This is equivalent to a laser source which is commonly used to provide incident light. The concept of plane-waves was introduced in Section 2.6 and gives the following relationships,

$$\begin{aligned} \mathbf{H} \text{ and } \mathbf{E} &\propto e^{-i\omega t} \\ &\propto e^{i\mathbf{k}\cdot\boldsymbol{\rho}} \end{aligned} \quad (4.13)$$

The specific photonic crystal lattice for study is introduced solely through the permittivity term in Maxwell's equations. The use of a plane-wave representation for the electric and magnetic fields makes it appropriate to express the permittivity as a Fourier series also. This allows for simplification later in the calculation due to the common complex exponential terms.

### 4.5.1 Permittivity

Bloch's theorem is a vital theorem for electronic structure calculations [125]. The theorem exploits the periodicity of a system to allow for the simplification of mathematical functions. It is applicable to any system possessing discrete translational symmetry in the direction of interest. The periodic dielectric modulation present in photonic crystals allows Bloch's theorem to be applied. The periodicity of photonic crystals allows it to be written that:

$$\epsilon(\boldsymbol{\rho}) = \epsilon(\boldsymbol{\rho} + \mathbf{R}) \quad (4.14)$$

The vector  $\mathbf{R}$  is any linear combination of the real space primitive lattice vectors that describe the periodicity of the crystal lattice. The primitive lattice vectors will differ for each individual crystal lattice and the method of their calculation is shown in the appropriate following chapters for both the square and hexagonal lattice types.

The final eigenvalue equation produced by the standard bandstructure method makes use of the quantity  $1/\epsilon(\boldsymbol{\rho})$ . This makes it appropriate to adopt a Fourier form of  $1/\epsilon(\boldsymbol{\rho})$  rather than  $\epsilon(\boldsymbol{\rho})$ . It should be noted that the notation  $\epsilon^{-1}$  will be used to refer to  $1/\epsilon$ , rather than

the matrix inverse of  $\epsilon$  written in matrix form. Clarification of the notation is required as alternative methods have shown that the use of the inverse matrix of  $\epsilon$  in the final eigenvalue equation may improve the efficiency of the standard plane-wave method [164–166]. The Fourier series for  $\epsilon^{-1}$  is composed of a summation over two-dimensional reciprocal lattice vectors,  $\mathbf{g}$ :

$$\epsilon^{-1} = \frac{1}{\epsilon(\boldsymbol{\rho})} = \sum_{\mathbf{g}} \epsilon_{\mathbf{g}}^{-1} e^{i\mathbf{g}\cdot\boldsymbol{\rho}} \quad . \quad (4.15)$$

Reciprocal lattice vectors are defined mathematically by equation (4.16), where the vector  $\mathbf{R}$  is any vector connecting any two equivalent lattice points. A lattice point may be taken to be the centre of one of the dielectric rods in the  $y$ - $z$  plane. For example, the centre of each of the circular dielectric rods shown in Fig. 4.1 could represent a lattice point.

$$e^{i\mathbf{g}\cdot\mathbf{R}} = 1 \quad (4.16)$$

## 4.6 Standard Bandstructure Method

Before continuing it is necessary to define the two important polarisations of light relative to the photonic crystal coordinate system. In the literature some variation concerning the labelling of the transverse magnetic (TE) and transverse magnetic (TM) polarisations exists. In this work, the TE polarisation is defined as the polarisation in which the magnetic field has a component only in the direction parallel to the direction of the dielectric rods ( $x$  direction), see Fig 4.2. Correspondingly, TM polarisation is defined as having an electric field component in the  $x$  direction only. In two-dimensional systems, with in-plane incident light, the two polarisations may be dealt with separately, as mixing of the two polarisations only occurs above two dimensions.

### 4.6.1 TE Modes

If the notation  $H_i$  is used to represent the component of  $\mathbf{H}$  in the  $i$  direction then it may be written that:

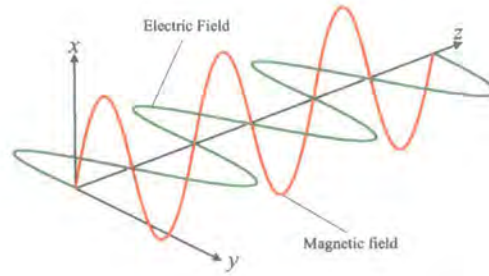


**Figure 4.2:** The electric and magnetic field directions for the transverse electric (TE) polarisation, shown using a single plane-wave. The propagation direction of the electromagnetic wave is the  $z$  direction and the magnetic field has a component in the  $x$  direction only.

$$H_y = H_z = 0 \quad . \quad (4.17)$$

Bloch's theorem [125] states that, since the dielectric constant is periodic in the  $y$ - $z$  plane, the solutions to Maxwell's equations may be represented as the product of a plane-wave term and a function possessing the same underlying periodicity as the dielectric constant. This may be achieved through writing the remaining magnetic field component as a summation over reciprocal lattice vectors:

$$H_x(\rho) = \sum_{\mathbf{g}} H_{\mathbf{g}} e^{i(\mathbf{k}+\mathbf{g})\cdot\rho} \quad . \quad (4.18)$$

### 4.6.2 Brillouin Zone

The use of Bloch's theorem means that allowed frequency solutions for a structure only need to be considered for solutions which lie within a region of reciprocal space known as the first Brillouin Zone (BZ), [7]. The frequency solutions to Maxwell's equations will be dependent on the direction which is under consideration. The direction of interest is normally described in reciprocal space by the photonic wavevector,  $\mathbf{k}$ . The Brillouin Zone is defined as the region in reciprocal space in which these wavevector values are unique solutions to Maxwell's equations. A unique solution is one which is not related to any other solution within the Brillouin Zone by a linear sum of reciprocal lattice vectors. If it were possible to

include an infinite number of reciprocal lattice vectors in the bandstructure calculation then the periodic nature of the structure would mean that the majority of  $\mathbf{k}$  solutions produced by the calculation were equivalent to solutions which existed within the first Brillouin Zone. Hence, it is usual practice to produce bandstructure plots which cover only specific directions within the first Brillouin zone. The plots usually consider the directions of the high symmetry points within the lattice. The labelling of these high symmetry points for the square and hexagonal lattices may be found within the appropriate chapters.

### 4.6.3 Eigenvalue Equation

The standard eigenvalue equation produces eigenvalues which correspond to the allowed frequency solutions dictated by Maxwell's equations. The equation only needs to contain magnetic field terms as the corresponding electric field solutions may be found by substituting the magnetic field back into the original Maxwell's equations. Alternatively, an eigenvalue equation containing only electric field terms could be derived. However, such an approach produces a generalised eigenvalue equation. The generalised eigenvalue equation is numerically a more difficult problem to solve than the simple eigenvalue problem produced by considering the magnetic field. It is possible to produce a simple eigenvalue equation using the electric field however then the operator is non-Hermitian. Proof of the non-Hermitian nature of the electric field eigenvalue operator is reasonably straightforward and available in the literature [13]. In this work an electric field eigenvalue equation is derived in Section 4.11.2 where it forms an aside to the main complex bandstructure calculation.

If the two plane-wave electromagnetic field representations are written with their frequency dependence factored then they are of the form:

$$H_x(y, z, t) = H_x(y, z)e^{-i\omega t} \quad (4.19)$$

$$\mathbf{E}(y, z, t) = \mathbf{E}(y, z)e^{-i\omega t} \quad (4.20)$$

For any solution to be physically valid it must satisfy all four of Maxwell's equations. The two divergence equations,

$$\nabla \cdot \mathbf{H} = \nabla \cdot \mathbf{D} = 0 \quad , \quad (4.21)$$

may be satisfied by the choice of plane-wave field forms which are transverse. Transverse fields have a direction of propagation which is perpendicular to the plane of oscillation. For example, if the magnetic field is given by:

$$\mathbf{H} = \mathbf{a}e^{i\mathbf{k}\cdot\boldsymbol{\rho}}e^{-i\omega t} \quad , \quad (4.22)$$

it will form a transverse wave if,

$$\mathbf{a} \cdot \mathbf{k} = 0 \quad . \quad (4.23)$$

Thus satisfying equation (4.21).

The two remaining Maxwell's equations, (4.10) and (4.11), can be satisfied by deriving the standard plane-wave eigenvalue equation. Equation (4.11) may first be divided by  $\epsilon(\boldsymbol{\rho})$  and then the curl of both sides of the equation taken. From the resultant equation the electric field terms may be removed by the substitution of equation (4.10). The partial derivative with respect to time may be evaluated at this stage due to the time dependence of the  $\mathbf{H}$  field being entirely attributable to the  $e^{-i\omega t}$  factor. The result of these manipulations is the general eigenvalue equation [13]:

$$\nabla \times \left( \frac{1}{\epsilon(\boldsymbol{\rho})} \nabla \times \mathbf{H}(\boldsymbol{\rho}) \right) = \left( \frac{\omega}{c} \right)^2 \mathbf{H}(\boldsymbol{\rho}) \quad . \quad (4.24)$$

The eigenvalue equation is applicable to both the TE and TM modes by the substitution of the appropriate field forms into the equation.

#### 4.6.4 Scaling Law

If equation (4.24) is the eigenvalue equation for a structure fully described by  $\epsilon(\boldsymbol{\rho})$  then the solution of a different problem, where the structure is of the same form but has all its length scales expanded by a factor  $a$ , may be easily deduced. If the substitution:

$$\boldsymbol{\rho}' = \frac{\boldsymbol{\rho}}{a} \quad , \quad (4.25)$$

is made in equation (4.24) then it yields:

$$\nabla' \times \left( \frac{1}{\epsilon(a\rho')} \nabla' \times \mathbf{H}(a\rho') \right) = a^2 \left( \frac{\omega}{c} \right)^2 \mathbf{H}(a\rho') \quad . \quad (4.26)$$

This provides a scaling law as it may be seen that if length scales are expanded by a factor  $a$  then the frequency solutions are reduced from their original values by the same factor  $a$ . The law is valid provided that in the regime of interest the permittivity of the materials forming the structure are independent of frequency. The scaling law is of great utility and assisted with the validation of the principle of photonic crystals. The intended regime of interest for photonic crystals may have always been the optical or infrared length scales. However, experimental investigations at microwave length scales enabled experimental confirmation of the photonic crystal operating principles, whilst lower length scales were still not experimentally viable.

#### 4.6.5 Matrix Methods

Solution of the eigenvalue equation (4.24) may be undertaken by the use of the plane-wave representation adopted for the magnetic field and the Fourier series form adopted for the permittivity. When adopting this approach it is of use to consider the curl of the magnetic field first:

$$\begin{aligned} \nabla \times \mathbf{H} &= \begin{pmatrix} \frac{\partial}{\partial x} \\ \frac{\partial}{\partial y} \\ \frac{\partial}{\partial z} \end{pmatrix} \times \begin{pmatrix} \sum_{\mathbf{g}} H_{\mathbf{g}} e^{i(\mathbf{k}+\mathbf{g}) \cdot \boldsymbol{\rho}} \\ 0 \\ 0 \end{pmatrix} e^{-i\omega t} \\ &= \begin{pmatrix} 0 \\ i \sum_{\mathbf{g}} [\mathbf{k} + \mathbf{g}]_z H_{\mathbf{g}} e^{i(\mathbf{k}+\mathbf{g}) \cdot \boldsymbol{\rho}} \\ -i \sum_{\mathbf{g}} [\mathbf{k} + \mathbf{g}]_y H_{\mathbf{g}} e^{i(\mathbf{k}+\mathbf{g}) \cdot \boldsymbol{\rho}} \end{pmatrix} e^{-i\omega t} \quad . \quad (4.27) \end{aligned}$$

A substitution may now be made for  $\nabla \times \mathbf{H}$  into the eigenvalue equation (4.24). Combining

this substitution with the Fourier form for  $\epsilon^{-1}$  given by equation (4.15) produces:

$$\sum_{\mathbf{g}\mathbf{g}'} \epsilon_{\mathbf{g}'}^{-1} H_{\mathbf{g}} [[\mathbf{k} + \mathbf{g}]_y [\mathbf{k} + \mathbf{g}' + \mathbf{g}]_y + [\mathbf{k} + \mathbf{g}]_z [\mathbf{k} + \mathbf{g}' + \mathbf{g}]_z] e^{i(\mathbf{g}+\mathbf{g}')\cdot\rho} = \frac{\omega^2}{c^2} \sum_{\mathbf{g}''} H_{\mathbf{g}''} e^{i(\mathbf{g}'')\cdot\rho} \quad (4.28)$$

Simplification of the mathematical expression has been achieved through the cancellation of the common  $e^{i\mathbf{k}\cdot\rho}$  and  $e^{i\omega t}$  terms. Coefficients of the exponentials in the equation may be equated to allow the final eigenvalue equation to be expressed as a summation of just two sets of reciprocal lattice vectors. Equating the coefficients leads to  $\mathbf{g} + \mathbf{g}' = \mathbf{g}''$  or  $\mathbf{g}' = \mathbf{g}'' - \mathbf{g}$ . Therefore, for a single  $\mathbf{g}''$  value, it may be written that:

$$\sum_{\mathbf{g}} \epsilon_{\mathbf{g}''-\mathbf{g}}^{-1} H_{\mathbf{g}} [[\mathbf{k} + \mathbf{g}]_y [\mathbf{k} + \mathbf{g}'' ]_y + [\mathbf{k} + \mathbf{g}]_z [\mathbf{k} + \mathbf{g}'' ]_z] = \frac{\omega^2}{c^2} H_{\mathbf{g}''} \quad (4.29)$$

Further simplification may be made by noting that the  $y$  and  $z$  component terms can be replaced by the dot product  $(\mathbf{k} + \mathbf{g}) \cdot (\mathbf{k} + \mathbf{g}'')$ ; this could equally be written in terms of the three dimensional wavevector,  $\mathbf{K}$ , as  $k_x = 0$ . The simplified form of equation (4.29) is:

$$\sum_{\mathbf{g}} \epsilon_{\mathbf{g}''-\mathbf{g}}^{-1} H_{\mathbf{g}} (\mathbf{k} + \mathbf{g}) \cdot (\mathbf{k} + \mathbf{g}'') = \frac{\omega^2}{c^2} H_{\mathbf{g}''} \quad (4.30)$$

The standard way to approach the solution of such an eigenvalue equation is to rewrite the equation in a matrix form. Standard matrix diagonalisation algorithms may then be employed to solve the equation numerically. The individual  $\mathbf{g}''$  terms given by equation (4.30) combine to form the final eigenvalue matrix equation which may be written as:

$$\mathbf{M} (\mathbf{H}_{\mathbf{g}''}) = \frac{\omega^2}{c^2} (\mathbf{H}_{\mathbf{g}''}) \quad (4.31)$$

The matrix elements of  $\mathbf{M}$  are defined by:

$$M_{\mathbf{g}\mathbf{g}''} = \epsilon_{\mathbf{g}''-\mathbf{g}}^{-1} (\mathbf{k} + \mathbf{g}) \cdot (\mathbf{k} + \mathbf{g}'') \quad (4.32)$$

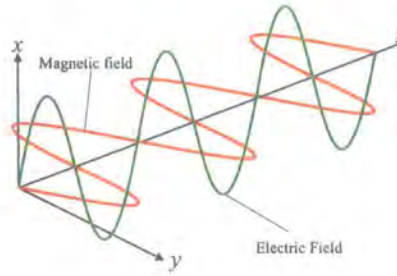


**Figure 4.3:** The electric and magnetic field directions for a single plane-wave of a transverse magnetic (TM) polarisation. The propagation direction of the electromagnetic wave is the  $z$  direction and the electric field has a component in the  $x$  direction only.

Equation (4.31) is applicable to any two-dimensional photonic crystal structure. Solution of the equation requires the specific system of interest to be defined. This is required for the permittivity,  $\epsilon^{-1}$ , and the reciprocal lattice vectors,  $\mathbf{g}_s$ , to be evaluated. Further consideration of the permittivity term may be found in Section 4.8. The reciprocal lattice vectors for the square and hexagonal lattice types may be found in the appropriate following chapters.

#### 4.6.6 TM modes

The eigenvalue equation for the TM modes follows from Maxwell's equations in a similar manner to the TE polarisation eigenvalue equation. The TM polarisation is defined with an electric field directed parallel to the dielectric rods and a magnetic field directed in the in-plane direction. The situation is demonstrated using a single plane-wave in Fig. 4.3. Hence,

$$E_y = E_z = 0 \quad . \quad (4.33)$$

The magnetic field may be represented by a plane-wave basis and in this instance the field will possess two field components,  $H_y$  and  $H_z$ . Writing these as a summation over reciprocal lattice vectors gives:

$$\mathbf{H}_{\mathbf{g}}(\boldsymbol{\rho}) = \sum_{\mathbf{g}} \mathbf{H}_{\mathbf{g}} e^{i(\mathbf{k}+\mathbf{g})\cdot\boldsymbol{\rho}} e^{i\omega t} \quad . \quad (4.34)$$

The conditions imposed by Maxwell's first and second equations, given in equation

(4.21), may be adhered to through the use of transverse plane-waves forms for the fields. The magnetic field must be polarised in a direction perpendicular to the direction of the electric field (the  $x$  direction) and also perpendicular to its own direction of propagation, the  $(\mathbf{k} + \mathbf{g})$  direction. The definition of  $\hat{\mathbf{i}}$  as a unit vector in the  $x$  direction allows the magnetic field direction to be found by evaluating the cross product:

$$(\mathbf{k} + \mathbf{g}) \times \hat{\mathbf{i}} = \begin{pmatrix} 0 \\ [\mathbf{k} + \mathbf{g}]_z \\ -[\mathbf{k} + \mathbf{g}]_y \end{pmatrix} . \quad (4.35)$$

It is convenient to define a unit vector  $\hat{\mathbf{e}}_{\mathbf{g}}$  in the direction of the magnetic field. This may be written as,

$$\hat{\mathbf{e}}_{\mathbf{g}} = \begin{pmatrix} 0 \\ e_y(\mathbf{g}) \\ e_z(\mathbf{g}) \end{pmatrix} , \quad (4.36)$$

where the components of  $\hat{\mathbf{e}}_{\mathbf{g}}$  are given by:

$$e_y(\mathbf{g}) = \frac{[\mathbf{k} + \mathbf{g}]_z}{[(\mathbf{k} + \mathbf{g}) \cdot (\mathbf{k} + \mathbf{g})]^{\frac{1}{2}}} \quad e_z(\mathbf{g}) = \frac{-[\mathbf{k} + \mathbf{g}]_y}{[(\mathbf{k} + \mathbf{g}) \cdot (\mathbf{k} + \mathbf{g})]^{\frac{1}{2}}} .$$

The definition of the unit vector allows for notation simplification when evaluating the cross product in the eigenvalue equation (4.24). The curl of the plane-wave magnetic field form is given by,

$$\begin{aligned} \nabla \times \mathbf{H} &= \sum_{\mathbf{g}} H_{\mathbf{g}} \begin{pmatrix} \frac{\partial}{\partial x} \\ \frac{\partial}{\partial y} \\ \frac{\partial}{\partial z} \end{pmatrix} \times \begin{pmatrix} 0 \\ e_y(\mathbf{g}) e^{i(\mathbf{k} + \mathbf{g}) \cdot \boldsymbol{\rho}} \\ e_z(\mathbf{g}) e^{i(\mathbf{k} + \mathbf{g}) \cdot \boldsymbol{\rho}} \end{pmatrix} e^{-i\omega t} \\ &= \sum_{\mathbf{g}} H_{\mathbf{g}} \begin{pmatrix} e_z(\mathbf{g}) i [\mathbf{k} + \mathbf{g}]_y - e_y(\mathbf{g}) i [\mathbf{k} + \mathbf{g}]_z \\ 0 \\ 0 \end{pmatrix} e^{i(\mathbf{k} + \mathbf{g}) \cdot \boldsymbol{\rho}} e^{-i\omega t} \quad (4.37) \end{aligned}$$

The result may be related back to the original  $x$ ,  $y$  and  $z$  coordinates by the use of the substitution for the unit vector  $\hat{e}_{\mathbf{g}}$  given by equation (4.36):

$$\begin{aligned}\nabla \times \mathbf{H} &= -i \sum_{\mathbf{g}} H_{\mathbf{g}} \begin{pmatrix} \frac{[k+g]_y^2 + [k+g]_z^2}{[(k+g)(k+g)]^{\frac{1}{2}}} \\ 0 \\ 0 \end{pmatrix} e^{i(\mathbf{k}+\mathbf{g}) \cdot \boldsymbol{\rho}} e^{-i\omega t} \\ &= -i \sum_{\mathbf{g}} H_{\mathbf{g}} \begin{pmatrix} |\mathbf{k} + \mathbf{g}| \\ 0 \\ 0 \end{pmatrix} e^{i(\mathbf{k}+\mathbf{g}) \cdot \boldsymbol{\rho}} e^{-i\omega t}\end{aligned}\quad (4.38)$$

The eigenvalue equation (4.24) also makes use of the curl of  $(1/\epsilon(\boldsymbol{\rho})\nabla \times \mathbf{H})$ . Considering this expression with the Fourier form for  $\epsilon$ , given in equation (4.15), yields:

$$\begin{aligned}\frac{\omega^2}{c^2} \sum_{\mathbf{g}''} H_{\mathbf{g}''} e^{i(\mathbf{k}+\mathbf{g}'') \cdot \boldsymbol{\rho}} &= \begin{pmatrix} \frac{\partial}{\partial x} \\ \frac{\partial}{\partial y} \\ \frac{\partial}{\partial z} \end{pmatrix} \times \begin{pmatrix} -i \sum_{\mathbf{g}\mathbf{g}'} \epsilon_{\mathbf{g}'}^{-1} H_{\mathbf{g}} |\mathbf{k} + \mathbf{g}| e^{i(\mathbf{k}+\mathbf{g}+\mathbf{g}') \cdot \boldsymbol{\rho}} \\ 0 \\ 0 \end{pmatrix} \\ &= \begin{pmatrix} 0 \\ \sum_{\mathbf{g}\mathbf{g}'} \epsilon_{\mathbf{g}'}^{-1} H_{\mathbf{g}} [\mathbf{k} + \mathbf{g} + \mathbf{g}']_z |\mathbf{k} + \mathbf{g}| e^{i(\mathbf{k}+\mathbf{g}+\mathbf{g}') \cdot \boldsymbol{\rho}} \\ -\sum_{\mathbf{g}\mathbf{g}'} \epsilon_{\mathbf{g}'}^{-1} H_{\mathbf{g}} [\mathbf{k} + \mathbf{g} + \mathbf{g}']_y |\mathbf{k} + \mathbf{g}| e^{i(\mathbf{k}+\mathbf{g}+\mathbf{g}') \cdot \boldsymbol{\rho}} \end{pmatrix}\end{aligned}\quad (4.39)$$

The common  $e^{i\mathbf{k} \cdot \boldsymbol{\rho}}$  factors may be cancelled and the coefficients of the remaining exponential terms equated. Equating the coefficients gives  $\mathbf{g} + \mathbf{g}' = \mathbf{g}''$ , or  $\mathbf{g}' = \mathbf{g}'' - \mathbf{g}$ , allowing the equation to be written as a summation over just two sets of reciprocal lattice vectors. The  $y$  component of equation (4.39) allows each individual  $\mathbf{g}''$  equation to be written as:

$$\sum_{\mathbf{g}} \epsilon_{\mathbf{g}''-\mathbf{g}}^{-1} H_{\mathbf{g}} [\mathbf{k} + \mathbf{g}'' ]_z |\mathbf{k} + \mathbf{g}| e^{i\mathbf{g}'' \cdot \boldsymbol{\rho}} = \frac{\omega^2}{c^2} H_{\mathbf{g}''} \frac{[\mathbf{k} + \mathbf{g}'' ]_z}{|\mathbf{k} + \mathbf{g}''|} e^{i\mathbf{g}'' \cdot \boldsymbol{\rho}} \quad (4.40)$$

This may be rearranged to give a set of equations for an individual  $\mathbf{g}''$  value:

$$\sum_{\mathbf{g}} \epsilon_{\mathbf{g}''-\mathbf{g}}^{-1} H_{\mathbf{g}} |\mathbf{k} + \mathbf{g}| |\mathbf{k} + \mathbf{g}''| = \frac{\omega^2}{c^2} H_{\mathbf{g}''} \quad . \quad (4.41)$$

This is equivalent to equation (4.30) for the TE mode. The TE mode eigenvalue equation was written in matrix form to aid with the computation of the eigenvalues. Adopting the same approach for the TM mode produces:

$$\mathbf{M} (H_{\mathbf{g}''}) = \frac{\omega^2}{c^2} (H_{\mathbf{g}''}) \quad (4.42)$$

This is of an identical form to the eigenvalue matrix equation for the TE polarisation. However, the individual matrix elements differ from those given for the TE polarisation in equation (4.32). The equivalent matrix elements for the TM polarisation are given by:

$$M_{\mathbf{g},\mathbf{g}''} = \epsilon_{\mathbf{g}''-\mathbf{g}}^{-1} |\mathbf{k} + \mathbf{g}| |\mathbf{k} + \mathbf{g}''| \quad . \quad (4.43)$$

## 4.7 Out of Plane Propagation

The discussion thus far has been concerned with light propagating in the in-plane direction. In Section 4.3.1 the coordinate system was defined for the structures under consideration. Although the dielectric modulation occurs in only two dimensions the structure may be assumed to be infinite in all three dimensions. For this study it is sensible to restrict electromagnetic propagation to the in-plane direction as this will provide the necessary physical effects for investigation without the complication of a three-dimensional wavevector. However, this study would not be complete without acknowledging the possibility of an out of plane, or off-plane, component for the three-dimensional photonic wavevector  $\mathbf{K}$ .

Investigations have shown that both the plane-wave method [167, 168] and the finite difference time domain methods [169] can both still be satisfactorily applied if an out of plane wavevector component exists. However, the calculations become computationally much more expensive. This is particularly true for the plane-wave method where an out of plane component doubles the eigenvalue matrix size [169].

The homogeneity of two-dimensional structures in the out of plane direction means they lack the regions of different dielectric constant which are responsible for the multiple scatterings present in the in-plane direction. Results from other authors have shown that, as the  $k_x$  component of the wavevector is increased, the bands present in the photonic band-structure tend to become increasingly flattened [13]. A flattening of the photonic bands may be detrimental to the effects under consideration here (see Section 4.12.2). A choice of  $k_x = 0$  was made for this reason and also due to the increased computational expense, and increased complexity of the equations if  $k_x \neq 0$ .

## 4.8 Permittivity

The solution of the matrix eigenvalue equation (4.31), or equation (4.42), provides the allowed frequencies for the propagation of electromagnetic modes through a photonic crystal structure. The permittivity term in the equation, together with the set of reciprocal lattice vectors, provides all the information on the type of photonic crystal structure being examined. In this section a method for calculating the dielectric constant pattern created by circular rods running through a uniform background dielectric material is given.

### 4.8.1 Circular Rods

Whilst complex rod designs utilising sharp edges may be used in theoretical studies, the most common rod profile used for experimental structures is circular. The primary reason for this is that sharp edges tend to be smoothed when realised experimentally due to the extreme difficulty in producing perfect straight edges on the length scales appropriate to optical photonic crystals [170]. This relative ease of fabrication combined with the demonstrated large absolute photonic band-gap, for certain lattice types, explains why the vast majority of, although not all, photonic crystals make use of circular rods [170].

The previous sections introduced the concept of representing the inverse permittivity,  $\epsilon^{-1}$ , as a Fourier series. In the general case any regular structure may be represented as a Fourier series by the inclusion of sufficient terms to represent the structure with the required level of accuracy. The general approach for calculating individual terms is a fine grid approach. By imposing a fine grid of points on a real space unit cell the necessary terms for

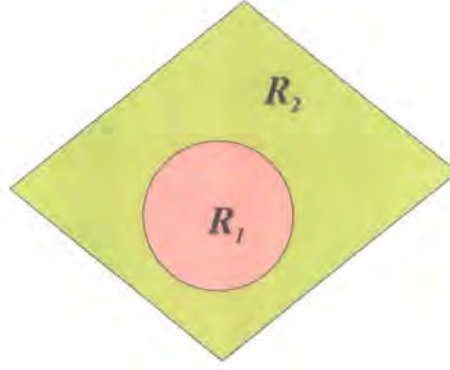


**Figure 4.4:** An arbitrarily shaped unit cell containing a circular dielectric rod of a different refractive index to the homogenous background dielectric. The different colours indicate the different dielectric materials.

the Fourier series may be evaluated by examining the value of the dielectric constant at discrete sampling points. For a structure consisting of circular rods a more accurate analytical method exists for evaluating the Fourier components. The analytical method may be applied to any arbitrarily shaped unit cell provided there is no overlap between the rods.

Consider an arbitrarily shaped unit cell which may be divided into two distinct regions, as shown in Fig. 4.4. The first region,  $R_1$ , encompasses the circular rod, and second region,  $R_2$ , consists of a uniform background dielectric which forms the remainder of the unit cell. The dielectric constants of regions  $R_1$  and  $R_2$  are  $\epsilon_1$  and  $\epsilon_2$ . The notation may be simplified by the use of the notation  $1/\epsilon_1 = \Upsilon_1$  and similarly  $1/\epsilon_2 = \Upsilon_2$ . The two combined regions may be written as a Fourier series summed over the reciprocal lattice vectors,  $\mathbf{g}$ . The series will consist of a set of individual Fourier coefficients, which may be denoted  $\Upsilon_{\mathbf{g}}$ . The total Fourier series, which describes the permittivity across the unit cell, may be written as:

$$\Upsilon(\rho) = \sum_{\mathbf{g}} \Upsilon_{\mathbf{g}} e^{i\mathbf{g}\cdot\rho} \quad . \quad (4.44)$$

The value of an individual coefficient,  $\Upsilon_{\mathbf{G}}$  for example, may be found by multiplying equation (4.44) by  $e^{-i\mathbf{G}\cdot\rho}$  and integrating over the entire unit cell:

$$\int_{\text{unit cell}} d\rho \Upsilon(\rho) e^{-i\mathbf{G}\cdot\rho} = \sum_{\mathbf{g}} \Upsilon_{\mathbf{g}} \int_{\text{unit cell}} d\rho e^{i(\mathbf{g}-\mathbf{G})\cdot\rho} \quad (4.45)$$

The integral on the right-hand side is non-zero only if  $\mathbf{G} = \mathbf{g}$ . This is due to the periodic nature of the system which means that under any other situation the exponential term will cause a zero value to be calculated when integration occurs over the whole unit cell [45]. If  $\mathbf{G} = \mathbf{g}$  then the integral will always give the area of the unit cell,  $A$ . An individual  $\Upsilon_{\mathbf{G}}$  coefficient may therefore be calculated via:

$$\begin{aligned}\Upsilon_{\mathbf{G}} &= \frac{1}{A} \int_{\text{unit cell}} d\rho \Upsilon(\rho) e^{-i\mathbf{G}\cdot\rho} \\ &= \frac{1}{A} \Upsilon_2 \int_{\text{unit cell}} d\rho e^{-i\mathbf{G}\cdot\rho} + \frac{1}{A} (\Upsilon_1 - \Upsilon_2) \int_{\text{rod}} d\rho e^{-i\mathbf{G}\cdot\rho} \quad . \quad (4.46)\end{aligned}$$

Further simplification may be undertaken as the integral over the unit cell will be zero if  $\mathbf{G} \neq 0$  and if  $\mathbf{G} = 0$  then integral is simply the unit cell area,  $A$ . It is of use to define  $A_{rod}$  as the area of  $R_1$  and also  $f$  as the rod area fraction, or photonic crystal fill factor.  $f$  is given by:

$$f = \frac{A_{rod}}{A} \quad (4.47)$$

The fill factor may be used to simplify equation (4.46), allowing it to be rewritten as:

$$\begin{aligned}\Upsilon_{(\mathbf{G}=0)} &= \frac{1}{A} \Upsilon_2 A + \frac{A_{rod}}{A} (\Upsilon_1 - \Upsilon_2) \\ &= (1 - f) \Upsilon_2 + f \Upsilon_1 \quad . \quad (4.48)\end{aligned}$$

If  $\mathbf{G} \neq 0$  then,

$$\Upsilon_{(\mathbf{G}\neq 0)} = \frac{\Upsilon_1 - \Upsilon_2}{A} \int_{\text{rod}} d\rho e^{-i\mathbf{G}\cdot\rho} \quad . \quad (4.49)$$

The previous Fourier expressions are applicable for any arbitrary rod shape. For the circular rod shape under consideration equation (4.49) may be written as [45]:

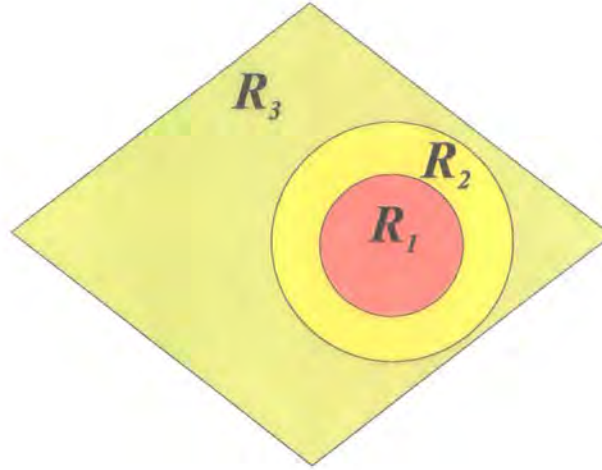


**Figure 4.5:** An arbitrarily shaped unit cell containing a circular dielectric rod, with a coating of a different refractive index, set in a homogenous background dielectric. Different colours indicate different dielectric materials.

$$\Upsilon_{(\mathbf{G} \neq 0)} = (\Upsilon_1 - \Upsilon_2) F \frac{2J_1(GR)}{GR} \quad (4.50)$$

$J_1$  is a Bessel function,  $R$  is the circular rod radius and  $G$  is the magnitude of the reciprocal lattice vector  $\mathbf{G}$ .

A similar method would also be applicable if the unit cell contained features additional to the circular rod. The unit cell could simply be subdivided into additional regions and each considered in turn. The following section discusses such a situation; a unit cell which contains a circular rod with some uniform coating.

### 4.8.2 Coated rods

An extension to the simple circular rod structure occurs when the fabrication technique creates circular rods which are coated in a uniform thickness oxide layer. This is considered as comparisons may then be made with experimental results to verify the computational implementation of our theoretical methods.

The unit cell now has three separate regions corresponding to the three different dielectric constants present in the material. It was previously shown that these may be represented by an overall permittivity function  $\Upsilon (= 1/\epsilon)$ . The function  $\Upsilon$  will now combine the functions  $\Upsilon_1$ ,  $\Upsilon_2$  and  $\Upsilon_3$  representing the three individual regions  $R_1$ ,  $R_2$  and  $R_3$ , as indicated

in Fig. 4.5. In a similar approach to the simple rod situation, the Fourier series form of  $\Upsilon$  may be written as in equation (4.44) and individual  $\mathbf{G}$  terms calculated from equation (4.45). Integration over the unit cell, of area  $A$ , may be performed by considering the three regions separately. If the area of the inner rod is denoted by  $A_1$  and the outer rod by  $A_2$  then

$$\Upsilon_{\mathbf{G}} = \frac{1}{A} \Upsilon_3 \int_{\text{unit cell}} d\rho e^{-i\mathbf{G}\cdot\rho} + \frac{1}{A} (\Upsilon_2 - \Upsilon_3) \int_{\text{rod}} d\rho e^{-i\mathbf{G}\cdot\rho} + \frac{1}{A} (\Upsilon_1 - \Upsilon_2) \int_{\text{rod}} d\rho e^{-i\mathbf{G}\cdot\rho} \quad (4.51)$$

This means that for  $\mathbf{G} = 0$ ,

$$\begin{aligned} \Upsilon_{(\mathbf{G}=0)} &= \frac{1}{A} \Upsilon_3 A + \frac{A_2}{A} (\Upsilon_2 - \Upsilon_3) + \frac{A_3}{A} (\Upsilon_1 - \Upsilon_2) \\ &= (1 - f) \Upsilon_2 + f_2 \Upsilon_2 + f_1 \Upsilon_1 \end{aligned} \quad (4.52)$$

The fraction of the unit cell area covered by region  $R_1$  is denoted  $f_1$ .  $f_2$  is the fraction covered by region  $R_2$  and  $f$  is the fraction covered by region  $R_3$ . The remaining Fourier series terms, when  $\mathbf{G} \neq 0$ , are given by:

$$\Upsilon_{(\mathbf{G} \neq 0)} = \frac{A_2 (\Upsilon_1 - \Upsilon_2)}{A} \int_{\text{rod}} d\rho e^{-i\mathbf{G}\cdot\rho} + \frac{A_2 (\Upsilon_2 - \Upsilon_3)}{A} \int_{\text{rod}} d\rho e^{-i\mathbf{G}\cdot\rho} \quad (4.53)$$

The Bessel function result given in Section 4.8.1 may again be used to provide an analytical evaluation of the integrals, yielding:

$$\Upsilon_{(\mathbf{G} \neq 0)} = (\Upsilon_1 - \Upsilon_2) F_1 \frac{2J_1(GA_1)}{GA_1} + (\Upsilon_2 - \Upsilon_3) F_2 \frac{2J_1(GA_2)}{GA_2} \quad (4.54)$$

## 4.9 Complex Bandstructure

The standard plane-wave bandstructure calculation method, presented in Section 4.6, provides a method for calculating the allowed electromagnetic frequencies within photonic crystal structures. The method requires that the wavevector of interest is well defined for

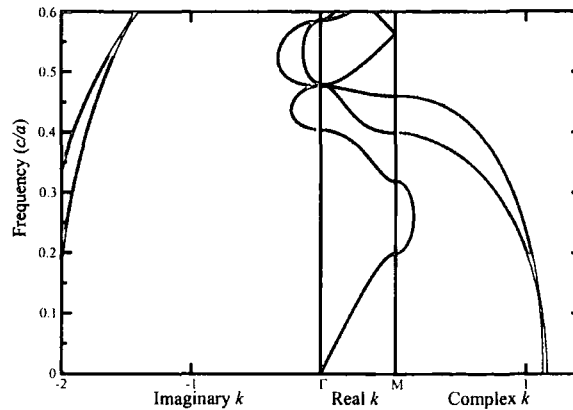


**Figure 4.6:** An example of a complex bandstructure. The example is for the TE polarisation in the  $\Gamma - M$  direction using a hexagonal lattice. Purely real (black), purely imaginary (purple) and general complex (green) solutions are shown.

the frequencies to be computed. Occasions exist when it is of greater utility to be able to fix the incident frequency and calculate the allowed wavevectors for the given frequency. This is equivalent, for example, to a laser source which has a fixed frequency and a beam propagation direction which may be varied.

Methods which allow for the calculation of how a particular frequency varies with wavevector are often referred to as  $\omega(\mathbf{k})$  methods. In this section a plane-wave approach to the fixed frequency problem is described. Two different approaches are presented. The first is derived from an analogy with a semiconductor method available in the literature [163] and the second is based on a method suggested by Prof. M. C. Burt. It is believed that neither of the two approaches have been generally presented in the published literature. Complex bandstructures can be produced by other methods though, for example through the FDTD methods proposed by Pendry [157].

The fixed frequency plane-wave approach has the additional benefit that it allows complex wavevector solutions to be generated in addition to the conventional real solutions. It is for this reason that the methods described are referred to as complex bandstructure calculation methods. Furthermore, the complex solutions are required for the interface matching calculation which is undertaken in Chapter 7.

### 4.9.1 Complex Wavevector

Photonic bandstructures are usually graphical representations of the set of allowed real frequencies for specified real wavevectors within the first Brillouin Zone. A complex bandstructure may be defined as the set of real, imaginary and complex wavevectors which exist within the first Brillouin Zone for specified real frequencies. For an example see Fig. 4.6. The definition of wavevectors which are not purely real as existing within the first Brillouin Zone requires an explanation; a general complex wavevector with an imaginary and real part is defined as existing within the first Brillouin Zone provided that the real component of the wavevector exists within the zone boundaries. The reason for this is that it remains true for complex solutions that wavevectors with a real component outside of the first Brillouin Zone are repeats of solutions within the Zone. The physical interpretation of wavevectors with imaginary components may be inferred from the plane-wave form of the electromagnetic fields. The fields contain an  $e^{i\mathbf{k}\cdot\rho}$  dependence and if an imaginary component of  $\mathbf{k}$  exists then the solution will represent either an increasing or an evanescent solution. The implications of this are considered further in Chapter 7.

## 4.10 Electronic Structure Analogy

Complex bandstructures are a tool originally developed for assisting with electronic structure studies. One of the now standard electronic structure approaches for such a calculation is to separate the Schrödinger equation into individual directional components. The components may then be rearranged to form an eigenvalue equation with eigenvalues which are one of the wavevector components [163]. An equivalent approach is employed in this section for complex photonic bandstructures. The eigenvalue equation (4.31) or (4.42) derived from Maxwell's equations may be split into a directional component form and rearranged to produce the required new eigenvalue equation.

### 4.10.1 TE Mode

The standard photonic crystal eigenvalue equation (4.31) may be rewritten in the following manner,

$$\left( \mathbf{M} - \frac{\omega^2}{c^2} \mathbf{I} \right) (\mathbf{H}_{\mathbf{g}}) = 0 \quad . \quad (4.55)$$

The notation  $\mathbf{I}$  has been used for the identity matrix and  $\mathbf{0}$  for the null matrix. The matrix elements for the TE mode remain those given in equation (4.32):

$$M_{\mathbf{g},\mathbf{g}'} = \epsilon_{\mathbf{g}'-\mathbf{g}}^{-1} (\mathbf{k} + \mathbf{g}) \cdot (\mathbf{k} + \mathbf{g}') \quad (4.56)$$

To assist with the expansion of the the matrix into component form it is convenient to write the matrix elements explicitly in terms of their cartesian components:

$$M_{\mathbf{g},\mathbf{g}'} = \epsilon_{\mathbf{g}'-\mathbf{g}}^{-1} (k_y^2 + k_y g'_y + k_z^2 + k_z g'_z + g_y k_y + g_y g'_y + g_z k_z + g_z g'_z) \quad (4.57)$$

The function is quadratic in terms of either  $k_y$  or  $k_z$ . One of these components must be fixed to allow the other to be calculated. If  $k_z$  is selected as the known component then equation (4.55) needs to be separated into terms involving  $k_z$  and  $k_z^2$ . The  $k_z$  dependence may then be factored to produce the following form for equation (4.55):

$$(\mathbf{M}^0 + k_y \mathbf{M}^1 + k_y^2 \mathbf{I}) (\mathbf{H}_{\mathbf{g}}) = 0 \quad . \quad (4.58)$$

This may be written as a matrix eigenvalue equation with eigenvalues  $k_y$ :

$$\begin{pmatrix} 0 & \mathbf{I} \\ -\mathbf{M}^0 & -\mathbf{M}^1 \end{pmatrix} \begin{pmatrix} \psi \\ \phi \end{pmatrix} = k_y \begin{pmatrix} \psi \\ \phi \end{pmatrix} \quad . \quad (4.59)$$

The individual matrix elements are given by:

$$\begin{aligned}
 M_{\mathbf{g},\mathbf{g}'}^0 &= k_z^2 + k_z (g_y + g'_y) + g_z g'_z + g_y g'_y - INV[\epsilon_{g'-g}^{-1}] \left( \frac{\omega^2}{c^2} \right) \\
 M_{\mathbf{g},\mathbf{g}'}^1 &= g_z + g'_z \\
 \psi_{\mathbf{g}} &= H_{\mathbf{g}} \\
 \phi_{\mathbf{g}} &= k_y H_{\mathbf{g}} \quad .
 \end{aligned} \tag{4.60}$$

The numerical solution of equation (4.59) may be achieved using standard matrix algorithms. The solutions will be real, imaginary and general complex eigenvalues for  $k_y$ , together with the associated eigenvectors for the predefined frequency and  $k_z$  component. It is possible to produce bandstructure diagrams corresponding to those produced by the standard bandstructure method by scanning through  $\omega$  and  $k_z$  values to find the allowed real solutions within the first Brillouin Zone. It should be noted that the matrix eigenvalue equation is twice the dimension of the standard eigenvalue equation leading to at least a factor of eight increase in the computational cost. The computational time is also increased by the non-Hermitian nature of the matrix and by the need to calculate the matrix inverse of the permittivity matrix, denoted  $INV[\epsilon_{g'-g}^{-1}]$ . This arises from the rearrangement of equation (4.55) into the form required for equation (4.58).

### 4.10.2 Directional Bandstructures

In order to solve equation (4.59) a value needs to be fixed for  $k_z$ . This value will be dependent on the defined coordinate system. It is possible for situations to exist when the allowed wavevectors in a specific direction are required, rather than the allowed solutions at a specific  $k_z$  value. The necessity of defining  $k_z$  prohibits such a calculation from being carried out efficiently. An example of such a situation is dispersion surfaces; a dispersion surfaces is an equi-frequency contour plot of allowed solutions for the entire Brillouin Zone. The most efficient method for producing such a diagram is to vary the direction of the wavevector and calculate the magnitude of the vector. This section describes a method which allows the coordinate system imposed restriction on the TE complex bandstructure method to be removed. The approach provides a method for calculating wavevector solutions in any general direction.



### General Direction

A general direction vector may be defined as the direction from the origin to some arbitrary point  $(a, b)$ , where  $a$  and  $b$  are the  $x$  and  $y$  components respectively. The general vector may be used to produce a unit vector  $(p, q)$  in the direction of the point. The unit vector will be given by:

$$(p, q) = \frac{1}{\sqrt{a^2 + b^2}}(a, b) \quad . \quad (4.61)$$

A new set of axes may now be defined in the unit vector direction,  $(p, q)$ , and the direction perpendicular to this,  $(-q, p)$ . Any arbitrary wavevector  $\mathbf{k}$ , with standard  $x$  and  $y$  components, may be defined relative to this new set of axes. The new definition for  $\mathbf{k}$  will have two components  $k$  and  $k^\perp$  where:

$$\mathbf{k} = k(p, q) + k^\perp(-q, p) \quad . \quad (4.62)$$

Similarly to Section 4.10.1 one of the wavevector components,  $k$  or  $k^\perp$ , needs to be defined in order to carry out the complex bandstructure calculation. If  $k^\perp$  is chosen as the known component then the eigenvalue matrix equation (equation (4.61)) becomes:

$$\begin{pmatrix} 0 & \mathbf{I} \\ -\mathbf{M}^0 & -\mathbf{M}^1 \end{pmatrix} \begin{pmatrix} \psi \\ \phi \end{pmatrix} = k \begin{pmatrix} \psi \\ \phi \end{pmatrix} \quad , \quad (4.63)$$

with elements that are dependent on the general direction defined by  $(p, q)$ :

$$\begin{aligned} M_{\mathbf{g}, \mathbf{g}'}^0 &= \frac{1}{(p^2 + q^2)} \left[ p(g_y + g'_y) + q(g_z + g'_z) - \frac{\omega^2}{c^2} \text{INV} [\epsilon_{\mathbf{g}'-\mathbf{g}}^{-1}] \right] \\ M_{\mathbf{g}, \mathbf{g}'}^1 &= \frac{1}{(p^2 + q^2)} \left[ k^\perp (p(g_z + g'_z) - q(g_y + g'_y)) \right. \\ &\quad \left. + (k^\perp)^2 (q^2 + p^2) + (g_y g'_y + g_z g'_z) \right] \\ \psi_{\mathbf{g}} &= H_{\mathbf{g}} \\ \phi_{\mathbf{g}} &= k H_{\mathbf{g}} \end{aligned}$$

Equation (4.63) is of great utility as it allows the wavevector solutions to be found for any general direction. This is achieved by setting  $k^\perp = 0$  and choosing values for  $p$  and  $q$  which give the required direction of interest.

### 4.10.3 TM mode

The electronic structure analogy method for producing complex bandstructures was reliant on the eigenvalue operator existing as a simple algebraic expression in terms of the wavevector and reciprocal lattice vectors. The simple algebraic form for the eigenvalue equation allowed the necessary rearrangements to be made. The eigenvalue matrix components for the TM mode were given in equation (4.43) by:

$$M_{\mathbf{g},\mathbf{g}'} = \epsilon_{\mathbf{g}'-\mathbf{g}}^{-1} |\mathbf{k} + \mathbf{g}| |\mathbf{k} + \mathbf{g}'| \quad . \quad (4.64)$$

The moduli signs in the matrix element prohibit the rearrangement of the element into a form suitable for applying the complex bandstructure approach described in Section 4.10.1. This made an alternative approach necessary for the TM polarisation. The alternative approach is given in Section 4.11.

The approach described in Section 4.10.2 for the TE polarisation was deemed to be the preferred complex bandstructure method, and was employed whenever TE complex bandstructures were required. The preference for this method was due to its exact agreement with the real solutions generated by the standard bandstructure method. Such agreement allowed the correct implementation of the complex bandstructure method to be confirmed without any convergence issues.

## 4.11 Dual Field Approach

The complex bandstructure approach described in this section combines Maxwell's equations in a manner which produces a final eigenvalue equation which solves both the electric and magnetic fields simultaneously. The eigenvalues of the final equation are the allowed wavevector components at a specific frequency. The corresponding eigenvectors are related to the electric and magnetic fields. The approach was suggested by Prof. M.C. Burt,

although it is not believed to have been previously published in the literature. The method is general enough to be applicable for all systems for which the standard plane-wave method is appropriate. For completeness, the dual field complex bandstructure approach described in this section has been applied to both the TE and TM polarisations.

### 4.11.1 Eigenvalue Equation

Section 4.4 made assumptions based on the nature of the dielectrics under consideration. The assumptions allowed Maxwell's equations to be written in the form given by equations (4.8) to (4.11). These equations formed the basis of the standard bandstructure method and also form the starting point for the dual field complex bandstructure method. Maxwell's two divergence equations (equations (4.8) and (4.9)), may be satisfied by the use of transverse plane-wave forms for the electromagnetic fields. This is identical to the manner described for the standard bandstructure method.

The time dependence of the electromagnetic fields is entirely proportional to  $e^{-i\omega t}$ . This allows the derivatives with respect to time in Maxwell's third and fourth equations, (4.10) and (4.11), to be trivially evaluated:

$$\nabla \times \mathbf{E} = i\omega\mu_0\mathbf{H} \quad (4.65)$$

$$\nabla \times \mathbf{H} = -i\omega\epsilon\mathbf{E} \quad (4.66)$$

In a similar manner to the original two-dimensional plane-wave method, the complex bandstructure calculation may be pursued by separating the TM and TE polarisations without the loss of information.

### 4.11.2 TM Mode

The TM mode was defined with  $E_y = E_z = 0$  and accordingly  $H_x = 0$ . If equations (4.65) and (4.66) are separated into component form they may be expressed as:

$$\nabla \times \mathbf{E} = \begin{pmatrix} 0 \\ \frac{\partial E_x}{\partial z} \\ -\frac{\partial E_x}{\partial y} \end{pmatrix} = \begin{pmatrix} 0 \\ i\omega\mu_0 H_y \\ i\omega\mu_0 H_z \end{pmatrix} \quad (4.67)$$

$$\nabla \times \mathbf{H} = \begin{pmatrix} \frac{\partial H_z}{\partial y} - \frac{\partial H_y}{\partial z} \\ 0 \\ 0 \end{pmatrix} = -i\omega\epsilon \begin{pmatrix} E_x \\ 0 \\ 0 \end{pmatrix} \quad (4.68)$$

At a later stage in the calculation a relationship between the field components of  $\mathbf{H}$  and the second derivative of the  $E_x$  field components will be required. This can be evaluated at this point by differentiating the  $y$  and  $z$  components of equation (4.67), with respect to  $z$  and  $y$  respectively. Separating the two components allows the following relationships to be written:

$$\frac{\partial^2 E_x}{\partial z^2} = i\omega\mu_0 \frac{\partial H_y}{\partial z} \quad (4.69)$$

$$\frac{\partial^2 E_x}{\partial y^2} = -i\omega\mu_0 \frac{\partial H_z}{\partial y} \quad (4.70)$$

The curl of the magnetic field (equation (4.68)) contains a single  $x$  component. This may be multiplied by  $-i\omega\mu_0$  to provide an equation in which the left-hand side consists of differentials which form the right-hand side of equations (4.69) and (4.70):

$$-i\omega\mu_0 \left( \frac{\partial H_z}{\partial y} - \frac{\partial H_y}{\partial z} \right) = -\omega^2\mu_0\epsilon E_x \quad (4.71)$$

Previous discussions in Section 4.6.3 explained that whilst it was preferential to use the magnetic field for the standard eigenvalue equation, it was also possible to produce an electric field eigenvalue equation. This can be shown here by the exchange of the differentials on the left hand-side of equation (4.71) with the electric field terms in equations (4.69) and (4.70). This gives:

$$\left( \frac{\partial^2}{\partial y^2} + \frac{\partial^2}{\partial z^2} \right) \mathbf{E} = -\omega^2 \mu_0 \epsilon \mathbf{E} \quad . \quad (4.72)$$

The electric field eigenvalue equation is usually rearranged into the following form (using  $c^2 = 1/\mu_0 \epsilon_0$ ):

$$\left( \frac{\partial^2}{\partial y^2} + \frac{\partial^2}{\partial z^2} \right) \mathbf{E} = -\frac{\omega^2}{c^2} \epsilon_r \mathbf{E} \quad . \quad (4.73)$$

The appearance is similar to the magnetic field eigenvalue equation. However, the relative permittivity term ( $\epsilon_r$ ) on the right-hand side makes the equation a generalised eigenvalue equation. Generalised eigenvalue equations are numerically more intensive to solve. This explains the preference for the use of a magnetic field eigenvalue equation in the standard method. This is an aside to the main complex bandstructure calculation.

A rearrangement of the  $x$  and  $y$  components of equation (4.67) yields:

$$H_y = -\frac{i}{\omega \mu_0} \frac{\partial E_x}{\partial z} \quad (4.74)$$

$$H_z = \frac{i}{\omega \mu_0} \frac{\partial E_x}{\partial y} \quad . \quad (4.75)$$

The dual field complex bandstructure method relies on the simultaneous solution of two sets of equations containing both the electric and magnetic fields. New notation will be introduced for the plane-wave field forms in order to simplify the appearance of the expressions. The plane-wave forms for the field will be written as,

$$E_x \hat{\mathbf{i}} = \sum_{\mathbf{g}} E_{\mathbf{g}} e^{i(\mathbf{k}+\mathbf{g}) \cdot \boldsymbol{\rho}} e^{-i\omega t} \hat{\mathbf{i}} = E_{\mathbf{g},x} e^{-i\omega t} \hat{\mathbf{i}} \quad , \quad (4.76)$$

$$H_z \hat{\mathbf{k}} = \sum_{\mathbf{g}} H_{\mathbf{g}}^z e^{i(\mathbf{k}+\mathbf{g}) \cdot \boldsymbol{\rho}} e^{-i\omega t} \hat{\mathbf{k}} = H_{\mathbf{g},z} e^{-i\omega t} \hat{\mathbf{k}} \quad . \quad (4.77)$$

The notation  $E_{\mathbf{g},x}$  has been used for the  $x$  component of the electric field as reminder that it is a sum over reciprocal lattice vectors. Similar notation has been used for the magnetic

field. The first of the set of simultaneous equations which contribute to the final eigenvalue equation may be directly found by substituting the plane-wave field forms into equation (4.75). This yields:

$$\mu_0\omega H_{\mathbf{g},z}e^{-i\omega t} = -(k_y + g_y)E_{\mathbf{g},x}e^{-i\omega t} \quad . \quad (4.78)$$

Cancelling the common time dependence, this can be rearranged to give:

$$-g_y E_{\mathbf{g},x} - \mu_0\omega H_{\mathbf{g},z} = k_y E_{\mathbf{g},x} \quad . \quad (4.79)$$

The second set of simultaneous equations comes from equation (4.72). Substituting for  $\partial^2 \mathbf{E} / \partial y^2$ , using equation (4.70), gives,

$$-i \frac{\partial H_z}{\partial y} + \frac{1}{\omega\mu_0} \frac{\partial^2 E_x}{\partial z^2} = -\omega\epsilon E_x \quad . \quad (4.80)$$

Use of the plane-wave field forms then yields,

$$(k_y + g_y) H_{\mathbf{g},z} - \frac{1}{\omega\mu_0} (k_z + g_z)^2 E_{\mathbf{g}',x} = -\omega\epsilon E_{\mathbf{g},x} \quad . \quad (4.81)$$

Adopting the Fourier form for the permittivity given by equation (4.15) and using the full field form notation produces

$$\begin{aligned} (k_y + g_y) \sum_{\mathbf{g}} H_{\mathbf{g}}^z e^{i(\mathbf{k}+\mathbf{g})\cdot\rho} - \frac{1}{\omega\mu_0} (k_z + g_z)^2 \sum_{\mathbf{g}} E_{\mathbf{g},x} e^{i(\mathbf{k}+\mathbf{g})\cdot\rho} \\ = -\omega\epsilon_0 \sum_{\mathbf{g}'} \sum_{\mathbf{g}''} \epsilon_{\mathbf{g}''} E_{\mathbf{g},x} e^{i(\mathbf{k}+\mathbf{g}'+\mathbf{g}'')\cdot\rho} \end{aligned} \quad (4.82)$$

It can be seen that the exponential terms may be equated to give  $\mathbf{g} = \mathbf{g}' + \mathbf{g}''$ . This allows the summation on the right-hand side to be written as a single summation. If a single  $\mathbf{g}$  is considered then:

$$(k_y + g_y) H_{\mathbf{g}}^z - \frac{1}{\omega\mu_0} (k_z + g_z)^2 E_{\mathbf{g}} = -\omega\epsilon_0 \sum_{\mathbf{g}'} \epsilon_{\mathbf{g}-\mathbf{g}'} E_{\mathbf{g}} \quad (4.83)$$

The second set of simultaneous equations comes from the following rearranged form of equation (4.83):

$$\frac{(k_z + g_z)^2}{\omega\mu_0} E_{\mathbf{g}} - \omega\epsilon_0 \sum_{\mathbf{g}'} \epsilon_{\mathbf{g}-\mathbf{g}'} E_{\mathbf{g}} - g_y H_{\mathbf{g}}^z = k_y H_{\mathbf{g}}^z \quad . \quad (4.84)$$

The two sets of simultaneous equations (4.79) and (4.84) combine to form the matrix eigenvalue equation:

$$\left( \begin{array}{c|c} -g_y \delta_{\mathbf{g},\mathbf{g}'} & -\mu_0 \omega \delta_{\mathbf{g},\mathbf{g}'} \\ \hline \frac{(k_z + g_z)^2}{\omega\mu_0} \delta_{\mathbf{g},\mathbf{g}'} - \omega\epsilon_0 \epsilon_{\mathbf{g}-\mathbf{g}'} & -g_y \delta_{\mathbf{g},\mathbf{g}'} \end{array} \right) \begin{pmatrix} E_{\mathbf{g}} \\ H_{\mathbf{g}}^z \end{pmatrix} = k_y \begin{pmatrix} E_{\mathbf{g}} \\ H_{\mathbf{g}}^z \end{pmatrix} \quad .$$

It is convenient to write this in the simplified form, given by equation (4.85), to assist with the numerical solution:

$$\begin{pmatrix} \mathbf{H}^{11} & \mathbf{H}^{12} \\ \mathbf{H}^{21} & \mathbf{H}^{22} \end{pmatrix} \begin{pmatrix} \psi \\ \phi \end{pmatrix} = k_y \begin{pmatrix} \psi \\ \phi \end{pmatrix} \quad (4.85)$$

The individual terms in the simplified form are given by:

$$\begin{aligned} H_{\mathbf{g},\mathbf{g}'}^{11} &= -g_y \delta_{\mathbf{g},\mathbf{g}'} \\ H_{\mathbf{g},\mathbf{g}'}^{12} &= -\mu_0 \omega \delta_{\mathbf{g},\mathbf{g}'} \\ H_{\mathbf{g},\mathbf{g}'}^{21} &= \frac{(k_z + g_z)^2}{\omega\mu_0} \delta_{\mathbf{g},\mathbf{g}'} - \omega\epsilon_0 \epsilon_{\mathbf{g}-\mathbf{g}'} \\ H_{\mathbf{g},\mathbf{g}'}^{22} &= -g_y \delta_{\mathbf{g},\mathbf{g}'} \\ \psi_{\mathbf{g}} &= E_{\mathbf{g}} \\ \phi_{\mathbf{g}} &= H_{\mathbf{g}}^z \quad . \end{aligned}$$

The method described in this section represents our only available plane-wave complex bandstructure method for the TM polarisation and has been used to provide the TM results given in the following chapters.

### 4.11.3 TE Polarisation

The derivation of an eigenvalue equation to allow the  $k_y$  components for the TE polarisation to be calculated follows in a similar manner to that employed for the TM polarisation. Two sets of eigenvalue value equations are required, which allow Maxwell's equations to be simultaneously solved for both the electric and magnetic fields.

The TE mode is defined as having a magnetic field in the  $x$  direction only and electric field components in the  $y$  and  $z$  directions. The  $e^{-i\omega t}$  time dependence of plane-waves allows Maxwell's third and fourth equations (Equations (4.10) and (4.11)) to be written in the following manner,

$$\nabla \times \mathbf{H} = \begin{pmatrix} 0 \\ \frac{\partial H_x}{\partial z} \\ -\frac{\partial H_x}{\partial y} \end{pmatrix} = \begin{pmatrix} 0 \\ -i\omega\epsilon E_y \\ -i\omega\epsilon E_z \end{pmatrix} \quad (4.86)$$

$$\nabla \times \mathbf{E} = \begin{pmatrix} \frac{\partial E_z}{\partial y} - \frac{\partial E_y}{\partial z} \\ 0 \\ 0 \end{pmatrix} = i\omega\mu_0 \begin{pmatrix} H_x \\ 0 \\ 0 \end{pmatrix} \quad (4.87)$$

A rearrangement of the  $y$  component of equation (4.86) permits the  $y$  component of the electric field to be written in terms of the magnetic field,

$$E_y = \frac{i}{\omega\epsilon} \frac{\partial H_x}{\partial z} \quad (4.88)$$

Correspondingly, for the  $z$  component,

$$E_z = -\frac{i}{\omega\epsilon} \frac{\partial H_x}{\partial y} \quad (4.89)$$

If equation (4.88) is substituted into the  $x$  component of equation (4.87) the resultant equation is:

$$\frac{\partial E_z}{\partial y} - \frac{\partial}{\partial z} \left( \frac{i}{\omega \epsilon} \frac{\partial H_x}{\partial z} \right) = i\omega \mu_0 H_x \quad , \quad (4.90)$$

which is equivalent to,

$$-i \frac{\partial E_z}{\partial y} - \frac{1}{\omega} \frac{\partial}{\partial z} \left( \frac{1}{\epsilon} \frac{\partial H_x}{\partial z} \right) = \omega \mu_0 H_x \quad . \quad (4.91)$$

The plane-wave field forms for the TE polarisation are

$$E_z \hat{\mathbf{k}} = \sum_{\mathbf{g}} E_{\mathbf{g}}^z e^{i(\mathbf{k}+\mathbf{g}) \cdot \boldsymbol{\rho}} e^{-i\omega t} \hat{\mathbf{k}} = E_{\mathbf{g},z} e^{-i\omega t} \hat{\mathbf{k}} \quad , \quad (4.92)$$

$$H_x \hat{\mathbf{i}} = \sum_{\mathbf{g}} H_{\mathbf{g}} e^{i(\mathbf{k}+\mathbf{g}) \cdot \boldsymbol{\rho}} e^{-i\omega t} \hat{\mathbf{i}} = H_{\mathbf{g},x} e^{-i\omega t} \hat{\mathbf{i}} \quad . \quad (4.93)$$

Use of the plane-wave field forms in equation (4.91), together with equating the exponential coefficients, provides the following expression for an individual  $\mathbf{g}$ :

$$(k_y + g_y) E_{\mathbf{g}}^z + \frac{1}{\omega} (k_z + g_z) \sum_{\mathbf{g}'} \epsilon_{\mathbf{g}-\mathbf{g}'}^{-1} (k_z + g'_z) H_{\mathbf{g}} = \mu_0 \omega H_{\mathbf{g}} \quad . \quad (4.94)$$

Since  $c^2 = 1/\mu_0 \epsilon_0$  equation (4.94) may be rearranged to form the first of the two sets of simultaneous electric and magnetic eigenvalue equations. For a single  $\mathbf{g}$ :

$$\begin{aligned} (k_y + g_y) E_{\mathbf{g}}^z + \frac{1}{\omega/c} (k_z + g_z) \sum_{\mathbf{g}'} \epsilon_{\mathbf{g}-\mathbf{g}'}^{-1} (k_z + g'_z) H_{\mathbf{g}} \sqrt{\frac{\mu_0}{\epsilon_0}} \\ = \frac{\omega}{c} \sqrt{\frac{\mu_0}{\epsilon_0}} \mu_0 H_{\mathbf{g}} \quad . \end{aligned} \quad (4.95)$$

The second set of simultaneous equations comes directly from the use of the plane-wave field forms in equation (4.89). If the coefficients of the exponentials are equated then, for a single  $\mathbf{g}$ :

$$(k_y + g_y) \sqrt{\frac{\mu_0}{\epsilon_0}} H_{\mathbf{g}} = \frac{\omega}{c} \sum_{\mathbf{g}'} \epsilon_{\mathbf{g}-\mathbf{g}'} E_{\mathbf{g}}^z \quad (4.96)$$

To produce the required form of the eigenvalue equation the  $y$  wavevector component must be separated from the other terms and relocated to the right hand side:

$$-g_y \sqrt{\frac{\mu_0}{\epsilon_0}} H_{\mathbf{g}} + \frac{\omega}{c} \sum_{\mathbf{g}'} \epsilon_{\mathbf{g}-\mathbf{g}'} E_{\mathbf{g}}^z = k_y \sqrt{\frac{\mu_0}{\epsilon_0}} H_{\mathbf{g}} \quad (4.97)$$

The first set of equations, given by equation (4.95), must also be written in a similar form with the  $y$  component of the wavevector on the right hand side. Undertaking this rearrangement yields

$$\frac{\omega}{c} \sqrt{\frac{\mu_0}{\epsilon_0}} H_{\mathbf{g}} - \frac{1}{\omega/c} (k_z + g_z) \sum_{\mathbf{g}'} \epsilon_{\mathbf{g}-\mathbf{g}'}^{-1} (k_z + g'_z) \sqrt{\frac{\mu_0}{\epsilon_0}} H_{\mathbf{g}} - g_y E_{\mathbf{g}}^z = k_y E_{\mathbf{g}}^z \quad (4.98)$$

Equations (4.97) and (4.98) may be combined to form the TE matrix eigenvalue equation,

$$\left( \begin{array}{c|c} -g_y \delta_{\mathbf{g},\mathbf{g}'} & \frac{\omega}{c} \delta_{\mathbf{g},\mathbf{g}'} - \frac{1}{\omega/c} (k_z + g_z) \epsilon_{\mathbf{g}-\mathbf{g}'}^{-1} (k_z + g'_z) \\ \hline \frac{\omega}{c} \epsilon_{\mathbf{g}-\mathbf{g}'} & -g_y \delta_{\mathbf{g},\mathbf{g}'} \end{array} \right) \begin{pmatrix} E_{\mathbf{g}}^z \\ \sqrt{\frac{\mu_0}{\epsilon_0}} H_{\mathbf{g}} \end{pmatrix} = k_y \begin{pmatrix} E_{\mathbf{g}}^z \\ \sqrt{\frac{\mu_0}{\epsilon_0}} H_{\mathbf{g}} \end{pmatrix} \quad (4.99)$$

This may be written in a more convenient form for numerical solution as:

$$\begin{pmatrix} \mathbf{H}^{11} & \mathbf{H}^{12} \\ \mathbf{H}^{21} & \mathbf{H}^{22} \end{pmatrix} \begin{pmatrix} \psi \\ \phi \end{pmatrix} = k \begin{pmatrix} \psi \\ \phi \end{pmatrix} \quad (4.100)$$

With matrix elements which are given by:

$$\begin{aligned} H_{\mathbf{g},\mathbf{g}'}^{11} &= -g_y \delta_{\mathbf{g},\mathbf{g}'} \\ H_{\mathbf{g},\mathbf{g}'}^{12} &= \frac{\omega}{c} \delta_{\mathbf{g},\mathbf{g}'} - \frac{1}{\omega/c} (k_z + g_z) \epsilon_{g-g'}^{-1} (k_z + g'_z) \end{aligned} \quad (4.101)$$

$$\begin{aligned} H_{\mathbf{g},\mathbf{g}'}^{21} &= \frac{\omega}{c} \epsilon_{\mathbf{g}-\mathbf{g}'} \delta_{\mathbf{g},\mathbf{g}'} \\ H_{\mathbf{g},\mathbf{g}'}^{22} &= -g_y \delta_{\mathbf{g},\mathbf{g}'} \\ \psi_{\mathbf{g}} &= E_{\mathbf{g}}^z \\ \phi_{\mathbf{g}} &= \sqrt{\frac{\mu_o}{\epsilon_o}} H_{\mathbf{g}} \end{aligned} \quad (4.102)$$

#### 4.11.4 Directional Bandstructure

The dual field complex bandstructure method requires that the wavevector component  $k_z$  is fixed. The only specific direction which may be considered using this approach is the  $y$  direction, by setting  $k_z = 0$ . There are two possible approaches which would allow for a more general method, where arbitrary directions could be considered. The first, and preferred method, would be a change of coordinate system, similar to that adopted for electronic structure analogy method in section 4.10.2. The alternative approach would be to rotate the permittivity Fourier components and the reciprocal lattice vectors. This would effectively leave the equations alone but rotate the structure being examined. The  $y$  and  $z$  axes would remain in their original directions and the structure would be rotated so that the required direction of interest lay in the same direction as the  $y$  axis. The rotated coordinate system needs to be used in both the calculation of the Fourier components and the reciprocal lattice vectors. If the coordinate system is rotated by an angle  $\theta$  to the  $x$  axis, then the new coordinates ( $y'$ ,  $z'$ ) may be calculated from the original coordinates by use of the rotation matrix:

$$\begin{pmatrix} y' \\ z' \end{pmatrix} = \begin{pmatrix} \cos(\theta) & -\sin(\theta) \\ \sin(\theta) & \cos(\theta) \end{pmatrix} \begin{pmatrix} y \\ z \end{pmatrix} \quad (4.103)$$

The reciprocal lattice vectors and Fourier component rotation method was implemented for the dual field complex bandstructure method as no appropriate coordinate transformation method was found.

## 4.12 Refraction Law

When light passes from one medium to another the light is refracted due to the different phase velocities of electromagnetic waves propagating in the different materials. This section considers the refraction of an incoming plane-wave travelling in air and incident on an interface with a photonic crystal structure. The method described utilises dispersion surfaces which may be calculated using the  $\omega(\mathbf{k})$  methods described in the previous sections. The refraction of light at an interface between two uniform materials is considered prior to the consideration of an interface with a photonic crystal interface. The uniform materials may be thought of as special cases of photonic crystals with negligible radius rods. The uniform material case is considered as it allows a possibly unfamiliar approach to the refraction of light to be presented in comparison to the relatively intuitive uniform material case. Photonic crystals are then dealt with using an identical method with relative ease.

### 4.12.1 Uniform Media

Consider a plane-wave propagating in a uniform material with an isotropic refractive index  $n_1$ . The wave is incident on another uniform material, with isotropic refractive index  $n_2$ . This is shown schematically in Fig. 4.7. The incident plane-wave has a frequency  $\omega$  and strikes the interface at an angle  $\theta_1$  to the normal. If the wavelength of the wave is  $\lambda_1$ , prior to the interface, the altered wavelength within the second material,  $\lambda_2$ , is given by:

$$\lambda_2 = \frac{\lambda_1}{n_2} \quad . \quad (4.104)$$

The law of refraction for an interface between two uniform media is the familiar Snell's Law. The law is the condition for the phase velocity tangential to the interface to remain the same for the both the incident and refracted waves. Its usual form is

$$n_1 \sin(\theta_1) = n_2 \sin(\theta_2) \quad . \quad (4.105)$$

The absence of a single constant refractive index in photonic crystals makes it appropriate to reformulate the refraction law as a conservation of momentum problem. The de

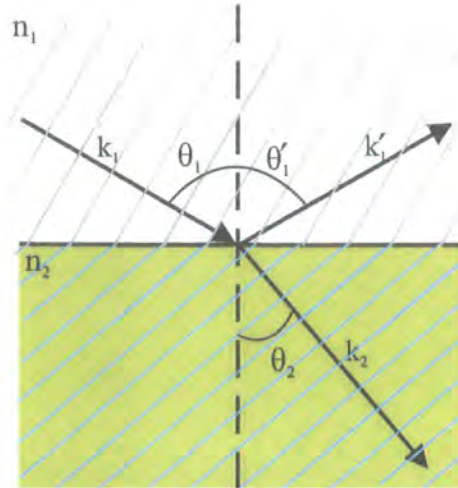


**Figure 4.7:** Conservation of phase at the interface between two uniform materials. Equi-phase lines are shown for the propagating light within both materials.

Broglie equation [171] means that the conservation of photon momentum for any situation is equivalent to the conservation of the photon wavevector. The two uniform material system possesses translational symmetry in the direction parallel to the interface, hence the photon wavevector must be conserved in this direction. If the incident plane-wave wavevector is denoted as  $k_1$ , the reflected wavevector as  $k_1'$  and the refracted wavevector as  $k_2$ , then the wavevector magnitudes are given by:

$$|k_1| = \frac{n_1\omega}{c} = |k_1'| \quad (4.106)$$

$$|k_2| = \frac{n_2\omega}{c} \quad (4.107)$$

The conservation of momentum means that the tangential wavevector components of all three wavevectors must be equal, therefore

$$\frac{n_1\omega}{c} \sin(\theta_1) = \frac{n_1\omega}{c} \sin(\theta_1') = \frac{n_2\omega}{c} \sin(\theta_2) \quad (4.108)$$

If the common  $\omega/c$  term is cancelled then the equation is equivalent to the familiar form of Snell's Law, which was given by equation (4.105). Fig. 4.8 shows a graphical interpretation of the conservation of wavevector approach. A construction line has been added to aid with

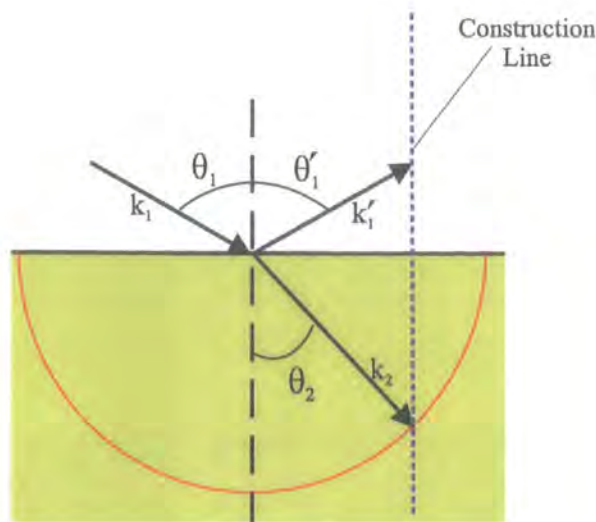


**Figure 4.8:** Refraction at an interface between two uniform materials. The equi-frequency curve within the second material is indicated. A construction line is included to assist with conserving the wavevector component parallel to the interface.

the conservation of the wavevector component parallel to the interface. The figure shows the range of possible refracted wavevectors through the use of a semi-circle with a radius which is the magnitude of the allowed refracted wavevector at the incident frequency. The required actual refracted wavevector may be calculated by simply tracing a line from the incident point to the intersection of the conservation of wavevector construction line and the equi-frequency curve.

The direction of propagation of the refracted light is not, by necessity, in an identical direction to the refracted wavevector direction. The directions are identical for uniform materials, due to the refracted wavevector direction coinciding with the direction of propagation of the radial energy. The direction of propagation of the energy velocity dictates the direction of propagation of the refracted wave. This may be shown to be equivalent to the group velocity of the refracted wave. The rigorous proof of this is lengthy and can be found reproduced in the literature by Sakoda [172]. The group velocity for a general refracted wave may be calculated from

$$\mathbf{v}_i^g = \frac{\partial \omega}{\partial k_i} \quad (4.109)$$

The expression for the group velocity gives a direction which is equivalent to the normal of the equi-frequency curve. The circular nature of the equi-frequency surface for the uniform material shown in Fig. 4.8 gives a group velocity in the same direction as the refracted wavevector,  $\mathbf{v}_2^g = c/n_2 \hat{\mathbf{k}}_2$ .

### 4.12.2 Superprisms

The wavevector conservation approach, adopted in Section 4.13.1 for the calculation of the refraction properties of uniform materials is equally applicable to photonic crystals. Consider a plane-wave travelling in any uniform dielectric, for example air, with a wavevector  $\mathbf{k}_1$  and a frequency  $\omega$ . The wave may then be incident on an interface between the uniform material and a photonic crystal, shown in Fig. 4.9. The angle of incidence of the plane-wave is denoted  $\theta_1$ . In a similar manner to the approach utilised for two uniform materials, the incident wavevector component parallel to the interface must be conserved. This is depicted with a construction line on the diagram. The refracted wavevector may then be calculated by examining the intersection of this construction line and the equi-frequency line forming the dispersion surface, at the appropriate frequency,  $\omega$ .

The dispersion surface at a particular  $\omega$  may be produced by plotting the bandstructure of the photonic crystal using an  $\omega(\mathbf{k})$  method. In this work one of the complex bandstructure methods previously described in this chapter will be used for this purpose. In an identical manner to that previously considered for the uniform media case; the direction of the group velocity of the transmitted wave will be given by the normal to the equi-frequency curve. In this instance the dispersion surface of a photonic crystal may be highly anisotropic. Such anisotropy may produce wide variations in the angle of refraction for small changes in the incident wavevector direction. This is the origin of the superprism behaviour under investigation in the following chapters.

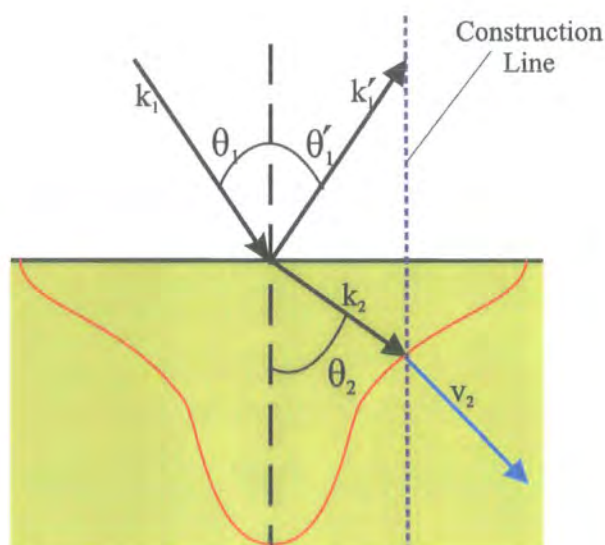


**Figure 4.9:** Photonic crystal refraction law. The allowed  $k$  vectors in the photonic crystal are given by the equi-frequency contour line (red), with the propagation direction given by the group velocity of the wave (blue), which is normal to the contour.

## 4.13 Summary

The standard plane-wave method is a well established approach for the calculation of photonic crystal bandstructures. The method permits the calculation of the allowed frequencies of electromagnetic waves within a photonic crystal for a fixed photonic wavevector,  $\mathbf{k}$ . In this chapter similar plane-wave methods were employed for the calculation of another type of bandstructure, known as a complex bandstructure. The complex bandstructure methods described provides the ability to calculate allowed wavevector solutions at a constant frequency. The method was reformulated to allow for any general direction within the photonic crystal to be considered. This ability is essential for the production of equi-frequency, or dispersion, surfaces. Dispersion surfaces are fundamental to the calculation of the angles of refraction for light incident on photonic crystals. A method for the calculation of photonic crystal refraction angles was also introduced in this chapter. The complex bandstructure methods shown are not available in the literature, as the work presented here represents their first implementation. They may be used in both the calculation of refraction angles and the calculation of transmission through photonic crystal interfaces. These two applications are discussed in the appropriate following chapters.

# Chapter 5

## Square Lattice Calculations

### 5.1 Introduction

In this chapter photonic structures which make use of an underlying square lattice are investigated. The square lattice is the simplest dielectric constant pattern which may be employed to form a two-dimensional photonic crystal. The photonic structures studied here differ from those previously considered, in Chapters 2 and 3, in two main respects: firstly, the dielectric constant modulation occurs in two-dimensions, compared to the previous single dimension and secondly, the modulation is now periodic, thus forming a regular two-dimensional lattice. The square lattice is a natural starting point for studies on photonic crystals due to its simplicity. In this work the square lattice system is used as an initial simple example, prior to the application of the theoretical methods to the hexagonal lattice. The square lattice is also considered due to its ease of incorporation into the interface matching calculation described in Chapter 7.

Theoretical and experimental studies which examine photonic crystals based on the square lattice type are available in the literature [169, 173–186]. Comparisons may be made with these studies to confirm that the previously described theoretical methods have been implemented correctly.

The square lattice is introduced in this chapter with its standard bandstructures and electric field profiles. These graphical representations of the solutions to Maxwell's equations allow for a discussion of the physical origin of the photonic band-gaps often associated with photonic crystals. The majority of the results presented are for a systematic study

conducted on the anisotropy of square lattice bandstructures. The study aims to optimise anisotropy with respect to refractive index contrast, rod radius and frequency. Bandstructure anisotropy is responsible for differences between the refraction properties of photonic crystals and those of uniform media. Finally, conclusions are reached regarding the suitability of the square lattice for refraction applications.

## 5.2 Square Lattice

A square lattice may be produced by the alignment of parallel dielectric rods, equally spaced in both the  $y$  and  $z$  directions, within some background dielectric. There are two main methods of fabrication for such structures; either high refractive index rods may be inserted into a low refractive index background, or low refractive index rods may be etched into a high refractive index background. Fig. 5.1 schematically shows a two-dimensional square lattice constructed using the former approach.

To carry out a bandstructure calculation the complete set of reciprocal lattice vectors for the lattice of interest must be known. For any lattice type these may be constructed from the primitive reciprocal lattice vectors of the given lattice. The primitive reciprocal lattice vectors are the smallest possible vectors pointing from one lattice point to another in reciprocal space. It is also possible to define a primitive unit cell as the smallest periodically repeating unit which can form the complete lattice.

The coordinate system was defined in the previous chapter. If  $\hat{i}$ ,  $\hat{j}$  and  $\hat{k}$  are unit vectors in the  $x$ ,  $y$  and  $z$  directions then a general real-space lattice consisting of two-dimensional square lattice planes separated by some arbitrary distance,  $c$ , may be defined in three-dimensions by the vectors  $\mathbf{a}$ ,  $\mathbf{b}$  and  $\mathbf{c}$ . The defining vectors are of the form:

$$\begin{aligned} \mathbf{a} &= c\hat{i} \\ \mathbf{b} &= a\hat{j} \\ \mathbf{c} &= a\hat{k} \end{aligned} \quad (5.1)$$

The lattice constant  $a$  is the same in both the  $y$  and  $z$  directions. In real space the in-plane lattice vectors,  $\mathbf{R}$ , may be used to describe the two-dimensional square lattice. The lattice

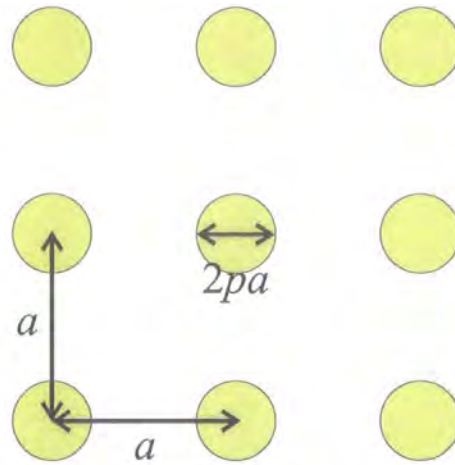


**Figure 5.1:** The two-dimensional square lattice type with lattice constant  $a$  and rods of radius  $pa$ . Four unit cells are shown each consisting of four shared lattice points. The section shown forms part of an infinite repeating lattice in both directions.

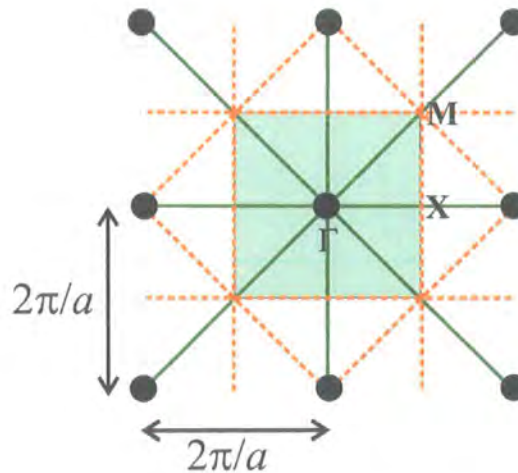


**Figure 5.2:** Reciprocal space showing the Brillouin Zone (light green) for the square lattice type with lattice constant  $a$ . Construction lines are shown (as described in the text) with reciprocal lattice vectors shown in green and their bisectors indicated by the dashed orange lines.

vectors are given by:

$$\mathbf{R} = a \left( n_y \hat{\mathbf{j}} + n_z \hat{\mathbf{k}} \right) \quad . \quad (5.2)$$

The use of two infinite integer sets,  $n_y$  and  $n_z$ , allows the entire lattice to be described by equation (5.2). In reciprocal space the corresponding reciprocal lattice vectors,  $\mathbf{g}$ , may be written as

$$\mathbf{g} = \frac{2\pi}{a} \left( n'_y \hat{\mathbf{j}} + n'_z \hat{\mathbf{k}} \right) \quad , \quad (5.3)$$

with  $n'_y$  and  $n'_z$  as integers. Equation (4.16) gave an expression which assists with the definition of reciprocal lattice vectors. It may be seen that equations (5.2) and (5.3) are consistent with this since

$$\mathbf{g} \cdot \mathbf{R} = \frac{2\pi}{a} a \left( n'_y n_y + n'_z n_z \right) = 2n\pi \quad , \quad (5.4)$$

where  $n$  is clearly an integer.

The square lattice has a single circular rod per unit cell, with radius  $pa$ , and the square lattice fill factor may be written as,

$$f = \frac{\text{rod area}}{\text{unit cell area}} = \frac{\pi p^2 a^2}{a^2} = \pi p^2 \quad . \quad (5.5)$$

### 5.2.1 Brillouin Zone

The discrete translational symmetry possessed by photonic crystals led to the introduction of the Brillouin Zone concept in Section 4.6.2. A graphical method for defining the square lattice Brillouin Zone is shown in Fig. 5.2. The Brillouin Zone has been constructed by drawing perpendicular bisectors to all reciprocal lattice vectors which begin at the origin. The resultant enclosed region containing the lattice point at the origin is the Brillouin Zone. The zone is indicated by the shaded region in Fig. 5.2 which extends from  $-\pi/a$  to  $\pi/a$  in both the  $y$  and  $z$  directions.

The allowed frequency solutions for a photonic crystal are often represented graph-

ically as bandstructures. In such a diagram it is usual to eliminate redundancy by only showing solutions which occur within the Brillouin Zone. Solutions are usually shown in the directions of the high symmetry points  $\Gamma - X$ ,  $\Gamma - M$  and  $X - M$ , these are indicated in Fig. 5.2. The coordinates of the points are given by:

$$\begin{aligned}\Gamma &= \frac{2\pi}{a}(0, 0) \\ X &= \frac{2\pi}{a}(0.5, 0) \\ M &= \frac{2\pi}{a}(0.5, 0.5) \quad .\end{aligned}$$

### 5.3 Convergence

In Section 4.5.1 it was stated that the dielectric constant was expanded as a Fourier series, also referred to as an expansion in plane-waves. The nature of most Fourier expansions means that they have an infinite number of terms. In practice for computational methods the Fourier series requires truncation so that the calculation is possible using a finite number of plane-waves. The higher the number of terms present the more accurately the series represents the original function. The smaller the number of terms included the less computational time is required for a solution to be calculated. The computational time required to diagonalise the operator matrix varies with the cube of the matrix size and thus significant savings in computational time are achievable by choosing the lowest number of plane-waves that is acceptable.

The convergence of the first six frequency bands was considered for an alumina rod in air system. The particular choice of system was made to allow for comparison with corresponding values available in the literature. This may be found in Section 5.4. Convergence was investigated by considering the percentage difference between a frequency solution at a specific number of plane-waves and the same frequency solution considered for a large number (1389) of plane-waves. Fig 5.3 shows convergence for both TE (Fig. 5.3a) and TM (Fig. 5.3b) modes at the  $\Gamma$  point ( $r = 0.2a$ ). The figure also shows the convergence at all the high symmetry points (Fig. 5.3c) and for a range of fill factors (Fig. 5.3d). The results indicate that a choice of 793 plane-waves is sufficient for the calculation of numerical values. At this level, convergence is to within approximately 1% of the 1389 plane-wave solution.

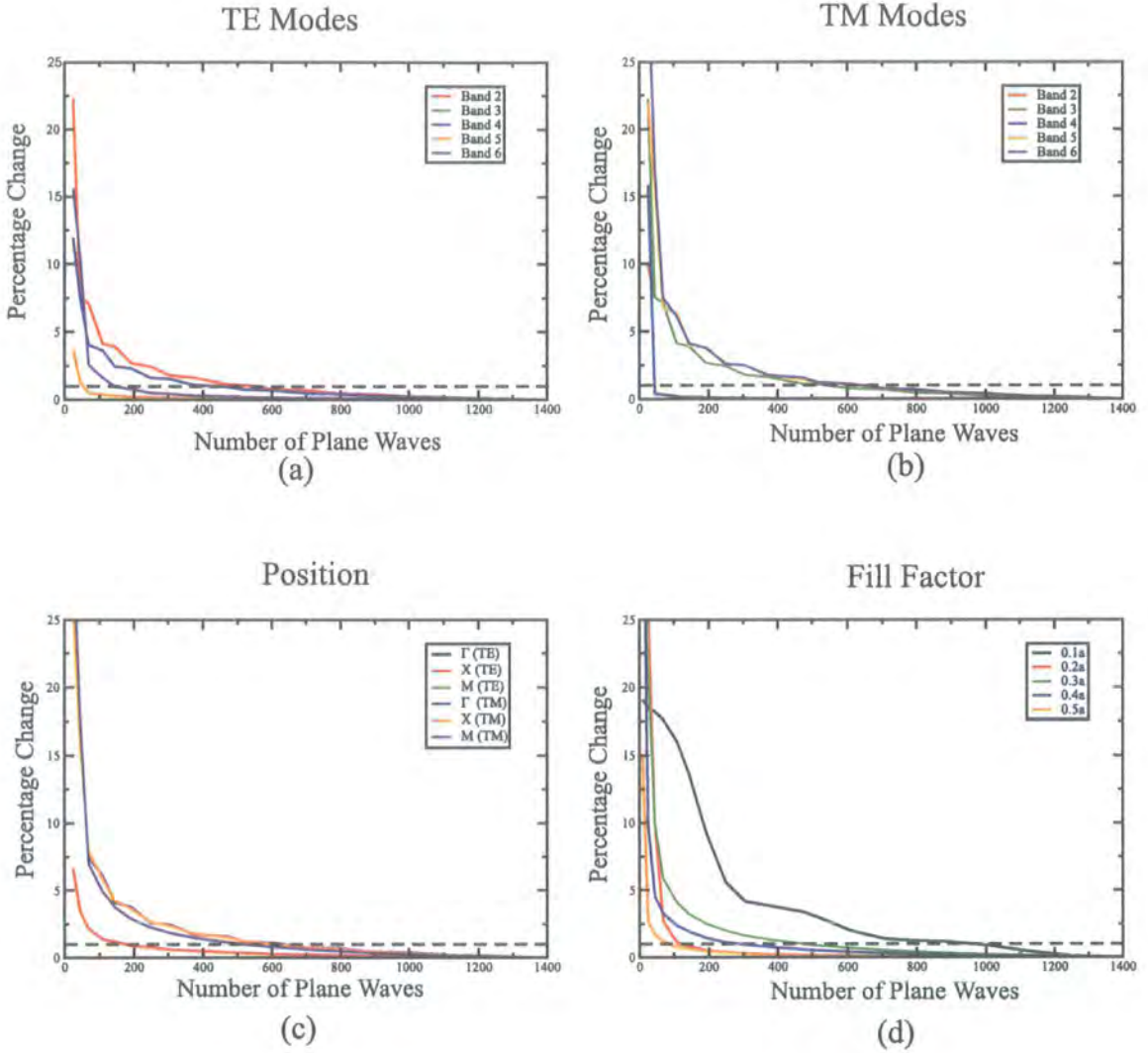


**Figure 5.3:** Convergence for an alumina rod square lattice as a function of band for the TE modes (a) and TM modes (b) at the  $\Gamma$  point ( $r = 0.2a$ ). The effect of position within the Brillouin Zone is also shown (c) for both polarisations using the slowest to converge band. Convergence for the slowest to converge point is considered as a function of rod radius in (d). The dashed line indicates the 1% convergence level (relative to the 1389 plane-wave result).

Although the 1389 plane-wave solution is not absolutely converged it does provide a satisfactory standard for comparison. Only the sixth band at one particular rod radius ( $r = 0.1a$ ) was slightly in excess of 1%. The inclusion of additional plane-waves would have little effect on the accuracy of the solutions but would be computationally more expensive.

Unfortunately, given the computational power available it was not possible to perform the anisotropy optimisation calculations with such a large number of plane-waves. A choice of 301 plane-waves was made to allow for an acceptable computational time. From Figure 5.3 it may be seen that the choice corresponds to convergence to within approximately 2.5% of the large number of plane-waves solution, for all but the one of the situations examined.

## 5.4 Bandstructures

Bandstructures for the square lattice type have undergone prior theoretical and experimental investigation by a number of workers. In this section a comparison is made with published results to ensure the validity of the computational implementation employed here. In addition to frequency solutions the standard bandstructure calculation also allows the electric and magnetic fields to be computed. Field profiles are fundamental to photonic crystals as they allow the solutions of Maxwell's equations to be visualised within a structure.

### 5.4.1 Standard Bandstructures

The first two-dimensional photonic structure to undergo experimental examination was created by Robertson *et al.* [173]. The structure consisted of alumina ( $\epsilon = 8.9$ ) rods with a rod radius of  $r = 0.2a$  arranged in air. A comparison may be made to these results to confirm that the theory has been correctly implemented. Fig 5.4 shows bandstructures calculated for alumina rods in air for a TE polarisation. The equivalent bandstructures for the TM polarisation are given in Fig. 5.5. Results are shown for a range of increasing rod radii. This is useful as it demonstrates the progression from uniform media to photonic crystal.

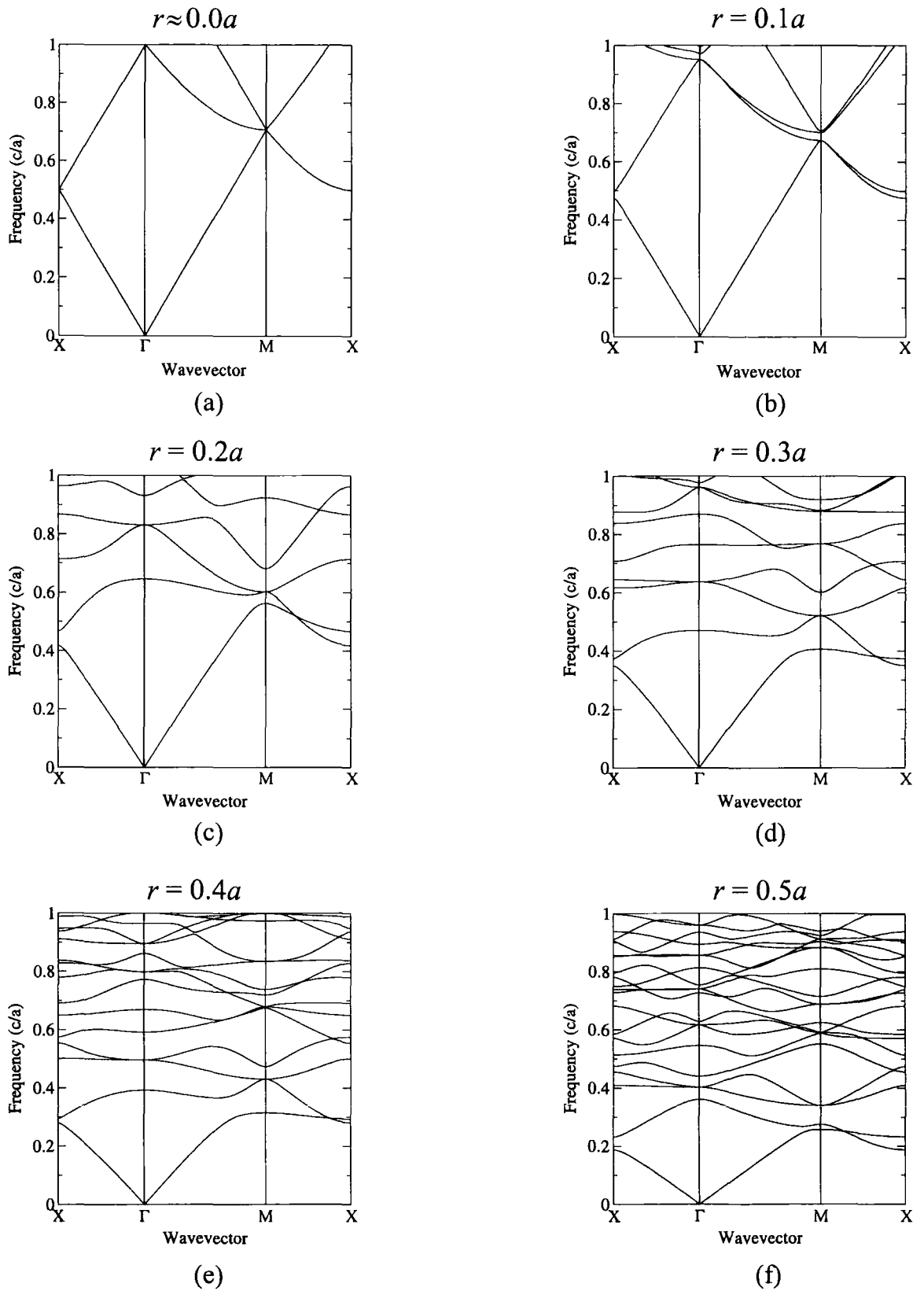


**Figure 5.4:** TE Square lattice bandstructures for alumina rods in air with rod radii of a)  $r \approx 0$ , b)  $r = 0.1a$ , c)  $r = 0.2a$ , d)  $r = 0.3a$ , e)  $r = 0.4a$ , f)  $r = 0.5a$ .

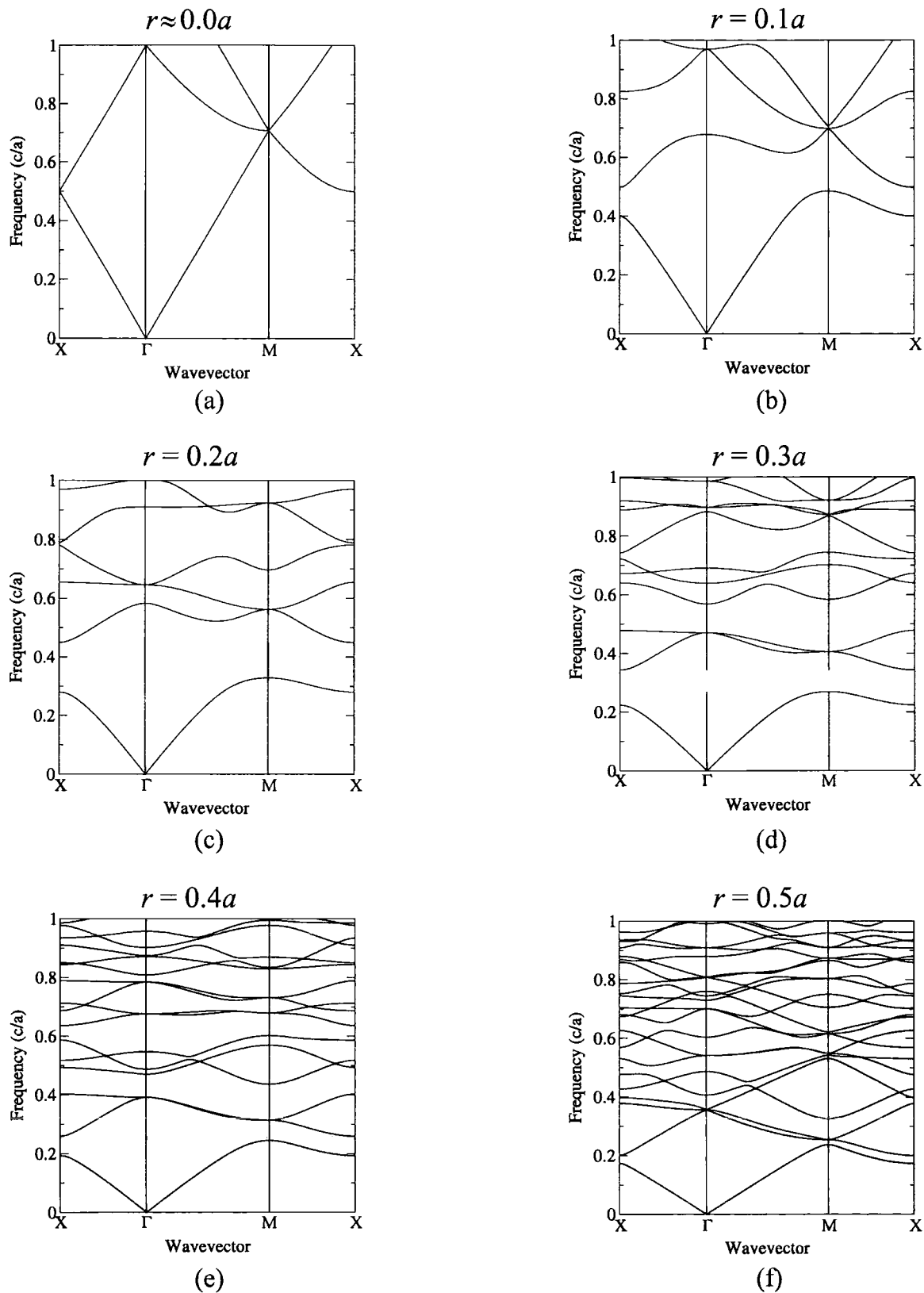


**Figure 5.5:** TM Square lattice bandstructures for alumina rods in air with rod radii of a)  $r \approx 0$ , b)  $r = 0.1a$ , c)  $r = 0.2a$ , d)  $r = 0.3a$ , e)  $r = 0.4a$ , f)  $r = 0.5a$ . Band-gaps have been highlighted in green.

If the rod radius of  $0.2a$  is considered, then both the TE and TM bandstructures show agreement with the published results of Robertson *et al.*

### Uniform Media

In both Fig. 5.4 and Fig. 5.5 the first structure considered is formed from rods with a radius of  $\approx 0$ , indicating that the material is almost a uniform dielectric media. Note that an arbitrary periodicity must be imposed to enable Bloch's theorem to be applied and for bandstructure plots comparable to the non-zero rod radius case to be calculated. Light travelling in uniform medium possesses a propagation speed which is the free space speed divided by the refractive index of the medium. This, gives the simple dispersion relation

$$\omega(k) = \frac{ck}{\sqrt{\epsilon_r}} \quad . \quad (5.6)$$

Both Fig. 5.5a and 5.4a demonstrate uniform material behaviour at low frequencies, below  $0.5c/a$ . The figures show a linear relationship between  $\omega$  and  $k$ , with a gradient equal to unity. This corresponds to the dispersion relation of the background air. To present the bandstructure plots  $k$  values from outside the imposed Brillouin Zone have been folded back into the zone. The wavevector,  $\mathbf{k}$ , contains two components  $k_y$  and  $k_z$ . When the original wavevector is directed along the primitive reciprocal lattice vectors a linear relationship may be seen in the dispersion diagram. If more than one component exists in  $\mathbf{k}$  then the dispersion relation shows an effect known as the anomalous group velocity [172]. The group velocity of a radiation mode is simply given by the slope of the dispersion curve since

$$\mathbf{v}_g = \frac{\partial \omega}{\partial \mathbf{k}} \quad . \quad (5.7)$$

An example of the anomalous group velocity may be seen by examining the second band in the  $\Gamma$ - $M$  direction in Fig. 5.5a. Whilst not of direct relevance to this work, the group-velocity anomaly is of use for certain applications due to the much reduced group velocity. The reduced group velocity is equivalent to a reduced energy velocity within the photonic crystal [172]. This allows for an enhanced interaction time between radiation modes and matter and is useful, for example, in increasing stimulated emission or absorption.

### Refraction Considerations

Examination of the square lattice bandstructures shown in Fig. 5.4 and 5.5 allows the identification of several features of interest. The appearance of a photonic band-gap was the feature which initially received the main focus of attention in the examination of photonic crystal dispersion characteristics. A complete photonic band-gap is a range of frequencies over which light propagation is forbidden for all directions for a single polarisation. Note this differs from the term ‘absolute’ band-gap which is reserved for those occasions when a range of forbidden frequencies exists for both polarisations. Complete band-gaps have been highlighted for the TM polarisation in Fig 5.5. The sequential figures show that as the radius of the alumina rods is increased the band-gap becomes larger until an optimum examined configuration is reached, around  $r = 0.2a$ . If the rod radius is further increased then the gap begins to close again. A physical explanation of this effect is considered in Section 5.4.2, which examines the electric field profiles for the same lattice. The TE polarisation does not possess a band-gap in all directions. In terms of the refraction properties of the structure a band-gap is significant as it will prevent refraction from occurring for a range of frequencies. Even partial band-gaps will be influential through the effect they have on the dispersion surfaces of a structure. Bands must begin and end at Brillouin Zone boundaries, so whether a band-gap exists, or not, will have an influence on the complete dispersion surface at a particular frequency.

Another noteworthy feature is the compression of bands which occurs with increasing fill factor. Increasing the area fill factor increases the average refractive index of the structure, reducing the frequency of individual bands. For example, consider the first band in the  $X$ - $\Gamma$  direction; the band may be seen to compress with fill factor. Examination of the bandstructures shown in both Fig. 5.4 and Fig. 5.5 allows it to be clearly seen that fill factor is an influential factor in bandstructure anisotropy.

Finally, anisotropy is clearly highly frequency dependent. Consider, for example, Fig. 5.5b at a frequency below  $0.4 c/a$ . In the  $\Gamma$ - $X$  and  $\Gamma$ - $M$  directions, at any specified frequency, the magnitude of the wavevector appears very similar. Thus, circular dispersion surfaces with refraction properties similar to uniform structures would be expected. At higher frequencies anisotropies are clearly evident. Small frequency changes can have a large effect on bandstructure anisotropy so it is important when optimising anisotropy (Section 5.7) to

use narrow frequency spacings. Frequency spacings of  $\delta\omega = 0.01c/a$  are used in this work.

### 5.4.2 Field Profiles

The physics of photonic crystals together with the physical origin of photonic band-gaps may be explained by the examination of the field profiles for the electromagnetic modes within the structures. The square structure is of particular interest because the system possesses a complete photonic band-gap for one polarisation but there is no corresponding band-gap for the other polarisation. This is an important consideration when designing photonic crystals for refraction applications. Fig. 5.5 shows that the square lattice ( $r = 0.2a$ ) contains a large band-gap for the TM polarisation at the  $M$  point. The electric field may be considered at this point by evaluating the field amplitude across a range of  $y$  and  $z$  positions. Bilinear interpolation may then be used to produce either a three-dimensional profile or a two-dimensional contour plot of the field amplitude. Fig. 5.6 shows the manner in which the three-dimensional profiles are related to the two-dimensional contour plots. The figure gives the electric field at the  $M$  point for the first and second bands with a TM polarisation. The second band is degenerate at the  $M$  point and one of the two degenerate Bloch Waves has been plotted.

The speed of light travelling in a uniform dielectric material is lower than when propagating in air; electromagnetic waves have a shorter wavelength in media than they do in a vacuum. An understanding of the physical origin of photonic band-gaps could come from the notion that the higher the proportion of the electric field which exists inside the higher dielectric constant material, the lower the frequency of the solution for the same wavevector. A lower order band is therefore expected to have a larger confinement in the dielectric rods than a higher order band. A higher order band would be expected to possess an increased proportion of the electric field in the air surrounding the rods. This is exactly the situation seen by examining the  $M$  point field profiles. The first band shows strong peaks in the rod regions and field nodes outside of the rods. The second order band still possesses peaks in the high dielectric constant rods. However, it is less localised within the rods and a significant proportion of the field exists outside of the rods. This difference in the location of the field intensity may therefore be used to explain the existence of a reasonably large band-gap at this point.

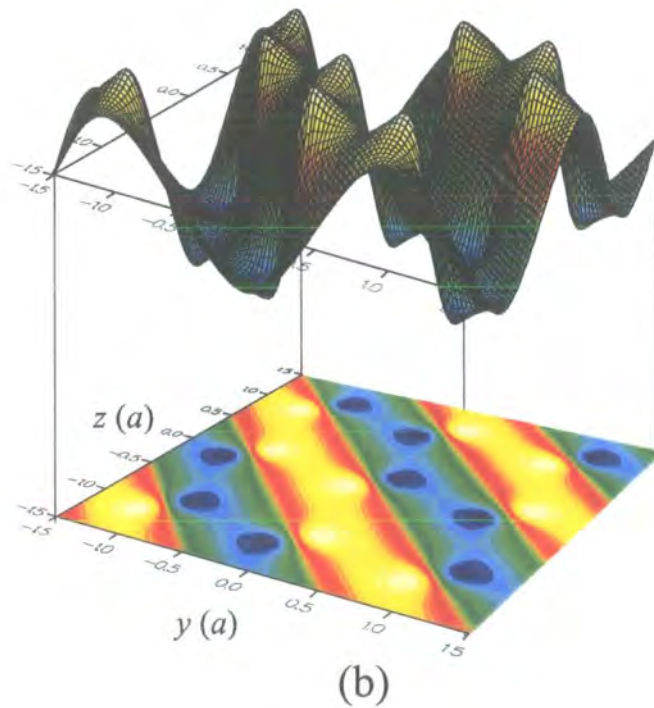
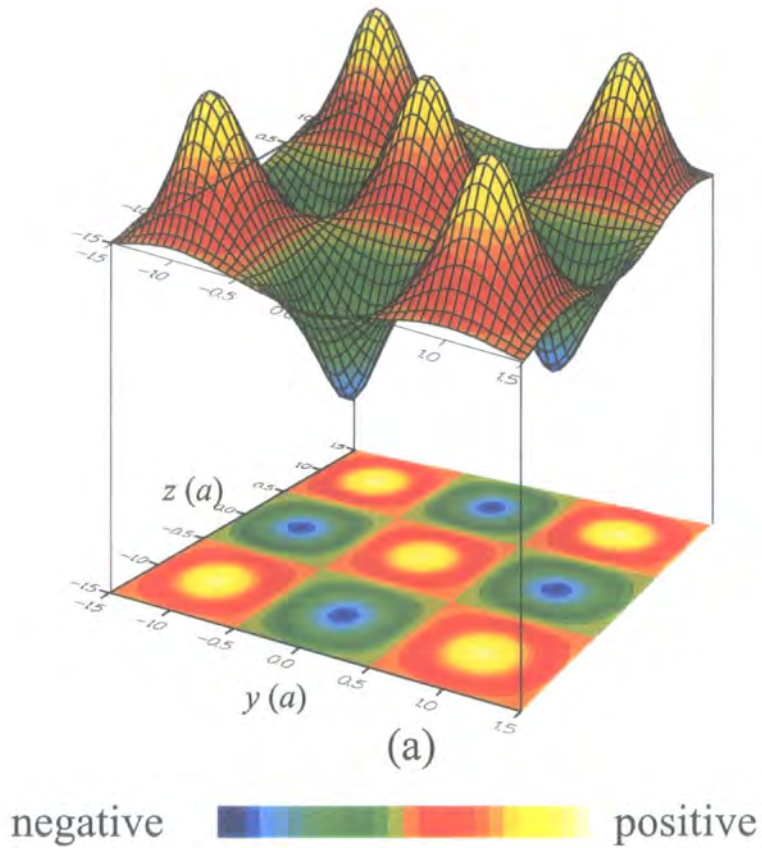


**Figure 5.6:** Electric field profiles for the first (a) and second (b) bands of the TM polarisation at the  $M$  point.

The field confinement principle may be confirmed by examining the standing waves at the other high symmetry points. These are shown in Figures 5.7 and 5.8. It can be clearly seen that the first band has electric fields which are largely confined to the high refractive index rods and the second band possesses more diverse field patterns. The corresponding TE polarisation bandstructures do not have a complete band-gap. Examination of the magnetic field profiles has been used for the TE mode as these are entirely in the  $x$  direction. The electric field will be largest in the nodal planes of the magnetic field hence this is where the energy is concentrated. It can be seen that the fields contain only slightly different proportions of their amplitude in the dielectric rods for the lowest two bands. A more rigorous way of showing this is to examine the displacement energy confinement. For this purpose it is of use to define a factor,  $f_e$ , indicating the proportion of the electric field energy located inside the dielectric rods. This approach was suggested by Meade *et al.* [187].

$$f_e = \frac{\int_{\text{rod}} E^*(\mathbf{r}) \cdot D(\mathbf{r}) d^3\mathbf{r}}{\int E^*(\mathbf{r}) \cdot D(\mathbf{r}) d^3\mathbf{r}} \quad (5.8)$$

Equation (5.8) may be written in more convenient form for computational use by the substitution of the plane-wave field forms into the equation. The magnetic field,  $\mathbf{H}$ , has been used due to the magnetic field coefficients being more readily accessible from the standard bandstructure method. Cancelling the common factors produces the following result for the TE modes:

$$f_e = \frac{\int_{\text{rod}} \frac{1}{\epsilon_r(\rho)} \sum_{\mathbf{g}, \mathbf{g}'} H_{\mathbf{g}}^* H_{\mathbf{g}'} (\mathbf{k} + \mathbf{g}) (\mathbf{k} + \mathbf{g}') d^2\rho}{\int \frac{1}{\epsilon_r(\rho)} \sum_{\mathbf{g}, \mathbf{g}'} H_{\mathbf{g}}^* H_{\mathbf{g}'} (\mathbf{k} + \mathbf{g}) (\mathbf{k} + \mathbf{g}') d^2\rho} \quad (5.9)$$

and correspondingly, for TM modes:

$$f_e = \frac{\int_{\text{rod}} \sum_{\mathbf{g}, \mathbf{g}'} \frac{\epsilon_r(\rho)}{|\mathbf{k} + \mathbf{g}| |\mathbf{k} + \mathbf{g}'|} H_{\mathbf{g}}^* H_{\mathbf{g}'} d^2\rho}{\int \sum_{\mathbf{g}, \mathbf{g}'} \frac{\epsilon_r(\rho)}{|\mathbf{k} + \mathbf{g}| |\mathbf{k} + \mathbf{g}'|} H_{\mathbf{g}}^* H_{\mathbf{g}'} d^2\rho} \quad (5.10)$$

Integration was carried out over a single unit cell using a simple trapezium rule. A sufficiently large number of divisions were made to allow for convergence to the stated values. The results are shown in Table 5.1. The results agree with those available in the literature [13, 187]. The numerical results confirm the previous observation: at both symmetry

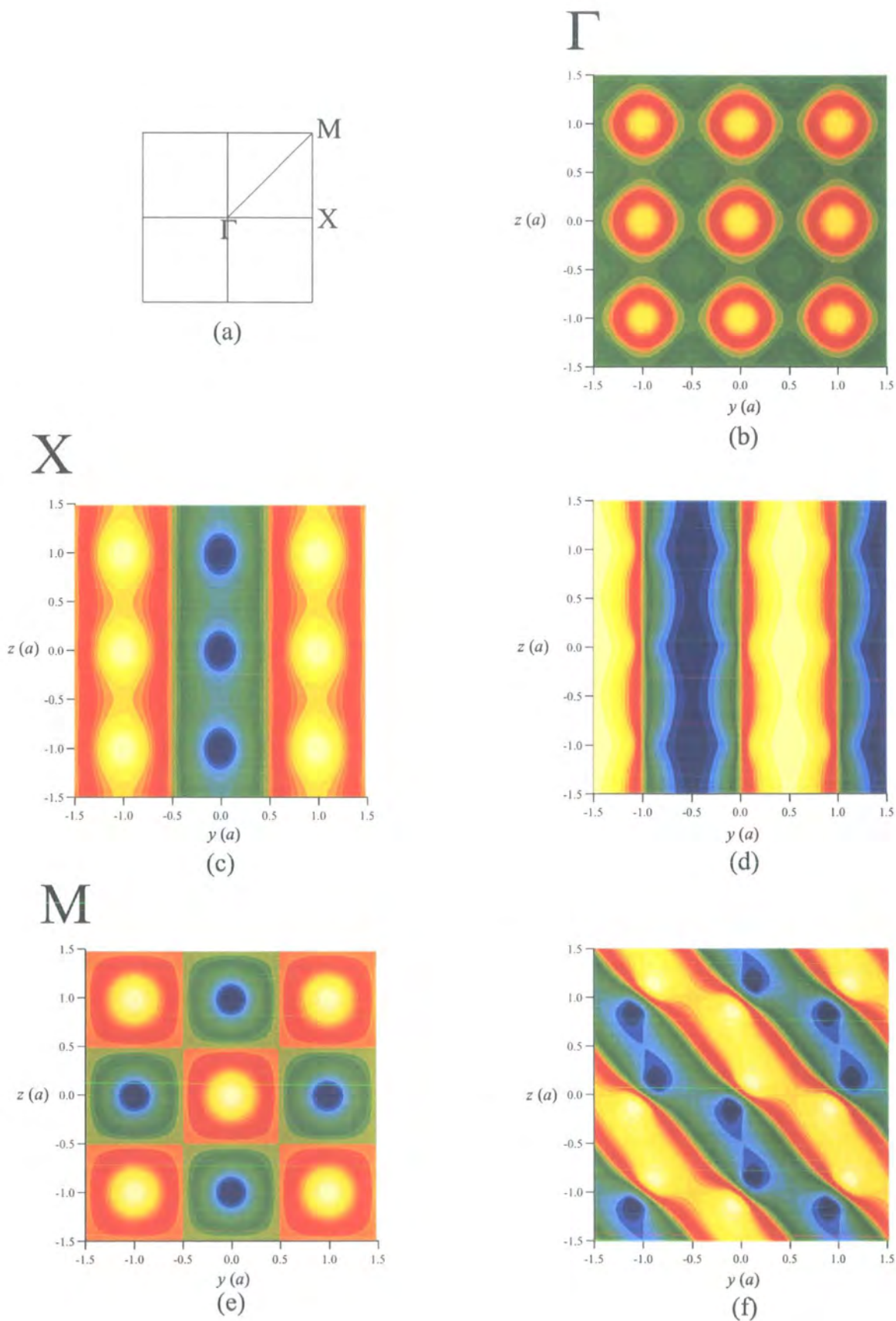


**Figure 5.7:** TM electric field profiles for the first (left column) and second (right column) bands at the high symmetry points shown in (a). For key see Fig 5.6.

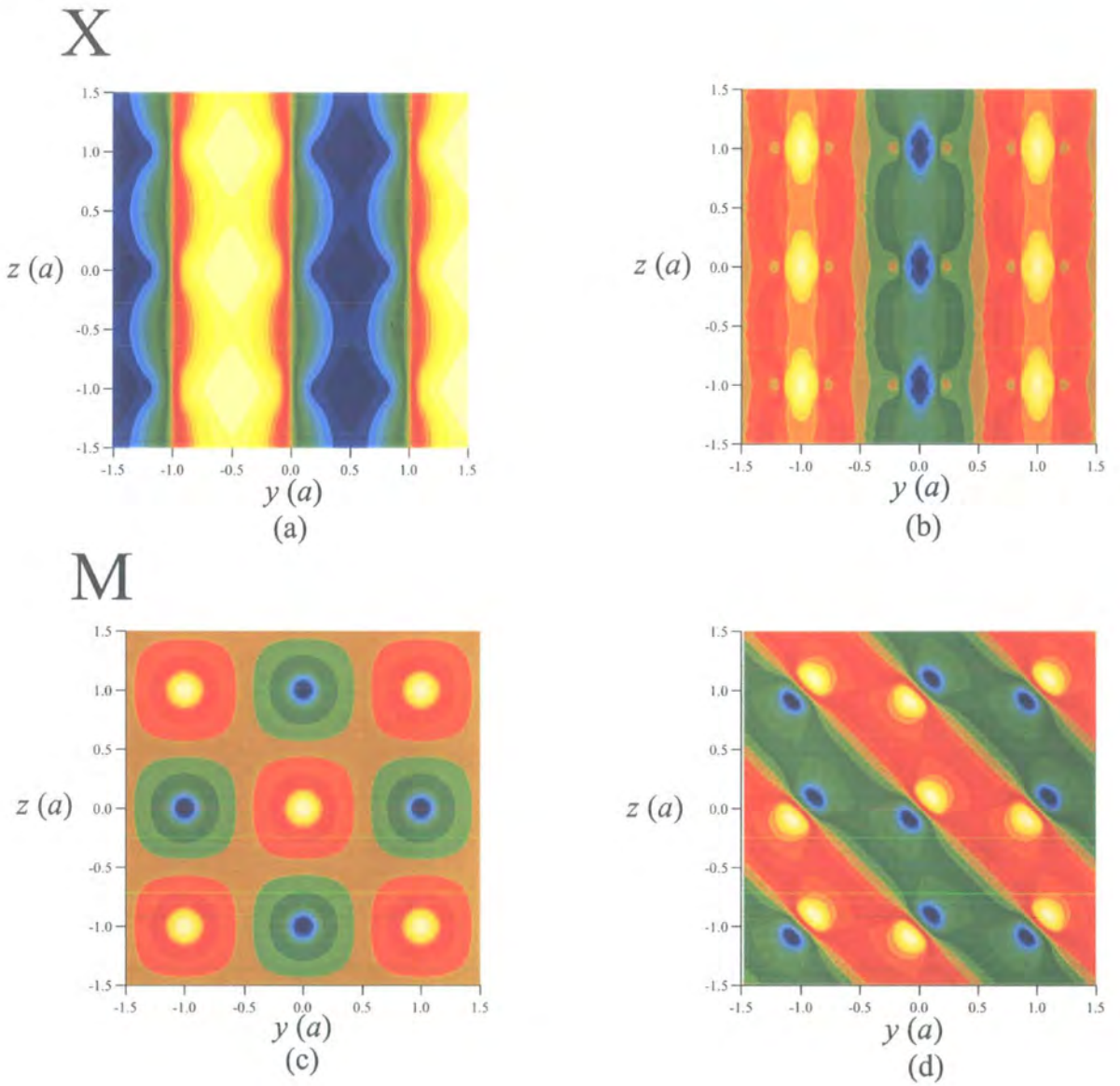


**Figure 5.8:** Magnetic field profiles for first (left column) and second (right column) bands for the TE modes at the high symmetry points in the Brillouin zone. For key see Fig 5.6.

Point	1st Band ( $X$ point)	2nd Band ( $X$ point)	1st Band ( $M$ point)	2nd Band ( $M$ point)
TM mode	0.8	0.3	0.9	0.6
TE mode	0.1	0.2	0.9	0.1

**Table 5.1:** Electric field factors for TM and TE modes at the high symmetry  $X$  and  $M$  points.

points the TM mode has a substantial difference in the confinement region for the two lowest order bands. Corresponding large differences are not seen for the TE modes. It should be noted that that whilst suggestive of a band-gap a high difference in energy confinement for two consecutive bands does not guarantee a band-gap and also band-gaps may exist without a significant difference in energy confinement [187].

Another manner for visualising why a TM complete band-gap exists is to consider the field forms for the two polarisations. A TE mode has an electric field which is in the in-plane direction. Accordingly all TE modes will have a significant proportion of their electric field amplitude in both the dielectric rods and the background dielectric. A TM mode has an electric field which exists in the  $x$  direction only. This makes it possible for the field to have peaks inside the rods and nodes outside or vice-versa. The large refractive index difference between the two dielectrics may then be used to explain the production of wide band-gaps.

## 5.5 Refraction Properties

In the previous chapter (Section 4.12) a method was presented which enabled the refraction angles to be calculated for plane-waves incident at an interface between a uniform material and a photonic crystal. The method utilised photonic dispersion surfaces to calculate the propagation direction of a refracted wave. The higher the level of anisotropy present in the dispersion surface the greater the refraction properties of a photonic crystal will differ from those of a uniform material. In this section the previously described method is applied to the square lattice. The refraction properties are discussed in general prior to an optimisation study on bandstructure anisotropy.

### 5.5.1 Multiple Solutions

The refraction properties of photonic crystals arise from interactions which occur between the incident light and the photonic bandstructure at a given frequency. It is evident from examining photonic bandstructures, for example those given in Fig 5.4 and 5.5, that it is possible for a structure to possess more than one wavevector solution in a specific direction at a given single frequency. For example, the  $r = 0.5a$  bandstructure in Fig. 5.5f clearly shows multiple solutions in the  $\Gamma - M$  direction at frequencies of around  $\omega = 0.6c/a$ . The number of solutions at a given frequency is an important consideration when designing photonic crystal structures for refraction applications. If, at the particular frequency of interest, multiple refraction angles exist then one of the main advantages of photonic crystals is negated. Photonic crystals are often considered for applications because of their low losses. The existence of multiple refraction angles may divide the intensity of the incident light between the refraction ‘channels’. This section looks at dispersion surfaces in detail to calculate the frequencies at which a specific structure will exhibit a maximum of one refraction angle for the range of possible angles of incidence.

#### Physical Solutions

Consider the dispersion surface shown in Fig. 5.9a. The surface is for a square lattice consisting of alumina rods in air with a rod radius of  $r = 0.2a$ ; it is for a low frequency ( $\omega = 0.3c/a$ ) and the TE polarisation. In Section 4.13 it was explained that when a plane-wave is incident on a photonic crystal structure the wavevector component parallel to the interface must be conserved. For Fig 5.9a if an incident wave has a wavevector which is directed in the positive  $k_y$ , then it is the  $k_z$  wavevector component which must be conserved. The wavevector component may be conserved by the use of a construction line of constant  $k_z$ , shown for some arbitrary  $k_z$  value in the figure. The construction line crosses the dispersion surface at two points which have been labelled  $A$  and  $B$ . The two crossing points create the possibility of two propagating solutions within the photonic crystal for a given  $k_z$  value. If the incident wave coupled to the photonic crystal modes propagates from the lower left to the upper right direction then only solution  $B$  is a valid solution for the system. Point  $B$  is the only point possessing a positive slope ( $\partial\omega/\partial k_y$ ), indicating propagation in the positive  $k_y$  direction. The positive slope gives a physically viable solution propagating to the right. Point

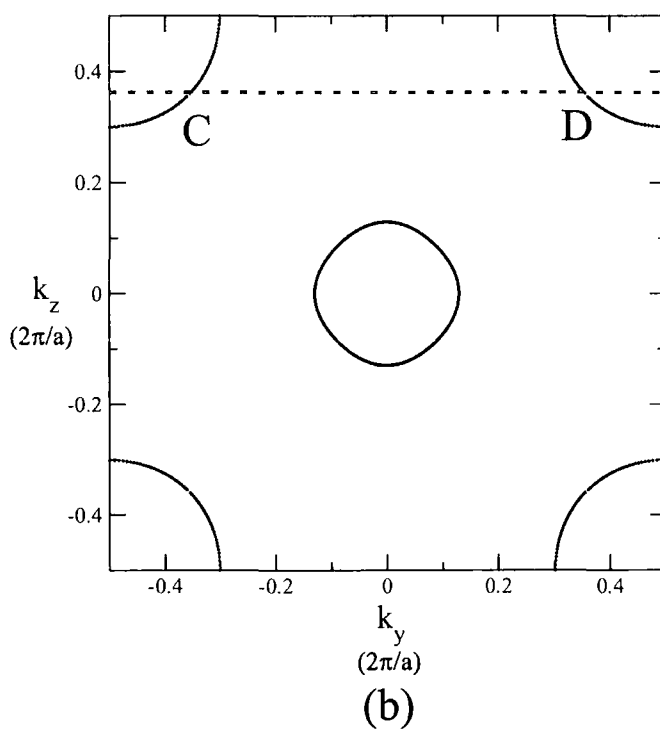
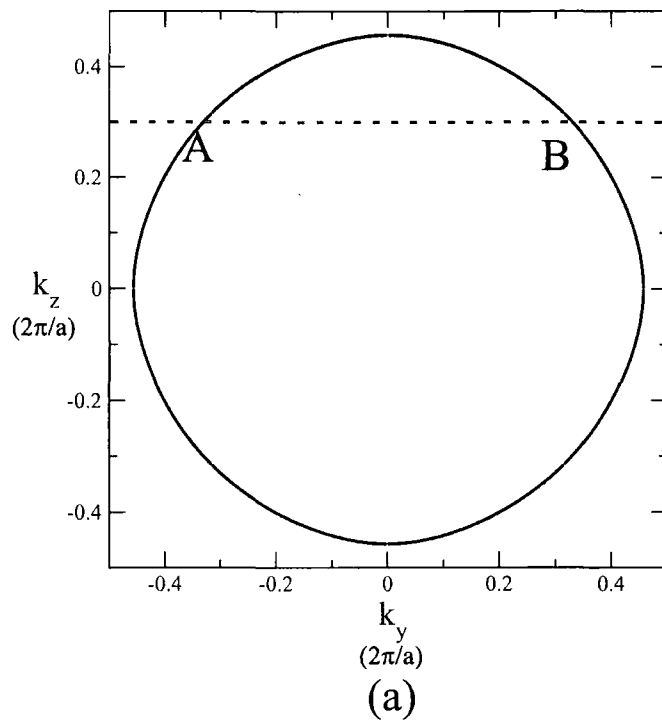


**Figure 5.9:** Equi-frequency curves for square lattice of alumina rods  $r = 0.2a$  at frequencies of a)  $\omega = 0.3c/a$  and b)  $\omega = 0.6c/a$  (TE modes)

$A$  implies a propagating wave in the negative  $k_y$  direction; which is physically forbidden given the incident wave propagation direction. The dispersion surface shown in Fig. 5.9a will consequently produce a single refracted wave from the incident wave.

### Negative Refraction

It should be noted that the need for a physical solution does not negate the possibility of refraction angles which propagate in a direction opposed to those seen in conventional materials. This effect is often referred to as negative refraction, as a negative refractive index would be required to produce such an occurrence in a uniform material [188]. Such an effect is potentially of use for creating perfect lenses [191]. Consider Fig. 5.9b; the dispersion surface is for the same structure as described in the previous section for Fig. 5.9a. However, the system is now operating at a slightly higher frequency ( $\omega = 0.6c/a$ ). In this instance a constant  $k_z$  construction line has again been included, crossing the dispersion surface at points  $C$  and  $D$ . The physically valid solution propagating to the right is solution  $D$ . On this occasion the refracted wave possesses a propagation direction which is positive. Luo *et al.* [192] recently showed that rotation of a square lattice arrangement similar to that shown in Fig. 5.9b can provide a situation in which negative refraction occurs. Such effects using photonic crystals have been reported in the literature for an un-rotated hexagonal two-dimensional lattice [193] and more recently for three dimensional structures [189, 190].

### Single Solutions

In general two or more physically acceptable refracted waves may exist for a single incident plane-wave. This is true in most situations apart from special cases such as the low frequencies considered previously. To identify structures which possess, at most, one refraction angle for all possible angles of incidence is a computationally intensive task. The only known rigorous method is an all inclusive scan through structure refractive index, rod radius, frequency and  $k_z$  values. Given the limited computational resources available such an approach is impracticable. This remains true even if it is acknowledged that the plane-wave requirements for the calculation may be relaxed due to the requirement, not for exact solutions, but merely for knowledge of another solution at the same  $k_z$  value.

Due to the impractical nature of the rigorous method a compromise method was re-

quired. One possible approach would be to restrict the study to the examination of the two high symmetry directions,  $\Gamma$ - $X$  and  $\Gamma$ - $M$ . It is not sufficient to simply examine the number of solutions in either direction and reject those structures with two or more solutions in either direction. Such an approach would lead to situations similar to those shown in Fig 5.9b to be rejected. The dispersion surface has two solutions in the  $\Gamma$ - $M$  direction, however, if a constant  $k_z$  line is imagined then it is evident that only a single refraction angle exists for each individual angle of incidence (each specific  $k_z$ ). The method which was adopted examined the  $\Gamma$ - $X$  and  $\Gamma$ - $M$  directions only, but also carried out a bandstructure calculation for each of the  $k_z$  solutions in these directions. This allowed for confirmation that more than one refraction angle existed at this frequency and the configuration should be disregarded.

The results of such an approach are shown in Fig. 5.10 for the TM polarisation. The results may be of interest for structure design and have been included in Appendix A for the TE polarisation. The results broadly indicate that for rods in air (for example Fig. 5.10) the lower the rod radii the larger the range of acceptable frequencies. This is attributable to the band compression effect discussed in Section 5.4.1; more solutions are likely to exist at a given frequency, and Brillouin Zone direction, as the bands compress.

## 5.6 Bandstructure Anisotropy

In the previous section results were provided for occasions when it was believed that there was a single allowed refraction angle across the entire Brillouin Zone. When looking for superprism behaviour such an approach is unnecessarily restrictive. The single refraction angle condition may be relaxed and in general multiple solutions will be permitted, provided that at the  $k_z$  value of interest only one solution exists.

### Reference Directions

One of the aims of this chapter was stated as optimising the anisotropy present in photonic bandstructures for structures based on the square lattice type. To optimise the anisotropy of a bandstructure requires a method for quantifying anisotropy. The simplest approach to adopt is to consider two Brillouin Zone directions and calculate the magnitude of the allowed wavevector in these directions at a particular frequency. Anisotropic band-

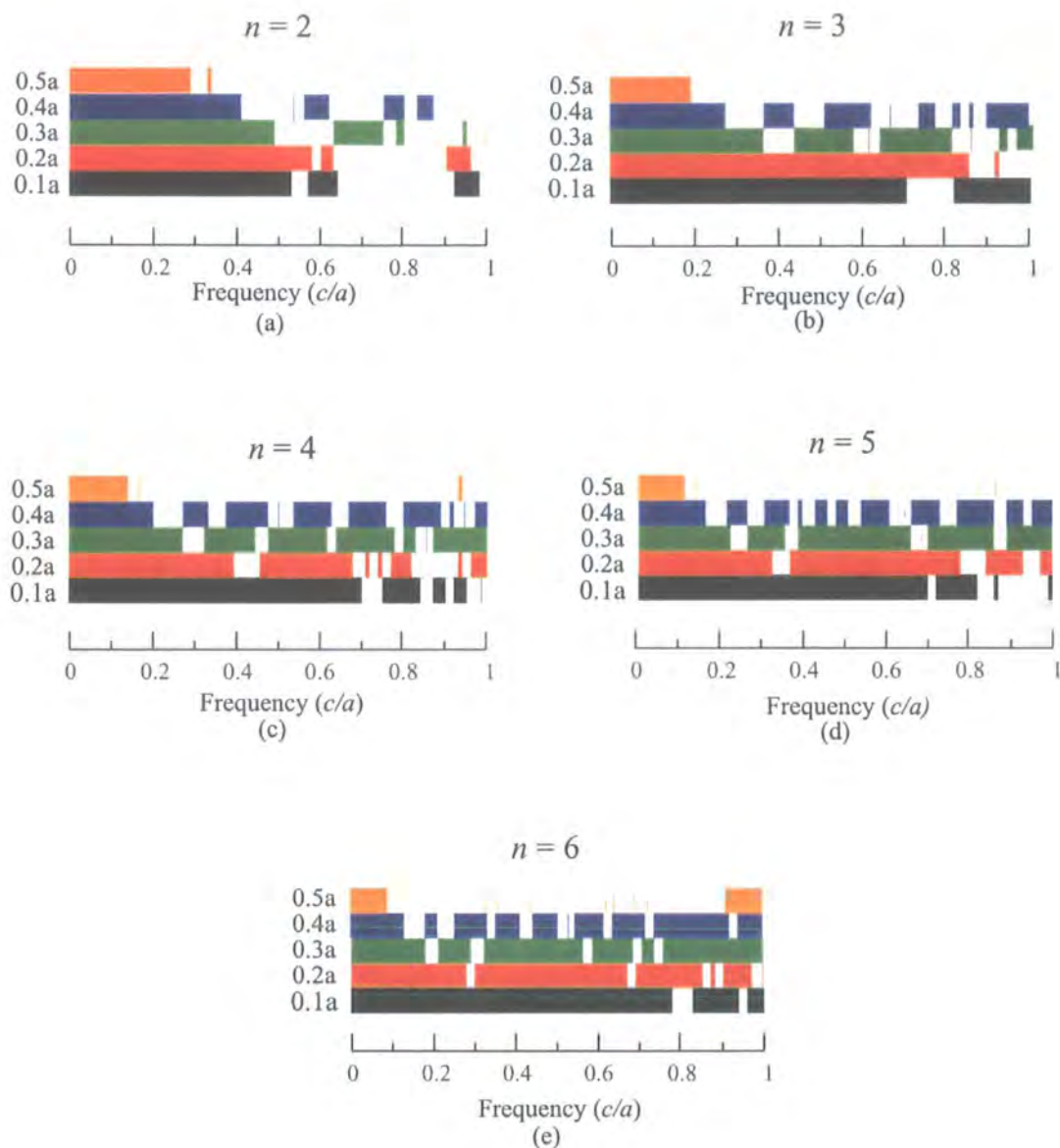


**Figure 5.10:** Frequencies which exhibit single refraction angles, shown by the coloured shading, for the TM polarisation and a square lattice structure consisting of dielectric rods in air. The results show a range of rod radii (indicated by different colours) and refractive index values of 2 (a), 3(b), 4(c), 5(d) and 6(e).

structures may then be described as existing when a large difference in the magnitude of the wavevector exists in the two directions. Whilst the approach is not a rigorous indication of anisotropy throughout the entire Brillouin Zone; it does offer the potential of identifying likely anisotropic candidates worthy of further investigation. It is possible to consider more than two directions. However, given the large range of possible structures and frequencies for consideration, it is sensible to restrict the choice of directions to the minimum number possible to gather the desired information.

The method employed here for identifying bandstructure anisotropy makes use of the  $\Gamma$ - $X$  and  $\Gamma$ - $M$  directions. The choice of these two directions was the result of the experience gained from considering multiple dispersion surfaces. The method may be justified by the use of the example bandstructure given in Fig. 5.11a. At low frequencies it may be seen that the wavevectors in the two reference directions are of similar magnitude. An example low frequency dispersion surface has been plotted for a specific frequency in Fig. 5.11b. The surface has a circular appearance indicating an isotropic bandstructure and uniform material type behaviour. The mid frequency indicated in Fig 5.11a produces the dispersion surface shown in Fig. 5.11c. It may be seen from the bandstructure diagram that the magnitude of the  $k$  solutions in the  $\Gamma$ - $X$  and  $\Gamma$ - $M$  directions differ slightly. The slight anisotropy creates a dispersion surface with refraction properties which differ from those of uniform materials. At the highest frequency indicated on the bandstructure (Fig. 5.11a) it may be seen that the  $k$  magnitude in the  $\Gamma$ - $M$  direction differs by a significant amount from the magnitude in the  $\Gamma$ - $X$  direction. The entire dispersion surface has been calculated and is shown as Fig. 5.11d. It possesses an anisotropic appearance with potentially interesting refraction properties. The two reference direction method would, in this instance, have allowed the two anisotropic dispersion surfaces to be successfully distinguished from the isotropic surface.

### Quantitative Results

To assist with identification of anisotropic bandstructures it is of use to define an anisotropy ratio  $I$ :

$$I(\omega) = \frac{|k_{\Gamma-M}(\omega)|}{|k_{\Gamma-X}(\omega)|} \quad (5.11)$$

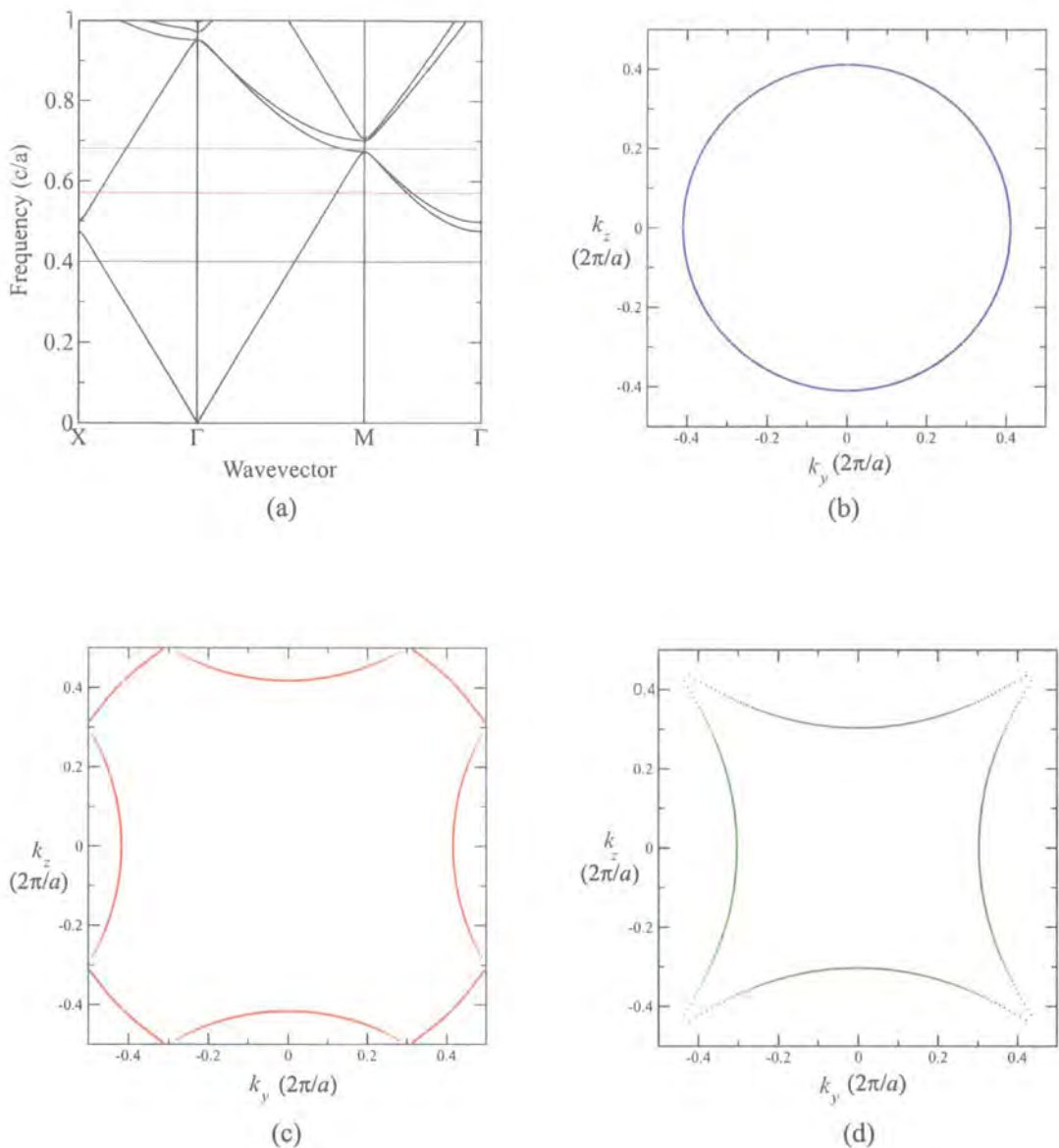


**Figure 5.11:** An example bandstructure (a) for a  $r = 0.1a$  system and a TE polarisation. Dispersion surfaces have been plotted for three different frequencies. The coloured frequencies in (a) relate to the correspondingly coloured dispersion surfaces (b)  $\omega = 0.4c/a$ , (c)  $\omega = 0.58c/a$  and (d)  $\omega = 0.69c/a$ .

Quantity	Minimum	Maximum	Interval
Rod radius	0.1a	0.5a	0.1a
Index contrast	2	6	1
Frequency	0.01	1.00	0.01

**Table 5.2:** Rod radii, refractive index contrast and frequency used for the anisotropy optimisation study.

The isotropy ratio is extremely useful as it allows us to quantify the anisotropy level of a bandstructure in a computationally relatively cheap manner. To simplify the approach only dispersion surfaces with a single solution in both the two reference directions were considered. A value of approximately unity for the ratio indicates a roughly circular type of dispersion curve, for example Fig. 5.11b. A value of greater than 1 indicates that a degree of anisotropy exists in the bandstructure and consequently also in the dispersion surface. Using the examples in Fig. 5.11, ‘c’ has a value for the ratio of  $\sim 1.5$  and ‘d’ has a value of  $\sim 2$ . It should be noted that in the following chapter a different method is used for identifying anisotropic dispersion surfaces as experience with the lattice type considered in Chapter 6 indicated a more suitable method for the different lattice type.

The range for the refractive index contrasts and rod widths considered in the study is given in Table 5.2. The refractive index contrast goes slightly beyond those available using current fabrication materials. Previously it was stated that the choice of the number of plane-waves for the calculations dictated the convergence of the solution. When considering the large range of frequencies and structures utilised here it is evident that convergence to the 1% level could not be achieved for all structures. For this reason, although higher refractive indices are considered, they are done so with the intention of qualitatively demonstrating if higher refractive indices and frequencies possess additional benefits.

## 5.6.1 Results

### TE modes

If the lowest refractive index ( $n = 2$ ) and lowest rod radius ( $r = 0.1$ ) are considered then the isotropy ratio ( $I$ ) may be plotted as a function of frequency for the structure. Fig. 5.12a shows a plot with three positions indicated. At low frequencies the ratio takes the value of approximately unity.

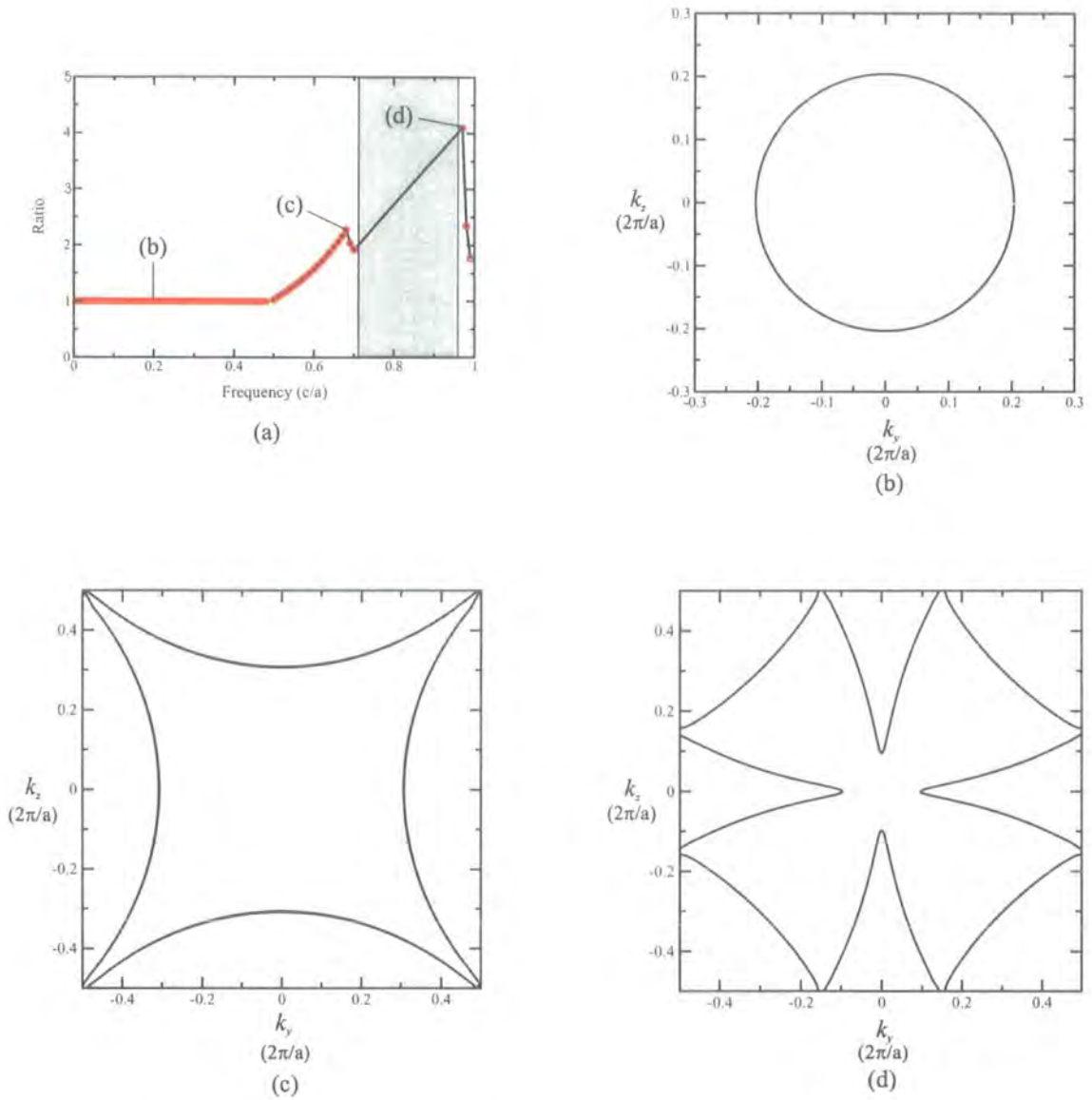


**Figure 5.12:** The anisotropy ratio plotted as a function of frequency for  $\tau = 0.1a$ ,  $n = 2$  and a TE polarisation (a). Dispersion surfaces are plotted for the points (b), (c) and (d), indicated in (a).

The corresponding dispersion surfaces are isotropic; for example the circular dispersion surface shown in Fig 5.12b. The value of the ratio increases as the frequency approaches that of the shaded frequency range. The shaded frequencies represent a range of frequencies over which it is not possible to find a single solution in both the reference directions, a requirement for the calculation of the isotropy ratio. Such a situation may arise due to either a band-gap existing for either or both directions, or due to one or both of the directions possessing multiple solutions at the chosen frequency. The highest value of the ratio before the gap is approximately 2.

The dispersion surface at point 'c' has been plotted in Fig. 5.12c. The surface is clearly a circular dispersion curve folded back into the Brillouin Zone. Such a dispersion surface possesses a point of interest around the  $M$  point. Around this point the high curvature of the dispersion surface implies that superprism behaviour may occur. However, there are two possible propagating refraction angles for each  $k_z$  value around the point. Whilst it could be considered for refraction applications this will not be done here due to the potential division of incident power between the two refraction angles.

The dispersion surface of most interest occurs at point 'd'. The point corresponds to the maximum ratio value in Fig. 5.12a. The dispersion surface at this frequency is shown by Fig. 5.12d. A single refraction angle will exist for a narrow range of  $k_z$  values about the zero position. The dispersion surface is also highly anisotropic in this region indicating that the structure is an ideal candidate for further study of its refraction properties. The refraction properties are considered in Section 5.7.

### Rod Radius and Refractive Index

Varying the rod radius, with the refractive index maintained at  $n = 2$ , will cause the bandstructures and their associated anisotropies to vary. The rod radius was varied in accordance with Table 5.2 and the resulting ratios, as a function of frequency, are given in Fig. 5.13. The results show several peaks, with ratio values of around 2. These would be expected to demonstrate similar behaviour to that shown in Fig. 5.12c. The most noteworthy value still remains the  $r = 0.1a$  value discussed in the previous section.

The effect of varying the refractive index between the limits given in Table 5.2 was also investigated. Fig 5.14 shows the rod radii which gave the most significant values of

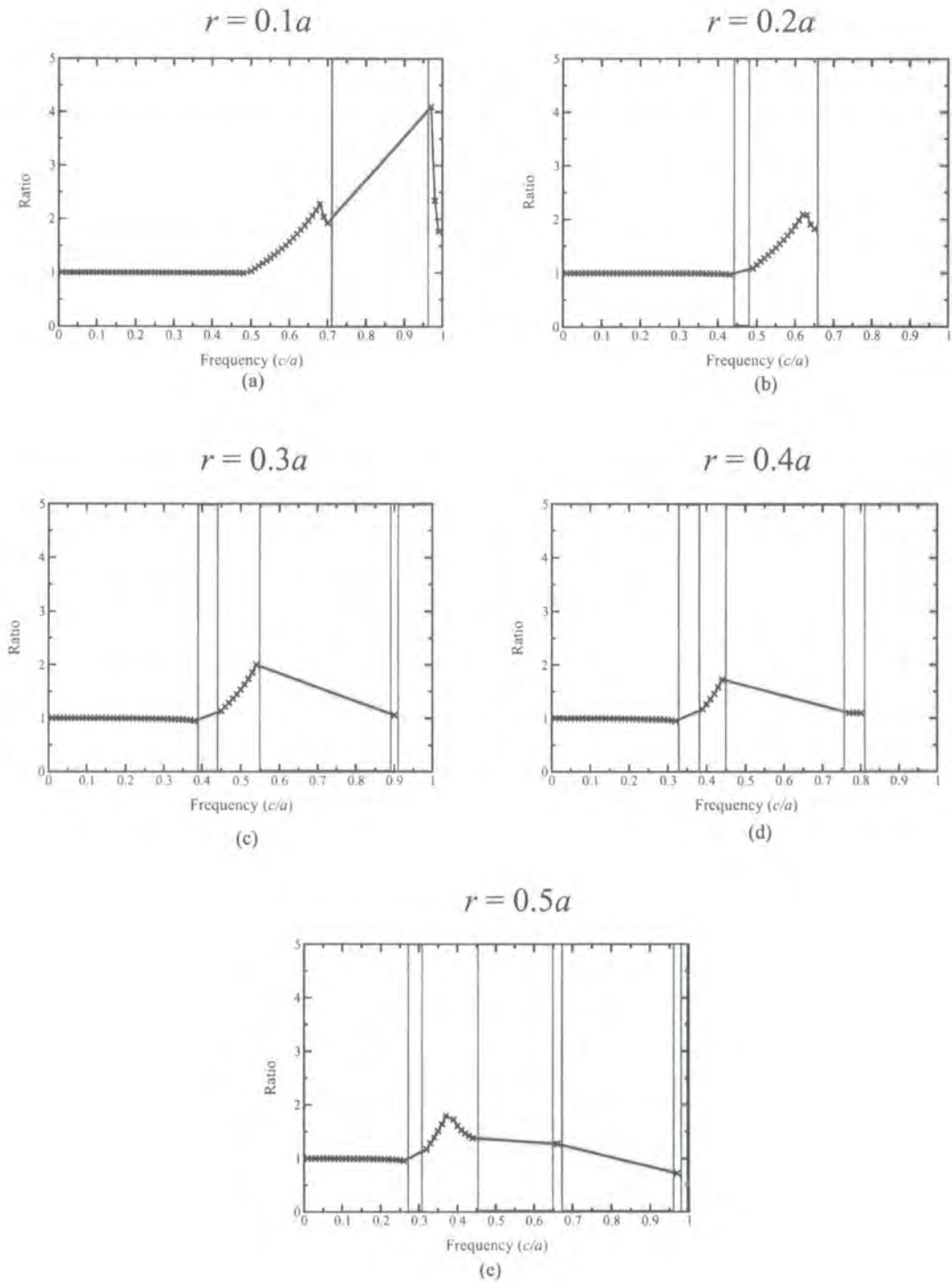
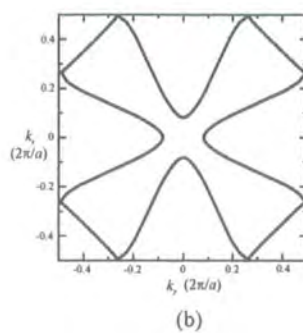
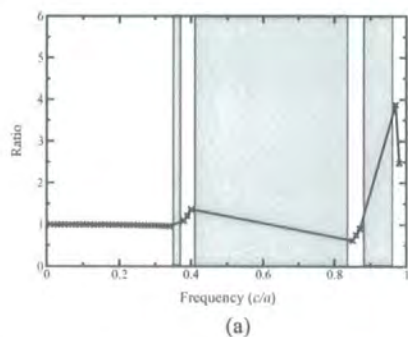
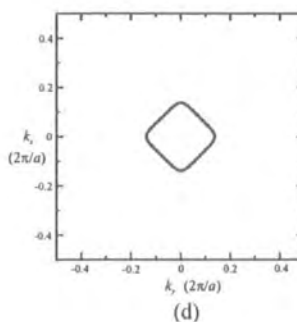
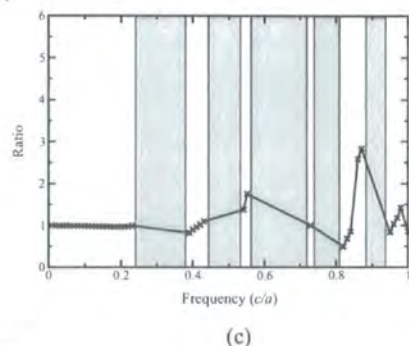


**Figure 5.13:** TE anisotropy ratios for rod radii of  $r = 0.1a$  (a),  $r = 0.2a$  (b),  $r = 0.3a$  (c),  $r = 0.4a$  (d) and  $r = 0.5a$  (e).

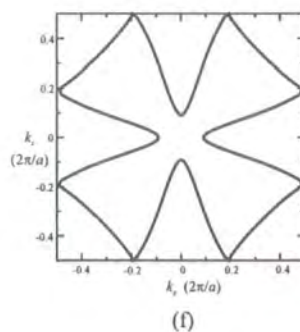
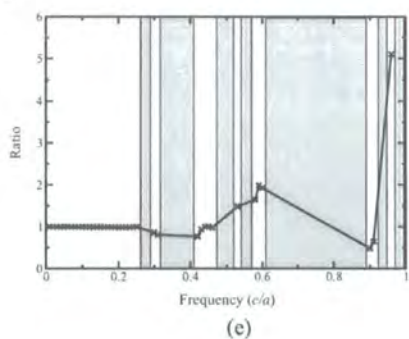
$n = 3$



$n = 4$



$n = 5$



$n = 6$

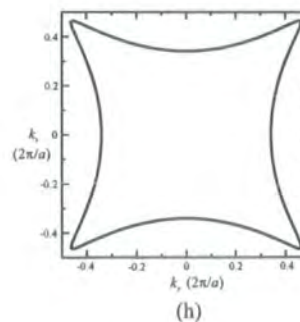
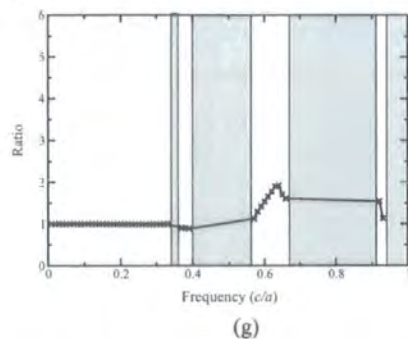


**Figure 5.14:** TE anisotropy ratios for the rod radii with the highest peak values. The ratios have been plotted as a function of frequency (a, c, e, g) and the peak value dispersion surfaces are shown (b, d, f, h).

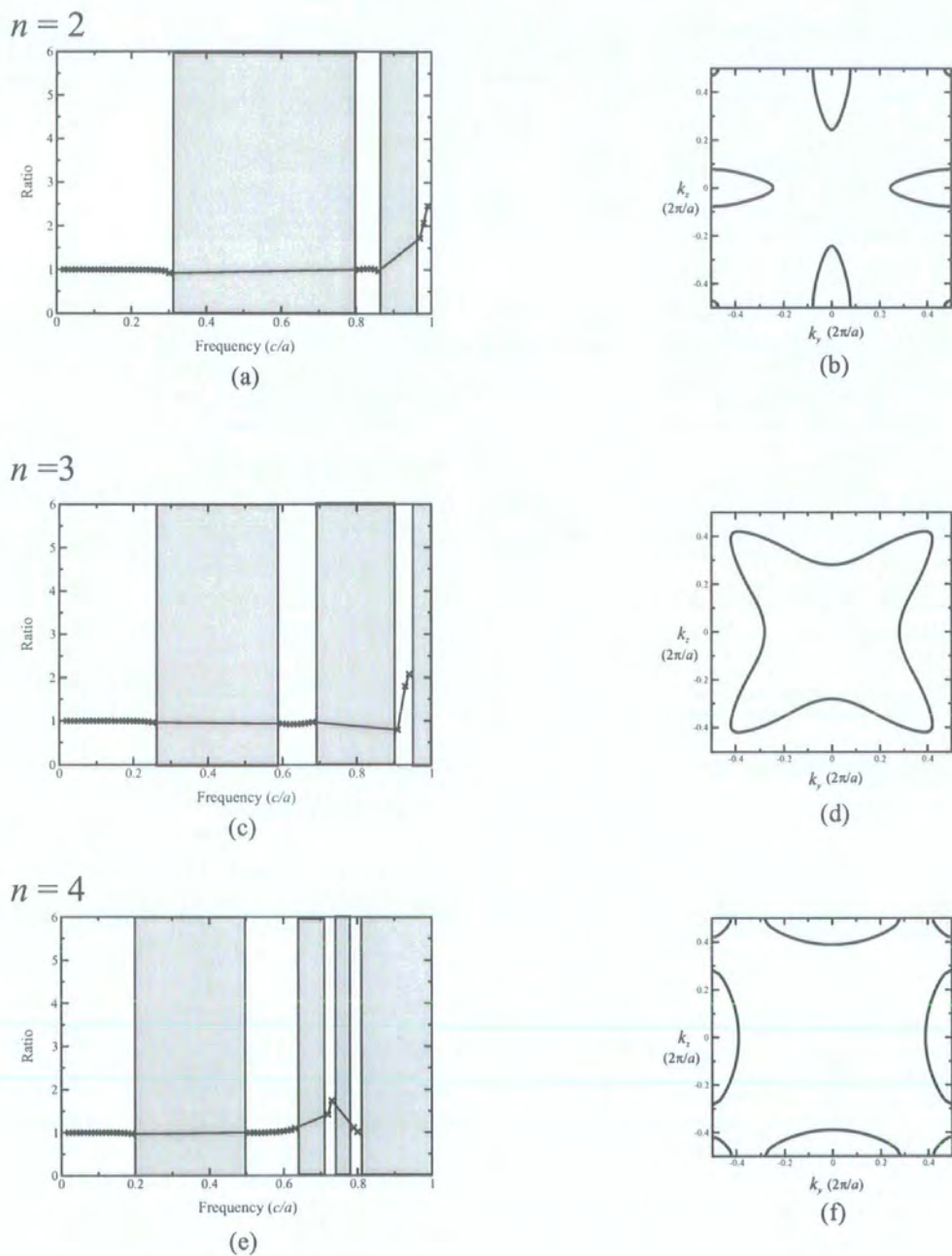
n	r	$\omega$ (c/a)	I
2	0.1a	0.97	4.1
3	0.3a	0.97	3.8
4	0.4a	0.87	2.8
5	0.3a	0.96	5.1
6	0.2a	0.64	1.9

**Table 5.3:** Highest anisotropy ratios for each refractive index value (TE polarisation).

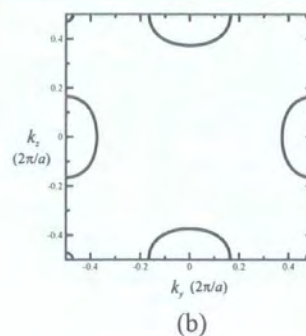
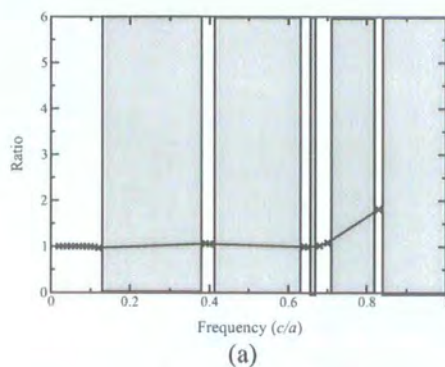
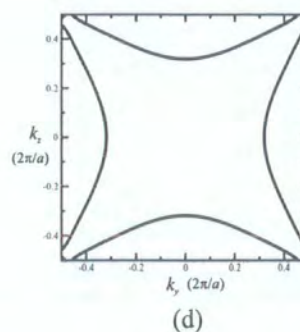
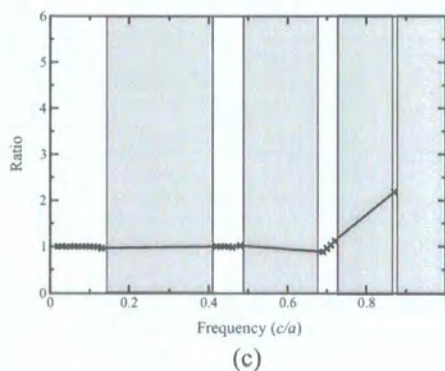
the anisotropy ratio at each refractive index. The results are summarised in Table 5.3. The results showed no great improvement in the anisotropy ratio with increased refractive index. The only structure to possess a similarly interesting value occurred for the structure with  $n = 5$  and  $r = 0.3a$ . The dispersion surface was discarded due to the lack of advantages over the  $n = 2$ ,  $r = 0.1a$  surface combined with a currently untenable refractive index and the previously discussed convergence issue. Thus, it was concluded that the optimum TE structure is the low refractive index, low rod radius structure described in the previous section.

### TM Modes

Similar results to those of the TE polarisation were seen when the TM polarisation was studied. These are shown in Fig. 5.15 and Fig. 5.16. and summarised in Table 5.4. Note that the weakness of the simple ratio approach may be seen in Fig 5.16b. The ratio value is high but the surface is not continuous and consists of two isotropic curves. Whilst this is a possible failing of the ratio approach if any other high ratio values had existed for the same refractive index these would also have been considered. In this instance this was unnecessary as the other ratio values did not differ significantly from unity. The TM results also show no significant benefit from the use of high refractive indices and high rod radii.



**Figure 5.15:** TM anisotropy ratios for the rod radii with the highest peak values. The ratios have been plotted as a function of frequency (a, c, e) and the peak value dispersion surfaces are shown (b, d, f).

$n = 5$  $n = 6$ 

**Figure 5.16:** TM anisotropy ratios for the rod radii with the highest peak values. The ratios have been plotted as a function of frequency (a, c) and the peak value dispersion surfaces are shown (b, d).

$n$	$r$	$\omega (c/a)$	$I$
2	0.4a	0.55	2.8
3	0.2a	0.94	2.1
4	0.2a	0.73	1.7
5	0.3a	0.83	1.8
6	0.2a	0.87	2.2

**Table 5.4:** Highest anisotropy ratios for each refractive index value (TM polarisation).

## 5.7 Refraction Properties

The previous section presented results for an optimisation study on bandstructure anisotropy for the square lattice type. The optimum system was selected as a structure with rods of refractive index  $n = 2$  and radius  $r = 0.1a$  operating at a frequency of  $\omega = 0.97c/a$  with TE polarised light. This section considers the refraction properties of such a structure using the method described in Section 4.12.

### 5.7.1 Angle Sensitivity

Anisotropic bandstructures are likely to give a photonic crystal refraction properties which differ greatly from those of a uniform material. The dispersion surface for the optimum structure is shown in Fig. 5.17a. There is a limited range of  $k_z$  values for which a single refraction angle exists. These are shaded on the diagram and limit the  $|k_z|$  to less than  $0.1(2\pi/a)$ . This is equivalent to limiting the angle of incidence to approximately 3 degrees. It is of interest to make a comparison between the photonic crystal refraction properties and those of a uniform material with the same average refractive index ( $n = 1.03$ ). The simple application of Snell's Law, equation (4.105), produces the result that the angle of refraction for the uniform material would be less than 3 degrees. Fig. 5.17b shows the dispersion properties of the photonic crystal structure. Angles of refraction of up to 62 degrees are achieved for the narrow range of incident values. Such performance is comparable to the superprism effects reported for the more complex hexagonal lattice in the literature. For example Kokaka *et al.* [47] and also Park *et al.* [194] have reported values of the order of 70 degrees for a 7 degree angle of incidence variation. Here a simple square lattice has been shown to produce comparable performance.

### 5.7.2 Wavelength Sensitivity

In addition to a sensitivity to initial angle of incidence the anisotropic equi-frequency lines may be highly wavelength dependent. One of the possible applications suggested for superprisms is the separation of different wavelengths of light. This may be of use in wavelength division multiplexing devices. Fig. 5.18 shows the dispersion properties for a 1% increase and 1% decrease in the incident frequency. It is immediately evident that the 1%

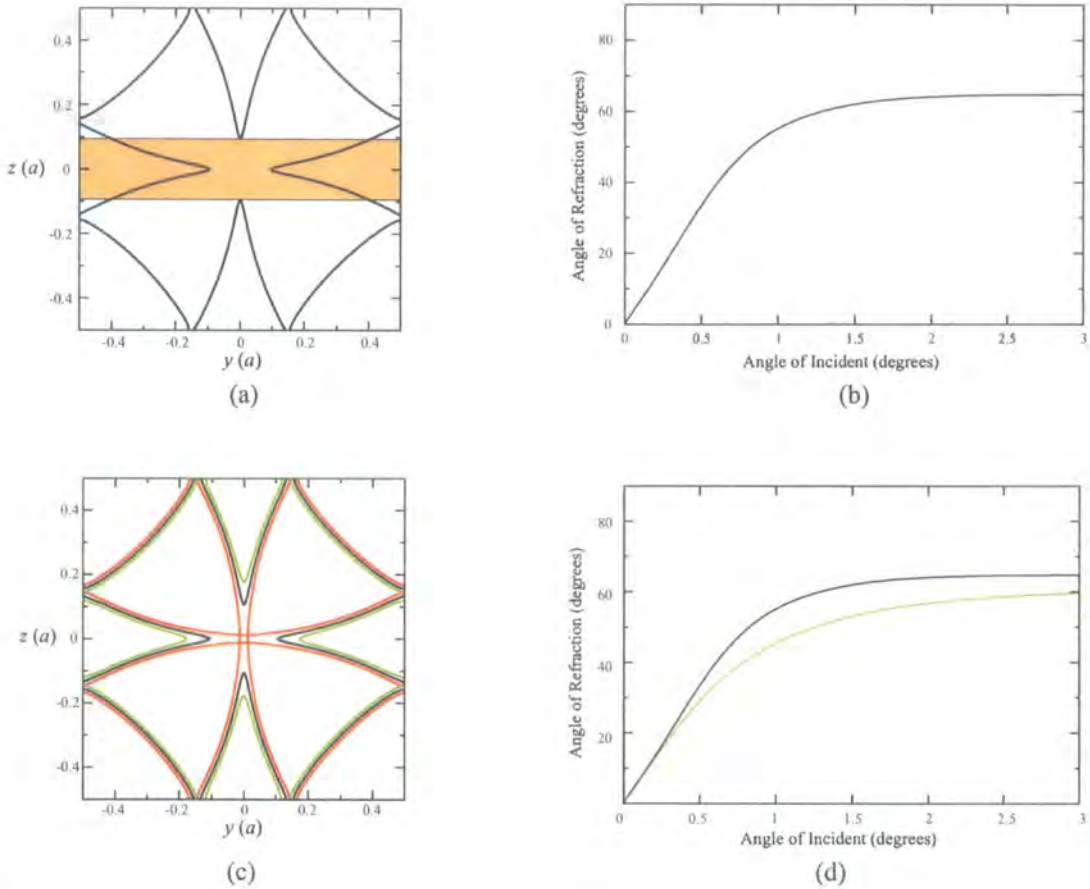


**Figure 5.17:** Dispersion surface for an optimum structure (a). The refraction properties are also shown for changes in angle of incidence (b). In (c) the dispersion surface for the optimum structure is shown with the black line indicating the original frequency, the green a 1% frequency increase and the red a 1% frequency decrease. The refraction properties are also shown (d). Note there is no 1% decrease line in (d) due to the existence of multiple refraction angles for a given angle of incidence.

decrease in frequency produces multiple refraction angles. For a 1% frequency increase the structure still possesses a single refraction angle. The dispersion properties for the 1% increase have been plotted in Fig 5.18b. There is up to a 10 degree difference between the two curves in the figure indicating that the structure may be of use for wavelength separation applications.

## 5.8 Conclusions

Two-dimensional photonic crystals with a square lattice have been considered. Initially bandstructures were produced directly comparable to data available in the literature to ensure the theoretical methods described in Chapter 4 had been correctly implemented. The original work presented was a discussion of the refraction properties of photonic crystals and particularly the square lattice. Optimisation calculations were presented which showed a dramatic variation in the angle of refraction was achievable compared to a uniform medium with the same average refractive index. For a 3 degree variation in incident angle ( $\pm 1.5$  degrees) a 120 degree variation ( $\pm 60$  degrees) in refracted angle was predicted. However, the maximum angle of incidence was only 3 degrees before multiple refraction angles were seen. This makes the device only of use for very small angles of incidence. Wavelength variation effects were also seen with a 1% increase in wavelength causing up to a 10 degree variation in the angle of refraction.

# Chapter 6

## Hexagonal Lattice Calculations

### 6.1 Introduction

The hexagonal, or triangular, lattice type is the most commonly implemented for the fabrication of two-dimensional photonic crystal structures. The popularity of the lattice type is due to the advantages which it offers, compared to the square lattice, for band-gap applications. It is believed that structures which present the most spherical (for three-dimensional) or circular (for two-dimensional) Brillouin Zones offer the greatest potential for large absolute photonic band-gaps [195, 197]. In the previous chapter it was stated that the presence of complete band-gaps was not a necessity for the existence of enhanced dispersion characteristics. This was further confirmed by the identification of an optimum structure which did not possess a complete band-gap. However, the higher order of symmetry of the hexagonal lattice Brillouin Zone may provide the potential for the lattice type to also display improved dispersion characteristics.

Superprism behaviour is attributable to the sharp features of anisotropic dispersion surfaces. In the previous chapter bandstructure anisotropy was considered through the examination of the difference in wavevector magnitude for equi-frequency surfaces in the direction of the high symmetry points,  $\Gamma - X$  and  $\Gamma - M$ . A large difference implied high curvature between the two points. The hexagonal lattice also possesses two high symmetry points. However, the complete hexagonal unit cell contains 12 such symmetry points compared to 8 for the square unit cell. The additional unit cell symmetry is expected to produce a higher number of sharp features per unit cell. More importantly, if the difference between the max-

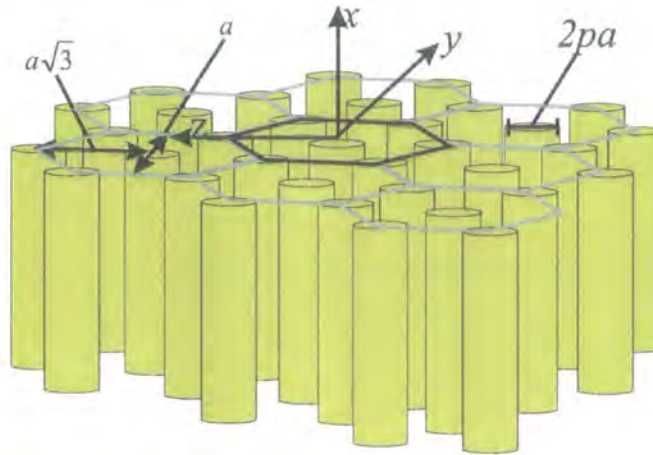


**Figure 6.1:** The hexagonal lattice type with a lattice constant  $a$  and rods of diameter  $2pa$ . The lattice consists of dielectric rods with a different refractive index to the background medium. A hexagonal unit cell is outlined in black demonstrating the repeating unit from which the entire crystal is assembled.

imum and minimum wavevector magnitudes is similar, then the surface curvature must be greater to allow for the increased number of maximum and minimum values in the Brillouin Zone. In this chapter the refraction properties of the hexagonal lattice type are considered.

A number of superprism studies involving the hexagonal lattice type are available in the literature [47, 48, 194, 196]. Existing studies have tended to focus on testing fabricated structures to determine their dispersion characteristics. In this work an alternative, less restrictive theoretical method of study is adopted. The study was undertaken with the aim of optimising the dispersion characteristics for the hexagonal lattice type. In this chapter a general discussion of electromagnetic fields of the hexagonal structure precedes the main refraction study. Dispersion characteristics are discussed and a systematic range of structures is considered allowing the superprism effect to be optimised with respect to refractive index, rod radius and frequency.

## 6.2 The Hexagonal Lattice

A two-dimensional hexagonal lattice is shown in Fig. 6.1. The lattice is also often referred to as a triangular lattice. The simplest spatially repeating unit which may be used to construct the entire lattice is a hexagon. Accordingly, throughout this work the lattice is referred to as the hexagonal lattice.

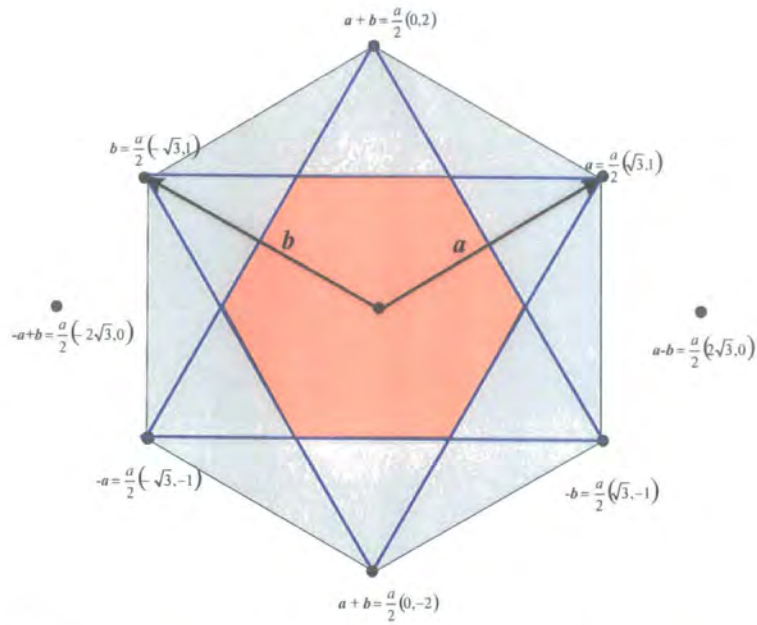


**Figure 6.2:** The hexagonal unit cell (grey) contains a single uniquely owned lattice point and six other lattice points each shared with three other unit cells. The figure shows the lattice points with their coordinates and additionally the single lattice point Wigner-Seitz unit cell (pink).

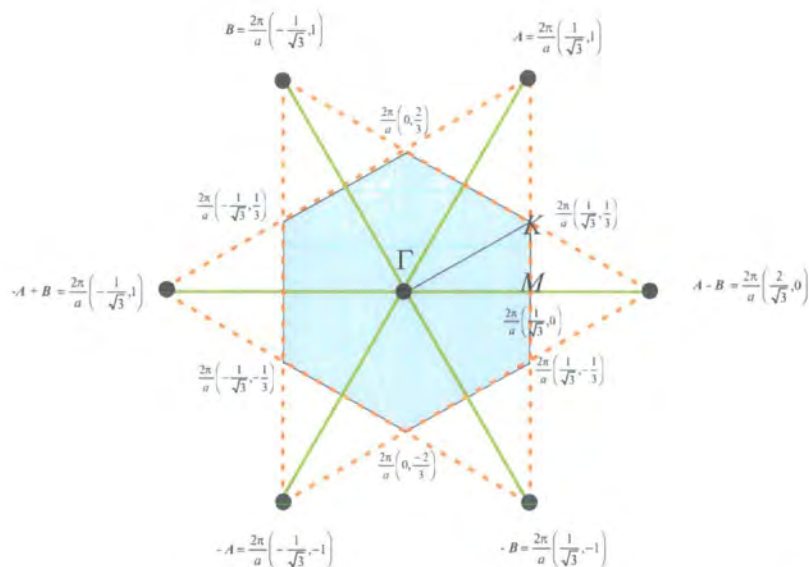


**Figure 6.3:** Brillouin Zone (light green) for hexagonal lattice type with lattice constant  $a$ . Construction lines are shown with reciprocal lattice vectors in green and their bisectors indicated by dashed orange lines.

### 6.2.1 Primitive Lattice Vectors

The two-dimensional hexagonal lattice of interest may be constructed from primitive lattice vectors in a manner similar to that previously applied to the square lattice. It is useful to define the full three-dimensional primitive lattice vectors as these may be used to derive the reciprocal lattice vectors. The primitive lattice vectors are given in equation (6.1), with  $\hat{i}$ ,  $\hat{j}$  and  $\hat{k}$  unit vectors in the  $x$ ,  $y$  and  $z$  directions respectively. The two in-plane vectors,  $\mathbf{a}$  and  $\mathbf{b}$  have also been indicated on Fig. 6.2 along with the lattice constant  $a$ . In addition Fig. 6.2 shows the Wigner-Seitz primitive unit cell. This is a representation of the unit cell with a single lattice point per unit cell. The Wigner-Seitz unit cell is particularly useful as it also gives the first Brillouin Zone when the lattice is converted into reciprocal space. In a general three-dimensional hexagonal lattice the two-dimensional hexagonal planes would be separated by some arbitrary distance,  $c$ . Hence,

$$\begin{aligned} \mathbf{a} &= \sqrt{3} \left(\frac{a}{2}\right) \hat{j} + \left(\frac{a}{2}\right) \hat{k} \\ \mathbf{b} &= -\sqrt{3} \left(\frac{a}{2}\right) \hat{j} + \left(\frac{a}{2}\right) \hat{k} \\ \mathbf{c} &= c \hat{i} \end{aligned} \quad (6.1)$$

The two-dimensional lattice vectors,  $\mathbf{R}$ , give all the possible in plane lattice points within the structure through the linear combination of the appropriate primitive vectors. The entire crystal lattice, consisting of multiple unit cells, can be calculated through the use of a range of positive and negative values for the integers  $n_a$  and  $n_b$  in equation (6.2).

$$\mathbf{R} = n_a \mathbf{a} + n_b \mathbf{b} \quad (6.2)$$

### 6.2.2 Reciprocal Lattice Vectors

The plane-wave bandstructure calculation utilises a summation over reciprocal lattice vectors making it necessary to construct the primitive reciprocal lattice vectors. These may be calculated from the definition of a reciprocal lattice vector, together with the requirement that  $\mathbf{g} \cdot \mathbf{R} = 2n\pi$  (from equation 4.16). Equation (6.3) shows this condition for the system

under consideration.  $\mathbf{A}$ ,  $\mathbf{B}$  and  $\mathbf{C}$  are the primitive reciprocal lattice vectors.

$$\begin{aligned} \mathbf{R} \cdot \mathbf{g} &= (n_a \mathbf{a} + n_b \mathbf{b} + n_c \mathbf{c}) \\ &\cdot (n'_a \mathbf{A} + n'_b \mathbf{B} + n'_c \mathbf{C}) = 2n\pi \end{aligned} \quad (6.3)$$

Equation 6.3 is assured through the choice of primitive reciprocal lattice vectors of the form given in equation (6.4). The well known property of the cross product,  $\mathbf{x} \cdot (\mathbf{x} \times \mathbf{y}) = 0$ , for any two vectors  $\mathbf{x}$  and  $\mathbf{y}$  has been applied [87].

$$\begin{aligned} \mathbf{A} &= 2\pi \frac{\mathbf{b} \times \mathbf{c}}{\mathbf{a} \cdot \mathbf{b} \times \mathbf{c}} = \frac{2\pi}{a} \left[ \frac{1}{\sqrt{3}} \hat{\mathbf{j}} + \hat{\mathbf{k}} \right] \\ \mathbf{B} &= 2\pi \frac{\mathbf{c} \times \mathbf{a}}{\mathbf{a} \cdot \mathbf{b} \times \mathbf{c}} = \frac{2\pi}{a} \left[ -\frac{1}{\sqrt{3}} \hat{\mathbf{j}} + \hat{\mathbf{k}} \right] \\ \mathbf{C} &= \frac{2\pi}{c} \hat{\mathbf{i}} \end{aligned} \quad (6.4)$$

For the bandstructure calculation the complete set of two-dimensional reciprocal lattice vectors are required. These are given by equation (6.5), where  $n_A$  and  $n_B$  are integers which differ from the real space integers:

$$\mathbf{g} = n_A \mathbf{A} + n_B \mathbf{B} \quad (6.5)$$

### 6.2.3 Brillouin Zone

The reciprocal lattice vectors are shown in Fig. 6.3 together with the Brillouin Zone for the hexagonal structure. For a description of the construction of Brillouin Zones from reciprocal lattice vectors see Section 5.2. The Brillouin Zone possesses three symmetry points of interest; the  $\Gamma$ ,  $M$  and  $K$  positions which are  $(0, 0)$ ,  $2\pi/a(1\sqrt{3}, 0)$  and  $2\pi/a(1\sqrt{3}, 1/3)$  respectively. The symmetry of the Brillouin Zone significantly reduces the range of wavevectors over which bandstructure calculations must be performed. The reflection and rotation of a  $\Gamma$ - $X$ - $M$  segment allows the complete Brillouin Zone to be described using calculations performed over the irreducible segment, one twelfth of the size of the complete Brillouin Zone. This leads to large computational savings.

## 6.3 Results

### 6.3.1 Convergence

In Section 5.3 the number of terms required in the Fourier expansion of the dielectric constant was considered for the square lattice. In this section convergence is considered for a hexagonal structure consisting of air holes ( $n = 1$ ,  $r = 0.2728a$ ) with an oxide coating ( $n = 1.5$ ,  $r = 0.3443a$ ) in a background material of GaAs ( $n = 3.42$ ). The structure was chosen to coincide with an experimental structure fabricated by Krauss *et al.* [46] which is used in the following section as an example of a bandstructure calculation of a hexagonal lattice.

Initially convergence was considered for the first six bands at the  $\Gamma$  point and for both the TE (Fig. 6.4a) and TM (Fig. 6.4b) modes. The results indicate that the sixth frequency band required the highest number of plane-waves for convergence to be achieved for the TM polarisation and the fourth band for the TE polarisation. Concentrating on the sixth band for the TM and fourth for the TE, Fig 6.4b shows the convergence at the three high symmetry points within the Brillouin Zone. The point identified as the slowest to converge was the  $\Gamma$  point for the TM polarisation. The final plot in Fig 6.4e examines the effect of the rod radius (with no oxide layer) at this point to aid the choice of a suitable number of plane-waves to produce the required level of accuracy. The choice of 805 plane-waves for the hexagonal lattice will give convergence to approximately 1% of the 1945 plane-wave solution for all rod radii. Although 805 plane-waves were used in Section 6.2, as previously (Section 5.3), the optimisation study made use of fewer plane-waves (337) due to the limitations imposed by the available computational resources.

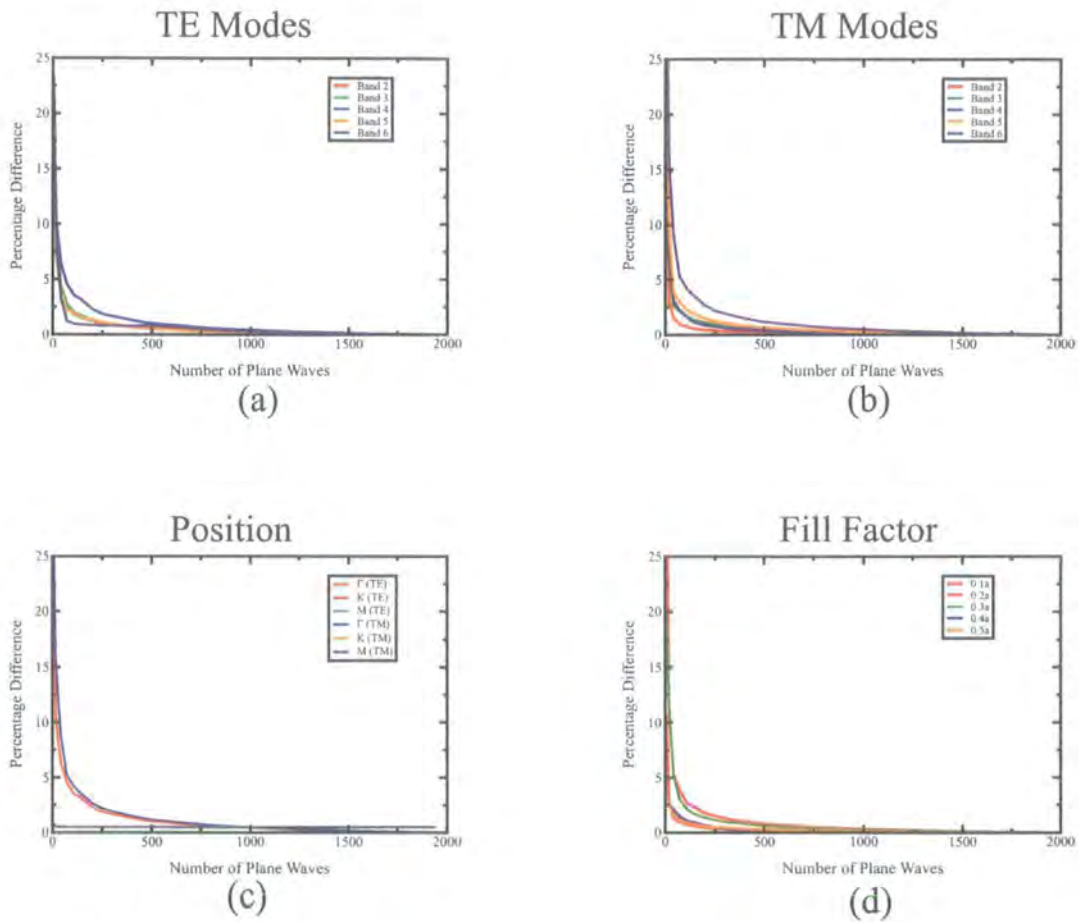


**Figure 6.4:** Convergence for a hexagonal lattice type (relative to 1945 plane-wave solution) as a function of band for the TM modes (a) and TE modes (b). The effect of position within the Brillouin zone on convergence is also shown (c) and the slowest to converge point has its convergence considered as a function of rod radius (d).

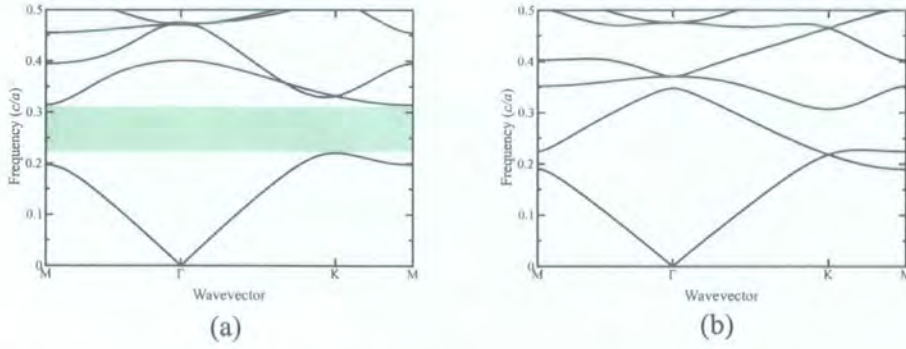


**Figure 6.5:** Bandstructure calculations for the structure consisting of 27% air ( $n=1$ ), 16% oxide ( $n=1.5$ ) and 57% semiconductor ( $n=3.42$ ). Both the TE (a) and TM (b) bandstructures are shown and demonstrate exact agreement with the literature values to the number of significant figures quoted.

## 6.4 Bandstructures

A comparison may be made with literature values for standard bandstructures to enable the validation of the basic bandstructure routines used in this study. In this section a structure fabricated by Krauss *et al.* [46] was selected from the literature to serve as an example structure. The particular example was selected due to the bandstructures being presented with numerical values at various bandstructure points. Figure 6.5 shows agreement, to at least the published number of significant figures, between the code used here and the results published in the reference. The following sections make use of similar algorithms to those used for the standard bandstructure calculation. The agreement with literature values for the standard bandstructures allows for confidence with the implemented algorithms.

### 6.4.1 Field Profiles

Field profiles help in understanding the advantages of the hexagonal lattice over the square lattice for band-gap applications. In Section 5.4 the square lattice was seen to possess a band-gap for the TM polarisation. This was explained by the concentration of the electric field in either the rods or the background material for the first two bands. If the bandstructure diagrams in Fig. 6.5 are examined then it may be seen that the TE mode for this particular hexagonal structure possess a complete band-gap. TE band-gaps are known to be favoured by structures which contain connected veins rather than holes or rods [187]. Consider the TE

TE			
	Band 1	Band 2	Band 3
K point	0.04	0.73	0.32
M point	0.05	0.56	0.53
TM			
	Band 1	Band 2	Band 3
K point	0.02	0.02	0.02
M point	0.02	0.02	0.01

**Table 6.1:** The fraction of the electric field energy found in the holes for TE and TM modes at the high symmetry X and M points. The structure is taken from [46].

field profiles shown for the first two bands of the hexagonal lattice in Fig. 6.6. It may be seen that the system acts as a veined structure with veins which are the regions between two holes. For example, the region around  $(0.58a, 0)$  in Fig 6.6d or the region around  $(-0.2a, 1.2a)$  in Fig. 6.6f. The first band has the majority of the field intensity in the holes and the second band in these veins. To aid with the comparison the proportion of the electric field intensity present in the rods (including coating) has been calculated from equation (5.8). These are shown in Table 6.1. A significant fill factor difference may be seen between the first and second TE bands.

If the TM mode is considered, see Fig. 6.7, then the structure is seen to be acting as a series of ‘spots’ or rods. The spots are the regions where three holes meet. For example the region around  $(0.5a, 2a)$  in Fig. 6.7d, or the region around  $(0.9a, 0.6a)$  in Fig. 6.7f. Although there is no complete band-gap for this particular hexagonal structure the spot like behaviour of the lattice does suggest there may be for different structures based on the same lattice type. This is discussed further in the following section.

## 6.4.2 Complete Band Gap

It has been explained that the hexagonal lattice is of particular interest for photonic band-gap applications as it can possess a large absolute photonic band-gap. The hexagonal lattice considered in the previous section did not possess an absolute band-gap. However, if a uniform high refractive index background is considered with air holes then it is possible to achieve an absolute band-gap. Fig. 6.8 shows the frequency width of the absolute band-gaps against hole radii for a range of refractive index backgrounds. Provided that the refractive

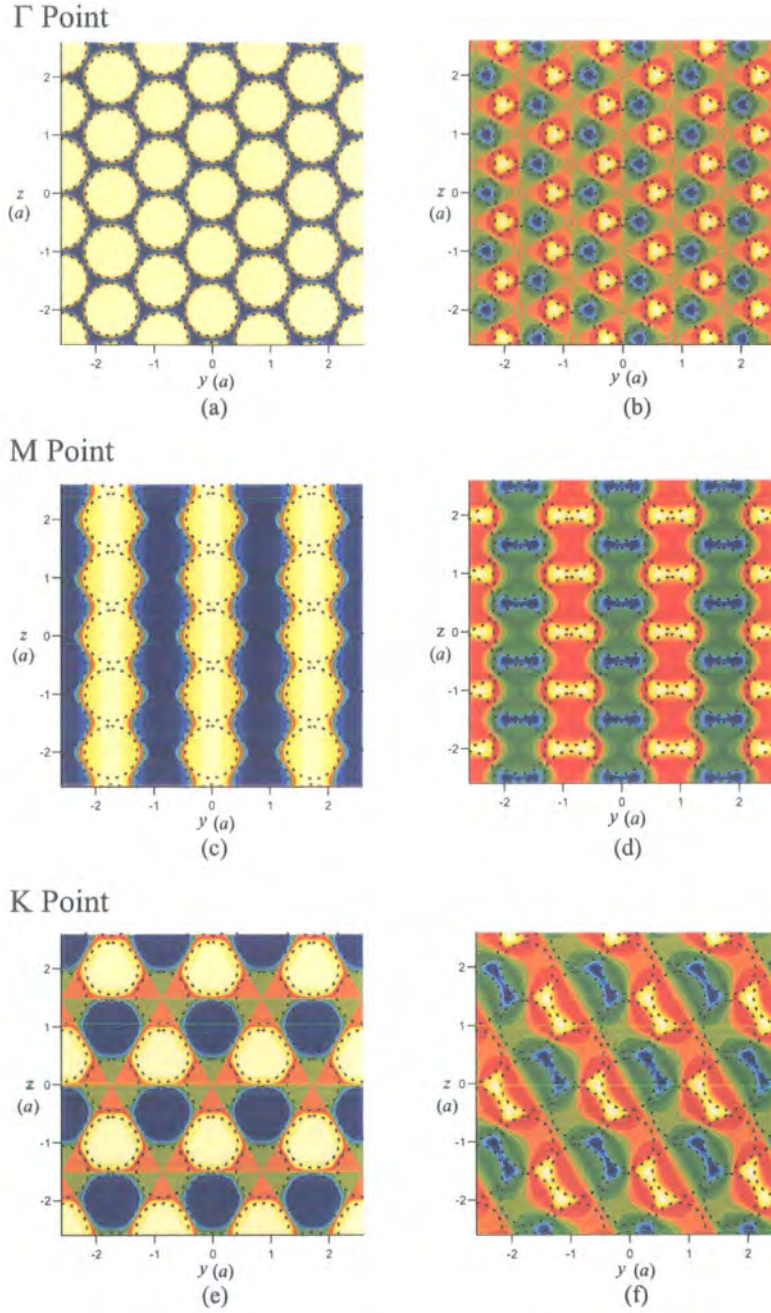


**Figure 6.6:** TE magnetic field profiles for the first (left column) and second (right column) bands at the high symmetry points indicated. For the second band at the  $K$  point one of two degenerate solutions has been plotted. Note that (a) shows the dielectric pattern of the structure plotted from the Fourier coefficients. For key see Fig 5.6.

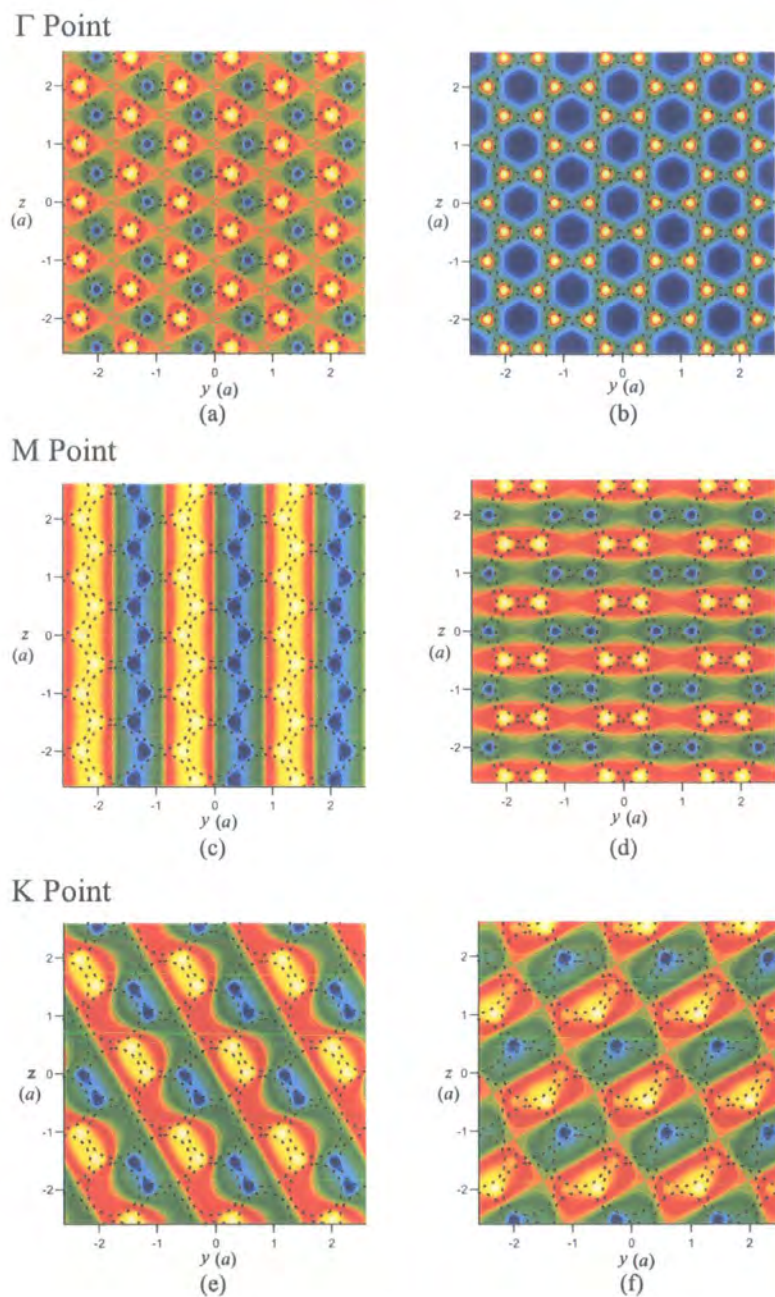


**Figure 6.7:** TM electric field profiles for the second (left column) and third (right column) bands at the high symmetry points indicated. For the second band at the  $K$  point one of two degenerate solutions has been plotted. For key see Fig 5.6.

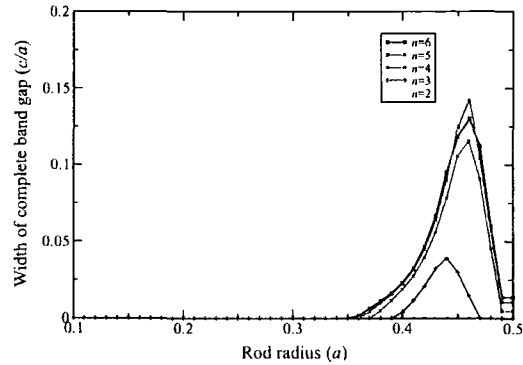


**Figure 6.8:** Width of absolute band-gaps for a variety of refractive indices and rod radii.

index contrast and hole radii are of suitable values then the figure shows absolute band-gaps exist. As previously stated this is due to the hexagonal lattice acting as connected veins for the TE polarisation and isolated spots for the TM polarisation.

If the bandstructure for the optimum structure is considered (Fig 6.4) with a background index of 5 and a rod radius of  $r = 0.46a$ , then the complete gap can be seen. The gap opens up above the first and second TE modes, and second and third TM modes, thus allowing a gap in both frequencies for a range of values. The interest from the point of view of refraction studies on the hexagonal lattice is the effect of this band-gap on the band anisotropy around it. The TE and TM bands for the optimum structure are shown below. These can be compared to the earlier bandstructures for the hexagonal lattice which do not show a complete band-gap. The presence of the band-gap seems to compress the bandstructure either side of it leading to there being less chance of single refraction angle conditions. However, the effect on bandstructure anisotropy is not clear without further investigation,

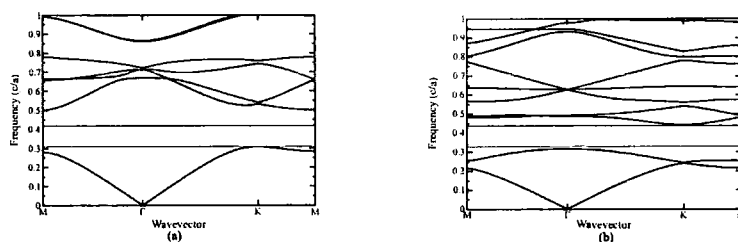


**Figure 6.9:** The TE (a) and TM (b) bandstructures for the optimum absolute band-gap structure. The range of frequencies forming the absolute band-gap are shaded.

although just above the TM band gap there appears an area of high potential for anisotropic bandstructures.

## 6.5 Refraction Properties

### 6.5.1 Bandstructure Anisotropy

The enhanced refraction properties of photonic crystals arise due to the sharp features in equi-frequency dispersion surfaces. In the previous chapter an anisotropy ratio was used as a suitable indicator for the existence of highly anisotropic dispersion surfaces. When the hexagonal lattice was considered it was evident that the sharp features of interest tended to occur in either the  $\Gamma - M$  or  $\Gamma - K$  directions. Rather than considering anisotropy in terms of the wavevector magnitude in two reference directions, a more direct indicator of refraction properties was used. The interesting refraction properties of photonic crystals arise due to 'peaks' in the dispersion surface. The sharper an individual peak, the greater the angular deviation for wavevectors which interact either side of it. The two natural reference directions were used,  $\Gamma - M$  and  $\Gamma - K$ . However, rather than simply considering the level of anisotropy of a dispersion surface, the additional computational expense was undertaken to calculate the sharpness of the dispersion surface in the two reference directions.

### 6.5.2 Gradient Method

To demonstrate the approach employed consider the previously shown TM bandstructure for the Krauss *et al.* experimental structure, shown again as Fig. 6.10a. The standard bandstructure plot has three frequencies of interest indicated. The dispersion surface for the lowest frequency ( $\omega = 0.15c/a$ ) indicated is shown in Fig. 6.10b. The dispersion surface is an uninteresting circular pattern. If the gradient of the surface was calculated in the  $\Gamma - M$  direction it would be a large number. To assist with identifying interesting structures it was decided to examine the inverse gradient,  $dk_z/dk_y$ . The quantity was evaluated using a point on the dispersion surface in the  $\Gamma - M$  and a point on the surface with a wavevector direction which differed by 1 degree. A small number for the quantity would therefore correspond to approximately circular type behaviour and, easily identifiable, large numbers to interesting

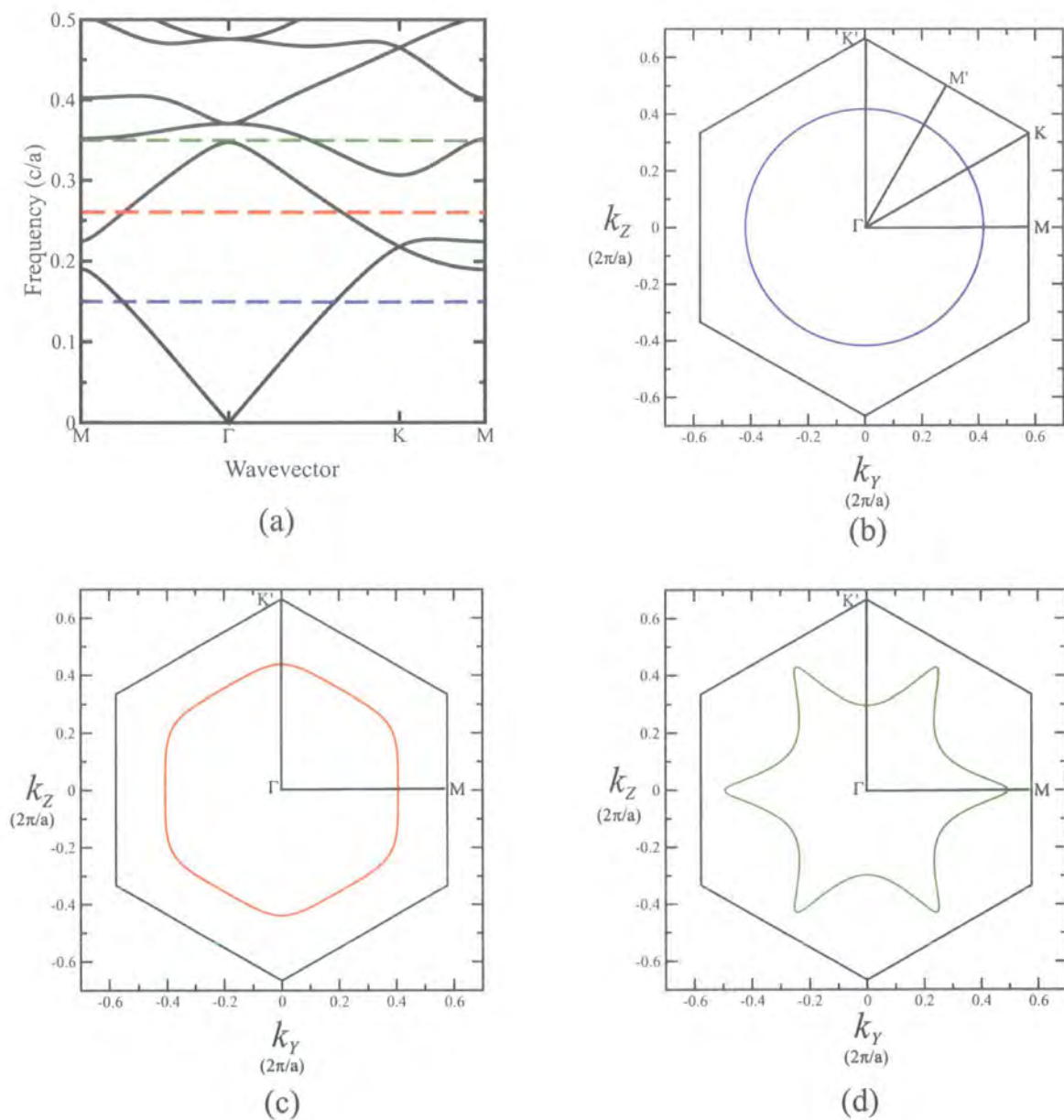


**Figure 6.10:** A bandstructure is shown (a) with three frequencies indicated for further consideration. The lowest frequency indicated produces a circular dispersion surface (b), the middle frequency a slightly anisotropic surface (c) and the highest frequency a highly anisotropic surface (d).

features.

For the  $\Gamma - K$  reference direction, rather than directly considering this direction the equivalent  $\Gamma - K'$  direction was used. This allows for easier comparison between the two reference directions through the use of the gradient and inverse gradient. If the gradient ( $dk_y/dk_z$ ) is considered at the dispersion surface in the  $\Gamma - K'$  direction then a low number is also equivalent to circular behaviour.

To see how this worked in practice consider the frequency of  $\omega = 0.26c/a$ , in Fig. 6.10c. The dispersion surface has some increased curvature around the  $\Gamma - K'$  direction, which will produce a slightly larger gradient in this direction. The  $\Gamma - M$  direction in this instance shows little curvature and accordingly a low inverse gradient. The final frequency indicated for discussion is at  $\omega = 0.35c/a$  and produces a star type pattern. In the  $\Gamma - K'$  direction the gradient is low but the inverse gradient is large in the  $\Gamma - M$  direction. The gradient method provides a more direct method to examine the potential of a structure for superprism behaviour.

## 6.6 Optimisation Results

The strategy selected for finding the optimum hexagonal structure and frequency was similar to the approach adopted in Section 5.6 for the square lattice. The same range of refractive indices, rod radii and frequencies were considered (see Table 5.2). However, in this instance the structures considered consisted of circular air holes in a higher refractive index background material. The choice was believed to correspond with the most convenient arrangement for structure fabrication.

The inverse gradients for the  $\Gamma - M$  direction were calculated using the complex bandstructure methods to find the real solutions in the directions with angles of  $\theta = 0^\circ$  and  $\theta = 1^\circ$  to the  $y$ -axis. Similarly in the  $\Gamma - K$  direction gradients were found by conducting complex bandstructure calculations at angles of  $\theta = 89^\circ$  and  $\theta = 90^\circ$ . The entire range of values was considered and the largest magnitude gradients (or inverse gradients) were found for each polarisation at each refractive index value. The results are given in Table 6.2 for the  $\Gamma - M$  direction, and in Table 6.3 for the  $\Gamma - K$  direction. Only instances when a single curve existed in the direction of interest were considered.

Whilst no significant trends were identified from the table it is possible to identify the extreme values; both large positive and negative values were found. The difference between a positive and negative gradient may be seen by considering Fig. 6.11. The figure shows the TE  $n = 4$ ,  $r = 0.41a$ ,  $\omega = 0.41c/a$  dispersion surface, which has a positive gradient in the  $\Gamma - M$  direction. It may be seen that a positive gradient, or inverse gradient, indicates a surface where the wavevector in the direction of interest is at a minimum, rather than the usual maximum value on the surface.

From the results four main points were identified for further consideration, the sharpest features for both the TE and TM polarisations at both the  $M$  and  $K$  points. The corresponding dispersion surfaces are shown in Fig. 6.12. The surfaces show that peaks may be produced in either the  $\Gamma - M$  or  $\Gamma - K$  directions. The optimum structure structure is clearly the TM polarisation dispersion surface with  $n = 2$ ,  $r = 0.4a$  and  $\omega = 0.65c/a$ . The low refractive index is beneficial as it means that convergence is to a higher level than would be seen for the higher refractive index contrast structures.

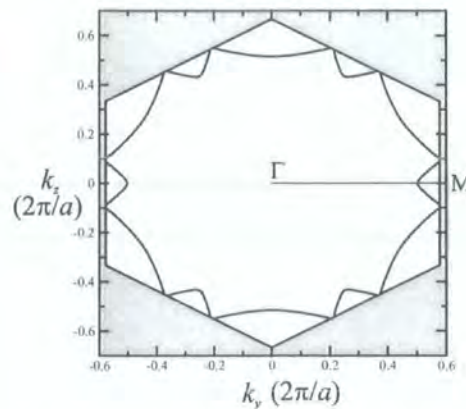


**Figure 6.11:** An example of a positive gradient in the  $\Gamma - M$  direction. The dispersion surface is for  $n = 2$ ,  $r = 0.4a$  and  $\omega = 0.65c/a$ .

Refractive Index	Rod Radius	TE	
		Frequency	1/Gradient
2	0.3	0.63	-0.1
3	0.4	0.58	-0.5
4	0.1	0.41	0.3
5	0.1	0.33	0.2
6	0.3	0.74	0.1
Refractive Index	Rod Radius	TM	
		frequency	1/Gradient
2	0.4	0.65	-1.4
3	0.5	0.71	-0.3
4	0.5	0.64	-0.2
5	0.5	0.57	-0.3
6	0.5	0.51	-0.2

**Table 6.2:** Extreme inverse gradient values for the  $\Gamma - M$  direction.

Refractive Index	Rod Radius	TE	
		Frequency	Gradient
2	0.3	0.78	-0.4
3	0.3	0.55	-0.2
4	0.2	0.63	0.2
5	0.3	0.61	-0.2
6	0.3	0.51	-0.1
Refractive Index	Rod Radius	TM	
		Frequency	Gradient
2	0.1	0.34	-0.6
3	0.1	0.23	0.2
4	0.1	0.17	-0.5
5	0.3	0.58	-0.2
6	0.5	0.75	0.4

**Table 6.3:** Extreme gradient values for the  $\Gamma - K$  direction.

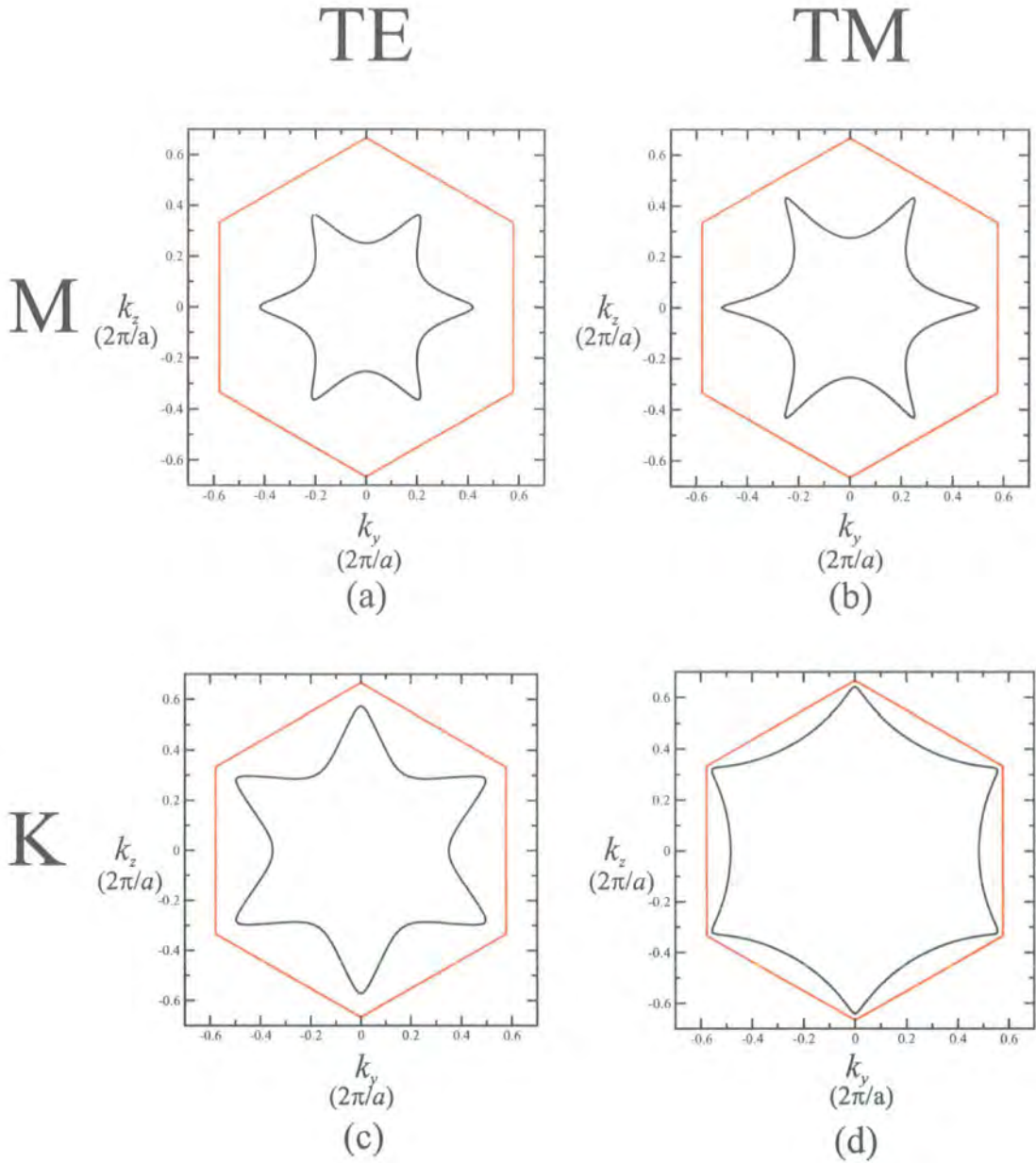


**Figure 6.12:** The sharpest dispersion surfaces identified for features in both the  $\Gamma - M$  and  $\Gamma - K$  directions. a) TE  $n = 3$ ,  $r = 0.4a$ ,  $\omega = 0.58c/a$  b) TM  $n = 2$ ,  $r = 0.4a$ ,  $\omega = 0.65c/a$  c) TE  $n = 2$ ,  $r = 0.3a$ ,  $\omega = 0.78$  d) TM  $n = 2$ ,  $r = 0.1a$ ,  $\omega = 0.34c/a$ .

## 6.7 Dispersion Characteristics

The previous section identified the optimum hexagonal structure and frequency for enhanced dispersion characteristics. In this section the refraction characteristics of the structure are calculated using the method given in Section 4.12. The light is incident in the positive  $y$  direction, hence the wavevector component parallel to the interface is the  $k_z$  component and this must be conserved at the interface. The optimum structure is shown in Fig. 6.13a with the single refraction angle  $k_z$  range indicated by the shaded region. The dispersion characteristics are shown (Fig. 6.13b) for situations when there is only one refraction angle. This limits the angle of incidence to  $\pm 25$  degrees which is much larger than the range found for the optimum square lattice in the previous chapter.

### 6.7.1 Angular Deviation

Fig 6.13b shows how the angle of refraction varies as the angle of incident is increased. The plot shows a peak at 2 degrees which produces an angle of refraction of 74 degrees. A 4 degree change in the angle of incidence is able to produce a deviation of 148 degrees in the refracted wave. The performance is superior to that calculated for the square lattice and that published by Kosaka *et al.* [47] for their experimental hexagonal structure. Their complex structure produced angular deviations approximately 10 times the incident angle deviations. The results shown here demonstrate a refracted angle deviation 37 times the incident angle deviation. It is also interesting to note the negative refraction angles. These occur for angles of incidence above 20 degrees, or  $k_z$  values above  $0.2a^{-1}$ .

### 6.7.2 Frequency Deviation

One of the potential applications suggested for superprism devices is for the separation of a multiple frequency beam into its individual component frequencies. The frequency sensitivity of the optimum structure was considered by calculating the effect of a 1% increase or 1% decrease in incident frequency. The effect on the dispersion surface may be seen in Fig 6.13c.

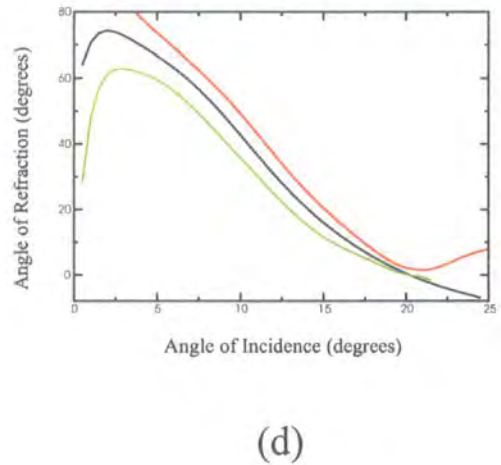
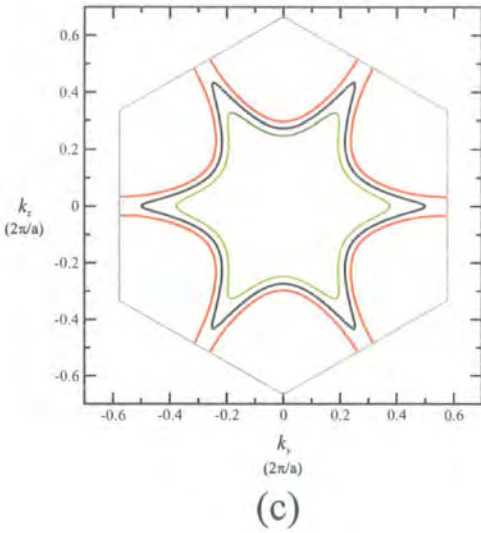
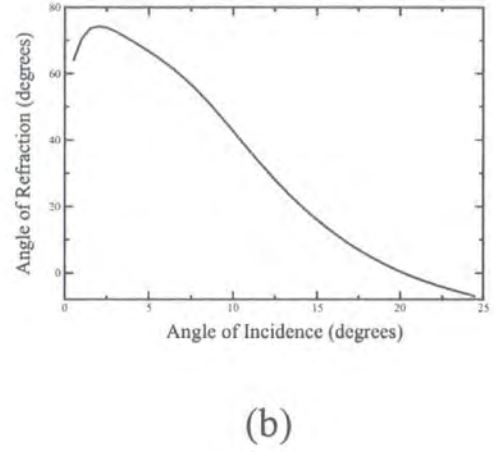
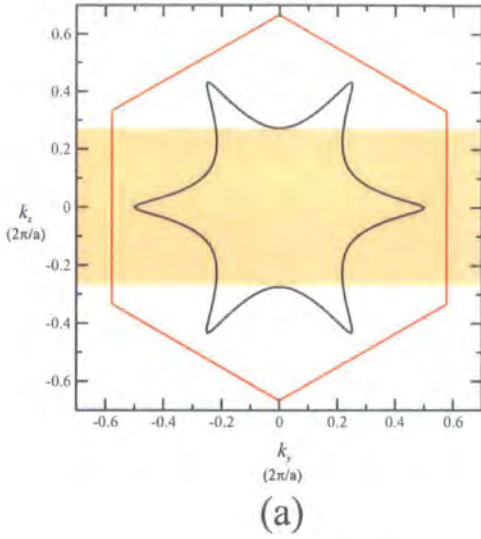


**Figure 6.13:** The optimum structure (a) is shown with the single refraction angle  $k_z$  range shaded. The corresponding refraction characteristics are shown in (b). The effect of a 1% increase (green) and 1% decrease (red) in frequency are also shown for both the dispersion surface (c) and the refraction characteristics (d).

The increase in frequency caused the dispersion surface to collapse maintaining the star shape but slightly reducing the range of available  $k_z$  values. The decrease in frequency caused a gap to occur in the  $\Gamma - M$  direction which corresponds to a gap in the refraction properties of the structure between approximately  $\pm 4$  degrees. The effect of the 1% increase in frequency on the refraction characteristics may be seen in Fig. 6.13d. For a 2 degree angle of incidence the refraction angle is 62 degrees, a change of 12 degrees on the original frequency. Fig. 6.13c shows that a 1% decrease in the incident frequency is responsible for extinguishing the refracted wave at the 2 degree angle of incidence. This is due to the absence of a real wavevector solution at this frequency in the direction of interest.

## 6.8 Conclusions

In this chapter two-dimensional photonic crystals formed using a hexagonal lattice were studied. The aim was to optimise the refraction characteristics of such a structure with respect to hole radius, background refractive index and frequency. The strategy for finding the optimum structure calculated the gradient of dispersion surfaces in the direction of the two high symmetry points,  $\Gamma - M$  and  $\Gamma - K$ . A range of refractive indices, rod radii and frequencies were considered and the optimum situation was found as a background refractive index of  $n = 2$  with air holes of radius  $r = 0.4a$ , operating at a frequency of  $\omega = 0.65c/a$  for TM polarised light. The structure was calculated to produce a 148 degree angular variation in the refracted beam direction for just a 4 degree change in the angle of incidence. This behaviour is believed to be superior to those published in the literature. Such a structure could form the basis of a beam steering and focusing device. The results presented show that considerable scope still exists for the fabrication of superprism structures beyond those currently employed. The structure also demonstrated a sensitivity to incident frequency with a 1% change in incident frequency producing a 12 degree change in the angle of refraction.

The optimisation study was limited by the consideration of only occasions where a single angle of refraction exists. The multiple refraction angle problem is considered in the following chapter.

# Chapter 7

## Interface Matching

### 7.1 Introduction

In this chapter an interface matching calculation is presented which allows the physics present when an electromagnetic wave impinges on an air/photonic crystal interface to be examined. The method allows the amplitudes of the individual Bloch waves propagating within the photonic crystal structure to be calculated. This is useful for determining the suitability of a particular configuration for superprism applications. A crucial factor for actual devices is the proportion of the incident intensity which couples to the superprism refraction ‘channel’ and the matching method presented enables this to be calculated.

The enhanced refraction properties of the hexagonal lattice were studied in the previous chapter with a restriction placed on the allowed  $k_z$  values. It was stated that the optimisation study would be limited to occasions when only a single angle of refraction existed for a single angle of incidence. This effectively limited the study to a small range of possible structures and frequencies. In general more than one band will exist in a bandstructure at a given frequency and accordingly multiple angles of refraction will exist. This is particularly true as higher frequencies are considered. Superprism work in the literature has not fully investigated the effects of moving to higher order bands. When multiple refraction angles exist the interface matching method described in this chapter may be used to determine whether an arrangement would channel significant power into the Bloch waves required for superprism behaviour to occur. The interface matching calculation makes use of the complex bandstructure calculation method which was described in Chapter 4. In this chapter complex

bandstructures are explained in greater detail together with the theory required for their use in interface matching. The results of such interface matching calculations are then presented for two optimum hexagonal lattice configurations, the single refraction angle optimum structure and a multiple refraction angle optimum structure.

## 7.2 Complex Bandstructures

Bandstructures were initially introduced as the set of allowed real frequencies for all real wavevectors within a range of values inside a full Brillouin Zone. Complex bandstructures are the full set of real, imaginary and complex wavevectors (within the Brillouin Zone) over a range of frequency values. The nature of complex bandstructures is considered in more depth here prior to their use for interface matching. To our knowledge complex bandstructures for photonic crystals have not been considered in depth in the literature. However, their properties are analogous to those of electronic complex bandstructures [198] and this section draws from that analogy.

### 7.2.1 Bloch States

Bloch's theorem gave the form of the magnetic field in a photonic crystal as a summation of individual Bloch waves corresponding to the different solutions of the bandstructure calculation. If the TE polarisation is considered as an example, the solution for a particular frequency and wavevector,  $\mathbf{k}$ , may be labelled  $\phi_{\mathbf{k}}(\boldsymbol{\rho})$  and written in the form:

$$\phi_{\mathbf{k}}(\boldsymbol{\rho}) = \sum_{\mathbf{g}} H_{\mathbf{g}} e^{i(\mathbf{k}+\mathbf{g})\cdot\boldsymbol{\rho}} = e^{i\mathbf{k}\cdot\boldsymbol{\rho}} \sum_{\mathbf{g}} H_{\mathbf{g}} e^{i\mathbf{g}\cdot\boldsymbol{\rho}} \quad . \quad (7.1)$$

The Bloch wave is itself formed from a product of a non-cell periodic term  $e^{i\mathbf{k}\cdot\boldsymbol{\rho}}$  and a sum of terms,  $H_{\mathbf{g}} e^{i\mathbf{g}\cdot\boldsymbol{\rho}}$ , with the same periodicity as the underlying lattice. If the photon wavevector  $\mathbf{k}$  has an imaginary component, i.e.  $\mathbf{k} = \mathbf{k}_{real} + i\mathbf{k}_{imag}$ , then the Bloch states for this particular wavevector will each have a real exponential coefficient. The Bloch wave may therefore be written in the form:

$$\phi_{\mathbf{k}}(\rho) = e^{\pm k_{\text{imag}} \cdot \rho} e^{i k_{\text{real}} \cdot \rho} \sum_{\mathbf{g}} H_{\mathbf{g}} e^{i \mathbf{g} \cdot \rho} \quad (7.2)$$

The Bloch wave has the same form as before except that it now possesses a factor that exponentially increases or decreases with distance. Both the increasing and decreasing solutions are perfectly valid mathematical solutions and may be included in complex bandstructure plots. These states may or may not have any real physical significance and this depends on the context.

### 7.2.2 Bandstructure Plots

At a particular frequency the total magnetic field in a photonic crystal will be a sum of Bloch waves with differing wavevectors. The complex bandstructure calculation calculates these when one of the wavevector components is fixed. The number of plane-waves chosen for the calculation, once again, gives the total number of solutions computed by the bandstructure calculation. In the original bandstructure method an increased number of plane-waves gave rise to an increased number of higher order frequency bands. In the complex bandstructure calculation an increased number of plane-waves corresponds to an increased number of  $\mathbf{k}$  vectors at a given frequency. Since the number of real solutions is finite these additional solutions must be imaginary or general complex. The higher magnitude imaginary terms are associated with more rapidly decaying, or increasing, states.

Fig. 7.1 shows a complex bandstructure for the optimum hexagonal lattice identified in the previous chapter. Complex bandstructures involve four distinctly different types of numerical solutions; purely real (shown in black), purely imaginary (blue), general in-Brillouin zone (dashed orange) and general at-the-Brillouin zone edge (green). Purely real solutions are equivalent to those produced by the original bandstructure calculation. Purely imaginary solutions and those at the Brillouin Zone edges are decaying, or increasing, solutions with different rates of decrease or increase. The general in-zone solutions occur between maxima and minima in a bandstructure to conserve the number of solutions. This number is dictated by the fixed number of reciprocal lattice vectors included in the plane-wave expansion. The need for conservation of the number of solutions follows the ‘rule’ proposed by Heine [199] for electronic complex bandstructures.

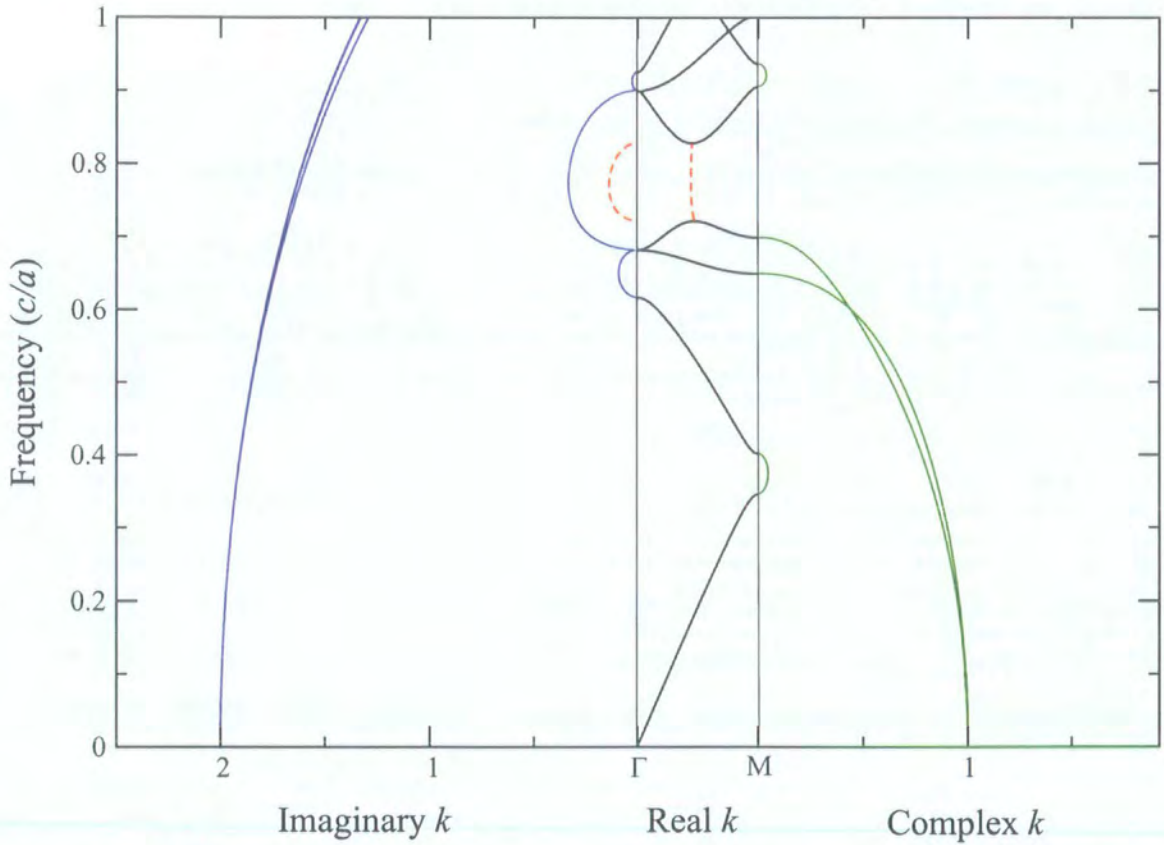


**Figure 7.1:** TM complex bandstructure for a hexagonal ( $n = 2$ ,  $r = 0.4a$ ) structure. Purely imaginary (blue), purely real (black), general at Brillouin Zone edge (green) and general in-zone (dashed orange) solutions are shown.

Each general solution containing a real and imaginary part exists in a set of 4 with 4 different  $k$ s corresponding to  $\pm k_{real}$  and  $\pm k_{imag}$ ; a pair of solutions exists at  $+k_{real}$  and at  $-k_{real}$ , giving the 4 solutions in total. At any frequency in the bandstructure the total number of solutions must be constant. This conservation of solution number provides a useful checking mechanism for identifying unique and repeated solutions. A further checking mechanism for the consistency of the computed bandstructure may be achieved by inputting the computed  $k$  values back into the standard bandstructure calculation and comparing the results.

### 7.2.3 Complex Bandstructure Convergence

Convergence tests were performed on the original bandstructure calculations. However this is no guarantee of convergence of the complex features of the bandstructure, particularly as the TM method makes use of a different approach to that used for the calculation of real bandstructures. Convergence tests are normally performed on a significant feature in the bandstructure, which is examined for a different number of plane-waves. The application being considered for complex bandstructures is interface matching; the most influential feature in the imaginary plane for this application is the lowest magnitude imaginary solution. This is due to this feature containing the exponential term which decays the least rapidly. For this reason convergence tests were performed on the first solution in the imaginary plane for both the TE and TM polarisations with a medium index contrast ( $n = 4$ ) and a medium rod radius ( $r = 0.3a$ ). The results are shown in Fig. 7.2. Rapid convergence exists for both polarisations. The TE polarisation was already converged to 1% (relative to 1945 plane-wave solution) with the lowest number of plane-waves tested (27). Similar convergence was seen for the TM polarisation for a choice of 69 plane-waves. The choice of 337 plane-waves made in the previous chapter for the optimisation study would appear to be sufficient to give reasonable convergence for the complex features, especially the most significant low magnitude features.

## 7.3 Interface Matching

The matching calculation follows as a progression from the complex bandstructure calculations presented in Chapter 4. The arrangement under consideration is an air/photonic

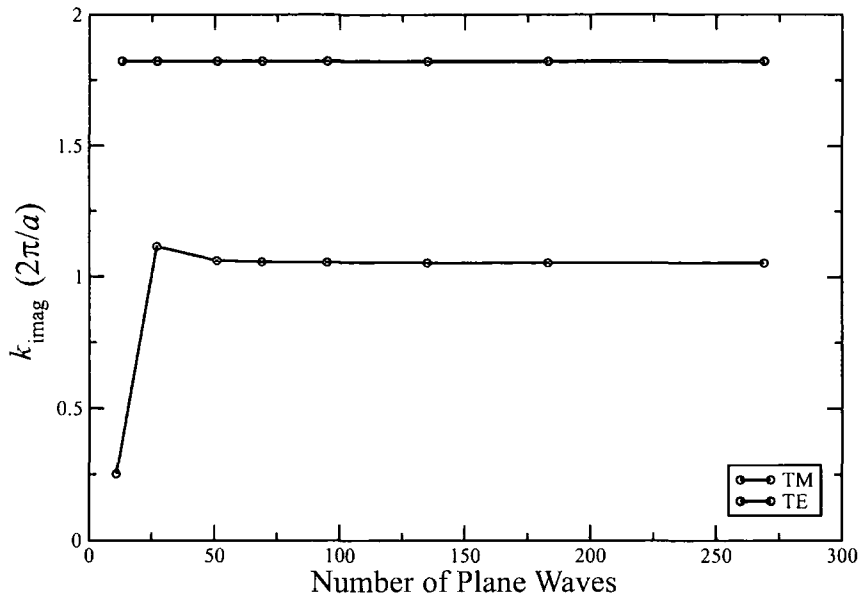


**Figure 7.2:** Convergence tests for imaginary solutions. The lowest magnitude imaginary solution is considered at a mid frequency at the  $\Gamma$  point.

crystal interface, as shown in Fig. 7.3. The main propagation direction is the  $y$  direction as this allows access to the feature of interest in the dispersion surface of the optimum single refraction angle hexagonal structure (Fig. 6.13a). For the electromagnetic fields to be continuous across the interface the tangential electric field and tangential magnetic field must be matched on either side at the interface. This will be sufficient for the matching calculation although it should be remembered that the remaining field components must also be continuous across the interface. The matching calculation involves all states at a given frequency. This explains the need for the complex bandstructure calculation previously described. The imaginary and general complex solutions produced by the calculation contain both increasing and decaying solutions. For the application under consideration the region to the right of the interface is unbounded, and any solutions which increase with distance from the interface will represent unphysical solutions in this instance. The increasing magnitude of the solutions implies increased total energy, making the solutions inconsistent with conservation of energy. For the interface matching calculation only attenuated solutions have a physical significance.

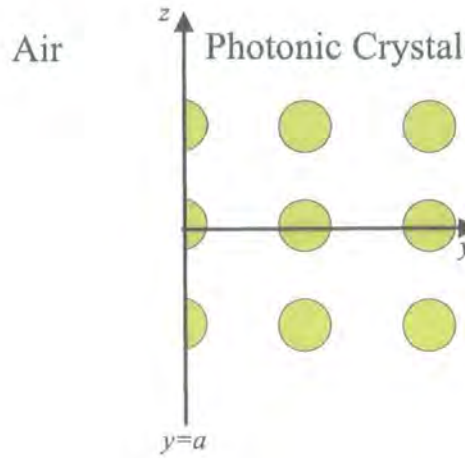


**Figure 7.3:** Matching was carried out for an interface consisting of air on the left and photonic crystal on the right. The planar interface is at  $y = a$ .

### 7.3.1 TE polarisation

#### Photonic Crystal (RHS)

The planar interface is assumed to exist at some arbitrary position  $y = a$  with a photonic crystal structure lying in the region  $y > a$  and air in the region  $y < a$ . For the TE polarisation  $\mathbf{H}$  is entirely in the  $x$  direction and the general solution for  $\mathbf{H}$  in the photonic crystal is constructed from some linear combination of the allowed Bloch waves within the photonic crystal. The notation  $\mathbf{H}^n$  may be introduced to denote each individual solution at a specific frequency. If  $b_n$  is used as the coefficient for each Bloch wave then it may be written that:

$$H_x^{RHS} e^{-i\omega t} = \sum_n b_n \mathbf{H}^n(y, z) e^{-i\omega t} \quad (7.3)$$

If the label  $\mathbf{g}$  is used to corresponding to one of the set of reciprocal lattice vectors then each of the allowed Bloch waves,  $\mathbf{H}^n$ , will consist of a sum of Bloch states with coefficients  $H_{\mathbf{g}}^n$ :

$$\mathbf{H}^n(y, z) = \sum_{\mathbf{g}} H_{\mathbf{g}}^n e^{i(\mathbf{k}+\mathbf{g})\cdot\rho} \quad (7.4)$$

The allowed Bloch waves are the solutions to the complex bandstructure calculation presented in the photonic crystal theory chapter. The calculation produces eigenvalues which

give the  $k_y^n$  wavevector components (of  $k^n$ ) and eigenvectors which provide the  $H_g^n$  coefficients for each Bloch state.

The symmetry of the system demands that  $k_z$  is the same on both sides of the interface or matching cannot occur. On the right-hand side (RHS) of the interface the valid  $k_y$  solutions are a subset of the  $k_y$  values produced by the complex bandstructure calculation. The solutions for inclusion are those which allow the magnetic field to either propagate, or to decay, to the right of the interface. All other solutions will represent un-physical situations for the given arrangement.

At the interface  $y = a$  and a Bloch wave within the photonic crystal can be expanded in the form:

$$\mathbf{H}^n(y = a, z) = \sum_{\mathbf{g}} H_{\mathbf{g}}^n e^{i(k_y^n + g_y)a} e^{i(k_z^n + g_z)z} \quad (7.5)$$

It is possible to simplify the appearance of the expression by grouping together terms with the same  $g_z$  value. These may be included in a new term, say  $P_{g_z}^n$ , to leave a summation over  $g_z$  values only:

$$\mathbf{H}_n(y = a, z) = \sum_{g_z} P_{g_z}^n e^{i(k_z^n + g_z)z} \quad (7.6)$$

$P_{g_z}^n$  contains Bloch states with the same  $g_z$  values and is given by:

$$P_{g_z}^n = \sum_{\substack{\text{same} \\ g_z}} H_{\mathbf{g}}^n e^{i(k_y^n + g_y)a} \quad (7.7)$$

For the case under consideration further simplification may be made by choosing the position of the air/photonic crystal interface as the special case where  $a = 0$ . Each  $P_{g_z}^n$  is then simply:

$$P_{g_z}^n = \sum_{\substack{\text{same} \\ g_z}} H_{\mathbf{g}}^n = \sum_{\mathbf{g}'} H_{\mathbf{g}'}^n \delta_{g_z, g_z'} \quad (7.8)$$

A second set of reciprocal lattice vectors,  $\mathbf{g}'$ 's, has been introduced to simplify the notation. The set will be of the same form as the original set describing the photonic structure period-

icity.

### Air (LHS)

A uniform material was chosen for the left-hand side (LHS) of the interface, although the calculation could in principle have been for another photonic crystal structure. The uniform refractive index was taken as  $n_r(\omega)$ , and it was assumed that the approximation  $n_r(\omega) = n_r$ , could be made for the material. Uniform media, like photonic crystals, may also be considered as possessing a variety of allowed  $k_y$  solutions, for a given frequency. If the notation  $k$  is reserved for an incoming wave then the notation  $k'$  may be used for some general LHS wavevector solution. Maxwell's equations govern the allowed solutions and, assuming a nonconducting uniform dielectric, lead to the following condition (from equation (2.18))

$$(k'_x)^2 + (k'_y)^2 + (k'_z)^2 = \frac{\omega^2 n_r^2}{c^2} \quad (7.9)$$

The light incident at the interface forms an incoming wave; this will be assumed to be of a plane-wave form with unit amplitude. Accordingly, the magnetic field component of the incoming wave,  $H_I^{LHS}$ , may be written as:

$$H_I^{LHS}(y, z)e^{-i\omega t} = e^{i(k_y y + k_z z)} e^{-i\omega t} \quad (7.10)$$

Clearly the result of the impingement of the initial plane-wave on the periodic structure can be expected to give rise to a series of reflected plane-waves and hence the total magnetic field will include all of these. This means a range of discrete  $k'_y$  solutions will exist on the LHS for any fixed  $k'_z$  and  $\omega$  combination. These can be calculated from equation (7.9) and as  $k'_x = 0$ :

$$(k'_y)^2 = \frac{\omega^2 n_r^2}{c^2} - (k_z + g_z)^2 \quad (7.11)$$

On the air side  $k'_z$  is not constrained to lie within a Brillouin Zone as none exists. However, it may be written in the form  $k'_z = k_z + g_z$  with a solution which exists within the Brillouin

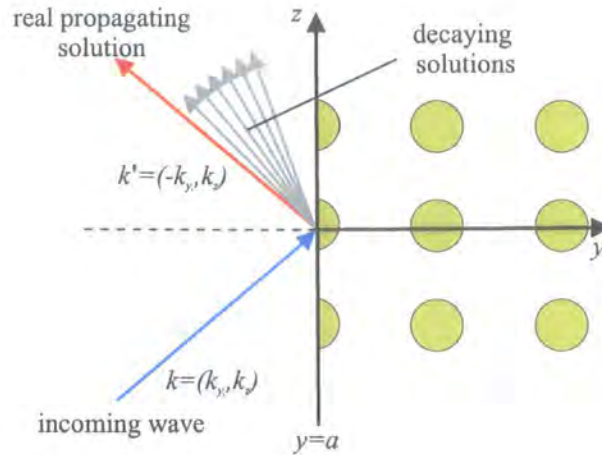


Figure 7.4: Allowed solutions on the air side of the interface (LHS).

Zone ( $k_z$ ), as it is defined on the RHS, and a reciprocal lattice vector term,  $g_z$ . The solutions on the LHS will then match the periodicity in  $z$  present on the RHS.

When  $g_z = 0$  the solution of equation (7.11) will be equivalent to the  $k = (k_y, k_z)$  solution which is the incident incoming wave. The set of reciprocal lattice vectors also produces a variety of other, mainly purely imaginary  $k_y$  solutions for any fixed  $k_z$ . For clarity the solution for a particular  $g_z$  value will be labelled  $k^{g_z}$ , with components  $k_y^{g_z}$  and  $k_z^{g_z}$ . As the magnitude of  $g_z$  increases these solutions will correspond to increasingly more rapidly decaying or increasing waves. The increasing solutions are un-physical solutions and only solutions which represent reflected, propagating or decaying waves to the left of the interface are valid. This is half the total number of solutions produced by equation (7.11).

For field continuity across the interface the tangential components of the electric and magnetic fields must match at the interface. For the magnetic field this is the entire field as  $H_y = H_z = 0$ . The frequency  $\omega$  and wavevector component  $k_z$  are dictated by the direction and frequency of the incoming wave and the general solution on the LHS is:

$$H^{LHS}(y, z)e^{-i\omega t} = e^{ik_y y + k_z z} e^{-i\omega t} + \sum_{g_z} a_{g_z} e^{ik_y^{g_z} y} e^{i(k_z + g_z)z} e^{-i\omega t} \quad (7.12)$$

The first term on the right is the incoming wave of unit amplitude and the second term is a

general combination of the allowed reflected waves with coefficients ( $a_{g_z}$ ) to be calculated by the matching calculation. The situation is shown diagrammatically in Fig. 7.4. At the interface  $y = a$ , hence

$$H^{LHS}(y = a, z)e^{-i\omega t} = e^{ik_y a + k_z z} e^{-i\omega t} + \sum_{g_z} a_{g_z} e^{ik_y^g a} e^{i(k_z + g_z)z} e^{-i\omega t} \quad (7.13)$$

For simplicity, the special case under consideration has  $a = 0$  and equation (7.13) reduces to the final LHS magnetic field equation:

$$H^{LHS}(y = 0, z)e^{-i\omega t} = e^{ik_z z} e^{-i\omega t} + \sum_{g_z} a_{g_z} e^{i(k_z + g_z)z} e^{-i\omega t} \quad (7.14)$$

### Matching

At the interface the tangential magnetic field on the LHS, given by equation (7.3), must be equal to that on the RHS, given by equation (7.14). Equating these two equations and cancelling the common  $e^{ik_z z}$  and  $e^{-i\omega t}$  factors gives:

$$1 + \sum_{g_z} a_{g_z} e^{ig_z z} = \sum_n b_n \sum_{g_z} P_{g_z}^n e^{ig_z z} \quad (7.15)$$

This forms a series of equations connecting  $a_{g_z}$  and  $b_n$ . The equation for a particular  $g_z$ , say  $G_z$ , may be found by multiplying both sides of the equation by  $e^{-iG_z z}$  and integrating over all  $z$ :

$$\int_{\text{all } z} e^{-iG_z z} dz + \sum_{g_z} a_{g_z} \int_{\text{all } z} e^{i(g_z - G_z)z} dz = \sum_n b_n \sum_{g_z} P_{g_z}^n \int_{\text{all } z} e^{i(g_z - G_z)z} dz \quad (7.16)$$

In practice the exponentials are all periodic in  $z$  and consequently integration only needs to be carried out over a single period, or unit cell,  $L$  say. If  $g_z \neq 0$  then  $\int_0^L e^{ig_z z} dz = 0$  and if  $g_z = 0$  then  $\int_0^L e^{ig_z z} dz = L$ . This means that, for  $G_z = 0$ , equation (7.16) gives:

$$L + L \cdot a_{g_z=0} = \sum_n b_n P_{g_z=0}^n L \quad , \quad (7.17)$$

which may be written in more suitable form for matching by rearranging and dividing through by  $L$ , to give:

$$1 = \sum_n b_n P_0^n - a_0 \quad . \quad (7.18)$$

The remaining terms from equation (7.16), for  $G_z \neq 0$ , are of the form:

$$a_{G_z} = \sum_n b_n P_{G_z}^n \quad . \quad (7.19)$$

This is due to only terms for which  $g_z = G_z$  contributing from the integration. A more convenient form of equation (7.19) for matching is:

$$0 = \sum_n b_n P_{G_z}^n - a_{G_z} \quad . \quad (7.20)$$

Equations (7.18) and (7.20) do not provide enough information to solve the simultaneous equations and find the  $2N$  matching coefficients. For a particular set of two-dimensional reciprocal lattice vectors there are  $N$  distinctly different  $g_z$  values, where  $N$  is some odd integer. The corresponding number of  $k_y$  solutions, computed from the complex bandstructure calculation, will be  $2N$ . However, only half of these will propagate or decay to the right, and hence correspond to allowed basis functions on the RHS of the interface. If the relationships are written in matrix form then the lack of sufficient information is evident. The  $a$  and  $b$  coefficients may be moved to a separate matrix and the RHS of equations (7.18) and (7.20) written as:

$$\begin{pmatrix} P_0^1 & P_0^2 & P_0^3 & \cdots & -1 & 0 & 0 & \cdots \\ P_{G_z=1}^1 & P_{G_z=1}^2 & P_{G_z=1}^3 & \cdots & 0 & -1 & 0 & \cdots \\ P_{G_z=2}^1 & P_{G_z=2}^2 & P_{G_z=2}^3 & \cdots & 0 & 0 & -1 & \cdots \\ \vdots & \vdots & \vdots & \vdots & \vdots & \vdots & \vdots & \vdots \end{pmatrix} \begin{pmatrix} b_0 \\ b_1 \\ b_2 \\ \vdots \end{pmatrix} \quad (7.21)$$

The vertical dimension of the matrix will be  $N$  and the horizontal dimension  $2N$ . To solve for the matching coefficients twice as many simultaneous equations are required. The second set of equations is obtained by also matching the tangential components of the electric field at the interface.

### Electric Field

The tangential component of the electric field may be found by considering Maxwell's fourth equation (previously equation 4.11). The previously stated assumptions,  $\mu = \mu_0$ ,  $\sigma = 0$  and  $\mathbf{E} \propto e^{-i\omega t}$ , allow us to write:

$$\nabla \times \mathbf{H} = \mu_0 \epsilon \frac{\partial \mathbf{E}}{\partial t} = -i\omega \epsilon_0 \epsilon_r \mathbf{E} \quad (7.22)$$

The Fourier form for the permittivity, introduced in Section 4.5.1 will be again used. In this instance the reciprocal lattice vectors will be labelled  $\mathbf{g}'$  to allow for the continued use of  $\mathbf{g}$  to represent the terms in the reciprocal lattice vector set used for the magnetic field. The electric field may then be written as:

$$\mathbf{E}(y, z)e^{-i\omega t} = \frac{-1}{i\omega \epsilon_0 \epsilon_0} \sum_{\mathbf{g}'} \epsilon_{\mathbf{g}'}^{-1} e^{i\mathbf{g}' \cdot \rho} \nabla \times \mathbf{H} \quad (7.23)$$

The RHS magnetic field, given by equation (7.3), may be substituted into this equation to give the electric field. If the tangential,  $z$ , component is considered then, using  $c^2 = 1/\mu_0 \epsilon_0$ ,

$$E_z^{RHS}(y, z)e^{-i\omega t} = \frac{\mu_0 c^2}{\omega} \sum_n b_n \sum_{\mathbf{g}, \mathbf{g}'} \epsilon_{\mathbf{g}'}^{-1} H_{\mathbf{g}}^n (k_y^n + g_y) e^{i(\mathbf{k}^n + \mathbf{g} + \mathbf{g}') \cdot \rho} e^{-i\omega t} \quad (7.24)$$

As previously the interface is at  $y = a = 0$ , which gives the field at the interface as:

$$E_z^{RHS}(y = 0, z)e^{-i\omega t} = \frac{\mu_0 c^2}{\omega} \sum_n b_n \sum_{\mathbf{g}, \mathbf{g}'} \epsilon_{\mathbf{g}'}^{-1} H_{\mathbf{g}}^n (k_y^n + g_y) e^{i(k_z + g_z + g'_z)z} e^{-i\omega t} \quad (7.25)$$

At the interface the RHS tangential electric field must match the LHS tangential electric field. It is sensible to consider the curl of the LHS magnetic field first, as it may then be used in equation (7.22) to give the LHS electric field:

$$\nabla \times \mathbf{H}^{LHS} = \begin{pmatrix} 0 \\ ik_z e^{i\mathbf{k} \cdot \boldsymbol{\rho}} + i \sum_{g_z} a_{g_z} (k_z + g_z) e^{i\mathbf{k}^{g_z} \cdot \boldsymbol{\rho}} \\ -ik_y e^{i\mathbf{k} \cdot \boldsymbol{\rho}} - i \sum_{g_z} a_{g_z} k_y^{g_z} e^{i\mathbf{k}^{g_z} \cdot \boldsymbol{\rho}} \end{pmatrix} e^{-i\omega t} \quad (7.26)$$

The LHS electric field may then be found by the substitution of this into equation (7.22). The tangential,  $z$ , component of the field is required for matching and considering this:

$$ik_y e^{i\mathbf{k} \cdot \boldsymbol{\rho}} + i \sum_{g_z} a_{g_z} k_y^{g_z} e^{i\mathbf{k}^{g_z} \cdot \boldsymbol{\rho}} e^{-i\omega t} = \frac{n_r^2}{\mu_0 c^2} i\omega E_z^{LHS}(y, z) e^{-i\omega t} \quad (7.27)$$

At the interface,  $y = a = 0$ , and the electric field component is:

$$E_z^{LHS}(y = 0, z) = \frac{\mu_0 c^2}{n_r^2 \omega} \left[ k_y e^{ik_z z} + \sum_{g_z} a_{g_z} k_y^{g_z} e^{i(k_z + g_z)z} \right] \quad (7.28)$$

Equating equation (7.25), for the RHS, and equation (7.28), for the LHS and cancelling the common  $e^{ik_z z}$  and  $e^{-i\omega t}$  factors gives

$$k_y + \sum_{g_z} a_{g_z} k_y^{g_z} e^{ig_z z} = n_r^2 \sum_n b_n \sum_{\mathbf{g}, \mathbf{g}'} \epsilon_{\mathbf{g}'}^{-1} H_{\mathbf{g}}^n (k_y^n + g_y) e^{i(g_z + g'_z)z} \quad (7.29)$$

Provided that grazing incidence is not considered then  $k_y \neq 0$  and equation (7.29) may be written as:

$$1 + \sum_{g_z} a_{g_z} \left( \frac{k_y^{g_z}}{k_y} \right) e^{ig_z z} = n_r^2 \sum_n b_n \sum_{\mathbf{g}, \mathbf{g}'} \epsilon_{\mathbf{g}'}^{-1} H_{\mathbf{g}}^n \frac{(k_y^n + g_y)}{k_y} e^{i(g_z + g'_z)z} \quad (7.30)$$

A specific  $g_z$  value, say,  $G_z$  may be found by multiplying by  $e^{-iG_z z}$  and integrating over all space. This equivalent to a unit cell, or period  $L$ , in the  $z$  direction due to the periodicity of

the system:

$$\int_0^L e^{-iG_z z} dz + \sum_{g_z} a_{g_z} \left( \frac{k_y^{g_z}}{k_y} \right) \int_0^L e^{i(g_z - G_z)z} dz = n_r^2 \sum_n b_n \sum_{\mathbf{g}, \mathbf{g}'} \epsilon_{\mathbf{g}'}^{-1} H_{\mathbf{g}}^n \frac{(k_y^n + g_y)}{k_y} \int_0^L e^{i(g_z + g'_z - G_z)z} dz \quad (7.31)$$

For  $G_z = 0$ , only those terms for which  $g'_z = -g_z$  contribute. Hence,

$$1 + a_0 \left( \frac{k_y^{G_z=0}}{k_y} \right) = n_r^2 \sum_n b_n \sum_{\mathbf{g}, \mathbf{g}'} \epsilon_{\mathbf{g}'}^{-1} H_{\mathbf{g}}^n \frac{(k_y^n + g_y)}{k_y} \delta_{0, g'_z - g_z} \quad (7.32)$$

As  $k^{G_z=0}$  represents the real reflected wave  $k_y^{G_z=0}/k_y = -1$ . If  $G_z \neq 0$ , only those terms for which  $g'_z = G_z - g_z$  contribute. Hence,

$$a_{G_z} \left( \frac{k_y^{G_z}}{k_y} \right) = n_r^2 \sum_n b_n \sum_{\mathbf{g}, \mathbf{g}'} \epsilon_{\mathbf{g}'}^{-1} H_{\mathbf{g}}^n \frac{(k_y^n + g_y)}{k_y} \delta_{g'_z, G_z - g_z} \quad (7.33)$$

To solve the simultaneous equations using matrix methods equations (7.32) and (7.33) must be rewritten in a more convenient form. The  $G_z = 0$  equation may be written as:

$$1 = \sum_n b_n Q_0^n + a_0 \quad (7.34)$$

and correspondingly for  $G_z \neq 0$ :

$$0 = \sum_n b_n Q_{G_z}^n - \left( \frac{k_y^{G_z}}{k_y} \right) a_{G_z} \quad (7.35)$$

The notation has been simplified by grouping together the terms which multiply the  $b_n$  reflection coefficients:

$$Q_{G_z}^n = n_r^2 \sum_{\mathbf{g}, \mathbf{g}'} \epsilon_{\mathbf{g}'}^{-1} \delta_{g'_z, G_z - g_z} H_{\mathbf{g}}^n \frac{(k_y^n + g_y)}{k_y} \quad (7.36)$$

This completes the information required for finding the TE matching coefficients at the interface. Equations (7.34), (7.35), (7.18) and (7.20) may be combined to give the final matching matrix equation as:

$$\begin{pmatrix} P_0^1 & P_0^2 & P_0^3 & \cdots & -1 & 0 & 0 & \cdots \\ P_{G_z=1}^1 & P_{G_z=1}^2 & P_{G_z=1}^3 & \cdots & 0 & -1 & 0 & \cdots \\ P_{G_z=2}^1 & P_{G_z=2}^2 & P_{G_z=2}^3 & \cdots & 0 & 0 & -1 & \cdots \\ \vdots & \vdots & \vdots & \vdots & \vdots & \vdots & \vdots & \vdots \\ Q_0^1 & Q_0^2 & Q_0^3 & \cdots & 1 & 0 & 0 & \cdots \\ Q_{G_z=1}^1 & Q_{G_z=1}^2 & Q_{G_z=1}^3 & \cdots & 0 & \frac{-k_y^{G_z=1}}{k_y} & 0 & \cdots \\ Q_{G_z=2}^1 & Q_{G_z=2}^2 & Q_{G_z=2}^3 & \cdots & 0 & 0 & \frac{-k_y^{G_z=2}}{k_y} & \cdots \\ \vdots & \vdots & \vdots & \vdots & \vdots & \vdots & \vdots & \vdots \end{pmatrix} \begin{pmatrix} b_0 \\ b_1 \\ b_2 \\ \vdots \\ a_0 \\ a_1 \\ a_2 \\ \vdots \end{pmatrix} = \begin{pmatrix} 1 \\ 0 \\ 0 \\ \vdots \\ 1 \\ 0 \\ 0 \\ \vdots \end{pmatrix} \quad (7.37)$$

To compute the matching coefficients, *as* and *bs*, the coefficients have also been combined into a column vector which may be labelled *C*. If the top  $2N$  by  $N$  component of the matrix is denoted as *P* and the bottom  $2N$  by  $N$  matrix as *Q*, then the final matrix equation is of the form:

$$\begin{pmatrix} P \\ Q \end{pmatrix} \begin{pmatrix} C \end{pmatrix} = \begin{pmatrix} 1 \\ 0 \\ \vdots \\ 1 \\ 0 \\ \vdots \end{pmatrix} \quad (7.38)$$

The solution can be found by multiplying both sides by the inverse of the first matrix on the LHS to yield the matching coefficients. Standard computational algorithms can be employed to calculate the inverse matrix.

### 7.3.2 TM Polarisation

#### Photonic Crystal (RHS)

In principle, matching for the TM polarisation is identical to the TE method described in the previous section. However, the tangential field components are different and the algebraic differences this creates make it necessary to outline the calculation. The interface situation remains that shown in Fig. 7.3, with a photonic structure assumed to lie in a region  $y > a$  on the RHS of a planar interface with a uniform material. As previously the frequency,  $\omega$ , and wavevector component,  $k_x$ , must be the same on both sides of the interface. The TM mode possesses an electric field which is entirely in the  $x$  direction. The field will consist of a sum of the allowed photonic crystal Bloch states,  $E^n$ :

$$E_x^{RHS}(y, z)e^{-i\omega t} = \sum_n b_n E^n(y, z)e^{-i\omega t} \quad . \quad (7.39)$$

Each of the allowed Bloch waves on the RHS has a coefficient  $b_n$  associated with them. The coefficients are to be determined by the matching calculation. The Bloch waves are themselves also formed from a sum of plane-waves. At the interface,  $y = a$  and an individual Bloch wave may be written as:

$$E_n(y = a, z) = \sum_{\mathbf{g}} E_{\mathbf{g}}^n e^{i(k_y^n + g_y)a} e^{i(k_x + g_x)z} \quad (7.40)$$

The individual plane-wave coefficients,  $E_{\mathbf{g}}^n$ , come from the complex bandstructure calculation and the summation over reciprocal lattice vectors produces the allowed RHS Bloch waves. The label  $n$  refers to the different allowed  $k_y$  solutions produced by the complex bandstructure calculation. The allowed RHS  $k_y$  solutions produced by the calculation are those which have physical meaning; solutions that either propagate or decay to the right of the interface. This means the surviving  $k_y$  values are either real or have a positive imaginary component. Simplification of equation (7.40) may be achieved by grouping together terms with the same  $g_z$  value to give:

$$E_x^{RHS}(y = a, z)e^{-i\omega t} = \sum_{g_z} P_{g_z}^n e^{i(k_x + g_x)z} e^{-i\omega t} \quad , \quad (7.41)$$

with  $P_{g_z}^n$  values which are given by:

$$P_{g_z}^n = \sum_{\substack{\text{same} \\ g_z}} E_{\mathbf{g}}^n e^{i(k_y^n + g_y)a} \quad (7.42)$$

For simplicity once again the interface was set at  $y = a = 0$ . Hence,

$$P_{g_z}^n = \sum_{\substack{\text{same} \\ g_z}} E_{\mathbf{g}}^n = \sum_{\mathbf{g}'} E_{\mathbf{g}}^n \delta_{g_z, g_z'} \quad (7.43)$$

A second set of reciprocal lattice vectors  $\mathbf{g}'$  has been introduced to simplify the notation. It will be of the same form as the original reciprocal lattice vector set.

### Air (LHS)

To the left of the interface an air region exists. This region contains the incoming wave, which will be assumed to be a plane-wave of unit amplitude:

$$E_I^{LHS}(y, z)e^{-i\omega t} = e^{i(k_y y + k_z z)} e^{-i\omega t} \quad (7.44)$$

In addition, the use of the same set of reciprocal lattice vectors on both sides of the interface produces a set of solutions,  $k_y^{g_z}$ , dictated by equation (7.11). The new allowed solutions represent the real reflected wave and those solutions which decay to the left of the interface. The total LHS solution electric field solution is therefore:

$$E^{LHS}(y, z)e^{-i\omega t} = e^{i\mathbf{k} \cdot \boldsymbol{\rho}} + \sum_{g_z} a_{g_z} e^{ik_y^{g_z} y} e^{i(k_z + g_z)z} e^{-i\omega t} \quad (7.45)$$

The first term on the RHS of the equation is the incoming wave and the second term is a general combination of all the allowed reflected wave solutions with matching coefficients  $a_{g_z}$ , which are to be determined by the matching calculation. At the interface  $y = a$  and this becomes:

$$E^{LHS}(y = a, z)e^{-i\omega t} = e^{i(k_y a + k_z z)}e^{-i\omega t} + \sum_{g_z} a_{g_z} e^{ik_y^z a} e^{i(k_z + g_z)z} e^{-i\omega t} \quad (7.46)$$

If the simplifying case of an interface at  $y = a = 0$  is considered then the electric field at the interface reduces to:

$$E^{LHS}(y = 0, z)e^{-i\omega t} = e^{ik_z z} e^{-i\omega t} + \sum_{g_z} a_{g_z} e^{i(k_z + g_z)z} e^{-i\omega t} \quad (7.47)$$

### Matching

Matching the LHS (equation (7.47)) and RHS (equation (7.41)) tangential electric fields at the interface and dividing out the common  $e^{ik_z z}$  and  $e^{-i\omega t}$  terms yields:

$$1 + \sum_{g_z} a_{g_z} e^{ig_z z} = \sum_n b_n \sum_{g_z} P_{g_z}^n e^{ig_z z} \quad (7.48)$$

This is identical in appearance to equation (7.15) which was derived for the TE polarisation. This means the two final matching equations follow through in an equivalent manner to equations (7.16) to (7.20). The equation for  $G_z = 0$  is therefore:

$$1 = \sum_n b_n P_0^n - a_0 \quad (7.49)$$

and for  $G_z \neq 0$ ,

$$0 = \sum_n b_n P_{G_z}^n - a_{G_z} \quad (7.50)$$

It should be recalled that  $P_{G_z}^n$  is of the form given in equation (7.43); which is different from the form required for matching with the TE polarisation.

### Magnetic Field

To provide enough simultaneous equations to solve for the matching coefficients the tangential ( $z$ ) component of the magnetic field must also be considered. If Maxwell's third equation (from equation (4.10)) is examined for plane-waves it dictates that:

$$\nabla \times \mathbf{E} = i\omega\mu_0\mathbf{H} \quad (7.51)$$

To find the RHS magnetic field it is useful to consider the curl the plane-wave field form for the electric field:

$$\nabla \times \mathbf{E}^{RHS} = \begin{pmatrix} 0 \\ i \sum_n b_n \sum_{\mathbf{g}} (k_z + g_z) E_{\mathbf{g}}^n e^{i(\mathbf{k}^n + \mathbf{g}) \cdot \boldsymbol{\rho}} \\ -i \sum_n b_n \sum_{\mathbf{g}} (k_y^n + g_y) E_{\mathbf{g}}^n e^{i(\mathbf{k}^n + \mathbf{g}) \cdot \boldsymbol{\rho}} \end{pmatrix} e^{-i\omega t} \quad (7.52)$$

This may be substituted into equation (7.51) to find the tangential  $z$  component of the magnetic field which is required for matching:

$$H_z^{RHS}(y, z)e^{-i\omega t} = \frac{-1}{\omega\mu_0} \sum_n b_n \sum_{\mathbf{g}} (k_y^n + g_y) E_{\mathbf{g}}^n e^{i(\mathbf{k}^n + \mathbf{g}) \cdot \boldsymbol{\rho}} e^{-i\omega t} \quad (7.53)$$

The interface remains the simplify case with  $y = a = 0$ . Hence, at the interface:

$$H_z^{RHS}(y = 0, z)e^{-i\omega t} = \frac{-1}{\omega\mu_0} \sum_n b_n \sum_{\mathbf{g}} E_{\mathbf{g}}^n (k_y^n + g_y) e^{i(k_z + g_z)z} e^{-i\omega t} \quad (7.54)$$

### Air (LHS)

On the LHS of the interface the tangential component of the magnetic field also needs to be calculated. This may be achieved through the use of the electric field form which was given by equation (7.45). The curl of the LHS electric field is:

$$\nabla \times \mathbf{E}^{LHS} = \begin{pmatrix} 0 \\ ik_z e^{i(k_y y + k_z z)} + i \sum_{g_z} a_{g_z} (k_z + g_z) e^{ik^{g_z} \cdot \rho} \\ -ik_y e^{i(k_y y + k_z z)} - i \sum_{g_z} a_{g_z} k_y^{g_z} e^{ik^{g_z} \cdot \rho} \end{pmatrix} e^{-i\omega t} \quad (7.55)$$

Therefore the  $z$  component of the magnetic field may be calculated by the substitution of equation (7.55) into equation (7.53):

$$H_z^{LHS}(y, z) e^{-i\omega t} = \frac{-1}{\omega \mu_0} \left( k_y e^{i(k_y y + k_z z)} + \sum_{g_z} a_{g_z} k_y^{g_z} e^{i(k_y^{g_z} y + (k_z + g_z)z)} \right) e^{-i\omega t} \quad (7.56)$$

The interface is at  $y = a = 0$  and hence the magnetic field field at the interface is given by:

$$H_z^{LHS}(y = 0, z) e^{-i\omega t} = \frac{-1}{\omega \mu_0} \left( k_y e^{ik_z z} + \sum_{g_z} a_{g_z} k_y^{g_z} e^{i(k_z + g_z)z} \right) e^{-i\omega t} \quad (7.57)$$

To match the  $z$  component of the magnetic field the RHS field equation (7.54) and LHS field equation (7.57) are equated. If the common  $e^{-i\omega t}$  term is cancelled then:

$$k_y e^{ik_z z} + \sum_{g_z} a_{g_z} k_y^{g_z} e^{i(g_z + k_z)z} = \sum_n b_n \sum_{\mathbf{g}} E_{\mathbf{g}}^n (k_y^n + g_y) e^{i(k_z + g_z)z} \quad (7.58)$$

The common  $e^{ik_z z}$  terms may also be cancelled and provided that grazing incidence is not considered (so  $k_y \neq 0$ ) the equation may be divided through by  $k_y$  to yield:

$$1 + \sum_{g_z} a_{g_z} \left( \frac{k_y^{g_z}}{k_y} \right) e^{ig_z z} = \sum_n b_n \sum_{\mathbf{g}} E_{\mathbf{g}}^n \frac{(k_y^n + g_y)}{k_y} e^{ig_z z} \quad (7.59)$$

An individual  $g_z$ , labelled  $G_z$ , can be selected if both sides are multiplied by  $e^{-iG_z z}$  and integration is carried out over all  $z$  direction. Due to the periodicity of the system this is equivalent to a period  $L$  in the  $z$  direction.

$$\int_0^L e^{-iG_z z} dz + \sum_{g_z} \left( \frac{k_y^{g_z}}{k_y} \right) \int_0^L e^{i(g_z - G_z)z} dz = \sum_n b_n \sum_{\mathbf{g}} E_{\mathbf{g}}^n \frac{(k_y^n + g_y)}{k_y} \int_0^L e^{i(g_z - G_z)z} dz \quad (7.60)$$

As previously stated, if  $g_z \neq 0$  then  $\int_0^L e^{ig_z z} dz = 0$  and if  $g_z = 0$  then  $\int_0^L e^{ig_z z} dz = L$ . Hence, if  $G_z = 0$ :

$$1 + a_0 \left( \frac{k_y^{G_z=0}}{k_y} \right) = \sum_n b_n \sum_{\mathbf{g}} E_{\mathbf{g}}^n \frac{(k_y^n + g_y)}{k_y} \delta_{g_z,0} \quad , \quad (7.61)$$

and if  $G_z \neq 0$ :

$$a_{G_z} \left( \frac{k_y^{G_z}}{k_y} \right) = \sum_n b_n \sum_{\mathbf{g}} E_{\mathbf{g}}^n \frac{(k_y^n + g_y)}{k_y} \delta_{g_z, G_z} \quad . \quad (7.62)$$

It is convenient to write the magnetic field simultaneous equations in the same form as equations (7.34) and (7.35) for the TE polarisation. This gives, for  $G_z = 0$ ,

$$1 = \sum_n b_n Q_0^n + a_0 \quad , \quad (7.63)$$

and for  $G_z \neq 0$ :

$$0 = \sum_n b_n Q_{G_z}^n - \left( \frac{k_y^{G_z}}{k_y} \right) a_{G_z} \quad (7.64)$$

The form for  $Q_{G_z}^n$  differs from the TE form and is given by:

$$Q_{G_z}^n = \sum_{\mathbf{g}} E_{\mathbf{g}}^n \left( \frac{k_y^n + g_y}{k_y} \right) \delta_{G_z, g_z} \quad . \quad (7.65)$$

Combining the magnetic and electric field matching conditions gives the final TM matching matrix equation in the form:

$$\begin{pmatrix} P \\ \\ \\ Q \end{pmatrix} \begin{pmatrix} \\ \\ C \\ \\ \end{pmatrix} = \begin{pmatrix} 1 \\ 0 \\ \vdots \\ 1 \\ 0 \\ \vdots \end{pmatrix} \quad (7.66)$$

This is of an identical form to the TE equation and completes the set of matching equations to allow both modes to be matched at an air/photonic crystal interface.

## 7.4 Fresnel Equations

One of the basic requirements when performing calculations to describe photonic crystals is that in the zero rod radius limit, or equivalently the uniform dielectric constant regime, the photonic crystal effectively becomes a uniform material and must reproduce the well documented behaviour of uniform media. We can use these standard results to test the correct implementation of our complex bandstructure matching scheme. The phenomenon of reflection and refraction at a boundary between two uniform media, shown in Fig. 7.5, is one such well documented case. The application of the relevant boundary conditions to Maxwell's equations lead to the Fresnel equations for the reflection and transmission coefficients at an interface between two uniform materials [171]. If the incident wave is assumed to be of unit amplitude then the amplitude of the reflected wave for the TE polarisation is given by:

$$r_{TE} = \frac{n_1 \cos(\theta_1) - n_2 \cos(\theta_2)}{n_1 \cos(\theta_1) + n_2 \cos(\theta_2)} \quad , \quad (7.67)$$

and correspondingly for the TM polarisation:

$$r_{TM} = \frac{n_2 \cos(\theta_1) - n_1 \cos(\theta_2)}{n_2 \cos(\theta_1) + n_1 \cos(\theta_2)} \quad . \quad (7.68)$$

Snell's law can be used to remove the dependence of the Fresnel equations on the angle of refraction. Snell's law (equation 4.105) may be rearranged to give:

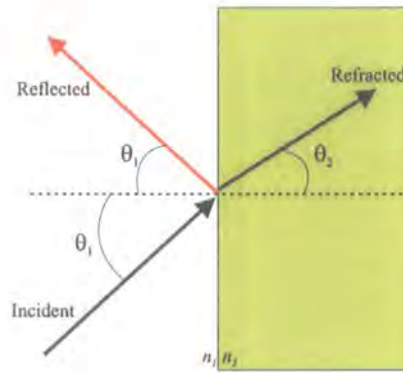


**Figure 7.5:** Reflection at an interface between two materials of uniform refractive index,  $n_1$  and  $n_2$ .

$$\theta_2 = \sin^{-1} \left( \frac{n_1}{n_2} \sin(\theta_1) \right) \quad , \quad (7.69)$$

which can be substituted into equations (7.69) and (7.70) to give a more convenient form for the coefficients. For the situation under consideration the material on the LHS of the interface is air; hence  $n_1 = 1$ , and the two reflections coefficients, as functions of angle of incidence only, are given by:

$$r_{TE} = \frac{\cos(\theta_1) - n_2 \cos(\sin^{-1}(\sin(\theta_1)/n_2))}{\cos(\theta_1) + n_2 \cos(\sin^{-1}(\sin(\theta_1)/n_2))} \quad , \quad (7.70)$$

and

$$r_{TM} = \frac{n_2 \cos(\theta_1) - \cos(\sin^{-1}(\sin(\theta_1)/n_2))}{\cos(\theta_1) + \cos(\sin^{-1}(\sin(\theta_1)/n_2))} \quad . \quad (7.71)$$

The intensities of the reflected waves may be calculated as the square of the reflection coefficients.

### Brewster Angle

The Fresnel equations may also be used to derive a special angle known as the Brewster angle. This is a particular angle of incidence ( $\theta_B$ ), at which the reflected intensity from a uniform material is zero. The effect exists for the TM polarisation only and the Brewster

angle is given by [12]:

$$\theta_B = \tan^{-1} \left( \frac{(n_2)}{(n_1)} \right) \quad (7.72)$$

Whilst this does not provide any additional checking mechanisms for our implementation of the interface matching calculation it is an interesting feature which will be seen when uniform materials are considered.

## 7.5 Results

### 7.5.1 Uniform Materials

The simple uniform media case greatly assists with ensuring the interface matching calculation is correct. Consider how the calculation progresses for a uniform block of material with a refractive index of  $n_r$ . A single incident plane-wave, with an angle of  $\theta_1$  degrees, and a frequency of  $\omega$  is incident on the material. On the air side of the structure there are two plane-wave solutions. The first is simply the incident plane-wave with wavevector components given by:

$$k_y = \frac{\omega}{c} \cos(\theta_1) \quad (7.73)$$

$$k_z = \frac{\omega}{c} \sin(\theta_1) \quad . \quad (7.74)$$

The second is the reflected wave with wavevector  $(-k_y, k_z)$ . On the RHS of the interface  $\omega$  and  $k_z$  are used in the complex bandstructure calculation to produce the same number of  $k_y$  solutions as there are plane-waves. There is a single real solution and enough imaginary and general solutions to equal the number of different  $g_z$  values in the reciprocal lattice vector set that has been used. The real solution will be the one that propagates with the same angle of refraction as dictated by Snell's law. If the eigenvectors associated with the propagating solution are examined they will show a single plane-wave, corresponding to  $g_z = 0$ , with some coefficient  $H_{g_z=0}^n$ , or  $E_{g_z=0}^n$ , assuming the frequency is low enough.

Matching may be achieved relatively simply as there are just two plane-waves on the LHS which will match to the single plane-wave on the RHS. The coefficient for the reflected wave on the LHS will also be the amplitude of the wave. On the RHS there will be a

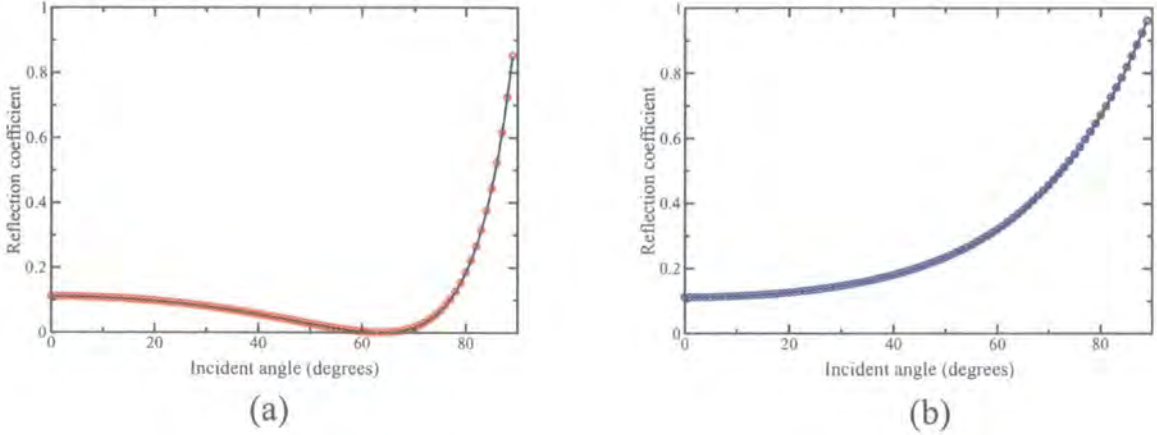


**Figure 7.6:** Fresnel Equations plotted for the TM (a) and TE (b) polarisations. The black curve represents values calculated from the Fresnel equations and the circles, red for TM and blue for TE, the results generated by the interface matching calculations. Exact agreement may be seen for the reflection at the interface with uniform block ( $n = 2$ ).

matching coefficient,  $b_0$ , which when multiplied by  $H_{g_z=0}^n$  (or  $E_{g_z=0}^n$ ) will give the amplitude of the plane-wave. As it is the only solution on the RHS its amplitude must equal the sum of both the LHS amplitudes.

Fig. 7.6 shows the reflection coefficients plotted as a function of angle of incidence for a uniform structure. The curves were calculated using the Fresnel equations and the data points were then calculated by the interface matching calculation. The ‘square’ and then the ‘hexagonal’ uniform structures were used and produced the same results. The results for the matching calculation were identical to those calculated from the Fresnel equations. This provides a high level of confidence in the correct implementation of the interface matching calculation. The Brewster Angle may also be seen for the TE polarisation. Further checks were carried out using a range of frequencies and refractive index values and it was confirmed that both the reflection coefficients and angles of refraction corresponded to those expected for uniform materials.

**Propagating solutions**

Continuing with the uniform material example, it is also of use to calculate the proportion the original incident intensity which has been transferred to a particular propagating solution on the RHS. This will be calculated as the square of the amplitude of propagating

solution divided by the sum of all the real amplitudes on the RHS squared, multiplied by the proportion of the intensity that was not reflected on the LHS. Evanescent solutions are not included in the calculation as for an unbounded RHS only the real solutions may carry energy. For this simple case (TE):

$$P = (1 - R) * \left( \frac{H_{g_z=0}^n * b_n}{\sum \text{all real RHS amplitudes}} \right)^2 = (1 - R) \quad , \quad (7.75)$$

Since, for a uniform system, there is only one plane-wave on the RHS.  $R$  is the square of the reflection coefficient, and  $P$  is the proportion of the original intensity in the propagating solution on the RHS. When considering photonic crystals there will be a range of Bloch waves and the value of  $P$  for each Bloch wave will be the coupling efficiency for the particular wave. Once satisfaction was achieved that the interface matching calculation could reproduce the results of uniform materials, photonic crystal structures were considered.

## 7.5.2 Photonic Crystals

In Sec. 7.3 it was stated that only half the  $k_y$  solutions produced by the complex bandstructure calculation, for a fixed  $k_z$  and  $\omega$ , are valid physical solutions. This meant a sorting algorithm was required to select the required set of solutions produced by the complex bandstructure calculation for use in the matching calculation. The algorithm is outlined in Fig. 7.7. The solutions are split into three categories: purely real, purely imaginary and general complex. The purely imaginary and general solutions are the most straightforward to sort. They must be unique solutions, not related to another by a linear combination of reciprocal lattice vectors, and must also decay to the right of the interface. The real solutions must also be unique solutions within the Brillouin Zone, but they also have the additional requirement that they must propagate in a physical manner. In Section 4.12 it was explained that for an incident plane-wave to couple to a Bloch wave it must have a physical propagation direction; it must have a positive group velocity in the  $y$  direction,  $[v_g]_y$ :

$$[v_g]_y = \frac{\partial \omega}{\partial k_y} \quad (7.76)$$

To ensure that this condition was met the group velocity in the  $y$  direction was calculated for

each real solution computed by the complex bandstructure calculation.

The most problematic issue of the interface matching calculation for photonic crystals was the need to carefully consider the integration across  $z$  which was briefly mentioned in Sec. 7.3. The integration has the effect of equating the sum of all the coefficients which project onto the one-dimensional interface. Integration occurs for a period or number of periods in the  $z$  direction at the interface. The calculation presented was for some general period  $L$  but this requires further consideration for each arrangement being considered. Appendix B contains further details which are of use for implementing the calculation using different interface arrangements.

### 7.5.3 Optimisation

The previous chapter considered the optimum superprism configuration using the hexagonal lattice type with the limitation that only a single refraction angle existed for a single incident plane-wave. The optimum configuration identified was  $n = 2$ ,  $r = 0.4a$ ,  $\omega = c/a$  and a TM polarisation. The aim of this section is to evaluate any additional benefits which may exist by considering superprisms which allow multiple refraction angles.

An optimisation study was carried out using the hexagonal lattice and a range of rod radii, refractive indices and frequencies. The range of structures remained the same as in the previous chapter (see Table 5.2). The method for identifying optimum structures was also the same as in the previous chapter: the gradient, or inverse gradient of the dispersion surface was calculated in the  $\Gamma$ - $K$  and  $\Gamma$ - $M$  directions. The appropriate complex bandstructure methods described in Chapter 4 were used to calculate the required wavevector magnitudes. The existence of multiple refraction angles in the study did introduce some additional complexity due to the existence of multiple equi-frequency curves in the reference directions. This was dealt with by the use of a sorting routine to ensure that only wavevector values forming a continuous equi-frequency curve were used in the gradient calculations.

The extreme gradient, or inverse gradient, values for each of the background refractive index values were identified for both the  $\Gamma$ - $K$  and  $\Gamma$ - $M$  directions, and both the TE and TM polarisations. The results are presented in Table 7.1 for the  $\Gamma$ - $K$  direction and Table 7.2 for the  $\Gamma$ - $M$  direction. Previously, when only a single refraction angle was permitted, no trends were identified in the results. For the multiple refraction angle case there seems to be a trend

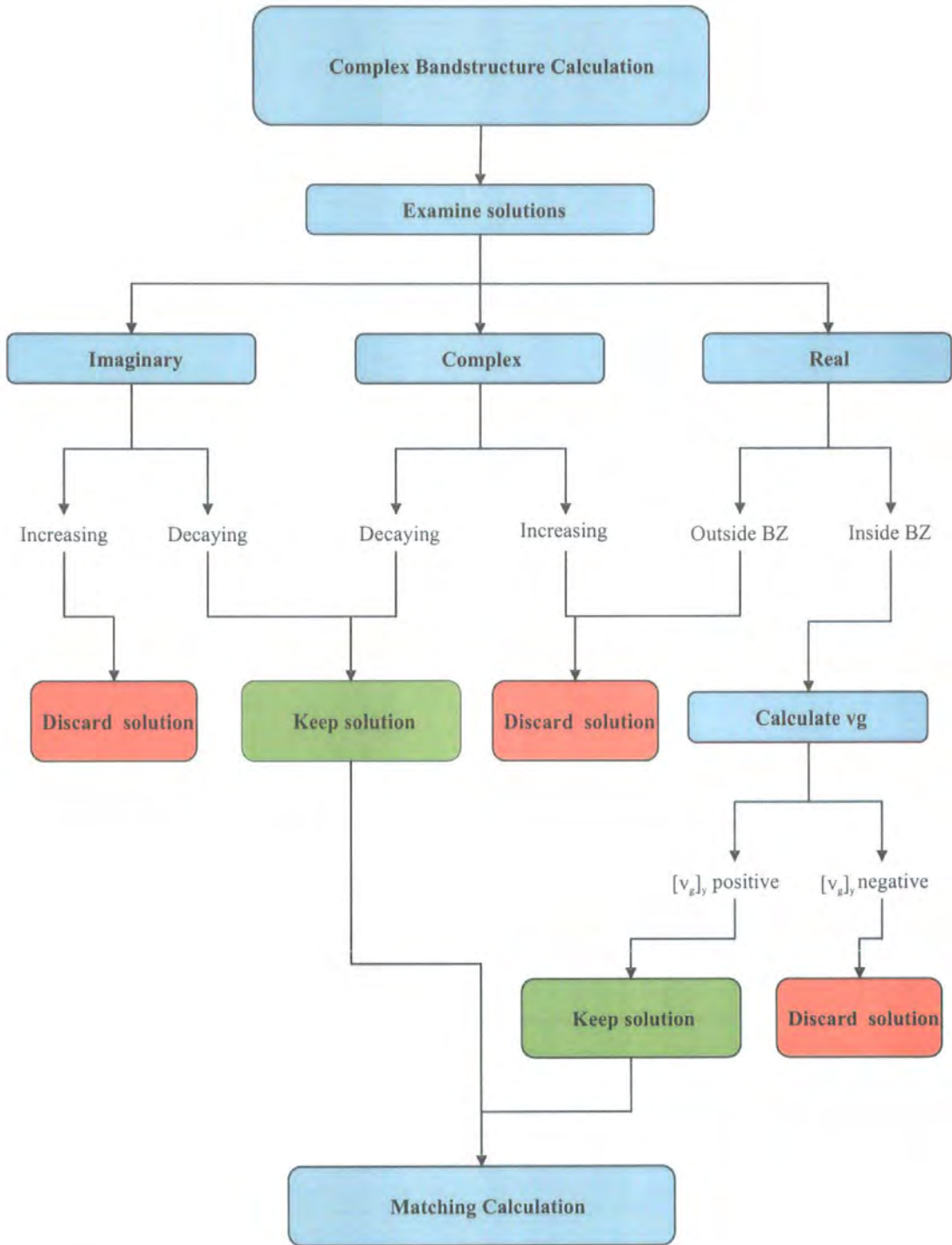


**Figure 7.7:** Outline of interface matching calculation. Note BZ is the first Brillouin Zone and  $v_g$  is the group velocity.

to the lowest rod radius. 20 extreme values were calculated and 14 of these occurred at the rod radius of  $r = 0.1a$ . This suggests that there are benefits to keeping the rod radius low when considering the dispersion characteristics of the hexagonal lattice.

The gradient for the optimum structure in the previous chapter had a value of -1.3. If the values given in Tables 7.1 and 7.2 are examined then it is evident that benefits may exist from considering multiple refraction angles. The lowest magnitude seen in the results was 1.7 (for  $n = 2$ ,  $r = 0.1a$  and a TM polarisation in  $\Gamma - K$  direction) and the highest magnitude seen was -9.1 (for  $n = 5$ ,  $r = 0.1a$  and a TE polarisation in  $\Gamma - M$  direction). The dispersion surfaces for most extreme values in the two reference directions were calculated for both polarisations. The results are shown in Fig. 7.8. The calculated dispersion surfaces are obviously more complex than the single refraction angle curves as they possess multiple equi-frequency curves. The sharp features are clearly visible and the feature corresponding to the most extreme inverse gradient value calculated may be seen figure 7.9c.

For the use in superprism applications though the utility of these structures is highly questionable. The features of interest have become so sharp that they exist for only a very narrow ranged on  $k_z$  values. Hence, whilst potentially offering superprism properties it is only for a very limited range of angles of incidence. This is especially evident when the dispersion surface for the optimum configuration ( $n = 5$ ,  $r = 0.1a$ ,  $\omega = 0.81c/a$  and a TE polarisation) shown in Fig. 9c is examined. In the direction of interest the surface may also be seen to possess three different wavevector magnitudes. Two of these values possess a level of curvature which would seem to make them of interest from a superprism perspective. The existence of multiple refraction angles introduces the need to perform an interface matching calculation to determine the coupling to the three different possible refraction channels. This is considered in the following section.

Refractive Index	TE		
	Rod Radius	Frequency	Gradient
2	0.3	0.97	-2.1
3	0.1	0.99	2.1
4	0.1	0.81	2.8
5	0.4	0.90	5.9
6	0.1	0.30	-1.9

Refractive Index	TM		
	Rod Radius	Frequency	Gradient
2	0.1	0.52	1.7
3	0.1	0.68	-5.1
4	0.1	0.52	-4.3
5	0.1	0.83	-2.9
6	0.1	0.34	-2.9

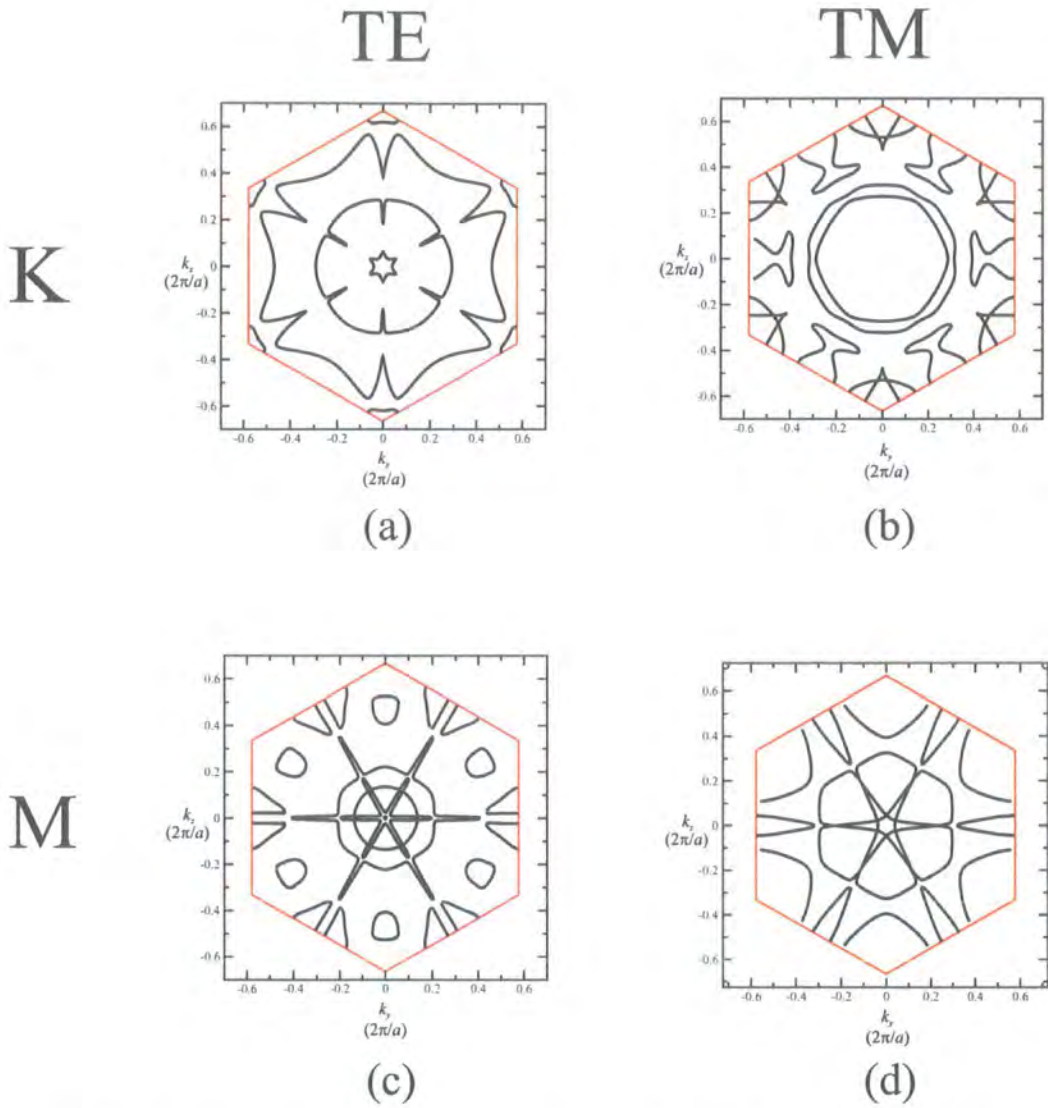
Table 7.1: Extreme values in the  $\Gamma - K$  direction.

Refractive Index	TE		
	Rod Radius	Frequency	1/Gradient
2	0.4	0.73	-6.7
3	0.1	0.70	-5.8
4	0.1	0.52	3.2
5	0.1	0.81	-9.1
6	0.1	0.35	-7.3

Refractive Index	TM		
	Rod Radius	Frequency	1/Gradient
2	0.2	0.90	-2.3
3	0.1	0.93	3.9
4	0.3	0.85	-1.9
5	0.1	0.94	-2.2
6	0.2	0.97	-2.5

Table 7.2: Extreme values in the  $\Gamma - M$  direction.



**Figure 7.8:** Optimum dispersion surfaces for the TE and TM polarisations in the directions  $\Gamma - K$  and  $\Gamma - M$ . a) TE  $n = 5$ ,  $\omega = 0.9c/a$ ,  $r = 0.4a$ . b) TM  $n = 3$ ,  $\omega = 0.68c/a$ ,  $r = 0.1a$ . c) TE  $n = 5$ ,  $\omega = 0.81c/a$ ,  $r = 0.1a$ . d) TM  $n = 3$ ,  $\omega = 0.93$ ,  $r = 0.1a$ .

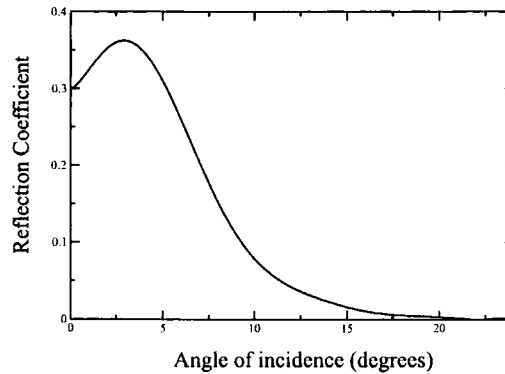


Figure 7.9: Reflection from the optimum single angle of refraction structure.

### 7.5.4 Matching

The matching calculation was used to investigate the optimum single refraction angle structure identified in the previous chapter and the optimum multiple refraction angle structure identified in this chapter. The structures will only be of use though if they demonstrate a significant coupling of the incident electromagnetic fields into the refraction channels of interest. The optimum single refraction angle structure ( $n = 2$ ,  $r = 0.4a$ ,  $\omega = 0.65c/a$  and a TM polarisation) was considered first and reflection from the structure plotted as a function of angle of incidence. The results are shown in Fig. 7.9. The figure shows that reflection at the first interface is relatively low, of the order of less than 36%, for the useful superprism range of the device. This could have been anticipated due to the low background refractive index combined with the low reflectance seen for interfaces between uniform structures with low refractive index contrasts. There is only one real wavevector solution in this instance and, as only real solutions may carry energy, at the peak value for superprism behaviour (3 degrees) 64% of the light which is incident on the structure couples to the superprism channel. This gives an overall coupling efficiency for the structure of  $P = 0.64$  and makes the structure potentially useful for superprism applications.

The interface matching calculation was also performed for the optimum multiple refraction angle structure identified in this chapter ( $n = 5$ ,  $r = 0.1a$ ,  $\omega = 0.81c/a$  and a TE polarisation). Reflection at the initial interface was found to be of the order of 58%. Reflection at the first interface would be expected to be higher due to the higher average refractive index of the structure. When the coefficients for each individual Bloch wave were considered it was found that a negligible quantity of the incident intensity was calculated to couple to

the required superprism refraction channel. This would make the configuration unsuitable for superprism applications.

The interface matching results strengthen the case for the single refraction angle structure to be identified as the optimum superprism structure and strongly suggests that the more complex, multiple refraction angle structure is of little utility for the proposed application.

## 7.6 Conclusions

In this chapter the physics present at an air/photonic crystal interface was investigated. The method used was a new method based on matching the tangential field components of an incident plane-wave to the Bloch waves in the photonic crystal, calculated using a complex photonic bandstructure method. The results of the calculation are the coefficients for both the Bloch waves in the photonic structure and the individual plane-waves on the air side.

The ability to consider the coupling to individual Bloch waves the hexagonal lattice superprism effect motivated a reconsideration of the hexagonal lattice superprism effect. An optimisation study was conducted, similar to the study undertaken in the previous chapter. However, without the single refraction angle restriction. The study showed that whilst it was possible to produce much sharper feature dispersion surfaces the utility of such extremely anisotropic surfaces was highly questionable for two reasons. Firstly, the optimum structures would only operate for a tiny range of incident angles; and secondly the coupling to the required Bloch wave in the optimum structure was negligible. The reflection coefficient for the optimum structure was calculated as 0.58 which allows just 42% of the incident light to couple to the photonic structure. This may be thought of as being at least partially attributable to the high average refractive index contrast. The coupling was predominantly to a propagating solution which did not provide the required superprism refraction channel. The superprism channel was calculated to channel a negligible fraction of the incident power.

The matching method was applied to the optimum single refraction angle hexagonal structure with much more promising results. Reflection at the first interface, for the superprism range of incident angles, was less than 36%. As only a single propagating solution existed the coupling efficiency to the superprism mode was therefore 0.64, indicating that the structure was predicted to be suitable for superprism applications.

The interface matching calculation described has been applied to two particular examples but the method is presented as a general approach suitable for further work. The approach could be applied to situations other than the superprism application considered here and there is also potential future work in the development of a calculation for other interface planes and also for matching across additional layers. The general method presented could form the basis of a range of further research projects.

# Chapter 8

## Conclusions and Suggestions for Future Work

### 8.0.1 Conclusions

This thesis has presented original theoretical work on one-dimensional and two-dimensional photonic structures. Plane-wave methods were used to consider two different dielectric systems: one-dimensional slab waveguide structures and two-dimensional photonic crystals.

#### One-Dimensional Structures

In Chapter 2 a theoretical model which is fundamental to a new biosensor technology was presented. The technology is currently being exploited internationally by Farfield Sensors Ltd. The technique provides a method for the real-time characterisation of thin films deposited on a waveguide structure. The model was applied to conduct a theoretical study on the effects of the structure manufacturing tolerances on the reliability of the characterisation of thin films. The study concluded that the resolution of the device was highly dependent on a well defined waveguide structure. To alleviate this concern a method of calibration was described which has been implemented to allow the high sensitivity of the device to be preserved. Experimental results of Cross *et al.* [80] analysed using the described model were also discussed, to allow the technique to be verified experimentally.

A vertically integrated dual-optical path slab waveguide arrangement, similar to the biosensor arrangement, formed the basis of Chapter 3. An athermal waveguide interferom-

eter device for the wavelength tracking of semiconductor diode lasers was proposed. It was shown that an athermal device design could be achieved by matching the thermal variations in the two guided mode propagation constants. The proposed athermal approach was optimised to maximise the sensitivity of the structure to wavelength fluctuations. The optimum structure was shown to be capable of tracking wavelength fluctuations to the level required for the wavelength locking diode lasers for DWDM applications.

### Two-Dimensional Structures

Initially a standard plane-wave eigenvalue method was described which can be used to calculate the allowed frequencies in photonic structures for a given wavevector. The method was then reformulated into a new TE complex bandstructure method. The complex bandstructure method enables the calculation of all allowed photonic crystal wavevectors, real, imaginary and general complex, at a fixed frequency. A second complex bandstructure approach was also presented. This allowed TM polarisation complex bandstructures to be calculated. It is believed that the results presented in this thesis using the described complex bandstructure approaches are the first of their kind. The complex bandstructure methods were also used as a component in the interface matching calculations described in Chapter 7. The refractive properties of an air/photonic crystal interface were also considered and a law of refraction for photonic crystal structures discussed.

The presented theoretical methods were applied first to square lattice photonic crystals, then also to hexagonal lattices. The main concern was with the refraction properties of the structures and their potential for producing enhanced refraction properties as a result of the appropriate “engineering” of their anisotropic bandstructures. In chapter 5 bandstructure anisotropy was optimised for the square lattice type. The results of the study showed that it was possible for the lattice type to provide refraction angles which were extremely sensitive to the incident angle, albeit only for a narrow range of incident angles. A large sensitivity to incident wavelength was also witnessed.

The hexagonal lattice was then studied and rather than optimising bandstructure anisotropy, a gradient method was used to optimise the refractive properties of the lattice. The gradient method was a more direct indicator of enhanced refractive properties. An optimum structure was found with a high sensitivity of the angle of refraction to the angle of incidence.

The configurations considered were initially restricted to situations in which a single angle of incidence produced a single refraction ‘channel’. The optimum hexagonal structure was able to produce superprism effects for a much larger range of possible incident angles than the square lattice. The refraction characteristics of the optimum structure were compared to experimental results in the literature and found to be superior. Negative refraction effects were also noted for the optimum structure.

Finally, the physics at an air/photonic crystal interface was considered. The approach employed complex bandstructures to allow the reflection coefficients at an interface to be calculated. The method also allowed the proportion of the incident light which coupled to individual Bloch waves in the photonic structure to be obtained. Whilst reflection may be considered by other methods this is believed to be the first occasion that the particular approach described has been used for such interfaces involving photonic structures. The results of the calculation confirmed the choice of the optimum superprism structure as a single refraction angle configuration, even when multiple refraction angles were permitted.

### 8.0.2 Suggestions for Future Work

The biosensor technology presented in chapter two has a wide range of potential for use in a variety of future work. Farfield Sensors has conducted and will continue to conduct research projects on a variety of biological systems. The diode wavelength tracker has potential but requires more research before it will be possible to develop a commercially viable device for inclusion in optical networks. A new company called Farfield Photonics is continuing to research the device with the aim of producing a commercially viable system. Experimental results are required and the design of a low cost compact device with inter-vendor compatibility needs to be addressed.

The photonic crystal work is, perhaps, of rather less immediate commercial applicability. Further work of interest in this area could involve confirming some of the predicted dispersion characteristics experimentally. The complex bandstructure matching method employed was used to calculate the fraction of the incident light reflected at an interface with a photonic crystal structure. This is an area which is beginning to be examined more seriously by experimentalists with possible ‘taper’ regions being suggested to improve coupling.

The use of a superprism for beam steering is also of interest. Research in this area could

investigate the possibility of designing optimised structures in which it would be possible to alter the direction of a refracted beam in response to some external factor, for example an applied electric field. This could form the foundation of some kind of optical switching device.

The interface matching approach could straightforwardly be extended to deal with finite layered systems; such analogous complex bandstructure work has already been performed for electronic structures. The first obvious candidate for such a calculation is a finite photonic crystal layer sandwiched between two semi-infinite bounding regions, although more complicated multilayered structures are also possible. It is conceded, of course, that such work can also be carried out using other methods.

Additionally the interface matching calculation could be applied to differing interface planes. The work presented included the simplest case with an interface in the  $z$  direction however other interface orientations may also be considered. This could potentially have an influence on not just reflectance at the interface but also on which refraction channels are accessed.

The new theoretical methods presented for photonic crystals could potentially be used for calculations on a wide range of photonic structures and offer useful tools for future research.

# APPENDIX A

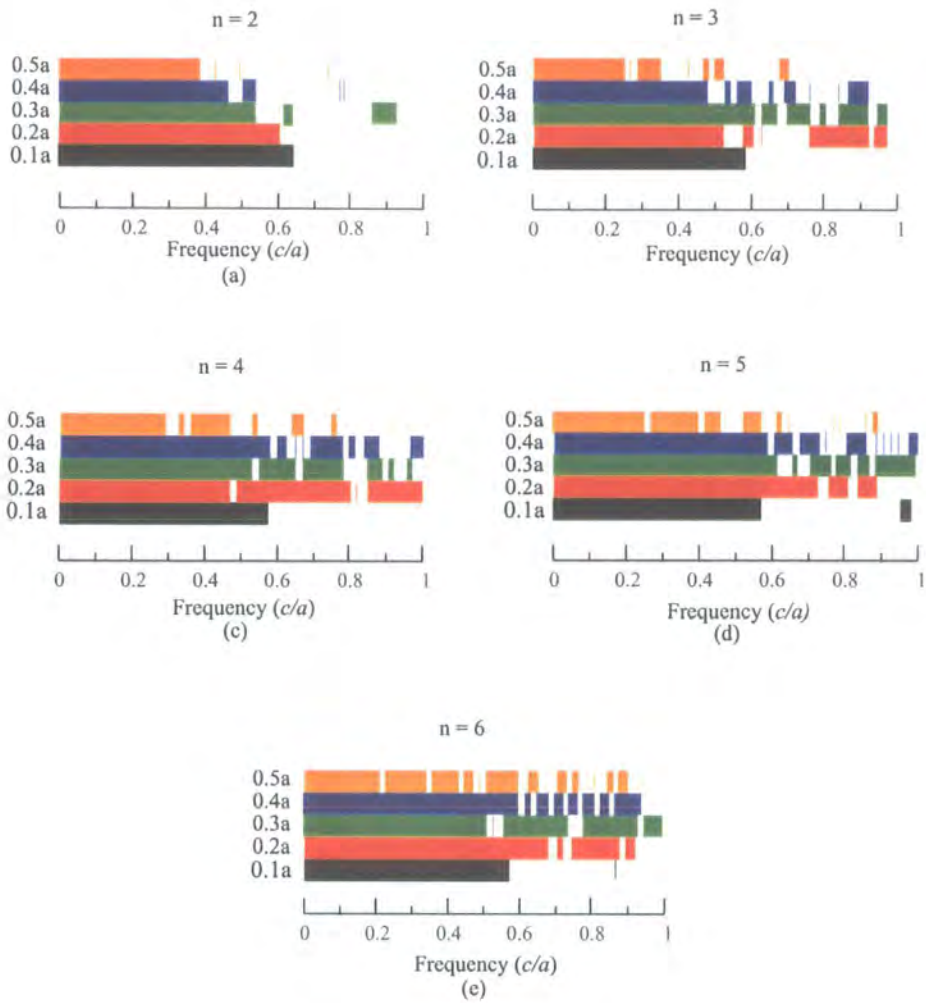


**Figure A-1:** Frequencies which exhibit single refraction angles for the TE polarisation and a square lattice structure consisting of dielectric rods in air. The results show a range of rod radii (indicated by different colours) and refractive index values of 2 (a), 3(b), 4(c), 5(d) and 6(e).

# APPENDIX B

## Interface Periodicity

The interface matching calculation in the main thesis is presented using an interface lying in the same direction as the  $z$  axis. Matching is carried out at the interface using the electric and magnetic field components which are tangential to the interface. If the TE polarisation is considered first then the field components for matching are calculated from the general magnetic field expression which was presented as equation (7.3):

$$H_x^{RHS} e^{-i\omega t} = \sum_n b_n H^n(y, z) e^{-i\omega t} \quad . \quad (\text{A-1})$$

The field is formed from a summation of individual Bloch waves which are of the form:

$$H^n(y, z) = \sum_{\mathbf{g}} H_{\mathbf{g}}^n e^{i(\mathbf{k}+\mathbf{g})\cdot\rho} \quad (\text{A-2})$$

The expression is for a general magnetic field which possess a periodicity which is defined by the two-dimensional reciprocal lattice vectors ( $\mathbf{g}$ s). To match the magnetic field on either side of the interface the general expression given by equation (A-2) must be evaluated at the interface plane for the particular structure under consideration. Consider first a photonic crystal based on the square lattice type:

### Square Lattice

In reciprocal space the square lattice is of the form shown in Fig. A-2. The defining set of reciprocal lattice vectors has individual vectors of the form:

$$\mathbf{g} = (g_y, g_z) \quad (\text{A-3})$$

Where:

$$g_y = \frac{2\pi}{a} n_y \quad (\text{A-4})$$

$$g_z = \frac{2\pi}{a} n_z \quad (\text{A-5})$$



**Figure A-2:** Square lattice in reciprocal space.

In general an interface may be defined by a unit vector which is normal to the interface. The interface under consideration lies in the same direction as the  $z$  axis and a unit vector  $\mathbf{q}$  may be defined perpendicular to the interface. This is shown in Fig. A-2. The reciprocal lattice vectors describe the periodicity of the magnetic field in general rather than at the interface. At the interface the magnetic field  $\mathbf{H}^{\text{a}}$  will still be periodic but this is not by necessity the same as the  $z$  periodicity of the reciprocal lattice vectors. The periodicity at the interface will be defined by the reciprocal lattice vectors which lie in the interface plane  $\mathbf{g}'$ . The required reciprocal lattice vectors are therefore of the form:

$$\mathbf{q} \cdot \mathbf{g}' = 0 \quad (\text{A-6})$$

For the case of an interface in the  $z$  axial direction the defining vector  $\mathbf{q}$  is of the form  $(1, 0)$ . The valid reciprocal lattice vectors must accordingly satisfy:

$$\frac{2\pi}{a} (1n_y + 0n_z) = 0 \quad (\text{A-7})$$

For this simple case this means that  $n_y = 0$  and the new set of reciprocal lattice vectors for use in the interface plane are of the form:

$$\mathbf{g}' = n_z \hat{\mathbf{k}} \quad (\text{A-8})$$

In fact this is superfluous for the square lattice case as when the interface is at  $y = 0$  the  $g_y$  dependence of the calculation is removed. The periodicity at the interface is the same as the reciprocal lattice vectors in the  $g$  direction ( $g_z$ s) and the calculation proceeds as in the main thesis.

### Hexagonal lattice

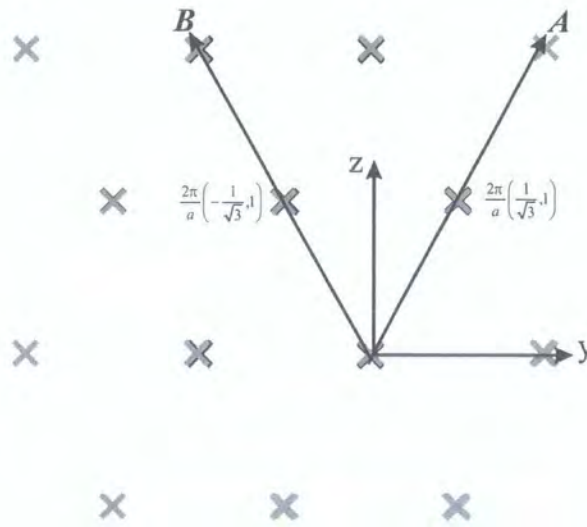


**Figure A-3:** Hexagonal lattice in reciprocal space.

Equation (A-1) may again be used to describe the magnetic field within the photonic crystal. The hexagonal lattice is shown in reciprocal space by Fig. A-3. The reciprocal lattice vectors were constructed from vectors in the **A** and **B** directions:

$$\mathbf{A} = \frac{2\pi}{a} \left[ \frac{1}{\sqrt{3}} \hat{\mathbf{j}} + \hat{\mathbf{k}} \right] \quad (\text{A-9})$$

$$\mathbf{B} = \frac{2\pi}{a} \left[ \frac{-1}{\sqrt{3}} \hat{\mathbf{j}} + \hat{\mathbf{k}} \right] \quad (\text{A-10})$$

These have been indicated on the figure and it may be seen that their periodicity differs from that of the structure in the  $y$  and  $z$  directions. This makes calculating the periodicity at the interface less trivial than for the square lattice. The choice of directions  $A$  and  $B$  was made to allow integer steps in the two directions to define the whole lattice:

$$\mathbf{g} = n_A \mathbf{A} + n_B \mathbf{B} \quad (\text{A-11})$$

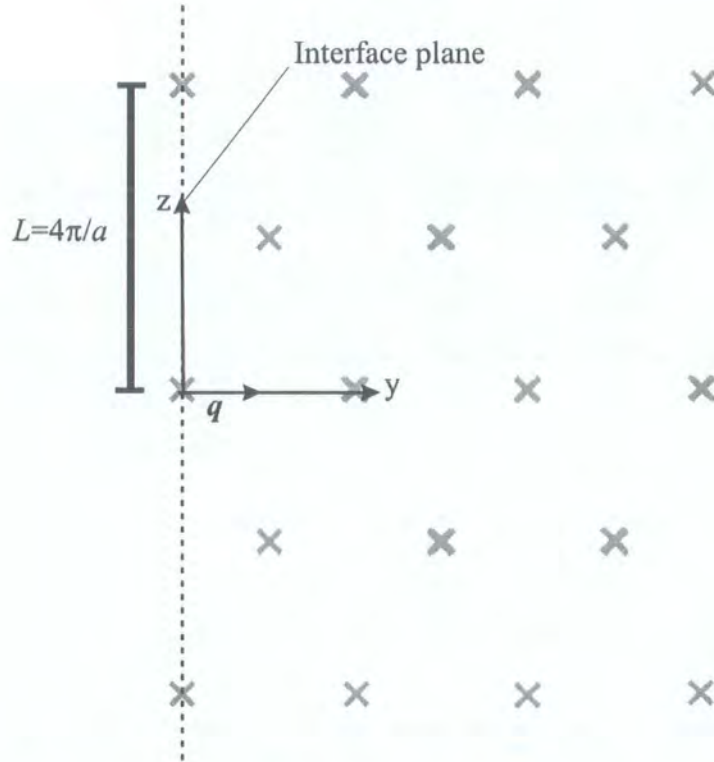


**Figure A-4:** Hexagonal lattice with an interface in the  $z$  direction.

Fig. A-4 shows the situation when an interface is introduced along the  $z$  direction. The normal to the interface,  $\mathbf{q}$ , has again been indicated. The set of reciprocal lattice vectors in the interface plane must still be defined by equation (A-6). In this instance:

$$\mathbf{g} \cdot \mathbf{q} = (1) \frac{2\pi}{a} \left( \frac{-n_B + n_A}{\sqrt{3}} \right) + (0) \frac{2\pi}{a} (n_A + n_B) = 0 \quad (\text{A-12})$$

By inspection it may be seen that the requirement is for  $n_B = n_A$ . Hence, the  $z$  component of the valid reciprocal lattice vectors at the interface ( $g'_z$ ) are given by:

$$g'_z = \frac{2\pi}{a} (2n_A) \quad (\text{A-13})$$

This is important as even for the simplifying case of an interface at  $y = 0$  the required reciprocal lattice vectors are not the complete set of the original  $g_z$  values, as in the simple square lattice case. The magnetic field at the interface will in this instance be of the form:

$$\mathbf{H}^n(y = 0, z) = \sum_{\mathbf{g}'} H_{\mathbf{g}'}^n e^{i(k'_z + g'_z)z} \quad (\text{A-14})$$

The calculation will now proceed along the same lines as in the main thesis but with the set of reciprocal lattice vectors,  $\mathbf{g}'$ , appropriate for the periodicity in the interface concerned. In addition it should be remembered that this set of reciprocal lattice vectors must also be used on the air side of the interface, where they dictate the allowed  $k_y$  solutions through equation (7.11).

### TM polarisation

The situation for the TM polarisation is equivalent to the TE polarisation. The matching calculation made use of an electric field which was of the form given by equation (7.39):

$$E_x^{RHS}(y, z)e^{-i\omega t} = \sum_n b_n E^n(y, z)e^{-i\omega t} \quad (\text{A-15})$$

With  $E^n$  of the form:

$$E_n(y, z) = \sum_{\mathbf{g}} E_{\mathbf{g}}^n e^{i(k'_y + g_y)y} e^{i(k_z + g_z)z} \quad (\text{A-16})$$

In this instance the new set of reciprocal lattice vectors, defined for TE polarisation, will again be required. The calculation may then proceed as in the main thesis.

# References

- [1] G Moore, *Electron.*, **38**, 8 (1965)
- [2] V M Dubin, *Microelectron. Eng.* **70**, 461 (2003)
- [3] S Borkar, *Queue* **1**, 28 (2003)
- [4] G Bourianoff G, *Computer* **36**, 44 (2003)
- [5] J Hecht, *City of Light: The Story of Fibre optics*, Oxford University Press, Oxford (1999)
- [6] N W Ascroft and N D Mermin, *Solid State Physics*, p330-352, Saunders College Publishing New York (1976)
- [7] B Tanner, *Introduction to the physics of electrons in solids*, Cambridge University Press, New York (1995)
- [8] A W Snyder and J D Love, *Optical Waveguide Theory*, Chaplin and Hall Ltd., London (1983)
- [9] O Parriaux and G J Veldhuis, *J. Lightwave Technol.* **16**, 573 (1998)
- [10] G J Veldhuis, O Parroaux, H J W M Hoekstra and P V Lambeck, *J. Lightwave Technol.* **18**, 677 (2000)
- [11] R Syms and J Cozens, *Optical Guided Waves and Devices*, McGraw-Hill, London (1992)
- [12] E Hecht and A Zajac, *Optics*, Addison-Wesley, Reading Mass. (1974)

- [13] J D Joannopoulos, R D Meade, J N Winn *Photonic Crystals*, Princeton University Press, Princeton N. J. (1995)
- [14] E Yablonovitch, *Phys. Rev. Lett.* **58**, 2059 (1987)
- [15] S John, *Phys. Rev. Lett.* **58**, 2486 (1987)
- [16] D W Tenquist, R M Whittle and J Yarwood, *University Optics*, Iliffe Books, London (1970)
- [17] A Yariv, *Optical electronics*, OUP, New York (1991)
- [18] G Kuriziki and A Z Genack, *Phys. Rev. Lett.* **61**, 2269 (1988)
- [19] E Yablonovitch, *J. Mod. Opt.* **41**, 173 (1994)
- [20] E Yablonovitch and T J Gmitter, *Phys. Rev. Lett.* **63**, 1950 (1989)
- [21] E Yablonovitch and T J Gmitter, *J. Opt. Soc Am. A* **7**, 1792 (1990)
- [22] E Yablonovitch, *J. Phys. Condens. Matter*, **5**, 2443 (1993)
- [23] E Yablonovitch, T J Gmitter and K M Leung, *Phys. Rev. Lett.* **67**, 2295 (1991)
- [24] S Noda, K Tomoda, N Yamamoto and A Chutinan, *Science* **289**, 604 (2000)
- [25] B T Holland, C F Blanford and A Stein, *Science* **281**, 538 (1998)
- [26] J. E. G. J. Wijnhoven and W. L. Vos, *Science* **281**, 802 (1998)
- [27] A Blanco, E Chomski, S Grubtchak, M Ibisate, S John, S W Leonard, F Meseguer, H Miguez, J P Mondia, G Ozin, O Toader and H M van Driel, *Nature* **405**, 437 (2000)
- [28] N Yamamoto, S Noda and A Chutinan, *Jpn. J. Appl. Phys., Part 2* **37**, L1052 (1998)
- [29] G Flemming and S.-Y. Lin, *Opt. Lett.* **24**, 49 (1999)
- [30] S G Johnson and J D Joannopoulos, *Appl. Phys. Lett.* **77**, 3490 (2000)
- [31] S Y Lin, J G Heterington, B K Smith, R Biswas, K M Ho, M M Sigalas, W Zubrzycki, S R Kurtz and J Bur, *Nature* **394**, 251 (1998)

- [32] S Noda, N Yamamoto and A Sasaki, *Jpn. J. Appl. Phys.* **35**, L909 (1996)
- [33] E Kuramochi, M Notomi, I Yokohama, J Takahashi, C Takahashi, T Kawashima and S Kawakami, *J. Appl. Phys.* **93**, 8848 (2003)
- [34] R Hillebrand, S Senz, W Hergert and U Gosele, *J. Appl. Phys.* **94**, 2758 (2003)
- [35] T Y M Chan and S John, *Phys. Rev. E* **68**, 046607 (2003)
- [36] M Campbell, D N Sharp, M T Harrison, R G Denning and A J Turberfield, *Nature* **404**, 53 (2000)
- [37] D N Sharp, A J Turberfield and R G Denning, *Phys. Rev. B* **68**, 205102 (2003)
- [38] M I Samoilovich, S M Samoilovich, A V Guryanov and M Y Tsvetkov, *Microelectron. Eng.* **69**, 237 (2003)
- [39] R D Meade, K D Brommer, A M Rappe and J D Joannopoulos, *Appl. Phys. Lett.* **61**, 495 (1992)
- [40] J N Winn, R D Mead and J D Joannopoulos, *J. Mod. Opt.* **41**, 257 (1994)
- [41] P R Villeneuve and M Piche, *Phys. Rev. B* **46**, 4969 (1992)
- [42] C Weisbuch, H Benisty, M Rattier, C J M Smith and T F Krauss, *Synth. Met.* **116**, 449 (2001)
- [43] Y Sugimoto, N Ikeda, N Carlsson and K Asakawa, *J. Appl. Phys.* **91**, 922 (2002)
- [44] W Robertson, G Arjavalingham, R D Meade, K D Brommer, A M Rappe and J D Joannopoulos, *Phys. Rev. Lett.* **68**, 2023 (1992)
- [45] M Plihal and A A Maradudin, *Phys. Rev. B* **44**, 8565 (1991)
- [46] T F Krauss, R M De La Rue and S Brand, *Nature* **383**, 699 (1996)
- [47] H Kosaka, T Kawashima, A Tomita, M Notomi, T Tamamura, T Sato and S Kawakami, *Phys. Rev. B*, **58**, R10096 (1998)
- [48] H Kosaka, T Kawashima, A Tomita, M Notomi, T Tamamura, T Sato and Kawakami S, *Appl. Phys. Lett.* **74**, 1370 (1999)

- [49] S-Y Lin, V M Hietal, L Wang and E D Jones, *Opt. Lett.* **21**, 1771 (1996)
- [50] D Scrymgeour, N Makkova, S Kim and V Gopalan, *Appl. Phys. Lett.* **82**, 3176 (2003)
- [51] T Prasad, V Colvin, D Mittleman, *Phys. Rev. B* **67**, 165103 (2003)
- [52] C Y Luo, M Soljacic and Joannopoulos JD, *Opt. Lett* **29**, 745 (2004)
- [53] A I Cabuz, E Centeno and D Cassagne, *Appl. Phys. Lett* **84**, 2031 (2004)
- [54] G H Cross, A Reeves, S Brand, M J Swann, L L Peel, N J Freeman, J R Lu, *J. Phys. D Appl. Phys.* **37**, 74 (2004)
- [55] P Yeh, *Optical Waves in Layered Media*, Wiley, New York (1988)
- [56] G H Cross, A A Reeves, S Brand, J F Popplewell, L L Peel, M J Swann and N J Freeman, *Biosens. Bioelectron.*, **19**, 383 (2003)
- [57] E Martin and R S Hien, *A Dictionary of Biology*, Oxford University Press, Oxford (2000)
- [58] A F Collins and F Caruso, *Rep. Prog. Phys.* **60**, 1397 (1997)
- [59] B Liedberg, C Nylander and I Lundstorm, *Biosensors and Bioelectronics* **10**, i (1995)
- [60] M Fivash, E M Towler, R J Fisher, *Current Opin. in Biotech.* **9**, 97 (1998)
- [61] E C Nice and B Catimel *Bioessays* **21**, 339 (1999)
- [62] T Turbadar, *Proc. Phys. Soc. (London)* **73**, 40 (1959)
- [63] B Liedberg, C Nylander, L Lundstorm, *Sens. Actuat.* **4**, 299 (1983)
- [64] R J Green, R A Frazier, K M Shakesheff, M C Davies, C J Roberts and S J B Tender, *Biomaterials* **21**, 1823 (2000)
- [65] V Silin and A Plant, *Trends in Biotech.* **15**, 353 (1997)
- [66] J Homola, S S Yee and G Gauglitz, *Sensors and Actuators B* **54**, 3 (1999)
- [67] M Malmqvist and R Karlsson, *Current Opin. Chem. Biol.* **1**, 378 (1997)

- [68] P R Edwards, A Gill, D V Pollard-Knight, M Hoare, P E Buckle, P A Lowe and R J Leatherbarrow *Anal. Biochem.* **231**, 210 (1995)
- [69] N J Goddard, K Singh, J P Hulme, C Malins and R Holmes, *Sens. and Actuators* **100**, 1 (2000)
- [70] D Yeung, A Gill, C H Maule and R J Davies, *Trends in Anal. Chem.* **14**, 49 (1995)
- [71] A A Michelson, *Studies in Optics*, University of Chicago Press, Chicago (1927)
- [72] G Bekefi and A H Barrett, *Electromagnetic Vibrations, Waves, and Radiation*, MIT Press, Cambridge, Mass. (1987)
- [73] R G Heideman, G J Veldhuis, E W H Jager and P V Lambeck, *Sensors Actuators B* **35**, 234 (1996)
- [74] B J Luff, J S Wilkinson, J Piehler, U Hollenbach, J Ingenhoff and N Fabricius, *J. Lightwave Technol.* **16**, 583 (1998)
- [75] A Bernard and H R Bosshard, *Eur. J. Biochem.* **230**, 416 (1995)
- [76] K Tiefenthaler and W Lukosz, *J Opt. Soc. Amer. B* **6**, 209 (1989)
- [77] G H Veldhuis, J H Berends, R G Heideman and P V Lambeck, *Pure Appl. Opt.* **7**, L23 (1998)
- [78] G J Veldhuis, O Parriaux, H J W M Hoekstra and P V Lambeck, *J. Lightwave Technol.* **18**, 677 (2000)
- [79] G J Veldhuis and P V Lambeck, *Appl. Phys. Lett.* **71**, 2895 (1997)
- [80] G H Cross, Y Ren and N J Freeman, *J. Appl. Phys.* **86**, 6483 (1999)
- [81] A Brandenburg and R Henninger, *Appl. Opt.* **33**, 5941 (1994)
- [82] R Kherrat, N Jaffrezic-Renault, P Greco, H Helmers, P Benech and R Rimet, *Sens. Actuators B* **37**, 7 (1996)
- [83] H Helmers, P Greco, R Rustad, R Kherrat, G Bouvier and P Beneche, *Appl. Optics.* **35**, 676 (1996)

- [84] J C Maxwell, *A Treatise on Electricity and Magnetism*, Oxford University Press, Oxford (1998)
- [85] W K H panofsk and M Phillips, *Classical Electricity and Magnetism*, Addison-Wesley Reading Mass. (1955)
- [86] J D Jackson *Classical Electrodynamics* , Wiley, New York (1962)
- [87] E kreyszig, *Advanced Engineering Mathematics* , Wiley, New York (1999)
- [88] R F Bunshan, *Handbook of Deposition Technologies for Films and Coatings*, Noyes Publications, Park Ridge N.J. (1994)
- [89] A Sherman, *Chemical Vapour Deposition for Microelectronics*, Noyes, Park Ridge (1987)
- [90] T A Scott and E I Mercer, *Concise Encyclopedia Biochemistry and Molecular Biology*, Walter de Gruyler, Berlin (1997)
- [91] L Puglise, A Coda, M Malcovati, M Bolognise, *J. Mol. Biol.* **231**, 698 (1993)
- [92] P C Weber, D H Ohlendorf, J J Wendoloski, F R Salemme, *Science* **243**, 85 (1989)
- [93] M Loesche, M Piepenstock, D Vakin, J Als-Nielsen, *Thin Solid Films* **210/211**, 659 (1992)
- [94] W Lukosz, D Clerc, P M Nellen, *Sens. Actuat. A* **25-27**, 181
- [95] D Vaknin, J Als-Nielsen, M Piepenstock, M Loesche, *Biophys. J.* **60**, 1545 (1991)
- [96] S Knoller, S Shpungin and E Prick, *J. Biol. Chem.* **266**, 2795
- [97] L J Harris, S B Larson, K W Hasel and A McPerson, *Biochemistry* **36**, 1581 (1997)
- [98] P Ferreira, W Lehr and L McKnight, *Technol. Forecast. Soc.* **69**, 741 (2002)
- [99] R O'Dowd, *Phonton. Network Comm.* **2:1** 97 (2000)
- [100] G P Agrawal, *Fiber-optic Communications Systems*, Wiley, New York (1997)

- [101] C Lin, *Optoelectronic Technology and Lightwave Communication Systems*, Van Nostrand Reinhold, New York (1989)
- [102] G H B Thompson, *Physics of Semiconductor Laser Devices*, Wiley, Chichester (1980)
- [103] W T Silfvast, *Laser Fundamentals*, Cambridge University Press, Cambridge (1996)
- [104] O Svelto, *Principles of Lasers*, Plenum Press, New York (1989)
- [105] J P Harbison and R E Nahory, *Lasers: Harnessing the Atom's Light*, Scientific American Library, New York (1998)
- [106] D Wood, *Optoelectronic Semiconductor Devices*, Prentice Hall, New York (1994)
- [107] D F Welch, *IEEE J. Sel. Top. Quant. Elect.* **6**, 1470 (2000)
- [108] J H Jang, S K Shin, H Kim, K S Lee, K J Park and Y C Chung, *IEEE Photon. Technol. Lett.*, **9**, 383 (1997)
- [109] Y Nakano, G Motosugi, Y Yoshikuni and T Ikegami, *Electronics Lett.* **19**, 437 (1983)
- [110] Y C Chung, J Jeong and L S Cheng, *IEEE Photon. Technol. Lett.* **5**, 792 (1994)
- [111] Y Park, S Lee and C Chae, *IEEE Photon. Technol. Lett.* **10**, 1446 (1998)
- [112] H Lee, G Y Lyu, S Y Park and J H Lee, *IEEE Photon. Technol. Lett.* **10**, 276 (1997)
- [113] K J Park, S K Shin, H C Ji, H G Woo and Y C Chung, *Optical Fiber Communication Conference, Baltimore USA* (2000)
- [114] Y C Chung and L W Stulz, *IEEE Photon. Technol. Lett.* **6**, 186 (1993)
- [115] Y Kokubun, M Takizawa and S Taga, *Electron. Lett.* **30**, 1223 (1994)
- [116] Y Kokubun, N Funato and M Takizawa, *IEEE Photon. Technol. Lett.* **5**, 1297 (1993)
- [117] B L Weiss, G T Reed, S K Toh, R A Soref and F Namavar, *IEEE Photon. Technol. Lett.* **3**, 19 (1991)
- [118] R A Soref, E Cortesi, F Namavar and L Friedman, *IEEE Photon. Technol. Lett.* **3**, 22 (1991)

- [119] G W C Kaye, and T H Laby, *Tables of Physical and Chemical Constants and Some Mathematical Functions*, Longman, London (1986)
- [120] G T Johnston, *Appl. Opt.* **16**, 1796 (1977)
- [121] Y Tsay, B Bendow, and S S Mitra, *Phys. Rev. B* **8**, 2688 (1973)
- [122] G Ghoush, *Handbook of Thermo-Optic Coefficients of Optical Materials with Applications*, Academic Press, London (1998)
- [123] G H Cross, personal communication (2003)
- [124] J D Joannopoulos, P R Villeneuve and S Fan, *Nature (London)* **386**, 143 (1997)
- [125] C Kittel, *Introduction to Solid State Physics*, Wiley, New York (1986)
- [126] R M Eisberg, *Quantum physics of atoms, molecules, solids, nuclei, and particles*, Wiley, New York (1985)
- [127] A J Ward, J B Pendry and W J Stewart, *J. Phys. Condens. Matter* **7**, 2217 (1995)
- [128] J B Pendry, *J. Phys. Condens. Matter* **8**, 1085 (1996)
- [129] S G Johnson and J D Joannopoulos, *Optics Express* **8**, 173 (2000)
- [130] K M Leung and Y F Liu, *Phys. Rev. B*, **41**, 10188 (1990)
- [131] E Economou and A Zdetsis, *Phys. Rev. B* **40**, 1334 (1990)
- [132] S John and R Ranagavajan, *Phys. Rev. B* **38**, 10101 (1988)
- [133] K M Ho, C T Chan and C M Soukoulis, *Phys. Rev Lett.* **65**, 3152 (1991)
- [134] S Datta, C T Chan, K M Ho and C M Soukoulis, *Phys. Rev. B* **17**, 10650 (1992)
- [135] S Satpathy, Z Zhang and M Salehpour, *Phys. Rev. Lett.*, **64**, 1239 (1990); **65**, 2478(E) (1990)
- [136] Z Zang and S Sataphy, *Phys. Rev. Lett.* **65**, 2650 (1990)
- [137] H S Sozuer and J W Haus, *Phys. Rev. B* **45**, 13962 (1992)

- [138] K Busch and S John, Phys. Rev. Lett. **83**, 967 (1999)
- [139] J Jin, *The Finite-Element Method in Electromagnetics*, Wiley, New York (1993)
- [140] A Figotin and Y A Godin, J. comput. Phys. **136**, 585 (1997)
- [141] W C Sailor, F M Mueller and P R Villeneuve, Phys. Rev. B **57**, 8819 (1998)
- [142] W Axmann and P Kuchment, J. Comput. Phys. **150**, 468 (1999)
- [143] D C Dobson, J. Comput. Phys. **149**, 363 (1999)
- [144] D Mogilevtsev, T A Birks, P St J Russell, J Lightwave Tech. **17**, 2078 (1999)
- [145] S J Cooke and B Levush, J, Comput. Phys. **157**, 350 (2000)
- [146] J P Albert, C Jouanin, D Cassiagne and D Bertho, Phys. Rev. B **61**, 4381 (2000)
- [147] E Lidorikis, M M Sigalas, E N Economou and C M Soukoulis, Phys. Rev. Lett. **81**, 1405 (1998)
- [148] R D Meade, A M Rappe, K D Brommer, J D Joannopoulos and O L Alerhand, Phys. Rev. B **48**, 8434 (1993).
- [149] S Xiao, L Shen, S He, Phys. Lett. A **313**, 132 (2003)
- [150] C T Chan, S Datta, Q L Yu, M Sigalas, K M Ho and C M Soukoulis, Physica A **211**, 411 (1994)
- [151] C T Chan, Q L Yu, K M Ho, Phys. Rev. B **51**, 16635 (1995)
- [152] S Fan, P R Villeneuve, R Meade and J D Joannopoulos, Appl. Phys. Lett. **65**, 1466 (1994)
- [153] K Sakoda and H Shiroma, Phys. Rev. B **56**, 4830 (1997)
- [154] J Arriaha, A J Ward and J B Pendry, Phys. Rev. B **59**, 1874
- [155] A J Ward and J B Pendry, Comput. Phys. Commun. **128**, 590 (2000)
- [156] J B Pendry and A MacKinnon, Phys. Rev. Lett. **69**, 2772 (1992)

- [157] J B Pendry, *J. Mod. Optics* **41**, 209 (1994)
- [158] J B Pendry, *J. Phys. [Condensed Matter]* **8**, 1085 (1996)
- [159] P M Bell, J B Pendry and A J Ward, *Computer Physics Commun.* **85**, 306 (1995).
- [160] J M Elson and P Tran, *Phys. Rev. B* **54**, 1711 (1996).
- [161] J M Elson and P Tran, *J. Opt. Soc. Am. A* **12**, 1765 (1995).
- [162] J Chongjun, Q Bai, Y Miao and Q Ruhu, *Opt. Commun.* **142**, 179 (1997)
- [163] S Brand and D T Hughes, *Semicond. Sci. Technol.* **2**, 607 (1987)
- [164] T Minami, K Sekine, H Ajiki and K Cho, *J. Lumin.* **87**, 378 (2000)
- [165] Y Ohfuti, H fukutome and K Cho, *J. Lumin.* **72**, 867 (1997)
- [166] K Cho, *J. Phys. Soc. Jpn.* **66**, 2496
- [167] A A Maradudin and A R McGurn, *J. Mod. Opt.* **41**, 275 (1994)
- [168] X P Feng, Y Arakawa, *IEEE J. Quantum Electron.* **32**, 535 (1996)
- [169] S Xiao and S He, *Physica B* **324**, 403 (2002)
- [170] R Padjen, J M Gerard and J Y Marzin, *J. Mod. Opt.* **41**, 295 (1994)
- [171] P A Tipler, *Physics for Scientists and Engineers*, Worth, New York (1991)
- [172] K Sakoda, *Optical Properties of Photonic Crystals*, Springer, London (2001)
- [173] W M Robertson, G Arjavalingam, R D Meade, K D Brommer, A M Rappe and J D Joannopoulos, *J. Opt. Soc. Am. B* **10**, 322 (1993)
- [174] A A Krokhin, J Arriaga and P Halevi, *Physica A* **241**, 52 (1997)
- [175] V V Poborchii, T Tada and T Kanayama, *Appl. Phys. Lett.* **75**, 3276 (1999)
- [176] T Zijlstra, E van der Drift, M J A de Dood, E Snoeks and A Polman, *J. of Vacuum Science and Technology B* **17**, 2734 (1999)
- [177] M Qiu and S He, *J. of Opt. Soc. Am. B-Opt. Phys.* **17**, 1027 (2000)

- [178] N Susa, Jpn. J. Appl. Phys. Part 1 **39**, 3466 (2000)
- [179] T Ohira, T Segawa, K Nagai, K Utaka and M Nakao, Jpn. J. Appl. Phys. Part 1 **41**, 1085 (2002)
- [180] M Galli M, M Agio, L C Andreani, L Atzeni, D Bajoni, G Guizzetti, L Businaro, E Di Fabrizio, F Romanato and A Passaseo, Euro. Phys. J. B **27**, 79 (2002)
- [181] M J A De Dood, E Snoeks, A Moroz and A Polman Opt. and Quantum Electron. **34**, 145 (2002)
- [182] L F Shen, Z Ye, S He, Phys. Rev. B **68**, 035109 (2003)
- [183] M J Escuti, J Qi, G P Crawford, Appl. Phys. Lett. **83**, 1331 (2003)
- [184] S Shoji, H B Sun, S Kawata, Appl. Phys. Lett. **83**, 608 (2003)
- [185] T Pan, F Zhuang and Z Y Li, Solid State Commun. **129**, 501 (2004)
- [186] Y-C Hsue and T-J Yang, Solid State Commun. **129**, 475 (2004)
- [187] R D Meade, A M Rappe, K D Brommer and J D Joannopoulos, J. Opt. Soc. Am. B **10**, 328 (1993)
- [188] S Foteinopoulou, E N Economou and C M Soukoulis, Phys. Rev. Lett. **90**, 107402 (2003)
- [189] B Gralak, S Enoch and G Tayeb, J. Opt. Soc. Am. A **17**, 1012 (2000)
- [190] C Y Luo, S G Johnson and J D Joannopoulos, Appl. Phys. Lett. **81**, 2352 (2002)
- [191] J B Pendry, Phys. Rev. Lett **85**, 3966 (2000)
- [192] C Luo, S G Johnson, J D Joannopoulos and J B Pendry, Phys. Rev. B **65**, 201104 (2002)
- [193] M Notomi, Phys. Rev. B **62**, 10696 (2000)
- [194] W Park and C J Summers, Opt. Lett. **16**, 1397 (2002)
- [195] F Garcia-Santamaria, C Lopez and F Meseguer, Appl. Phys. Lett. **79**, 2309 (2001)

- [196] T Baba and M Nasanori, IEEE J. Quantum Electron. **38**, 909 (2992)
- [197] R D Meade, A Devenyi, J D Joannopoulos, O L Alerhand, D A Smith and K Kash, J. Appl. Phys. **75**,4753 (1994)
- [198] I Bolland, *Complex Bandstructure Calculations of the Electronic Sturcture of Nitride Quantum Wells* (PhD Thesis), University of Durham (2003)
- [199] V Heine, Proc. Soc. London **81**, 300 (1963)

